Hand X-ray absorptiometry for measurement of bone mineral density on a slot-scanning X-ray imaging system

RONALD DENDERE

Thesis presented for the degree of DOCTOR OF PHILOSOPHY

in the Department of Human Biology

UNIVERSITY OF CAPE TOWN

February 2014

DECLARATION

I declare that this thesis is my own work. Where collaboration with other people has taken place, or material generated by other researchers is included, the parties and/or materials are indicated in the acknowledgements or are explicitly stated with references as appropriate.

This work is being submitted for a Doctor of Philosophy (PhD) in Biomedical Engineering at the University of Cape Town. It has not been submitted to any other university for any other degree or examination.

_____ _____

Signature Date

ACKNOWLEDGEMENTS

I would like to thank the following individuals and organisations for their assistance and contribution towards the project.

First and foremost I would like to thank my supervisor and co-supervisor, Professor Tania Douglas and Dr Sarah Whiley, whose guidance and advice was an invaluable resource during the course of the project.

I also acknowledge and thank the following people for their contribution:

- Herman Potgieter for providing some useful insights and making several suggestions that contributed to the outcome of the project.
- Stef Steiner for sharing his vast knowledge of the Lodox Statscan as well as providing training on the use of the Lodox Statscan.
- Charles Harris and the staff at the Human Biology Departmental Workshop for the manufacture of the phantoms and the various devices used in the project.
- Michael Cassar and the rest of the staff members in the Human Biology Departmental Mortuary for their help in sourcing cadaver hands.
- Caroline Powrie at the Human Biology Museum for providing the excised bones.
- Gordian Kabelitz who assisted in the training of the active shape model algorithm and the evaluation of the segmentation algorithms.
- Radiographers, Nafeesah Karriem and Linda Bewerunge for taking the scans of the participants on the Lodox Statscan and Hologic machines, respectively, for the evaluation study.
- Veruschka Bailie, Manager at Maitland Crematorium, for granting permission to incinerate bones and the staff members at the crematorium who assisted with incineration.
- The students and university staff members who volunteered to participate in the evaluation study.

A special acknowledgement goes to the Medical Research Council, the University of Cape Town, Lodox Systems, and the National Research Foundation (THRIP programme) for their generosity in funding the project.

I also thank my parents, family and friends for their support throughout my academic career.

Above all, I would like to thank God, without whom life itself is not possible.

ABSTRACT

Bone mineral density (BMD) is an indicator of bone strength. While femoral and spinal BMDs are traditionally used in the management of osteoporosis, BMD at peripheral sites such as the hand has been shown to be useful in evaluating fracture risk for axial sites. These peripheral locations have been suggested as alternatives to the traditional sites for BMD measurement. Dual-energy X-ray absorptiometry (DXA) is the gold standard for measuring BMD due to low radiation dose, high accuracy and proven ability to evaluate fracture risk. Computed digital absorptiometry (CDA) has also been shown to be very effective at measuring the bone mass in hand bones using an aluminium step wedge as a calibration reference.

In this project, the aim was to develop algorithms for accurate measurement of BMD in hand bones on a slot-scanning digital radiography system. The project assessed the feasibility of measuring bone mineral mass in hand bones using CDA on the current system. Images for CDA-based measurement were acquired using the default settings on the system for a medium sized patient. A method for automatic processing of the hand images to detect the aluminium step wedge, included in the scan for calibration, was developed and the calibration accuracy of the step wedge was evaluated. The CDA method was used for computation of bone mass with units of equivalent aluminium thickness (mmAl). The precision of the method was determined by taking three measurements in each of 16 volunteering subjects and computing the root-mean-square coefficient of variation (CV) of the measurements. The utility of the method was assessed by taking measurements of excised bones and assessing the correlation between the measured bone mass and ash weight obtained by incinerating the bones.

The project also assessed the feasibility of implementing a DXA technique using two detectors in a slot-scanning digital radiography system to acquire dual-energy X-ray images for measuring areal and volumetric BMD of the middle phalanx of the middle finger. The dual-energy images were captured in two consecutive scans. The first scan captured the low-energy image using the detector in its normal set-up. The second scan captured the high-energy image with the detector modified to include an additional scintillator to simulate the presence of a second detector that would capture the low-energy image in a two-detector system. Scan parameters for acquisition of the dual-energy images were chosen to optimise spectral separation, entrance dose and image quality. Simulations were carried out to evaluate the spectral separation of the low- and high-energy spectra. Detective quantum efficiency

(DQE) was used for assessing image quality at various tube settings and entrance dose was measured using a dosimeter with an ionisation chamber.

To facilitate the computation of BMD, the dual-energy images were aligned using an automated, intensity-based image registration technique. A method for automatic identification of the target bone was designed, allowing for automated initialisation of model-based segmentation in the images used for both the CDA and DXA measurement techniques. Deformable and active shape models were compared for segmenting the bone from hand images in order to identify and select the more accurate method. The accuracy of the two segmentation techniques was quantified using the Hausdorff distance, with manual segmentation as a reference. Results showed that the active shape model segmented the bone of interest with higher accuracy and was selected for use in the measurement algorithms. A calibration phantom for hand DXA was designed and evaluated. The calibration expression derived by imaging the phantom was used to compute areal BMD from dual-energy images of test subjects.

A limitation of central DXA is that it provides areal BMD, which can be affected by bone size and patient positioning. This project suggests a method for measuring volumetric BMD, which is not affected by bone size, using basis material decomposition. The accuracy of DXA-derived measurements was evaluated by comparing measured bone mineral content and ash weight, obtained through incineration, of excised bones. The performance of the developed DXA system was also validated against a clinical DXA machine by assessing the agreement of areal BMD and bone mineral content (BMC) measurements in volunteers; agreement was quantified using the concordance correlation coefficient.

The CDA technique yielded *ex-vivo* bone mineral mass that ranged between 1.37 and 2.66 mmAl while the *in-vivo* bone mineral mass range was 2.34 – 5.18 mmAl. The CDA *in-vivo* bone mineral mass precision was 0.49%. The CDA measurements showed good correlation with ash weight, yielding a correlation coefficient of 0.92. The DXA measurements had good agreement with those taken on an established clinical DXA machine as shown by concordance correlation coefficient values of 0.92 and 0.98 for BMD and BMC, respectively. The DXA-derived BMC had an average accuracy error of 4.85% while the average areal BMD accuracy error was 5.49% and the average volumetric BMD accuracy error was 12.77%. The average accuracy error for the computation of bone volume was 10.91%. Precision studies yielded CV values of 1.35% for areal BMD, 1.48% for BMC and 1.80% for

volumetric BMD. The CV values of all measurement methods were within 2%, indicating that the methods have clinically acceptable precision.

Based on these results, it is concluded that phalangeal CDA-based bone mass measurements as well as DXA measurements of areal and volumetric BMD taken on a slot-scanning radiography system can potentially be used in the clinical management of osteoporosis.

CONTENTS

LIST OF FIGURES

LIST OF TABLES

LIST OF ABBREVIATIONS

μm – micrometre

μSv – microSievert

*a*BMD - areal BMD

Al – aluminium

ASM - active shape model

BMC - bone mineral content

BMD - bone mineral density

BUA - broadband ultrasound attenuation

CDA - computed digital absorptiometry

Cu – copper

CV - coefficient of variation

DM - deformable model

DPA - dual-photon absorptiometry

DQE - Detective quantum efficiency

DXA - dual-energy X-ray absorptiometry

DXL - dual-energy X-ray laser

DXR - digital X-ray radiogrammetry

ES - evolution strategy

ESF - edge spread function

FDA - Food and Drug Administration

FNAL - femoral neck axis length

FRAX - Fracture Risk Assessment Tool

GPS - generalised procrustes analysis

HAL - hip axis length

HD - Hausdorff distance

IEC - International Electrotechnical Commission

ISCD - International Society for Clinical Densitometry

keV – kilo electron volts

kVp – peak kilo volts

lp/mm – line pairs per millimetre

LSF - line spread function

LSSR - Linear Slot-Scanning Radiography

mA – milli-Amps

MI - mutual information

mm/s – millimetres per second

mmAl - equivalent aluminium thickness in mm

MSE - mean square error

MTF - modulation transfer function

NOF – National Osteoporosis Foundation

NOFSA - National Osteoporosis Foundation of South Africa

NOS - National Osteoporosis Society

NPS - noise power spectrum

PDF - probability distribution function

PDM - point distribution model

pQCT - peripheral quantitative CT

QCT - quantitative computed tomography

QMR - quantitative magnetic resonance

QUI - quantitative ultrasound index

QUS - quantitative ultrasound

R - Pearson product-moment correlation coefficient

R^2 - coefficient of determination

RA - radiographic absorptiometry

RMS - root-mean-square

RMSE - root mean square error

ROI – region of interest

SI - stiffness index

Sn – tin

SNR - signal-to-noise ratio

SOS - speed of sound

SPA - single-photon absorptiometry

SSE - summed square of residuals

SST - sum of squares about the mean

SXA - single-energy X-ray absorptiometry

TPS - thin plate splines

UNFPA - United Nations Population Fund

*v*BMD - volumetric BMD

VPA - volume per area

WHO - World Health Organisation

1. INTRODUCTION

The human skeletal system has a wide range of functions, which include providing structural support, locomotion, protection of certain organs, and calcium storage. The general health of this system is therefore crucial for the well-being of any individual. A common disease of the skeleton is osteoporosis, which is characterised by low bone mass and weakened bones that predispose patients to low-trauma fractures. Although the disease is common among post-menopausal white women, prevalence among elderly men is increasing (Damilakis et al., 2007).

The level of bone mineral density (BMD) is an indicator of the general health of the skeletal system. In particular, it is used in the diagnosis of osteoporosis and in follow-up visits to monitor disease progression or efficacy of treatment. The diagnosis of osteoporosis involves taking a femoral, spinal or forearm BMD measurement and comparing it with the mean of a sex-matched, young population using a scoring system. Dual-energy X-ray absorptiometry (DXA) is widely considered the gold standard for BMD measurement for the diagnosis of osteoporosis due to its high accuracy and precision as well as its proven ability in evaluating the risk of fracture in patients (El Maghraoui & Roux, 2008; Vaananen et al., 2011). Computed digital absorptiometry (CDA), which measures bone mass in finger bones in arbitrary units using aluminium as reference calibration, has also shown potential for the detection of osteoporosis (Bouxsein et al., 1997; Wasnich, 1998).

Early detection of osteoporosis is crucial for successful treatment and reduction of fracture risk. A DXA examination is, therefore, recommended for women above the age of 65 years or those who have reached menopause and have risk factors for osteoporosis (ISCD, 2013). A DXA examination is also recommended for men above the age of 70 years (ISCD, 2013). However, the rising population of people aged 60 years and above poses a challenge in the management of osteoporosis as the number of people requiring a BMD test will rise. This challenge is aggravated by the fact that DXA examination of the axial skeleton is not recommended for mass screening as it is relatively expensive (Nayak et al., 2011), is only available at specialist centres and is an ionising technique despite the radiation dose being extremely low. There is a need, therefore, for simpler, cheaper and more widely available methods for diagnosis and mass screening of patients. Screening tools such as the Fracture Risk Assessment Tool (FRAX), clinical decision tools based on machine learning techniques and BMD assessment at the peripheral skeleton using ionising or non-ionising techniques have been suggested for mass screening. This project addresses the measurement of

peripheral BMD and bone mass on a digital, linear slot-scanning radiography (LSSR) system (the Lodox Statscan) using DXA and CDA.

CDA computes bone mineral mass of the middle phalanx of the middle finger in ordinary digital radiographs of the hand using an aluminium step wedge, included in the image, as a calibration device (Bouxsein et al., 1997; Fiter et al., 2001; Ross, 1997). DXA uses two radiographic images acquired using different X-ray energies for quantitative assessment of bone or soft tissue. This project explores the possibility of acquiring the low- and high-energy images on a slot-scanning digital radiography system using two detectors. The project proposes that the BMD measurements are taken in the hand, since it does not have internal organs that are more susceptible to the effects of ionising radiation. BMD measurements in hand bones have been shown to be effective for screening and evaluation of fracture risk in the assessment of osteoporosis.

A limitation of central DXA is that it provides a mass-per-area density instead of the 'true' mass-per-volume density. Areal BMD measurements are affected by bone size and errors in placement of the bone during the scan can result in over-estimation of the BMD which may lead to misdiagnosis. In this project, an attempt is made to measure the volumetric BMD from a single DXA scan set. Volumetric BMD, which is not affected by bone size or bone placement, could potentially provide a more reliable bone measurement for screening and diagnosis of osteoporosis.

The BMD methods addressed in this project are primarily aimed at mass screening of potential osteoporosis patients.

1.1 Objectives

The Lodox Statscan is a low-dose, full-body, digital X-ray machine that is available primarily in trauma departments. An earlier study concluded that DXA-based BMD measurements are feasible on the Lodox Statscan with respect to the hip region (Flash, 2002). Addition of bone density measurement capability on existing machines that are used for different applications, particularly mammography machines, is becoming an acceptable method for enabling wider screening and identification of those with reduced axial BMD and higher risk of fractures (Bi et al., 2006; Hobert et al., 2006; Huo et al., 2010; Wilczek et al., 2013). For example, Sectra (Sectra, Sweden) have an add-on facility which enables their mammography machines to measure BMD in hand bones. Thus, a BMD screening examination can be conducted on patients who are available for another examination (e.g. mammography). In the case of the

Lodox Statscan, added BMD functionality would enable BMD screening to be performed, for example, on elderly patients undergoing X-ray imaging for a suspected fracture.

The aim of this project was to develop methods for accurate measurement of BMD and bone mineral content (BMC) in hand bones for screening patients for osteoporosis on the Lodox Statscan. In addition to DXA, CDA was implemented as an alternative method. The objectives of the project can be summarised as follows:

- Assess the feasibility of acquiring the dual-energy images for DXA on a slot-scanning digital radiography system (Lodox Statscan) using two detectors.
- Develop automated methods that require minimum user interaction for measurement of areal BMD in hand bones using DXA and CDA.
- Extend DXA to measure volumetric BMD with unit g/cm^3 using a single pair of low- and high-energy images.
- Evaluate the methods in terms of accuracy and precision.
- Conduct an evaluation study to compare areal BMD on the Lodox Statscan with a commercially produced clinical DXA machine.

Approval for the project was obtained from the university's Human Research Ethics Committee.

1.2 Thesis outline

This thesis describes the work carried out and the results obtained in an effort to realise the objectives stated above. The thesis has been organised as follows:

Chapter 2 provides an overview of human bone, osteoporosis and current techniques used in the measurement of BMD for diagnosis of the disease. The chapter also discusses the limitations of DXA and possible future trends in the assessment of osteoporosis. The contribution and relevance of this project to the future of management of osteoporosis is also discussed in this chapter.

Chapter 3 is a review of the principles of digital radiography in general, including factors that affect the image quality in digital radiography. The physical principles of DXA and CDA as well as current methods used in DXA technologies are discussed.

Chapter 4 discusses the method used for identification of the middle finger in the hand images and determination of the centroid of the middle phalanx in the detected middle finger. The centroid of the bone was used to automate the initialisation of model-based

segmentation. The theory, implementation and evaluation of two model-based segmentation methods are discussed.

Chapter 5 discusses the implementation and evaluation of the CDA method for measurement of bone mass.

Chapter 6 discusses the acquisition of the dual-energy images and the determination of values for the technical parameters of the scan.

The implementation of BMD measurement using DXA is described in Chapter 7. The chapter describes how areal and volumetric BMD are computed. The chapter also discusses the evaluation of the DXA method using measurements of excised bones and human subjects.

The thesis concludes with Chapter 8, which gives an overall conclusion of the outcomes of the project and recommendations for future work.

2. BACKGROUND

This chapter provides an overview of human bone, osteoporosis and current techniques used in the measurement of BMD for diagnosis of the disease. It also reviews the field of densitometry.

2.1 Human bone

The human skeleton consists of over 200 bones of different shapes and fulfils a variety of functions which include providing a structural framework, locomotion, calcium storage, and protection of internal organs. The hand, which is the anatomical region of interest in this project, consists of carpal bones, metacarpal bones and phalanges as shown in Figure 2.1.

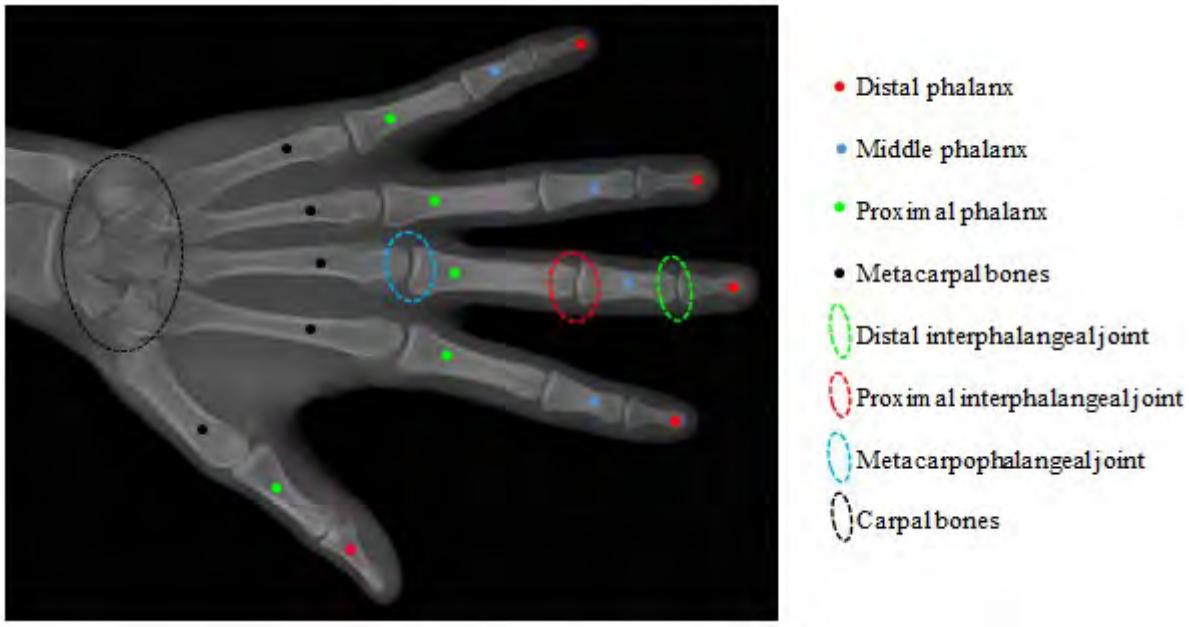

Figure 2.1: Radiographic image showing bones found in the hand.

A typical adult human skeleton is composed of 80% cortical bone and 20% trabecular bone (Clarke, 2008). The ratio of cortical to trabecular bone varies across bones and skeletal sites within the skeleton. Cortical bone is dense and solid whereas trabecular bone is composed of a honeycomb-like network of trabecular plates and rods interspersed in the bone marrow compartment (Clarke, 2008). Bone tissue is largely composed of mineral crystals as well as small amounts of organic matrix (collagen) and water (Augat & Schorlemmer, 2006; Clarke, 2008). Bone mineral provides mechanical rigidity and load-bearing strength, whereas the organic matrix provides elasticity and flexibility (Augat & Schorlemmer, 2006; Carter & Spengler, 1978; Clarke, 2008; Reilly & Burstein, 1974). The mineral content of bone is

mostly calcium hydroxyapatite, $Ca_{10}(PO_4)_6(OH)_2$, with small amounts of carbonate, magnesium, and acid phosphate (Clarke, 2008).

Bone undergoes growth, modelling, and remodelling during life. Osteoclasts are bone cells that remove calcium from bone while osteoblasts are cells that absorb blood calcium to build bone. Modelling is the process by which bones change their overall shape in response to physiological influences or mechanical forces. Bones may widen or change axis by removal or addition of bone to the appropriate surfaces by independent action of osteoblasts and osteoclasts in response to biomechanical forces (Clarke, 2008). Bone remodelling is the process by which bone is renewed to maintain bone strength and mineral homeostasis. The remodelling process, which lasts through the lifetime of the skeleton, resorbs old bone and forms new bone to prevent accumulation of bone micro-damage (Clarke, 2008).

During childhood and adolescence, bone formation exceeds resorption as osteoblasts build more bone than the amount removed by osteoclasts, leading to growth and development of the skeleton. Between 30 and 35 years of age, bone resorption begins to exceed bone formation resulting in a gradual decrease of bone mass with age (Fink et al., 2006). Women experience higher rates of bone loss after reaching menopause due to oestrogen deficiency (Ralston, 2005), a hormone that is important for maintaining bone balance in women (Krassas & Papadopoulou, 2001). This may result in a skeletal disease called osteoporosis when the reduction in bone mass results in weak and highly fragile bones.

2.2 Osteoporosis

Osteoporosis is a skeletal disease characterised by low bone mass and micro-architectural deterioration of bone tissue, with a consequent increase in bone fragility and susceptibility to fracture (WHO, 2003). Figure 2.2 illustrates the differences in a healthy and an osteoporotic femoral bone.

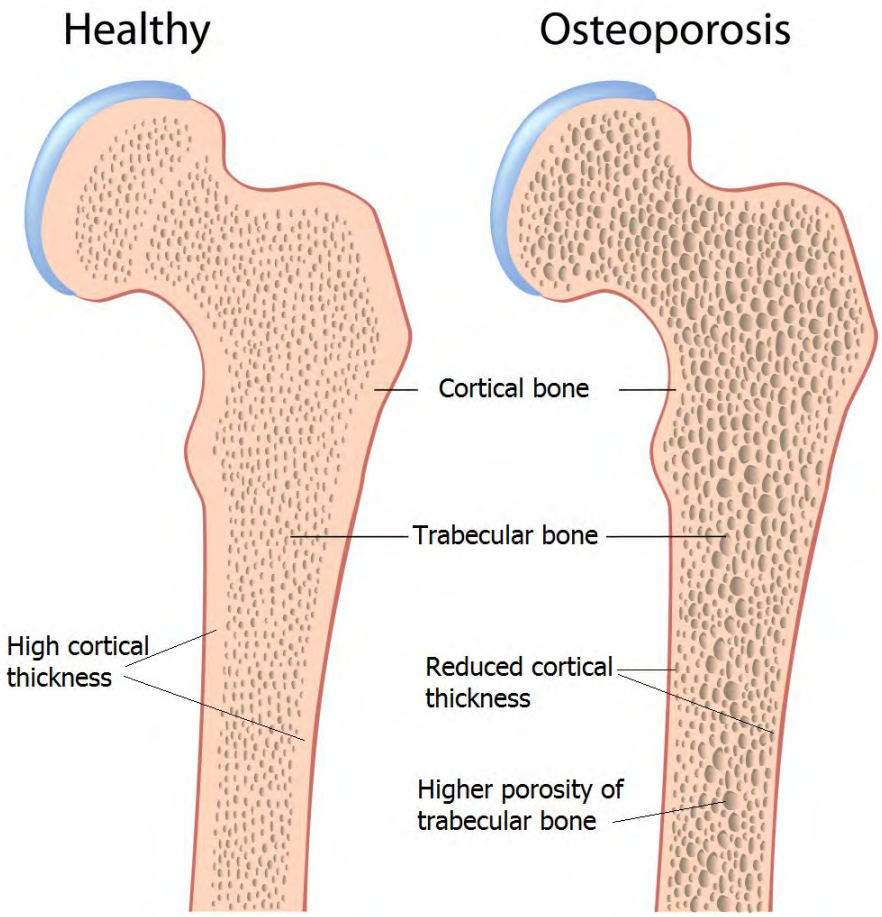

Figure 2.2: Difference between healthy and osteoporotic bone. (Source – http://www.healthtipscentre.com)

Low energy fractures are a clinical manifestation of osteoporosis. The disease has been dubbed a 'silent epidemic' by the National Osteoporosis Foundation (NOF) because no symptoms are observed until a fracture occurs. It is estimated that one in three women and one in five men will develop this disease in South Africa (NOFSA, 2013). The most common skeletal sites for osteoporotic fractures are the hip, spine and proximal forearm (Blake & Fogelman, 1997; Boehm & Link, 2004; WHO, 2003). Hip fractures are the most serious; 20% of patients die within a year of fracture, while more than 50% of the remainder are unable to live independently again (Blake & Fogelman, 2010; NOFSA, 2013). In the United States, 2 million people are estimated to suffer a fragility fracture every year, with 300 000 patients being hospitalised and disabled due to hip fractures alone (Blake & Fogelman, 2010). Annual fragility fractures are estimated at more than 12 000 in South Africa, resulting in an average hospitalisation of 7-9 days (NOFSA, 2013).

The pathophysiology of the disease is complex and many factors contribute to the fracture of bones (Lotz et al., 1991). However, bone mineral density (BMD) accounts for about 75–85% of the variance in bone strength in normal individuals (McCalden et al., 1993; Rosen, 2004). The remaining variance in bone strength may be accounted for by other factors such as bone size, shape, collagen, the amount and orientation of the organic matrix (Rosen, 2004) as well as fluoride therapy, hypermineralisation states and microstructure (Clarke, 2008). BMD is used as a surrogate for quantifying bone strength and as a direct measure of an individual's fracture risk (Augat & Schorlemmer, 2006).

2.3 Non-invasive measurement of bone mineral density

Bone densitometry (non-invasive measurement of BMD), is the first port of call for assessment and management of patients with osteoporosis. Invasive techniques such as bone biopsies are reserved only for cases where non-invasive techniques have produced inconclusive results (Ralston, 2005). According to an annotated bibliography on densitometry (Garn, 1962), non-invasive methods have been used in the assessment of the skeleton and measurement of bone density since as early as 1901.

Techniques for BMD measurement include single-photon absorptiometry (SPA), dual-photon absorptiometry (DPA), radiographic absorptiometry (RA), digital X-ray radiogrammetry (DXR), single-energy X-ray absorptiometry (SXA), dual-energy X-ray absorptiometry (DXA), computed digital absorptiometry (CDA), quantitative computed tomography (QCT), quantitative ultrasound (QUS) and quantitative magnetic resonance (QMR). These methods can be classified into ionising (SPA, DPA, RA, DXR, SXA, CDA, DXA and QCT) and non-ionising techniques (QMR and QUS). Ionising methods deliver radiation dose to a patient during examination while non-ionising methods do not deliver a radiation dose to the patient.

DXA is the most commonly used technique (Blake & Fogelman, 1997; Blake & Fogelman, 2010; Damilakis, 2007; Genant et al., 1996; Looker et al., 1998; Ralston, 2005), and is considered the gold standard for the measurement of BMD due to its low radiation dose and proven ability in the evaluation of fracture risk (El Maghraoui & Roux, 2008; Kanis & Glüer, 2000; Vaananen et al., 2011). The method for diagnosis of osteoporosis recommended by the World Health Organisation (WHO) involves measuring spine, hip or forearm BMD using DXA and calculating a T-score (WHO, 2003). The T-score describes the number of standard deviations by which the BMD in an individual differs from the mean value expected in young, healthy individuals (Kanis et al., 2013):

$$\text{T\_score} = \frac{\text{Measured BMD} - \text{Young adult mean BMD}}{\text{Young adult population SD}}$$

where *SD* is the standard deviation. Table 2.1 summarises how the T-score is interpreted.

Table 2.1: Interpretation of T-scores (Adapted from Kanis & Glüer (2000)).

T-score	Classification
$T \geq -1$	Normal bone
$-2.5 < T < -1$	Osteopenia
$T \leq -2.5$	Osteoporosis
$T \leq -2.5$ with one or more fragility fractures	Established Osteoporosis

2.3.1 Single and dual-energy absorptiometry

Absorptiometric methods are based on the absorption of photons (γ-rays or X-rays) by body tissues and the fact that different body tissues have different absorption characteristics. The behaviour of γ-rays and X-rays in matter is the same but X-rays are currently the type of photon used for bone measurements (Njeh & Shepherd, 2004). Absorptiometric methods include single and dual photon absorptiometry (SPA and DPA) as well as single and dual-energy X-ray absorptiometry (SXA and DXA).

SPA was first introduced for *in-vivo* assessment of bone in the 1960s (Cameron et al., 1968; Cameron & Sorenson, 1963) and has a proven ability in fracture prediction (Glüer et al., 1997). SPA is based on the measurement of the attenuation of a collimated photon beam produced by a single-energy radionuclide source. The anatomical site of interest is immersed in a water bath or surrounded by water bags to ensure a uniform thickness of overlying soft tissue (Adams, 1997). SPA has been shown to be capable of predicting fractures of the forearm, spine and hip (Glüer et al., 1997). SPA was restricted to peripheral sites and dual photon absorptiometry (DPA) was introduced to enable measurement of bone density at the femur or spine (Wahner & Fogelman, 1994). DPA uses photons with two distinct energy levels, allowing for correction of the variation of soft tissue without the need for a water bath. The earliest DPA machines had two radionuclide sources, typically ^{125}I (iodine) and ^{241}Am (Americium), as photon sources which were later replaced by a gadolinium source (^{153}Gd) that emits photons at two distinct energies (Wahner & Fogelman, 1994). However, major drawbacks of SPA and DPA include the need for regular replacement of the radioactive

source as well as low photon flux which results in lengthy scan times and poor spatial resolution (Glüer et al., 1997).

SPA and DPA are generally considered to be outdated methods that have since been replaced by SXA and DXA (Glüer et al., 1997). The principle of SXA is similar to that of SPA, with the radionuclide source in SPA replaced by an X-ray tube. This results in SXA having better precision, improved spatial resolution and shorter scan times (Kelly et al., 1994). However, DXA has found greater favour than SXA because it eliminates the need for the water bath used in SXA (Glüer et al., 1997). In addition to the diagnosis and monitoring of osteoporosis, DXA scans are also used for assessing the effectiveness of new therapies for treatment of osteoporosis (Blake & Fogelman, 2010; Glüer et al., 1993; Liberman et al., 1995; Orwoll & Oviatt, 1991).

DXA uses two radiographic images acquired at different energies to generate a bone image using image processing techniques. After proper calibration using phantoms of known density, the BMD of individual bones can be measured. The physical principles of single and dual-energy absorptiometry are discussed in detail in Chapter 3.

Some of the advantages of DXA are (Adams, 2013; Blake & Fogelman, 1997; Blake & Fogelman, 2010):

- Low radiation dose - radiation dose from DXA scans is generally equivalent to the radiation exposure levels associated with a few days of background radiation (Lang, 2010).
- Short scan times.
- High precision and accuracy.
- Stable calibration.
- High resolution images.
- Proven ability to predict fractures and diagnosis of osteoporosis.

Common sites evaluated using this technique include the lumbar spine and the proximal femur (Blake & Fogelman, 1997; Njeh & Sherpherd, 2004). The proximal femur is normally used for diagnosis of osteoporosis while the lumbar spine (L1-L4) is normally used for follow-up scans due to the higher content of trabecular bone which responds faster to treatment (Blake & Fogelman, 1997; Jones et al., 1987).

2.3.2 Radiographic absorptiometry

Introduced as far back as 1939 (Mack et al., 1939), radiographic absorptiometry (RA) measures bone mass in the peripheral skeleton using a radiographic image that includes a calibration standard usually in the form of an aluminium wedge. RA on standard, film X-ray machines involved capturing an image of the hand along with a calibration wedge on a film. The film would then be sent to an offsite central processing centre or processed locally where it would be digitised using a high-resolution video camera or laser digitiser. Bone mass would then be computed by comparing the optical density of the middle phalanges of the index, middle and ring fingers to that of the aluminium wedge to compute the equivalent aluminium thickness for each bone. The result was reported as the average equivalent aluminium thickness of the three bones and expressed in units of mmAl (Ross, 1997). The use of early RA techniques was limited due to poor precision, however advances in computer hardware and analysis methods have resulted in a return of and rise in the use of RA methods (Bouxsein et al., 1997; Ross, 1997).

Computed digital absorptiometry (CDA) is similar to RA, making use of a single-energy X-ray source, an aluminium step wedge and a charge-coupled device-based detector system for BMD estimation in the middle phalanx of the third digit (Bouxsein et al., 1997). The precision and accuracy of this technique are capable of making it a primary method for rapid assessment of patient risk for osteoporotic fractures (Wasnich, 1998). The physical principles of CDA and RA are discussed in Chapter 3.

2.3.3 Digital X-ray radiogrammetry

Introduced in the early 1960s (Barnett & Nordin, 1960), radiogrammetry is a radiographic technique for evaluating bone status in the metacarpals. This technique was initially implemented on ordinary film images of the hand. The advent of digital radiography increased interest in the technique, leading to digital radiogrammetry (DXR) which estimates metacarpal BMD using basic geometric measurements obtained from a single radiographic image of the hand (Rosholm et al., 2001).

Studies have shown that BMD measurements derived using this technique have high precision, are strongly correlated with forearm BMD and are lower in individuals with prevalent fractures (Bouxsen et al., 2002; Bach-Mortensen et al., 2006; Dhainaut et al., 2010; Reed et al., 2004; Wilczek et al., 2013).

2.3.4 Quantitative Computed Tomography

The high X-ray attenuation coefficient of bone allows for good contrast from surrounding tissue, thus making computed tomography (CT) a useful imaging modality for bone. Also, the relationship between the attenuation coefficient and BMD is highly linear. Therefore, with proper calibration, the Hounsfield units (the standard scale for representing grey-scale values in CT imaging) can be used to estimate the volumetric density of bone (Lang, 2004). For these reasons, quantitative CT (QCT) has been suggested for measuring BMD in trabecular and cortical regions of vertebrae. It can also be used to quantify BMD in the peripheral skeleton, in which case it is termed peripheral QCT (pQCT).

QCT uses a bone calibration phantom to convert the Hounsfield unit (HU) into a volumetric density with unit g/cm^3 (Langton et al., 2009). During a vertebral assessment of a patient, the calibration phantom is placed beneath the patient in order to minimise the effect of beam hardening (Lang, 2004). A software program analyses the phantom image, converting the HU into BMD and then places a region of interest on the resulting CT image before computing the average BMD in the vertebral region of interest.

Some of the advantages of QCT include the ability to assess cortical and trabecular bone separately; high-resolution QCT can be used to visualise the microstructure of trabecular bone which may improve the fracture risk evaluation. Also, QCT provides complete information about the distribution of bone mineral within a slice, making it possible to compute other biomechanical properties such as cross-sectional moment of inertia that describe bone strength (Glüer et al., 1997). Precision errors of between 1% and 2% have been reported for spinal BMD using QCT (Lang et al., 1999; Steiger et al., 1990). QCT is, however, associated with high patient dose that limits its use for routine BMD measurements; the effective dose for a spinal QCT is approximately 60 μSv compared to only 1 μSv for DXA (Lang, 2004).

2.3.5 Quantitative magnetic resonance

Quantitative magnetic resonance (QMR) uses the impact of the trabecular bone network on the relaxation times of marrow to assess the properties of trabecular bone (Pothuaud & Majumda, 2004). Interactions between bone marrow and bone cause a change in the relaxation times of the marrow. The magnitude of the change depends on the surface area-to-volume ratio of the bone-marrow interface and it increases with magnetic field strength and bone density. The spin-spin relaxation time, T_2, also depends on diffusion. The diffusion of

water along the bone-marrow interfaces causes an irreversible loss of magnetisation which in turn shortens the T_2 relaxation time of marrow, an effect which increases with magnetic field strength. The presence of trabecular bone also results in the modification of the magnetic field inhomogeneity-induced relaxation time, T_2*, of marrow. When a bone is placed in a magnetic field, magnetic lines of force are distorted at the bone/marrow interfaces and this gives rise to localised inhomogeneities in the magnetic field. Field inhomogeneities may cause further loss in magnetisation which results in a characteristic relaxation time T_2* that includes the contribution due to field inhomogeneities as well as the T_2 relaxation properties; this is the basis of QMR (Pothuaud & Majumda, 2004).

A correlation between T_2* values and vertebral strength has shown that MR imaging may potentially be used to predict fracture risk in patients (Brismar et al., 1997). T_2* in healthy persons has been found to increase slightly with age. Also, patients with osteoporosis have significantly longer T_2* values, which can be attributed to an increase in the inter-trabecular space caused by bone degradation (Wehrli et al., 1991). Marrow T_2 relaxation times have been shown to be dependent on BMD at low field strengths (Remy & Guillot, 1998). T_2* measures of the proximal femur have also been shown to be capable of differentiating between postmenopausal women with and those without osteoporotic hip fractures (Link et al., 1998).

The major limitation for the widespread use of QMR for assessment of osteoporosis is lower cost-effectiveness compared to DXA and QUS since measurements are taken on a whole-body MRI machine (Wehrli et al., 2002). However, compact MRI systems have been developed to lower the costs associated with QMR (Kose et al., 2004; Yoshioka et al., 2006). Other disadvantages include limited availability, long acquisition times and involuntary motion artefacts (D'Elia et al., 2009).

2.3.6 Quantitative ultrasound

Quantitative ultrasound (QUS) was first investigated as far back as the 1960s (Lang, 1969). Although limited success was realised through the 1970s, by the late 1980s the potential for ultrasound in the assessment of osteoporosis had become apparent and a number of medical device manufacturers began introducing devices for QUS assessment at peripheral sites of the skeleton (Glüer et al., 1997). In addition to being radiation-free, QUS devices are usually portable and inexpensive. However, widespread use of QUS is hampered by the fact that measurements differ significantly between machines (Hans & Krieg, 2009).

The basis of QUS is that an ultrasound beam is attenuated during transmission through the bone (Glüer et al., 1997; Pisani et al., 2013). For bone characterisation, the most useful frequency range is between 0.1 and 1 MHz and the relationship between the total attenuation and frequency in this range is linear; with the gradient being known as broadband ultrasound attenuation (BUA) (Glüer et al., 1997).

The discussion that follows is derived from Hans & Krieg (2009). QUS can be used to measure certain parameters that are related to bone density and those that are related to the velocity and attenuation of ultrasound waves as they travel through bone. Caution must be practiced when interpreting parameters such as sound velocity and attenuation as these are calculated differently depending on manufacturer and model. There are significant differences between QUS devices from different manufacturers and this affects interpretation of results and limits the comparison of results between devices. Devices that evaluate the heel seem to have the most clinical value because of the high metabolic turnover rate (Damilakis et al., 2007). Generally, the recommended parameters considered are the stiffness index (SI) and the quantitative ultrasound index (QUI). QUI combines the results of BUA and speed of sound (SOS) to improve precision (Glüer, 1997). Currently, there is sufficient evidence to support the ability of QUS to assess fracture risk in some but not all populations. QUS is also considered to be just as effective as DXA in predicting osteoporotic fractures in postmenopausal women. The diagnosis of osteoporosis using QUS is, however, more complicated due to the large variations in QUS measurements by skeletal site and the device-dependence of results.

2.4 The future of osteoporosis diagnosis

Although the disease is most common among postmenopausal Caucasian women (Blake & Fogelman, 2010; Kanis, 1994), elderly men are also affected (NOFSA, 2013) and the number of men and women experiencing low-energy fractures is rising worldwide (Damilakis et al., 2007). Age has been identified as a risk factor for fractures (Augat & Schorlemmer, 2006; Fink et al., 2006). According to the United Nations Population Fund (UNFPA) the global population of people aged over 60 years is rising and is set to reach 1 billion in 10 years, doubling to 2 billion by 2050 (UNFPA, 2012). The number of people affected by osteoporosis is expected to increase with the growth in the elderly population (Boehm & Link, 2004; Damilakis et al., 2007) and this requires measures to be put in place to mitigate the health burden caused by the disease.

Identifying individuals at risk of fractures and placing them on preventative treatment remains an effective method for reducing the occurrence of fractures (Black et al., 2000; Blake & Fogelman, 1997; Damilakis et al., 2007). In some centres, those who are receiving preventative treatment are required to have annual or biennial follow-up scans to monitor their response to treatment (Blake & Fogelman, 1997; Blake & Fogelman, 2010). This means that the number of people requiring BMD assessment is rising and is likely to continue rising. While DXA examination of the axial skeleton remains the most widely accepted technique for diagnosis of osteoporosis, its use for mass screening is not recommended as it is relatively expensive (Kim et al., 2013; Nayak et al., 2011; Pisani et al., 2013) and traditional BMD measurements should be restricted to those at high risk of osteoporosis as indicated by clinical risk factors (Ralston, 2005). Therefore, there is a need for innovative, cost-effective and efficient mass screening methods for osteoporosis. To this end, low-cost solutions have been suggested including clinical decision tools based on machine learning techniques, questionnaires and scanning of the peripheral skeleton using DXA and other techniques. A significant development in this regard is the Fracture Risk Assessment Tool (FRAX) by a WHO task force, which enables physicians to use information about a patient's clinical risk factors to assess the 10-year probability of fracture (Blake & Fogelman, 2010; FRAX-WHO, 2009). The tool has a questionnaire that elicits information about clinical risk factors such as age, gender, history of fractures, smoking habits and use of corticosteroids; the fracture risk can be computed with or without the knowledge of a femoral BMD.

Clinical decision tools based on machine learning use health status variables to identify those with high risk of osteoporotic fractures. Some of these variables are based on patient history such as duration of breastfeeding and onset of menopause (Kim et al., 2013). The use of such variables could reduce the accuracy of clinical decision tools for patients that have mental illnesses and memory loss who may not be able to provide precise information. BMD measurements at peripheral sites such as the hand and calcaneus could be a useful alternative screening tool to questionnaires as they would provide quantifiable and definitive information about the bone status of a patient. Peripheral BMD measurements can also be used as an alternative to central DXA for diagnosis of osteoporosis in cases where central DXA is not available (Glüer et al., 1997) and a number of studies have shown that BMD at peripheral sites can predict fractures at the femur and spine (Bouxsein et al., 1997; Buch et al., 2010; Dhainaut et al., 2011; Fiter et al., 2001; Friis-Holmberg et al., 2012; Glüer et al., 1997; Gulam et al., 2000; Ross, 1997; Wasnich, 1998). The use of peripheral densitometry devices in clinical practice is rising (Clowes et al., 2006). The United Kingdom National

Osteoporosis Society (NOS) acknowledges that peripheral BMD measurements can be used to predict fracture risk (Patel et al., 2011). They recommend that a triage approach be implemented to interpret peripheral BMD measurements in centres where such measurements are used for clinical examination. In this approach, upper and lower thresholds for a particular device have to be determined so that patients with osteoporosis, as per the WHO definition, can be identified on the device with 90% sensitivity and 90% specificity (Blake et al., 2005a; Patel et al., 2011). This means that 90% of patients with no osteoporosis should have a peripheral measurement that is above the upper threshold and 90% of patients with osteoporosis should have a measurement below the lower threshold. Recommendations by the NOS based on these thresholds are as follows (Patel et al., 2011):

- Treatment is recommended for patients with measurements below the lower threshold, particularly if other major risk factors for osteoporosis and/or fractures are present.
- A central DXA examination must be performed in patients with measurements between the thresholds to obtain a definite diagnosis.
- If the measurement is above the upper threshold and no low-trauma fracture is present then no treatment is required.

The NOS provides triage thresholds for some peripheral BMD devices and recommends that local studies should be done to establish the triage thresholds for a particular peripheral device should they not be available (Patel et al., 2011).

Another limitation of using only DXA-based BMD measurements for the diagnosis of osteoporosis is that despite the strong association between reduced BMD and increased fracture risk, there is considerable overlap of BMD levels in patients with and without fractures (Augat & Schorlemmer, 2006; Schuit et al., 2004). About 50% of fractures occur in women having a T-score above the WHO diagnosis threshold for osteoporosis (Siris et al., 2004; Sornay-Rendu et al., 2005). Furthermore, there is a weak correlation between changes in BMD and fracture risk after treatment with antiresorptive agents; while BMD stabilises or mildly increases, the risk of fracture appears to be considerably diminished (Augat & Schorlemmer, 2006). This suggests that BMD alone cannot adequately evaluate the fracture risk for individuals (Vaananen et al., 2011) and other factors affecting bone strength may be required to augment the measured BMD to yield a complete evaluation. For example, QCT has the ability to examine regions of interest in cortical and trabecular bone separately and to

provide accurate information on bone geometry. Geometry is of particular interest in the femoral neck where a QCT image can provide information for finite element analysis to estimate the elastic modulus of the bone, cross-sectional moment of inertia and other variables of interest that are related to bone strength (Ralston, 2005). The combination of BMD measurements and geometric parameters such as hip axis length (HAL) and femoral neck axis length (FNAL) has been shown to enhance the evaluation of fracture risk (Boehm & Link, 2004; Crabtree et al., 2002; Duboeuf et al., 1997; Griffiths et al., 1997; Lang et al., 1997).

The optimum skeletal site for the prediction of osteoporosis is a topic of great debate. Longitudinal studies suggest that most of the sites that are currently measured (spine, femur, radius) are useful in estimating the risk of fracture for any skeletal site (Njeh & Sherpherd, 2004). In clinical practice BMD measurements are taken at the proximal femur, distal forearm or lumbar spine since these are the most common fracture sites (Blake & Fogelman, 1997; Boehm & Link, 2004) and the WHO definition for osteoporosis is based on BMD measurements at those sites. However, there are several difficulties arising from measuring BMD at these sites, for instance, the distribution pattern of bone mineral in the spine becomes less uniform with age. When significant non-uniformity is present, there is less confidence that the measured BMD is a true representation of the skeletal status (Njeh & Sherpherd, 2004) and therefore spine DXA scans are less reliable for osteoporosis diagnosis in the elderly (Ralston, 2005). Posterior-anterior (PA) BMD measurements are also elevated in cases where degenerative and hypertrophic changes of the spine have occurred (Drinka et al., 1992; Ito et al., 1993; Reid et al., 1991). While lateral spine scans may be used to avoid the elevated BMD values in the presence of degenerative and hypertrophic changes in the spine, lateral scans are more demanding in terms of acquisition and processing while accurate repositioning is more difficult leading to reduced precision (Njeh & Sherpherd, 2004).

Regions of the proximal femur that are commonly evaluated are the femoral neck, the trochanter and total hip (weighted mean of the trochanter and femoral neck). The femoral neck is the most frequently used region in the diagnosis of osteoporosis (Blake & Fogelman, 1997). Positioning of the femoral neck is critical in order to maintain precision; errors as high as 6.7% and 3.5% have been observed due to varying angles of rotation and abduction respectively (Njeh & Sherpherd, 2004). DXA scans of axial sites are longer and deliver a higher radiation dose to the patient than those at peripheral sites (Wasnich, 1998).

Another drawback of DXA is that it only provides areal density with units of g/cm^2 instead of the 'true' volumetric density with units of g/cm^3. Areal BMD (*a*BMD) is highly dependent on bone size (Adams, 2013; Blake & Fogelman, 2010; Wehrli et al., 2006), thus if two bones have the same volumetric BMD (*v*BMD), the larger bone will have a higher *a*BMD (Srinivasan et al., 2012). This causes difficulties in universally applying the T-score system as the dependence on bone size causes differences in BMD measurements across gender and race (Blake & Fogelman, 2010). Currently, QCT is the only technique that can provide clinical volumetric BMD measurements (Lang, 2004; van Kuijk, 2010; Zhang et al., 2010). However, routine use of QCT is not recommended due to the high radiation dose associated with the technique (Lang, 2004; Langton et al., 2009).

These limitations suggest that, in the future, the management of osteoporosis may shift from an absolute reliance on BMD measurements at central sites using DXA for identifying those at risk of fractures towards a multistage approach. This approach could include screening methods to identify candidates for DXA examination with further steps for assessing other bone strength properties to provide a more comprehensive evaluation of bone status. Mass screening would prevent the needless exposure of patients to radiation if clinical risk factors indicate an obvious absence of osteoporosis. BMD measurements at peripheral sites, having lower effective dose than measurements at central sites, may complement the screening process in cases where questionnaires have not yielded conclusive results. Those identified, through screening, as being at risk of having osteoporosis could subsequently be requested to have a central DXA examination to confirm the presence of the disease according to the WHO definition. Other properties of bone strength such as hip axis length (HAL), femoral neck axis length (FNAL) and 3-D BMD distribution as measured by other techniques can be evaluated to provide an improved estimation of the fracture risk so that the most suitable treatment may be prescribed.

2.5 Contribution of current project

This project makes two contributions to the field of BMD measurement. First, a comprehensive study is carried out to assess the feasibility of acquiring dual-energy images on a slot-scanning radiographic machine and to perform phalangeal BMD measurements using those images. The second contribution is the suggestion of a method to measure volumetric BMD from a single dual-energy scan set using basis material decomposition. The measurement of volumetric BMD addresses the drawback of current DXA techniques which

provide areal BMD that is affected by bone size. The resulting DXA system may be used as a screening device or for making a diagnosis for osteoporosis.

2.5.1 Region of interest

Osteoporosis is a systemic disease (Chun, 2011; Glüer, 1997; Njeh et al., 1999; Ralston, 2005; Wehrli et al., 2006); any loss in mineral content affects the whole skeleton. While it is true that the best site for risk assessment of a particular site is a BMD measurement at the site itself (Miller et al., 1996), any site can be measured to evaluate the initial fracture risk for the common fracture sites (Ross, 1997; Wasnich, 1998). Measurement of BMD at a peripheral site would, therefore, suffice for an initial screening for osteoporosis. It has been shown that phalangeal bone measurements obtained using DXA and RA are highly correlated to axial BMD, can be used to identify individuals with reduced axial BMD and can predict major osteoporotic fractures (Alioglu et al., 2013; Buch et al., 2010; Dhainaut et al., 2011; Friis-Holmberg et al., 2012; Glüer et al., 1997; Gulam et al., 2000; Hansen et al., 2009; Mulder et al., 2000; Ohtsuka et al., 2002; Patel et al., 2010; Picard et al., 2004; Ross, 1997; Wasnich, 1998). Furthermore, it has been shown that the highest rates of major osteoporotic fractures occur in patients with low phalangeal bone mass measured using RA and high fracture probability as determined by the FRAX tool (Friis-Holmberg et al., 2014). The phalanges are a particularly useful site because there is little soft tissue surrounding bone; greater soft tissue thickness can complicate BMD measurements (Lang, 2010; Wasnich, 1998). Early manifestations of demineralisation are most pronounced in the middle and proximal phalanges of the middle and index fingers (Cheng et al., 1994; Fiter et al., 2001).

There appears to be no consensus amongst scientific studies and manufacturers of densitometers on which hand the measurements should be taken. Some manufacturers of hand densitometers such as the MetriScan (Alara, USA) recommend that measurements be taken in the non-dominant hand. Some earlier manufacturers including Bonalyzer (Teijin, Japan) and Osteoradiometer (NIM, Italy) suggested the use of both hands while others such as the Osteogram (Osteogram Analysis Center, USA) suggest that measurements should be taken in the left hand (Ross, 1997). A phalangeal DXA study by Alioglu et al. (2013) found no significant difference in the BMD of the non-dominant and dominant hands while in another study, Lekamwasam et al. (2005) found that BMD and BMC in the dominant hand are generally higher than in the non-dominant hand. Interestingly, it has also been found that there is better correlation between dominant hand-BMD than non-dominant hand-BMD measured on the MetriScan and hip DXA despite the recommendation by the manufacturer to

use the non-dominant hand (Thorpe & Steel, 2008). This thesis addresses accurate and precise measurement of BMD in hand bones and therefore the issue of which hand to use was considered non-critical at this stage. In that regard, the measurement site proposed for this project is the middle phalanx of the middle finger of the left hand; previous studies have used the same bone and hand (Bouxsein et al., 1997; Cosman et al., 1991; Gulam et al., 2000). This would also present an advantage of lower effective dose to the patient and faster scanning; both attributes are desirable for a mass screening device.

3. DUAL-ENERGY X-RAY AND COMPUTED DIGITAL ABSORPTIOMETRY: THEORY

3.1 Introduction

Dual-energy X-ray absorptiometry (DXA) and computed digital absorptiometry (CDA) are among some of the common densitometry techniques based on photon absorption. These two techniques are implemented in this project because, as discussed in the previous chapter, numerous studies have proven that they can provide accurate BMD measurements with acceptable precision at low radiation dose which makes them useful for assessment of osteoporosis. This chapter discusses the basic principles of X-ray imaging and the theory behind the DXA and CDA techniques.

3.2 Principles of Digital Radiography

X-rays are a form of electromagnetic radiation discovered by Wilhelm Röntgen, a German scientist in the late 1800s (Röntgen, 1896). The nature and energy of X-rays enables them to penetrate matter to an extent that is dependent on the material, its thickness and density as well as the X-ray energy. During patient examination, the X-ray photons are attenuated as they traverse the patient's body. The transmitted X-rays represent a measure of the attenuation along the beam path and are recorded using a detector unit which generates an image of the anatomy under examination.

3.2.1 Production of X-rays

The major components of a modern X-ray generation apparatus are the X-ray tube and generator as illustrated in Figure 3.1.

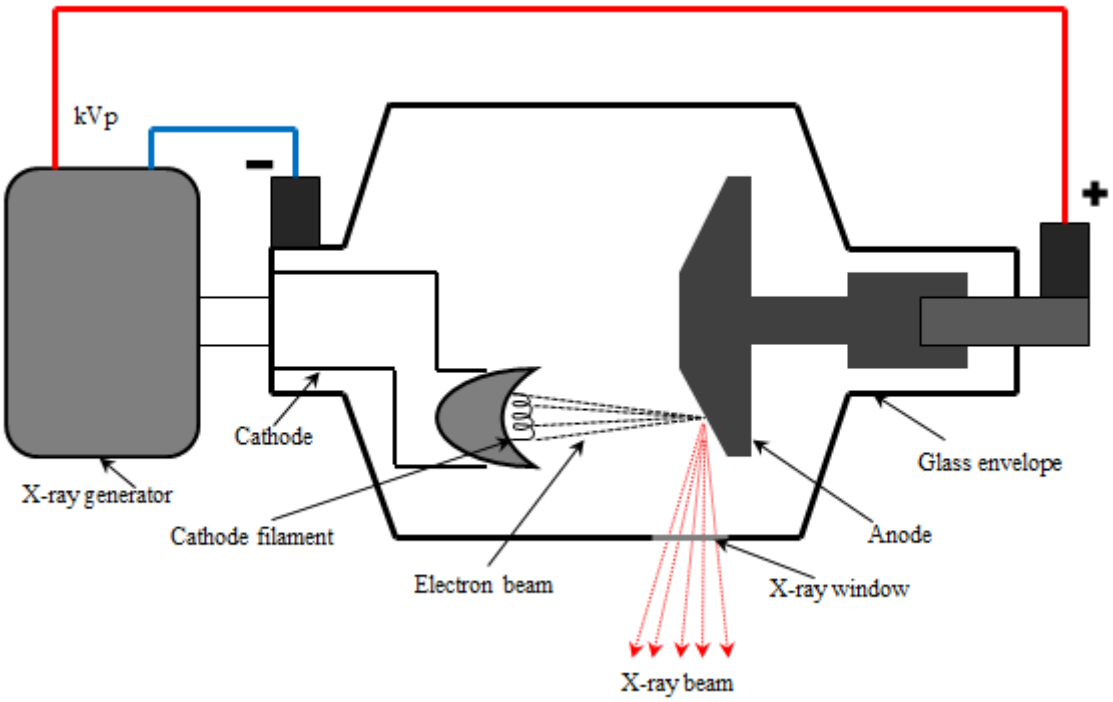

Figure 3.1: Apparatus for X-ray production.

The X-ray generator is the source of the X-ray energy and enables the user to control the tube voltage (kVp), tube current (mA), and exposure time. The X-ray tube consists of a cathode and an anode in an evacuated glass envelope. X-ray generation begins with the production of free electrons by a process of thermionic emission in the cathode. A very high voltage is applied between the cathode and anode, which accelerates the electrons towards the anode. The electrons gain kinetic energy as a result of the acceleration. Figure 3.2 illustrates how X-rays are produced at the target by the energetic electrons.

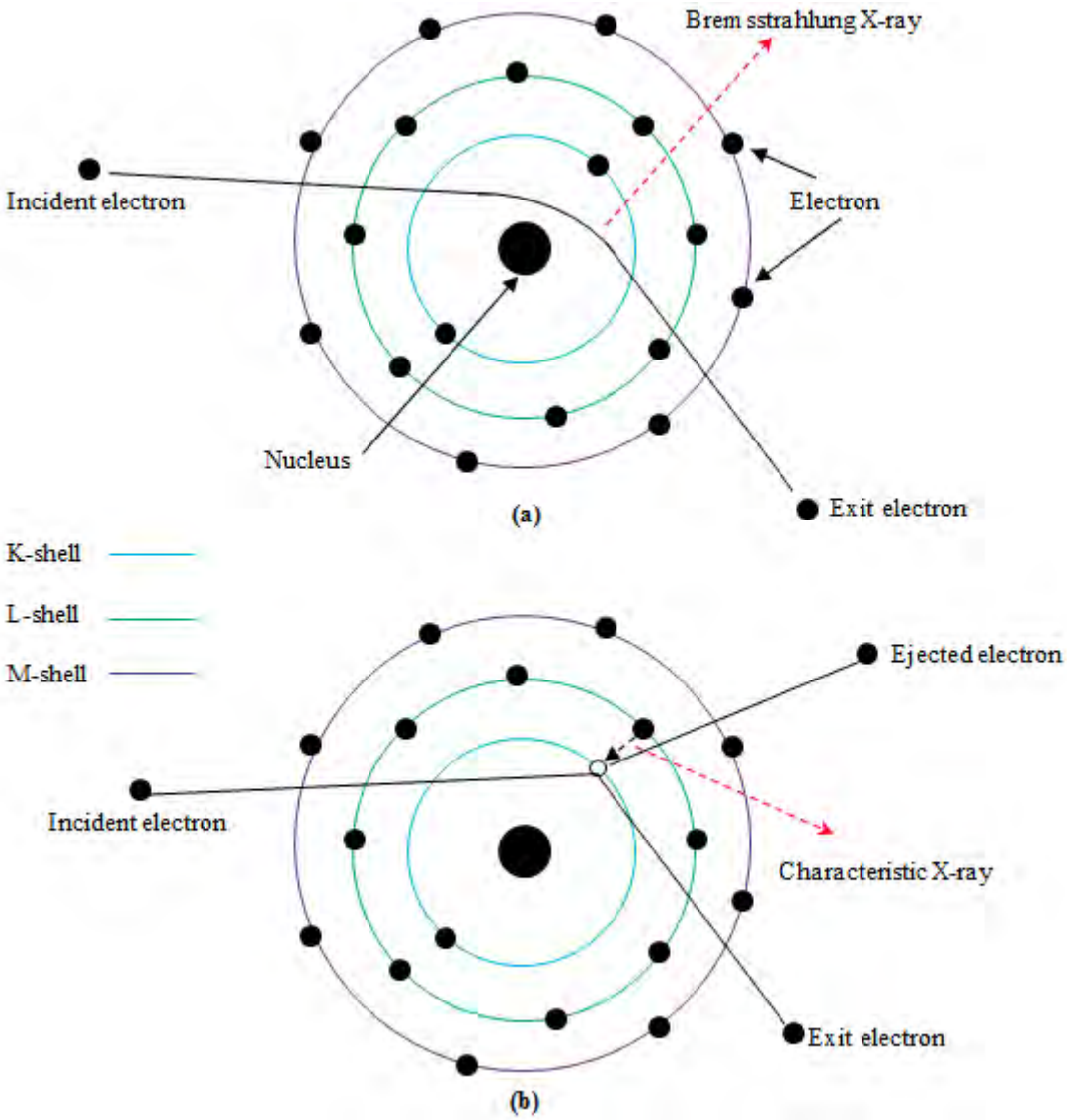

Figure 3.2: Production of X-rays at the anode: (a) Bremsstrahlung X-rays; (b) Characteristic X-rays.

A portion of the highly energetic electrons strike the target (anode) and are decelerated by collisions with the nuclei of target atoms, losing a fraction of their kinetic energy as a result. The kinetic energy lost by the braking effect of the electrons is released in the form of electromagnetic radiation termed Bremsstrahlung. Characteristic X-rays occur when some of the energetic electrons interact with atomic electrons in the anode material. An atomic electron is ejected from its shell during the interaction with the energetic electron. The ejected electron has energy that is equal to or higher than the binding energy of the electron shell holding the ejected electron (energy required to release an electron from the force that keeps it bound to the nucleus). The remaining vacancy in the shell is filled by an electron

from an outer shell. The electron that transitions from an outer shell to an inner shell loses energy equal to the difference between the binding energies of the two shells. The energy lost by the transitioning electron is released as characteristic X-ray.

The output of an X-ray tube is a poly-energetic (has X-ray photons with varying energies) X-ray beam with continuous and characteristic X-rays, as shown in Figure 3.3, with maximum energy (in keV) determined by the peak tube voltage.

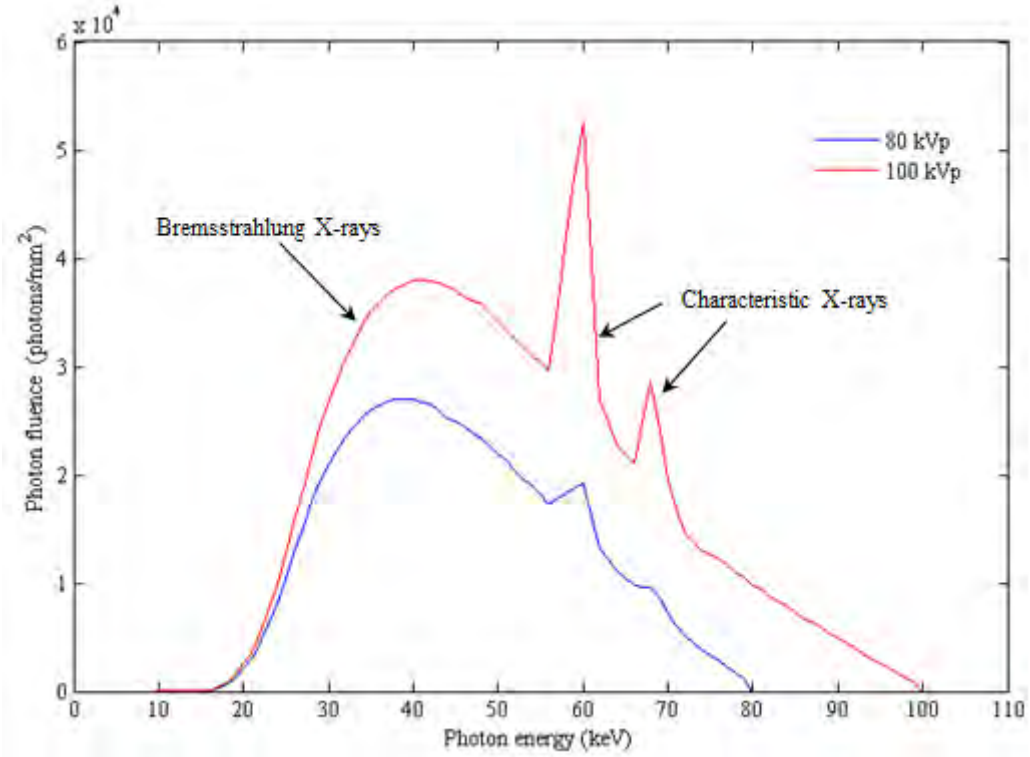

Figure 3.3: X-ray spectra for a tungsten X-ray tube with source voltages of 80 and 100 kVp.

The anode in most diagnostic X-ray tubes is made of tungsten, chiefly because of its high atomic number and extremely high melting point (Seibert, 2004). The focal spot is the area of electron interaction and emanation of X-rays from the target surface. Normally, the use of small focal spots is preferred to minimise geometric blurring of patient anatomy in the acquired images. A collimator assembly, constructed with movable lead shutters, is situated adjacent to the tube output port to define the X-ray beam shape incident on the patient (Seibert, 2004). The energy and quantity of the X-rays are controlled by adjusting the supply voltage and current, respectively. The exposure time (the amount of time that a patient is irradiated with X-rays) can also be used to control the quantity of X-rays.

3.2.2 Interaction of X-rays with matter

X-rays that penetrate matter unaffected constitute the primary radiation. X-rays may interact with atoms of the matter being examined, transferring energy to electrons in the process. In the medical X-ray energy range, X-ray interactions result in photoelectric absorption, coherent (Rayleigh) scattering and Compton scattering. Photoelectric absorption occurs when an X-ray photon is completely absorbed by an inner shell electron. If the energy of the incident photon is greater than the binding energy of the electron (but not too large to cause penetration), photoelectric absorption causes the electron to be ejected resulting in an ionised atom and a free electron. An electron in an adjacent shell may fill the vacant spot left by the ejected electron, releasing its excess energy as a characteristic X-ray in a manner similar to the production of characteristic X-rays by energised electrons at the tube anode. The energy of the ejected electron is equal to the difference between the incident photon and the electron binding energy. Electron binding energies are material-specific and the binding energy for electrons in the K-shell is termed the K-edge, L-edge for electrons in the L-shell and so on. The term 'edge' refers to the abrupt jump in the probability of photoelectric absorption once the process becomes energetically feasible i.e. when the energy of the incident photon becomes equal to the binding energy (Boone, 2000). Coherent scatter occurs when a photon deviates from its path without a loss in energy. In Compton scatter, incident photons interact with outer shell electrons resulting in scattered photons that travel in a different direction, with less energy than the incident photons. Scattered photons may reach the X-ray detector and degrade the quality of the image.

The combined effect of the interactions of X-rays and matter result in the attenuation of an incident beam as it traverses matter by removal of photons. The relationship between the number of photons in the incident beam, N_0, and in the transmitted beam, N, is given by the Beer-Lambert law:

$$N = N_0 e^{-\mu t} \quad \mathbf{3.1}$$

where μ is the linear attenuation coefficient and t is the thickness of the material. The linear attenuation coefficient is material-specific (depends on the effective atomic number) and is also dependent on the energy of the X-ray energy and material density.

3.2.3 X-ray detection

X-ray detectors convert the transmitted X-rays into useful, measurable signals. Solid state detectors contain crystals whose atoms are arranged in a regular three dimensional structure.

When X-rays interact with atoms in the detector, energy is transferred to the electrons and is handled according to the type of detector. In a screen-film detector, the deposited energy is converted into multiple visible light photons that travel through the screen, depositing energy in the film grains found in the emulsion layers of the film. The image is stored in the film emulsion. Screen-film images can be converted into a digital format using a film digitiser (Williams et al., 2007). In the photostimulable phosphors used in computed radiography (CR), the energy is stored and can be read out by light stimulation. The CR plates are read out pixel-by-pixel using a laser and the image can be stored on a computer, printed on film or viewed on a monitor. Digital flat panel detectors can be classified into direct and indirect systems (Boone, 2000; Huda, 2010; Williams et al., 2007). Direct systems such as photoconductors produce an electronic signal that is proportional to the deposited energy and can be directly measured (Huda, 2010). Indirect detectors make use of scintillators that convert the deposited energy into light which is subsequently propagated to a photodetector through optic diffusion. The photodetetcor records the pattern of visible light emitted by the scintillator as an image (Boone, 2000).

3.3 The Lodox Statscan

The Lodox Statscan, shown in Figure 3.4, is a low-dose, digital X-ray machine that uses a Linear Slot-Scanning Radiography (LSSR) technique. The machine produces high-resolution images at a lower radiation dose compared to traditional screen-film and digital radiography systems for a wide range of radiographic modalities (Irving et al., 2008; Maree et al., 2007). For example, an anterior-posterior abdomen examination in a medium-sized patient results in an effective dose of 80 µSv on the Statscan compared to between 320 and 700 µSv on other systems (Irving et al., 2008). The lower radiation dose of the Statscan may be attributed to the use of a digital detector, beam geometry and low scatter-to-primary ratio (Irving et al., 2008). An X-ray tube is mounted on one end of a C-arm, which can rotate up to 100°. The attenuated beam is captured by a detector unit on the other end of the C-arm, allowing digital images of any region of the body to be acquired with minimal interruption to the patient's management (Irving et al., 2008). The width of the collimator can be set to either 0.4 or 1 mm. The detector has a fundamental pixel size of 60 µm and can capture 14-bit images with a maximum size of 12 283×8 000 pixels with spatial resolution between 1.04 and 5 lp/mm (Irving et al., 2008). With a full speed of 140 mm/s, the Statscan is capable of scanning the whole body (up to 1.8 m in length) in 13 seconds. Scans at half-speed (70 mm/s), quarter speed (35 mm/s) and 1/8 (17.5 mm/s) speed are also possible.

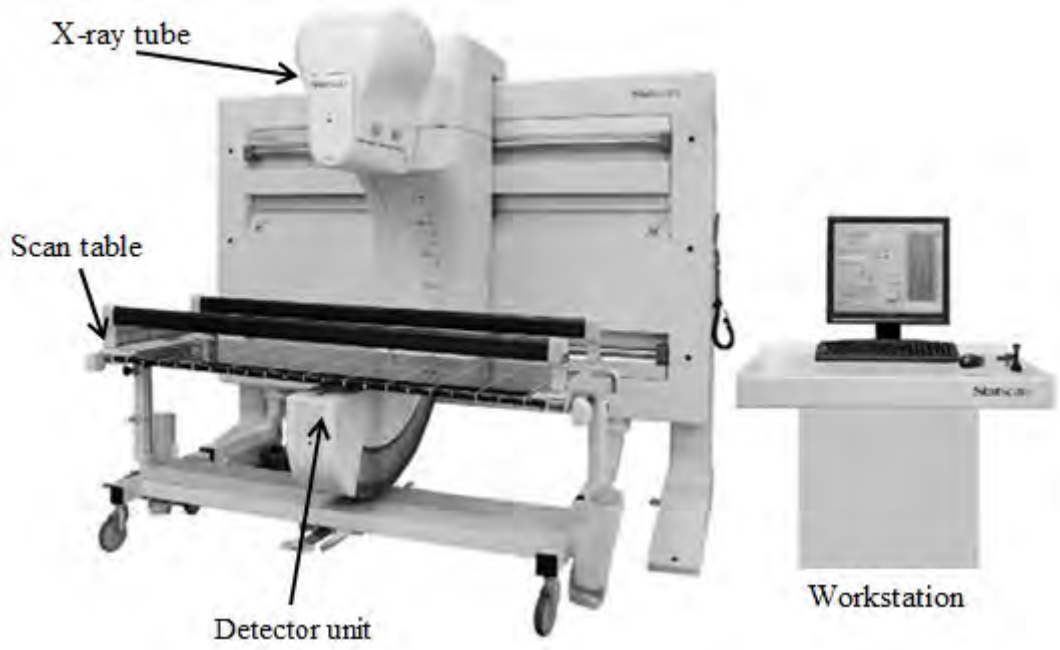

Figure 3.4: The Lodox Statscan.

Figure 3.5 shows the difference in the geometries of conventional and slot-scanning radiography.

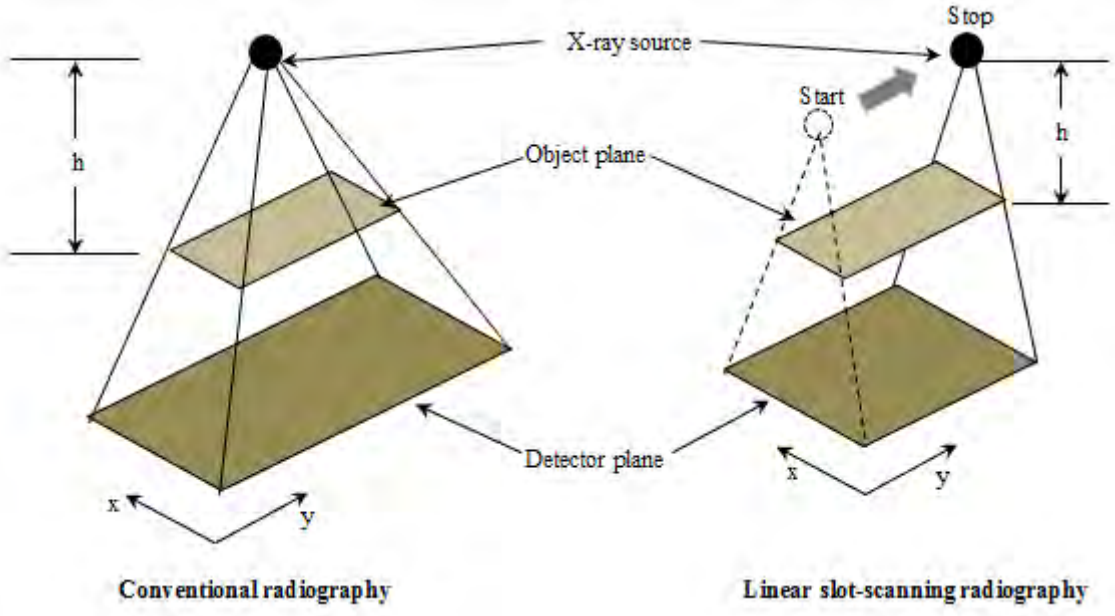

Figure 3.5: Beam geometries for conventional and linear slot-scanning radiography, which produce a cone beam and a moving fan beam, respectively.

The patient region that is imaged by radiographic systems is not uniformly irradiated due to the following reasons (Chalker et al., 1985):

1. The edges of the irradiated region are farther from the X-ray source compared with the centre of the region and X-ray intensity decreases with lateral distance from the central axis of the beam. This is illustrated in Figure 3.6. In conventional geometry radiography, the X-ray beam has a cone shape and diverges in the *x* and *y* directions but diverges only in the *x* direction (slot direction) for LSSR because it is collimated in the *y* direction (scan direction). Therefore X-ray intensity varies with the inverse of the square of the distance from the source ($1/h^2$) in conventional geometry radiography but varies with the inverse of the same distance (1/h) in LSSR (Irving et al., 2008; Potgieter et al., 2005).
2. X-rays passing towards the edges of the irradiated region pass more obliquely and consequently undergo greater attenuation than X-rays directed more centrally. This is illustrated in Figure 3.7.
3. X-ray intensities emitted from the anode side of the central beam are greater than those emitted from the cathode side.
4. X-rays emitted from the anode side are absorbed more by the target (anode) since they have to traverse a greater distance to exit the target; this is known as the anode heel effect.

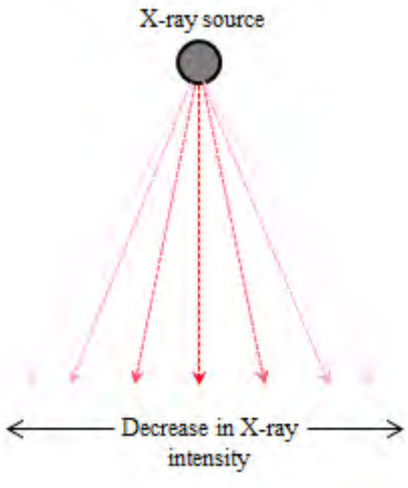

Figure 3.6: Decrease in X-ray intensity with distance from the central axis of beam.

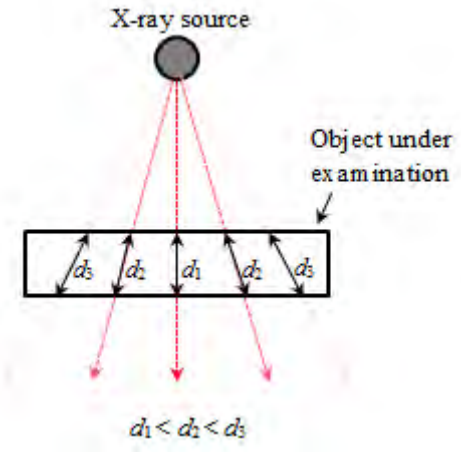

Figure 3.7: Increase in distance traversed by X-rays with increasing distance from central axis of beam.

The X-ray tube on the Lodox Statscan, is mounted with the plane of the rotating anode in the slot direction. As a result, the heel effect occurs in the scan direction and is of little consequence since the slot is open only to a very narrow portion of the beam (Scheelke et al., 2005).

3.4 Image quality assessment in digital radiography

Image quality assessments are required for the optimisation and performance specification of digital radiography systems (Tapiovaara, 2005). Artefacts, noise and resolution are the main parameters of image quality (Alsleem & Davidson, 2012; Goldman, 2007; Williams et al., 2007). Artefacts are unwanted image features that mask or mimic clinically relevant features (Willis et al., 2004). Noise results from the random nature of X-ray production as well as from the amorphous array and readout electronics of the detector (Alsleem & Davidson, 2012). Spatial resolution refers to the system's ability to discern adjacent regions of different tissues and is a function of system parameters such as focal spot size, source-detector distance and detector blur as well as patient motion. The cumulative effect of these factors is loss of detail and an overall reduction in image quality.

Image quality evaluations can be divided into objective and subjective methods (Alsleem & Davidson, 2012). Objective techniques are based on statistical measurements while subjective methods are based on human observation. While subjective techniques are considered to be highly valid, they are time-consuming. On the other hand, objective techniques are faster and highly reliable (Alsleem & Davidson, 2012). Several objective image quality techniques have

been suggested in the literature, each with its own advantages and disadvantages. Detective quantum efficiency (DQE) is regarded as the best metric for evaluating image quality in digital detectors (Stierstorfer & Spahn, 1999; Williams et al., 1999). Its distinct advantage is the fact that it takes into account detection efficiency, spatial resolution and noise. DQE can be considered as the system's ability to preserve the signal-to-noise between the input and output stages (Williams et al., 2007):

$$DQE = \frac{SNR_{out}}{SNR_{in}} \quad \mathbf{3.2}$$

DQE is generally plotted against spatial frequency and decreases with increasing spatial frequency due to declining spatial resolution and increasing noise (Williams et al., 2007). DQE requires measurements of the system's modulation transfer function (MTF) and noise power spectrum (NPS). MTF refers to the spatial frequency response of an imaging system or component (Krupinski et al., 2007). The NPS of a digital radiographic image provides an estimate of the spatial frequency dependence of the pixel-to-pixel fluctuations present in the image. Such fluctuations are due to the quantum noise in the X-ray beam incident on the detector, and any noise introduced by the series of conversions and transmissions of quanta in the stages between detector input and output (Williams et al., 1999). MTF and NPS can be used independently as image quality parameters (Alsleem & Davidson, 2012; Tapiovaara, 2005).

3.5 Physical principles of absorptiometry

This section discusses the fundamental principles and mathematical background of absorptiometric techniques. These techniques are based on the absorption of photons by body tissue and the fact that different body tissues have different absorption characteristics. The discussion in this section is adapted from Wahner & Fogelman (1994) and Njeh & Shepherd (2004).

3.5.1 Single energy absorptiometry

The theory of single energy absorptiometry is exemplified here by SPA. It is based on the Beer-Lambert law that describes the attenuation of a photon beam as it traverses through body tissue (Boone, 2000):

$$I = I_0 e^{-\mu t} \quad \mathbf{3.3}$$

where I and I_0 are the output and input beam intensities respectively, μ (in cm^{-1}) is the linear attenuation coefficient of the tissue and t (in cm) is the material thickness. In reality, however, the tissue being traversed is not homogeneous but consists of several types of tissue and the Beer-Lambert equation therefore becomes:

$$I = I_0 e^{-\sum_{i=1}^{N}\left(\frac{\mu}{\rho}\right)_i \rho_i t_i} \quad \mathbf{3.4}$$

where N is the number of different tissues in the attenuating material, ρ (in g/cm^3) is the density and μ/ρ (in cm^2/g) is the mass attenuation coefficient.

Single energy absorptiometry assumes that the path traversed by the beam consists of only bone and soft tissue and Equation 3.4 therefore becomes:

$$I = I_0 e^{-\left(\left(\frac{\mu}{\rho}\right)_s \rho_s t_s + \left(\frac{\mu}{\rho}\right)_b \rho_b t_b\right)} \quad \mathbf{3.5}$$

where the subscripts s and b denote soft tissue and bone, respectively.

Figure 3.8 is a schematic diagram illustrating the principle of single energy absorptiometry. If the anatomical site under examination is immersed in a soft tissue-equivalent fluid of constant thickness such as water, then attenuation in areas without bone becomes constant. The attenuation in the regions with no bone provides the baseline attenuation and the bone mineral content in regions with bone is proportional to the additional attenuation caused by bone (shaded area in the attenuation profile in Figure 3.8b).

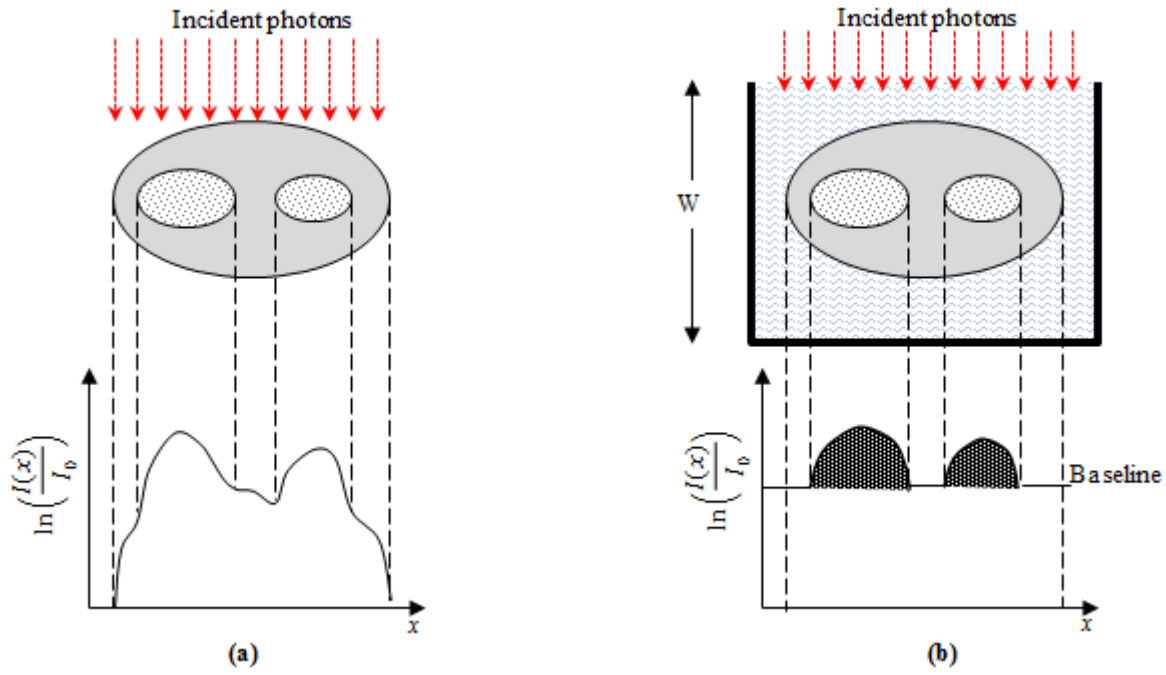

Figure 3.8: Principle of operation of single energy absorptiometry: (a) a simulated forearm being scanned and the profile of attenuation across the forearm; (b) scanning the simulated forearm in a water bath and the profile of attenuation across the forearm with the shaded area representing the amount of bone mineral in the bones.

Figure 3.8a shows a simulated forearm being scanned and a curve showing a profile of the attenuation. When the forearm is immersed in water as shown in Figure 3.8b and the level of water (W) is kept constant, the constant t_s can be eliminated from Equation 3.5 and the equation re-written as:

$$\ln\left(\frac{I_0}{I}\right) = \left(\frac{\mu}{\rho}\right)_s \rho_s (W - t_b) + \left(\frac{\mu}{\rho}\right)_b \rho_b t_b \quad \mathbf{3.6}$$

The path length through the bone can computed as follows:

$$t_b = \frac{\ln\left(\frac{I_0}{I}\right) - \left(\frac{\mu}{\rho}\right)_s \rho_s W}{\left(\frac{\mu}{\rho}\right)_b \rho_b - \left(\frac{\mu}{\rho}\right)_s \rho_s} \quad \mathbf{3.7}$$

where

$$\left(\frac{\mu}{\rho}\right)_s \rho_s W = \ln\left(\frac{I_s}{I_0}\right) \quad \mathbf{3.8}$$

where I_s denotes the beam that has been attenuated by soft tissue only and is referred to as the baseline. Substituting into Equation 3.7 yields:

$$t_b = \frac{\ln\left(\frac{I_s}{I}\right)}{\left(\left(\frac{\mu}{\rho}\right)_b \rho_b - \left(\frac{\mu}{\rho}\right)_s \rho_s\right)} \quad \mathbf{3.9}$$

By integrating t_b over all the pixels, the total bone mineral content (corresponding to the shaded area in Figure 3.8b) can be computed:

$$T_b = \rho_b \int_{t=0}^{W} t_b dt \quad \mathbf{3.10}$$

On old, single line scanning SPA systems, T_b is referred to as the bone mineral content (BMC) despite being expressed in g/cm. To obtain the BMD, expressed in g/cm^2, the BMC is divided by the bone width. SXA substitutes an X-ray tube for the radionuclide source to overcome the shortcomings of SPA as discussed in Section 2.3.1.

3.5.2 Dual-energy absorptiometry

Application of single energy absorptiometry techniques was limited to peripheral sites where there is little variation of soft tissue composition and thickness. The technique could not be applied to axial sites where there is greater variation in soft tissue composition and thickness. Dual-energy techniques were introduced to overcome this drawback and thus eliminating the need for a water bath. However, quantitative dual-energy imaging techniques make the following assumptions:

- The transmission of the photons through the site under examination is a monoexponential process i.e. photons in the beam have the same energy.
- The path traversed by the beams consists only of bone and soft tissue.

Figure 3.9 is a schematic diagram illustrating the principle of operation of dual-energy absorptiometry. Two scans are acquired at different energies. By multiplying the soft tissue attenuation in the high-energy image by a constant such that the difference between the two scans becomes zero over the soft tissue-only areas, the algorithm creates the same effect as introducing a water bath in single-energy absorptiometry. The shaded area in Figure 3.9 represents the amount of bone present in the scanned area.

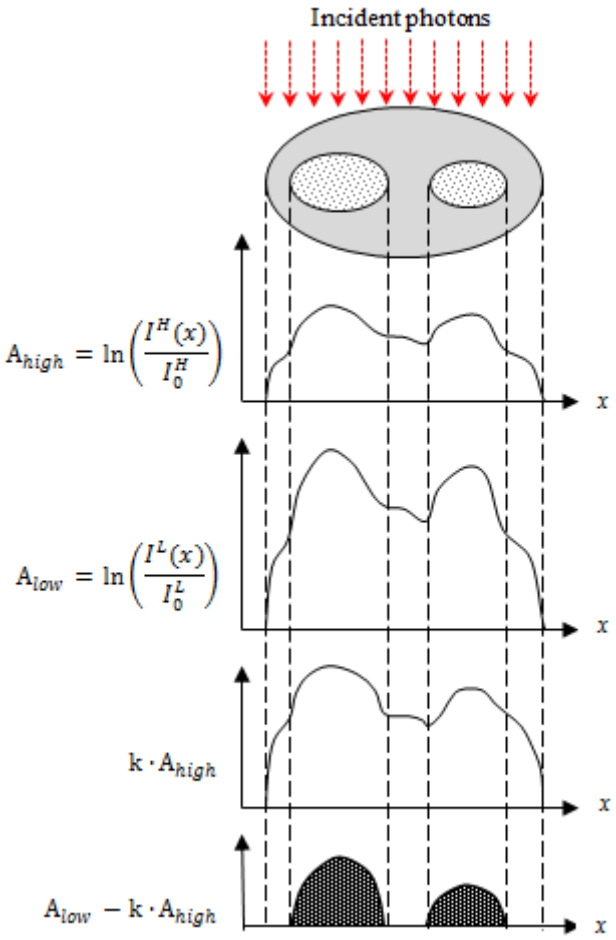

Figure 3.9: Principle of operation of dual-energy absorptiometry: a simulated forearm is scanned using two beams to yield two attenuation profiles A_{high} and A_{low}. The high-energy attenuation is multiplied by a constant k and subtracted from the low-energy attenuation to yield the attenuation caused by bone only (shaded area).

To demonstrate, mathematically, that it is possible to find BMD using two energy beams, the product ρt in Equation 3.4 is replaced by σ which denotes areal density with unit g/cm^2. The transmission equations for each energy level are given by:

$$I^L = I_0^L e^{-\left(\left(\frac{\mu}{\rho}\right)_s^L \sigma_s + \left(\frac{\mu}{\rho}\right)_b^L \sigma_b\right)} \quad \mathbf{3.11}$$

$$I^H = I_0^H e^{-\left(\left(\frac{\mu}{\rho}\right)_s^H \sigma_s + \left(\frac{\mu}{\rho}\right)_b^H \sigma_b\right)} \quad \mathbf{3.12}$$

where the superscripts L and H denote low and high energy, respectively. Equations 3.11 and 3.12 can be solved simultaneously for σ_b (BMD) as follows:

$$\sigma_b = \frac{\left(\left(\frac{\mu}{\rho}\right)_s^L \Big/ \left(\frac{\mu}{\rho}\right)_s^H\right) \ln\left(I^H / I_0^H\right) - \ln\left(I^L / I_0^L\right)}{\left(\frac{\mu}{\rho}\right)_b^L - \mu\left(\frac{\mu}{\rho}\right)_b^H \left(\left(\frac{\mu}{\rho}\right)_s^L \Big/ \left(\frac{\mu}{\rho}\right)_s^H\right)} \quad \mathbf{3.13}$$

As Equation 3.13 demonstrates, by measuring attenuation at any point using two photon energies, it is possible to compute the areal density of bone. If we define R_s as:

$$R_s = \left(\left(\frac{\mu}{\rho}\right)_s^L \Big/ \left(\frac{\mu}{\rho}\right)_s^H\right) \quad \mathbf{3.14}$$

Equation 3.13 can be re-written as follows:

$$\sigma_b = \frac{R_s \ln\left(I^H / I_0^H\right) - \ln\left(I^L / I_0^L\right)}{\left(\frac{\mu}{\rho}\right)_b^L - \left(\frac{\mu}{\rho}\right)_b^H R_s} \quad \mathbf{3.15}$$

Equation 3.15 provides a basis for calculating the BMD but requires the values of the mass attenuation coefficients of soft tissue and bone at both energies to be known. However, the composition of soft tissue varies widely between individuals so that it is not possible to use pre-set values for the mass attenuation coefficient at the two energies. To overcome this issue, a measurement in a region with no bone can be used to estimate the value of R_s. At a point where no bone is present, BMD (σ_b) is zero and Equation 3.15 can be solved for R_s:

$$R_s = \frac{\ln\left(I_s^L / I_0^L\right)}{\ln\left(I_s^H / I_0^H\right)} \quad \mathbf{3.16}$$

The estimated value for R_s is used together with known values for mass attenuation coefficients of bone and measured intensity values to compute the BMD using Equation 3.15.

3.6 Dual-energy X-ray Absorptiometry

Dual-energy X-ray absorptiometry (DXA) uses an X-ray tube as the source of photons. The first DXA machines were introduced in the late 1980s (Mazess et al., 1989). Early DXA machines employed pencil beam geometry with a single detector while the majority of modern machines have fan beam geometry with a multi-detector array (Lang, 2010) as illustrated in Figure 3.10. Dual-energy images on fan beam systems are acquired by the scanning arm performing a single sweep across the patient while pencil beam systems carry out a two-dimensional raster scan. As a result, fan beam systems have shorter examination times.

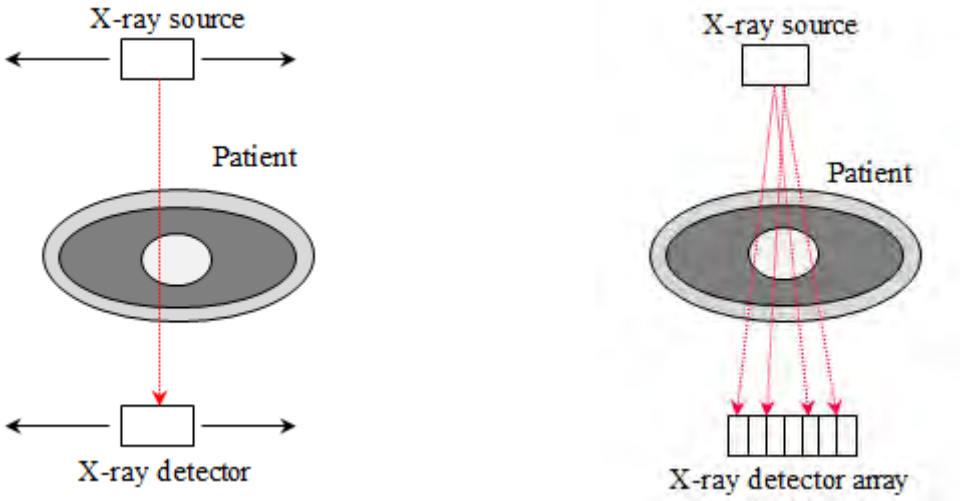

(a) **(b)**

Figure 3.10: DXA system geometries (a) pencil beam and (b) fan beam.

The DXA scan analysis creates a pixel-by-pixel map of BMD over the entire scanned field using Equation 3.15. An edge detection algorithm is used to find the bone edges. Edge detection methods vary between manufacturers. The total projected area of bone is then derived by summing the pixels within the bone edges and the BMD is calculated as the mean

BMD over all the pixels identified as bone. Finally, bone mineral content (BMC) is derived by multiplying BMD by the projected area (Njeh & Shepherd, 2004). Alternatively, the BMC at each bone pixel can be computed and the BMD found by dividing the total BMC by the sum of bone pixels (Wahner & Fogelman, 1994). Figure 3.11 shows examples of central DXA scans.

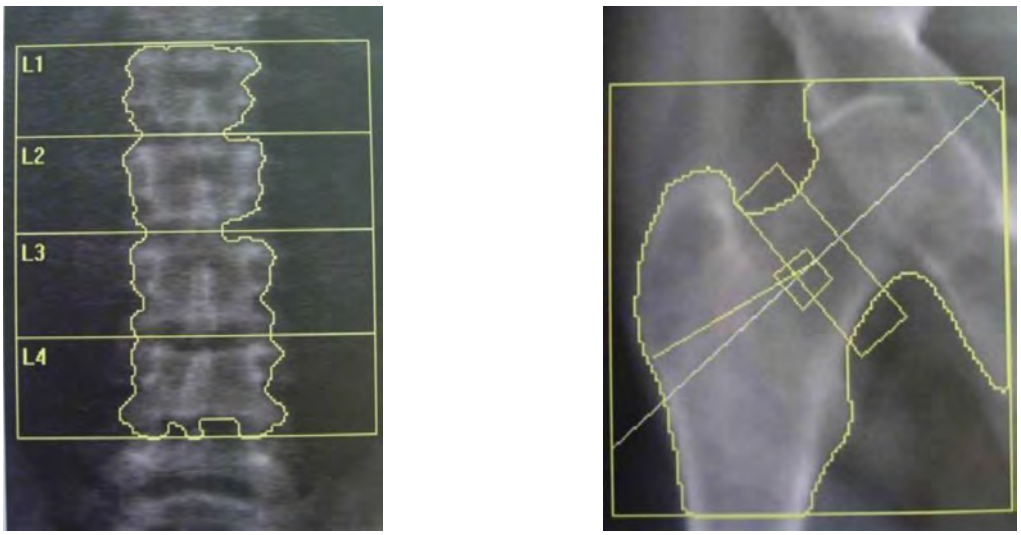

(a) (b)

Figure 3.11: Typical DXA scans (a) Lumbar spine and (b) Femur (source - http://openi.nlm.nih.gov).

3.6.1 Image acquisition

The major manufacturers of DXA machines are Hologic (Waltham, MA) and GE (Madison, WI). Other manufacturers include Norland (Fort Atkinson, WI) and DMS (Montpellier, France) (Lang, 2010). In general, two methods are used to generate the low- and high-energy X-ray spectra namely K-edge filtration and source voltage switching (Blake & Fogelman, 1997; Genton et al., 2002; Lang, 2010; Njeh & Shepherd, 2004; Wahner & Fogelman, 1994).

In systems based on K-edge filtration, a highly stable X-ray generation apparatus is used to emit a poly-energetic X-ray beam at a constant source voltage. K-edge absorption filters made of rare earth materials such as cerium or samarium are used to separate the X-ray beam into low- and high-energy components (Njeh & Shepherd, 2004). K-edge filters remove photons with energy higher than the K-edge of the filtering material from the incident beam. In Lunar devices made by GE, a beam emitted at a source voltage of 76 kVp is filtered by cerium filters to produce a low-energy spectrum with effective energy of 38 keV and a high-energy spectrum with effective energy of 70 keV for a spectral separation of 32 keV (Bolotin

et al., 2001; Genton et al., 2002; Lang, 2000). Norland devices use a source voltage of 110 kVp and employ samarium filtration to produce low- and high-energy spectra with effective energies of 45 and 80 keV respectively for a spectral separation of 35 keV (Bolotin et al., 2001; Lang, 2010).

Systems that use K-edge filtration require two, pulse-counting detectors that selectively detect low- and high-energy photons (Wahner & Fogelman, 1994). Pulse counting detectors carry out pulse height analysis for each incoming photon in order to determine if the photon is counted as a high- or low-energy photon. The major problems associated with systems based on pulse counting are detector pile-up and energy cross-over (Wahner & Fogelman, 1994). Detector pile-up is the phenomenon of a photon reaching the detector while the detector is still processing another photon. This problem is more pronounced in thin body regions due to higher pulse rates. Detector cross-over occurs when high-energy photons are erroneously counted as low-energy photons, but it can be corrected by assigning a fraction of the low-energy counts to the high-energy count (Wahner & Fogelman, 1994).

Source voltage switching produces the low- and high-energy X-ray spectra by switching the voltage generator between two source voltage levels in sync with the AC power supply; such systems require only one detector. Hologic machines switch the source voltage between 100 and 140 kVp to yield low- and high-energy components with effective energies of 52 and 105 keV respectively (Lang, 2010).

Other techniques for generating the dual-energy spectra that have been used have attributes of the K-edge or switching methods. Deych (2006) patented a dual-energy detector made of an array of detector elements consisting of two scintillators arranged in a stack. A schematic diagram of the detector element is shown in Figure 3.12.

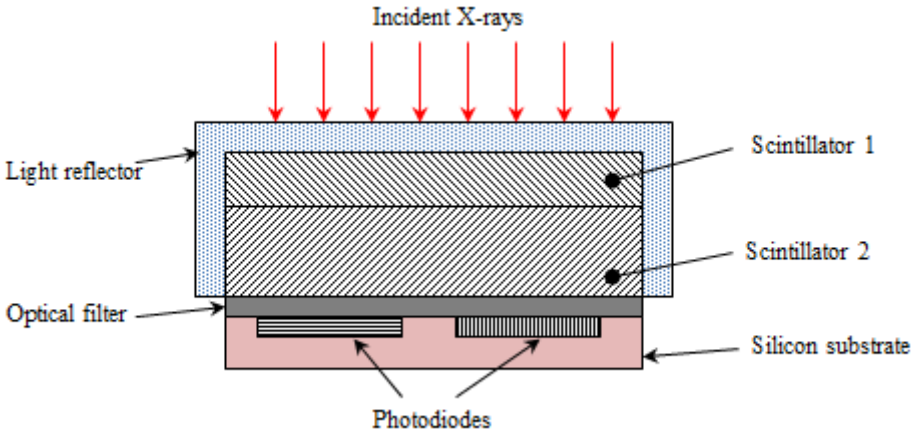

Figure 3.12: The dual-energy detector element of Deych (2006) consisting of a two stacked scintillators and a 2-channel sensor.

Scintillator1 absorbs low-energy X-rays and converts them into light of a certain wavelength while *Scintillator2* absorbs high-energy X-rays and converts them into light of a different wavelength. The photodiodes are designed to be selectively sensitive to the different light wavelengths emitted by the scintillators. The light reflector prevents the visible light produced by the scintillators from escaping and the optical filter enhances the spectral sensitivity of the photodiodes. The detector was tested by imaging a water bath with 10 cm water thickness and 166 kVp source voltage. The designer does not specify the method for generating the dual-energy X-ray beam but the use of a constant voltage source in the test suggests that the detector may have been designed primarily for a constant source voltage. It appears, however, that this kind of detector may also be used with a switching voltage source. The designer claims that this type of detector is cheaper and easier to manufacture and has better noise performance than ordinary digital X-ray detectors.

Seely et al. (2001) patented a dual-energy system for conventional radiography that has aspects of both K-edge filtration and source voltage switching. A schematic for their system is shown in Figure 3.13.

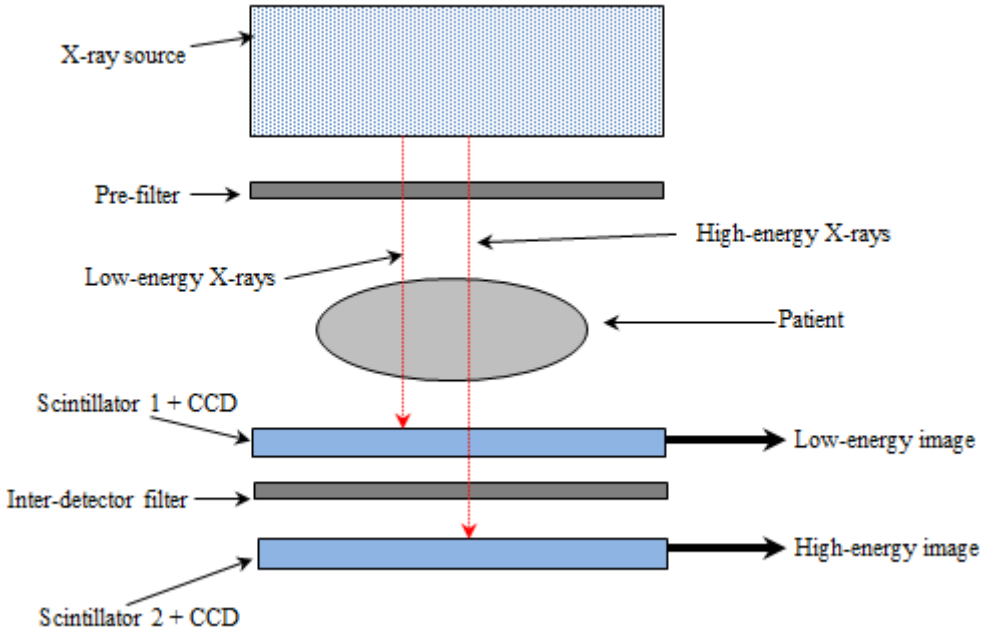

Figure 3.13: Dual-energy system suggested by Seely et al. (2001) including X-ray detectors arranged sequentially for capturing the dual-energy images.

In the system illustrated in Figure 3.13, the X-ray source is switched between a low and high voltage in a short pulse thus emitting the low-energy X-rays during one half of the pulse and high-energy X-rays during the other half. The system has two detectors that generate the low- and high-energy images. The pre-filter and inter-detector enhance the spectral separation of the dual-energy spectra. The designers claim that this system reduces patient dose during DXA examinations due to the short exposure time.

Yun et al. (2005) patented a dual-energy detector that adds two angled mirrors to an arrangement similar to that of Seely et al. (2001). The first mirror is located between the first and second scintillators and reflects the visible light emitted by *Scintillator1* out of the X-ray path onto a detector unit that captures the low-energy image. The second mirror is placed after *Scintillator2* and reflects visible light from the scintillator onto a second detector unit that captures the high-energy image. The designers do not specify the method for generating the X-ray beam although it appears that the detector may be used for a switched or constant source voltage tube. The designers claim that this type of detector results in high spatial resolution and signal-to-noise ratio.

3.6.2 Calibration of DXA systems

In order for X-ray images to provide quantitative information for DXA, they need to be calibrated. Commercial DXA systems are generally calibrated using a continuously rotating disc with bone-equivalent material or basis material decomposition (Lang, 2010; Mazess et al., 1991). BMD studies on radiographic machines that are not dedicated DXA machines have also used basis material decomposition (Gulam et al., 2000; Holdsworth et al., 2000).

Hologic DXA machines are calibrated using the rotating disc technique. The disc is positioned so that a part of it obstructs the X-ray beam. The disc has 4 quadrants and is synchronised with the frequency of the power supply (Stein, 1989). Quadrants 1 and 2 contain bone-equivalent material with known density, typically 1 g/cm^2, while quadrants 3 and 4 do not contain any attenuating material. As discussed in Section 3.6.1, Hologic machines switch the source voltage between two levels to produce the dual-energy spectra. When quadrants 1 and 3 (*Q1* and *Q3*) are obstructing the beam, the source voltage is high (*HE*) and when quadrants 2 and 4 (*Q2* and *Q4*) are obstructing the beam, the source voltage is low (*LE*). Every *HE*/*LE* pulse has 4 measurements:

1. *HE*, no bone-equivalent material (*H*)
2. *LE*, no bone-equivalent material (*L*)
3. *HE*, with bone-equivalent material (*HB*)
4. *LE*, with bone-equivalent material (*LB*)

A function, *F*, for every pixel across the patient is computed:

$$\mathrm{F(B)} = \ln(\mathrm{LB}) - \mathrm{k} \cdot \ln(\mathrm{HB}) \quad \mathbf{3.17}$$

$$\mathrm{F(NB)} = \ln(\mathrm{L}) - \mathrm{k} \cdot \ln(\mathrm{H}) \quad \mathbf{3.18}$$

where $F(B)$ is the function value for bone-equivalent material, $F(NB)$ is the function value without bone-equivalent material and k is the ratio of the low-energy attenuation coefficient of soft tissue to the high-energy attenuation coefficient of soft tissue. A normal baseline and calibration baseline are defined. Normal baseline is $F(NB)$ in the soft tissue region adjacent to the bone i.e. F when *Q3* or *Q4* are above the no-bone region adjacent to the bone. Calibration baseline is $F(B)$ in the soft tissue region adjacent to the bone i.e. F when *Q1* or *Q2* are above the adjacent soft tissue region. The baseline separation, y, is computed as the average of the pixel-by-pixel difference between $F(NB)$ and $F(B)$ in the soft tissue region adjacent to the bone. The baseline separation calibrates the bone measurements in the patient directly against

known density of the bone-equivalent calibration material of the calibration disc. To compute the patient BMD, suppose that for a pair of *HE*/*LE* images, the difference in the value of *F* at a point in the region with bone is *x* then the BMD at that point is given by:

$$BMD = \frac{x}{y}d \quad \mathbf{3.19}$$

where *d* is the density of the bone-equivalent material in the calibration disc. The calibration disc method has been refined over the years but the working principle has remained unchanged.

Norland and Lunar DXA systems are calibrated using the basis material decomposition method (Lang, 2010). This method assumes that any tissue can be represented by a combination of bone-equivalent and soft tissue-equivalent materials. Aluminium and Perspex are good examples of bone-equivalent and soft tissue-equivalent materials respectively. Dual-energy images of a phantom consisting of several combinations of different thicknesses of aluminium and Perspex are captured. Polynomials are fit to the log attenuation measurement in the low- and high-energy images for each combination. During patient examination, the polynomials are used to compute the equivalent thickness of aluminium and Perspex of the patient's anatomy. The equivalent thicknesses of the aluminium and Perspex are mapped to a BMD value using a special calibration block containing a precise and known bone mineral content (Lang, 2010).

3.7 Physical principles of computed digital absorptiometry

Computed digital absorptiometry (CDA) is based on the fact that the linear attenuation coefficient of any material mainly depends on the effective atomic number, Z_{eff}. The effective atomic numbers of aluminium and bone are 13 and 12.5, respectively; suggesting that the materials have similar X-ray attenuation characteristics (Sotoca et al., 2003). In CDA, an aluminium step wedge is exposed to X-rays simultaneously with the anatomical site being examined. Consider a pixel under the bone region that has received photon intensity given by:

$$I_b = I_0 e^{-\left(\frac{\mu}{\rho}\right)_b \sigma_b} \quad \mathbf{3.20}$$

and a pixel under an aluminium region that has received photon intensity given by:

$$I_{Al} = I_0 e^{-\left(\frac{\mu}{\rho}\right)_{Al} \sigma_{Al}} \quad \mathbf{3.21}$$

If the two pixels have the same grey level and assuming that the X-ray beam is monoenergetic, then the X-ray intensity at those locations is the same:

$$I_b = I_{Al} \quad \mathbf{3.22}$$

It means, therefore, that:

$$\left(\frac{\mu}{\rho}\right)_b \sigma_b = \left(\frac{\mu}{\rho}\right)_{Al} \sigma_{Al} \quad \mathbf{3.23}$$

The aluminium wedge has a calibrated step-thickness to grey level relationship. The average grey level in the region of interest in the bone can be found and the corresponding thickness of aluminium calculated from the aluminium calibration relationship. The mass of the bone can now be found and expressed using the equivalent aluminium thickness unit (mmAl) (Ross, 1997; Sotoca et al., 2003).

3.8 Developments in DXA and CDA

Although there have been significant advances in the hardware used for implementing DXA and CDA, the basic principles have remained the same. However, attempts have been made to improve the DXA technique. For example, triple-energy absorptiometry has been suggested (Kotzki et al., 1991; Swanpalmer et al., 1998). This technique assumes that the human body consists of bone, lean tissue and fat, and captures three images at different energy levels resulting in three attenuation equations. The equation system is solved to yield bone mineral density. The technique has failed to gain widespread use or generate research interest, possibly due to lower precision than DXA and higher complexity (Swanpalmer et al., 1998). In another example, laser technology has been incorporated into the DXA technique for measuring heel BMD using a technique termed dual-energy X-ray laser (DXL). DXL attempts to circumvent the assumption in DXA that the soft-tissue in the region adjacent to the bone and that overlying the bone is constant by measuring the total tissue thickness at the heel using a laser reflection technique. This enables the fat-to-lean tissue ratio to be computed at the measurement site which can then be used to correct the BMD measurements (Hakulinen et al., 2003). The DXL Calscan heel densitometer (Demetech AB, Sweden) is based on this technique (Thorpe & Steel, 2006). Despite the high precision recorded using DXL (Thorpe & Steel, 2006), there is insufficient data to prove its use as a standard measurement technique for osteoporosis assessment (Yumru et al., 2009). It seems that research in the DXA field is aimed towards efficient dual-energy generation and detection

and it is unlikely that the physical principles of operation will undergo a radical change given its high precision and accuracy, and proven role in the assessment of osteoporosis.

3.9 Devices for hand densitometry

The advantages of phalangeal BMD assessment discussed in Section 2.5.1 and the proven ability of such measurements in the management of osteoporosis have inspired the manufacture of several devices for phalangeal BMD measurement.

The Metriscan (Alara Inc, CA) is a compact computed digital absorptiometry device capable of determining phalangeal bone mineral density in arbitrary units from the middle phalanges of the middle three digits (Thorpe & Steel, 2008). Several studies have shown that the Metriscan is capable of discerning osteoporotic patients from normal patients with high accuracy and may be useful as a screening device (Dhainaut et al., 2011; Friis-Holmberg et al., 2012; Hansen et al., 2009; Thorpe & Steel, 2008).

The accuDXA2 (Lone Oak Medical Technologies, USA) is a portable, peripheral DXA machine that measures BMD and BMC in the middle phalanx of the middle finger. The accuDXA2 is a recent upgrade of the accuDEXA device which was shown to have high correlation with ash weight and acceptable fracture risk evaluation (Michaeli, 1999). This device is also capable of detecting low axial BMD (Mulder et al., 2000) by assessing the finger. In addition to providing BMD and BMC, the accuDXA2 provides a T-score computed using the mean reference BMD of a young, healthy normal population supplied by the manufacturer (Lone Oak Medical Technologies, 2012; Keim et al., 2014). Thus, the accuDXA2 is more than just a screening device as it can be used to make a diagnosis for osteoporosis using finger BMD.

CompuMed (CompuMed, Inc) offers the Osteogram, a program that enables RA-based measurements to be conducted on an ordinary X-ray machine by providing a software tool that can be used to analyse hand radiographs to produce a bone density report (CompuMed Inc., 2014). According to the manufacturer, Osteogram has high precision, high correlation to axial DXA and ash weight, and is cleared by the Food and Drug Administration (FDA) to screen, diagnose and monitor therapy for osteoporosis.

The Sectra OneScreen (Sectra, Sweden) is an add-on component developed by Sectra which allows a mammography machine to perform bone assessment using digital X-ray radiogrammetry. The measured BMD value is compared with a reference group to diagnose

osteoporosis (Sectra, 2014). Several studies have shown that this device is capable of identifying individuals with reduced axial BMD and those at higher risk of osteoporotic fractures (Bach-Mortensen et al., 2006; Dhainaut et al., 2010; Reed et al., 2004; Wilczek et al., 2013). Digital X-ray radiogrammetry (DXR) is a bone assessment technique that uses automated image analysis of standard hand radiographs to estimate metacarpal bone mineral density (Bouxsein et al., 2002). The fundamental radiogrammetric methodology of the DXR technique is an automated segmentation of a given metacarpal diaphysis into cortical and medullar regions, enabling the measurement of the average cortical thickness (*T*) and bone width (*W*) in a given region of interest. The bone volume per area (VPA) is then derived and assuming that the cross-section of the metacarpal bone is elliptical, the following equation holds (Rosholm et al., 2001):

$$VPA = f \times T \times \left(1 - \frac{T}{W}\right) \quad \mathbf{3.24}$$

where *f* is a general geometrical factor. The VPA of the metacarpal bones of the second to the fourth fingers, the radius and ulnar VPAs are computed in order to improve precision and a weighted formula is then used to compute the aggregate VPA. The DXR technique incorporates a minor correction for porosities in cortical bone using a porosity measure, *p*, and the final BMD estimate is given by:

$$BMD_{DXR} = f \times VPA_{agg} \times (1 - p) \quad \mathbf{3.25}$$

where VPA_{agg} is the aggregate VPA.

The presence of these devices on the market and in clinical practice as well as the fact that some of these devices are approved by the FDA for osteoporosis screening and diagnosis is an indication that phalangeal BMD is considered to have an important role to play in the management of osteoporosis.

4. SEGMENTATION

4.1 Introduction

This chapter discusses the stages and techniques used to segment the bone of interest from the radiographic images of the hand. The stages include identification and isolation of the middle finger, and segmentation of the middle phalanx of the middle finger (the bone of interest).

The chapter first gives an overview of segmentation methods that are employed in commercial DXA machines and those that have been reported in studies involving hand radiographic images. This is followed by a discussion of the method used for identifying and isolating the middle finger. The method designed to locate the bone centroid is described; the bone centroid was used for initialising the segmentation methods. The theory, implementation and evaluation of the segmentation methods are then discussed. Results of the implemented methods are given and a discussion follows to conclude the chapter.

4.2 Overview

The role of image segmentation is to divide an image into distinct, homogenous regions to identify objects and their borders, enabling the measurement of object attributes for description and recognition (Gonzalez & Woods, 2002).

Manufacturers of DXA machines use different segmentation techniques to identify bone regions in dual-energy images. GE devices use a gradient search algorithm which computes the gradient of an image. The high contrast between soft tissue and bone regions results in sharp changes in the gradient at the soft tissue/bone border. The segmentation algorithm searches for these sharp changes in the gradient to identify the border of the bone (Lang, 2010). Hologic devices use a local threshold method to find bone edge pixels in an image (Ruth et al., 2005). In this technique, the image is smoothed using a rectangular averaging box where the width and height of the box depend on the orientation of the bone edge. Given a starting point located at or near a bone edge, the following steps are carried out to find all points on the bone edge:

1. A local vector is defined containing a set of connected pixels centred on the starting point.

2. The background is subtracted from the vector. The background is defined as the average value of a specified number of pixels located near a specified end point of the vector.
3. The maximum value of the background-subtracted vector is determined and a threshold is defined as a percentage of this maximum.
4. The pixel values are tested sequentially from both ends of the vector to find the location(s) where values are greater than or equal to the threshold. These locations belong to the bone edge.
5. The edge pixel closest to the previous point (starting point if the second point is being selected) is used as the next starting point.
6. Steps 1-5 are repeated until the bone edge is fully identified.

Precise segmentation of the ROI is crucial for correct and accurate BMD measurements using DXA (Kwon et al., 2009). Automated segmentation of the bone of interest is required for automated BMD measurement for screening a large population (Sotoca et al., 2003). An automated segmentation method that eliminates or significantly limits user dependence on the final result is essential for achieving high precision in the BMD measurements. Active shape models (ASMs) are a popular technique for segmentation of the middle phalanx and other hand bones from radiographic hand images. ASMs have been used in the measurement of BMD (Kauffman et al., 2004; Mahmoodi et al., 2000; Sotoca et al., 2003; Thodberg & Rosholm, 2003) and in the assessment of bone age (Niemeijer et al., 2003). Other techniques that have been employed for segmentation of hand bones in radiographic images for age assessment and measurement of BMD include deformable models (Chuaychunu et al., 2007; Gulam et al., 2000; Han et al., 2007), region growing (Manos et al., 1994; Pietka, 1995), thresholding (Cheng et al., 1994), watershed segmentation (Han et al., 2007) and edge detection (Chang et al., 2003; Sharif et al., 1994). Classification techniques have also been attempted for segmenting hand radiographic images (Levitt et al., 1993; Rucci et al., 1995).

In this project, the use of active shape models (Cootes et al. 1995) and deformable models (Kass et al., 1988) for segmentation of the middle phalanx in the hand images was explored, with an aim of identifying the technique that yields more accurate results. Active shape models are statistical models derived from a set of shape examples. The model can change shape according to the possible deformations allowed in the set while searching a test image for an object with a similar shape to the training set examples. Deformable models evolve a contour under the constraint of image forces and the internal forces of the contour to find

object borders in images. These techniques were chosen due to the reported success in applying them for segmentation of radiographic hand images for BMD measurement (Chuaychunu et al., 2007; Gulam et al., 2000; Kauffman et al., 2004; Sotoca et al., 2003). There is no evidence in the literature of the evaluation of the accuracy of these techniques for this application. Both techniques require some form of initialisation and in line with achieving the goal of an automated system, a method for estimating the location of the bone centroid, which is used for initialisation for both techniques, was designed.

4.3 Identification and isolation of the middle finger

The purpose of this stage is to reduce the amount of image data to be processed in later stages in order to minimise the processing time. This was achieved by retaining only the middle finger, which has the bone of interest, in the images used for calculating bone mineral density.

For an input image, a threshold was applied to discriminate the hand from the background. A non-parametric and unsupervised technique was applied for automatic selection of a threshold that maximises the separation of the resulting classes of grey levels (Otsu, 1979). The thresholding algorithm is given in Appendix A. An example of the application of the algorithm to a typical image used in this project is shown in Figure 4.1.

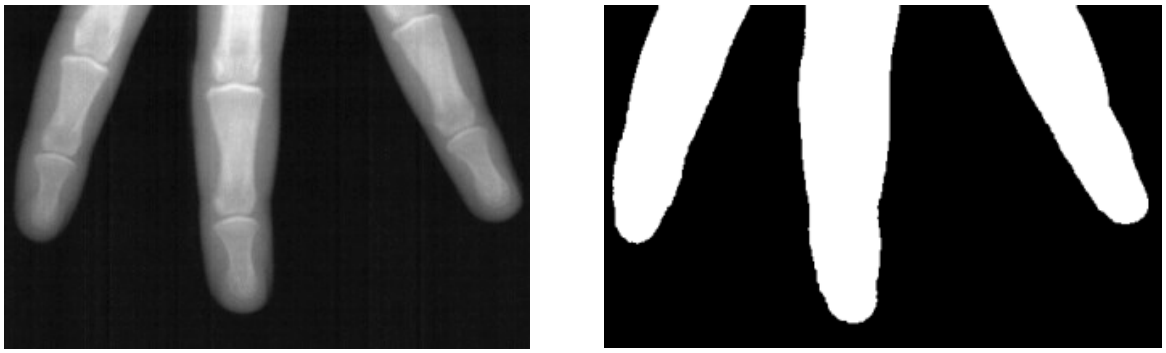

(a) **(b)**

Figure 4.1: Thresholding using Otsu's method. (a) Input image [Contrast has been enhanced for visualisation] and (b) Result.

The area of each detected object was evaluated as the sum of constituent pixels. The middle finger would normally be the largest finger and therefore the largest detected object was assumed to be the middle finger. The input image was automatically cropped around the detected middle finger by specifying a rectangle whose sides are 20 pixels from the extreme

finger points as shown in Figure 4.2. The cropped image was used in subsequent processing stages.

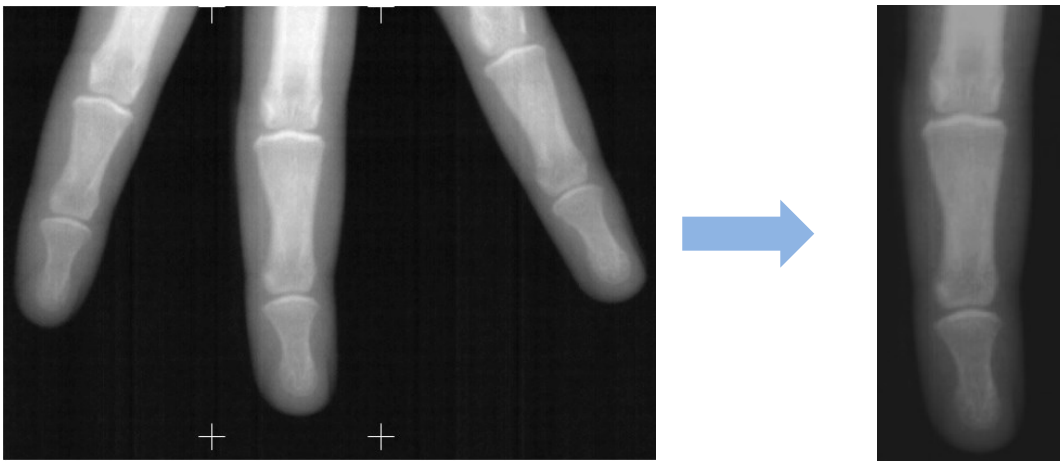

Figure 4.2: Cropping out the middle finger from an input image: image is cropped at the points indicated by the white crosses. [Contrast has been enhanced for visualisation].

In the second step, the orientation of the finger in the image (lengthwise) was determined by measuring the angle between vertical-axis and the major axis of an ellipse that has the same second-moments as the region covered by the finger (θ in Figure 4.3).

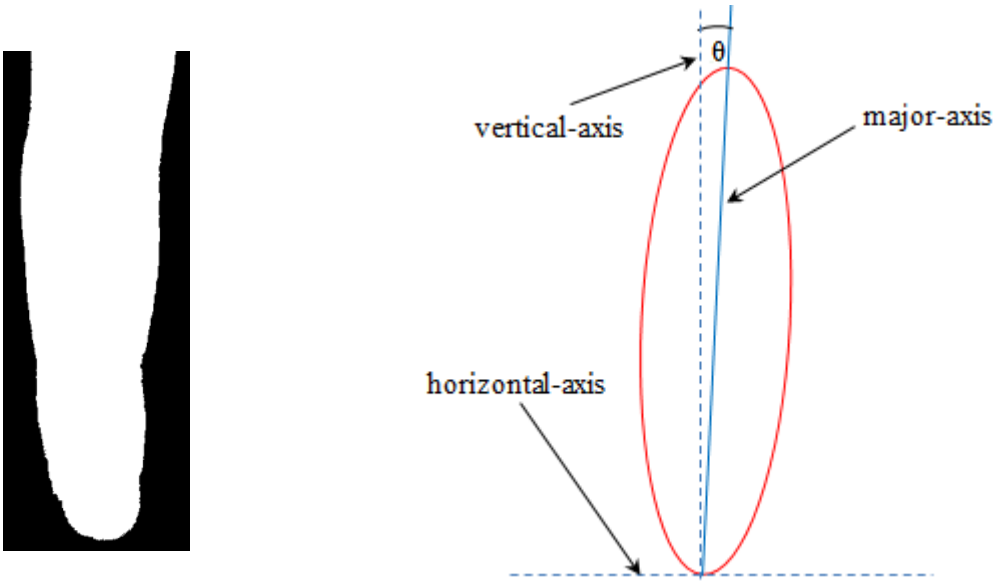

(a) **(b)**

Figure 4.3: Determination of orientation angle: (a) image to be re-orientated; (b) ellipse used for finding orientation angle of finger.

The input image was subsequently rotated by angle θ so that the output image contained only the middle finger that is approximately parallel to the vertical edge of the image as shown in Figure 4.4.

Figure 4.4: Typical radiographic image of middle finger after rotation to make finger approximately parallel to vertical edge of image. [Contrast has been enhanced for visualisation].

4.4 Determination of bone centroid

The centroid of the middle phalanx was the starting point for the segmentation stage in this project and its approximate location was determined by a heuristic search. The process is illustrated in Figure 4.5.

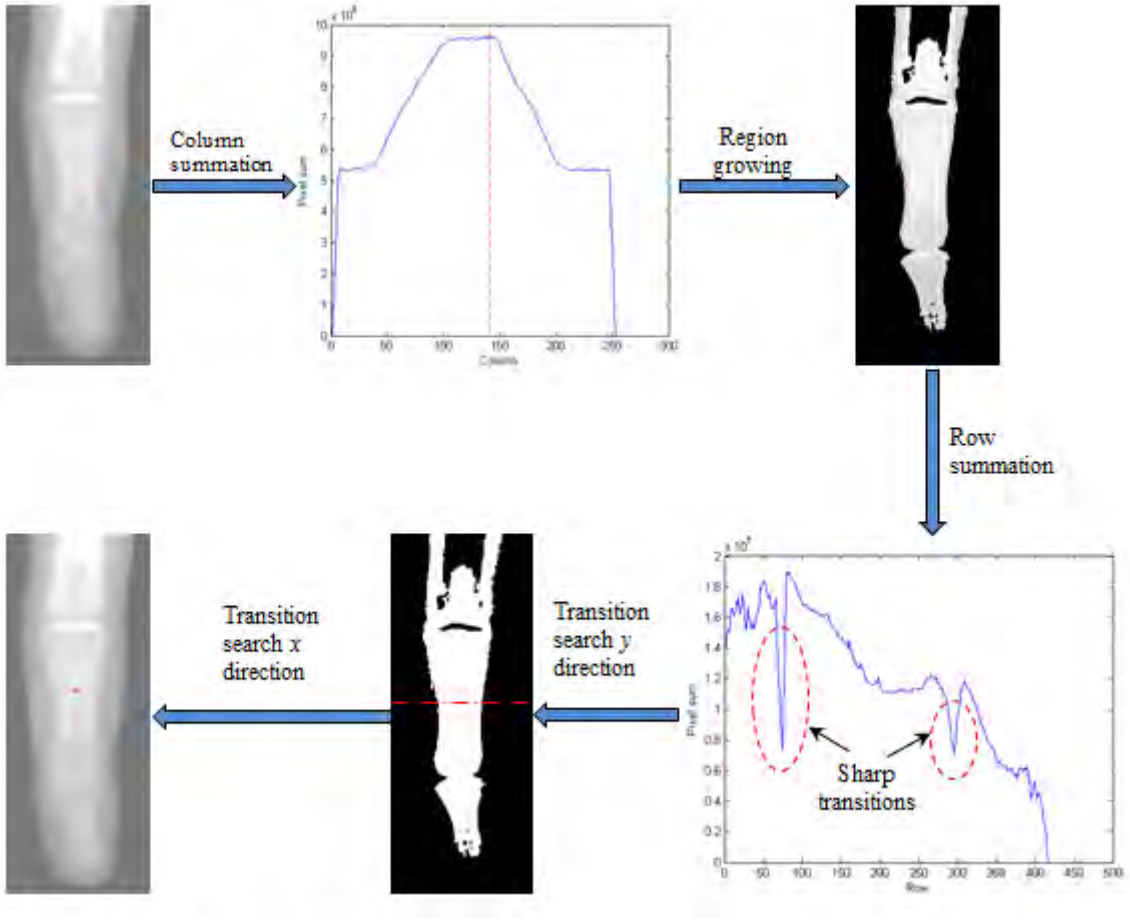

Figure 4.5: Steps in searching for the centroid (red cross): starting at the top left and following the arrows, input image; plot of column sums (dashed line represents the column with the highest sum; bone pixels identified by region growing; plot of row sums with transition points marked by the ellipses; the halfway point between the transition points of the row summation is the *y*-coordinate of the centroid (dashed line); the halfway point between transition points in the *x* direction in the logical image resulting from the region growing is the *x*-coordinate of the centroid.

First, pixel values in each column of the image matrix were summed. The column with the highest sum was taken as the approximate position of the midline through the middle finger since this is expected to have the highest number of bone pixels. Assuming that the middle finger covers more than half the length of the image, a pixel that is located at the halfway mark of the column with the highest sum was used as the seed point for a region growing algorithm to identify all bone pixels. The region growing algorithm was implemented using the following steps:

1. Start at the seed point.
2. Compute the pixel difference of each of the 4 neighbouring pixels of the seed.

3. Assign pixels whose difference is below the threshold to the bone region and assign those that are above the threshold to the background region.
4. Compute mean grey level of pixels currently assigned to the bone region.
5. Move to next pixel and compute the difference of each of its un-assigned neighbours with the mean of the bone region.
6. Repeat steps 3-5 until all pixels have been assigned to the bone or background regions.

An empirically determined threshold value was used for the algorithm. The region growing algorithm yields an image with non-zero values for bone pixels only. A row summation of the new image matrix was carried out, yielding a profile with distinct transitions caused by the proximal and distal interphalangeal joints. The middle phalanx is found in the region between the interphalangeal joints. The distance (L) between the transitions represents the length of the middle phalanx and $L/2$ is the y-coordinate of the centroid. At this height, y, the distance (W) between the intensity transitions occurring at the bone/soft tissue border represents the width of the bone and therefore $W/2$ is the x-coordinate of the centroid.

4.5 Deformable models

4.5.1 Theory

Deformable models for image segmentation were proposed by Kass et al. (1988) and have since become a popular technique in segmentation of medical images due to better performance in the presence of noise compared to traditional techniques (Brigger et al., 2000).

A deformable model (DM) is a curve or surface defined within an image domain that can move under the influence of internal forces generated from within the model and external forces computed from the image data such that the model will conform to object boundaries (Xu & Prince, 1998a; Xu & Prince, 2000).

DMs are classified as parametric or geometric, based on representation of the model and implementation (Han et al., 2003; Xu et al., 2000a; Xu & Prince, 2000). A Lagrangian formulation is used for defining a parametric model and explicitly represents the model as a parameterised curve. Eulerian formulation is used to define geometric deformable models and implicitly represents the models as level sets of 2-D distance functions. Only parametric

deformable models were considered in this project because of their computational efficiency and simplicity (Jacob et al., 2004), which would enable faster implementation.

To achieve segmentation, a DM has to be initialised in the image. This involves specifying an initial shape and position of the DM in the image being analysed. All the parameters of the DM are specified during initialisation after which it deforms towards an object border by solving a partial differential equation that is formulated as an energy minimisation process. Convergence is achieved when the model reaches a border and cannot deform any further. At the point of convergence, the final position and shape of the DM represents the detected border.

A 2-D parametric deformable model can be represented mathematically as:

$$\boldsymbol{V}(s) = \big(x(s), y(s)\big)\ s\,\epsilon\,[0,1] \quad \mathbf{4.1}$$

where *s* can be any parameter - the most common parameter is arc length.

The model is represented by two vectors that specify the coordinates of points on the DM. There are two common ways of formulating a parametric DM, namely, energy minimisation and dynamic force formulation (Xu et al., 2000b; Xu & Prince, 1998b). The discussions of these two methods that follow are derived from Xu et al. (2000a), Xu et al. (2000b) and Li et al. (2005).

Energy minimisation formulation

This technique defines a parametric model that minimises the weighted sum of the model's internal energy and external energy computed from the image data. Minimising the total energy yields internal forces and external forces that will drive the deformation of the model towards the required borders. The energy function, $\varepsilon(\boldsymbol{V})$, to be minimised is of the form:

$$\varepsilon(\boldsymbol{V}) = S(\boldsymbol{V}) + \mathcal{P}(\boldsymbol{V}) \quad \mathbf{4.2}$$

where $S(\boldsymbol{V})$ is the internal energy calculated as follows:

$$S(\boldsymbol{V}) = \frac{1}{2}\int_0^1 \alpha \left|\frac{\partial \boldsymbol{V}}{\partial s}\right|^2 + \beta \left|\frac{\partial^2 \boldsymbol{V}}{\partial s^2}\right|^2 ds \quad \mathbf{4.3}$$

The first and second terms of the integral constrain the stretching (elasticity) and bending (rigidity) of the model respectively, causing the model to behave like an elastic, rigid rod. The elasticity and rigidity of the model are regulated by the parameters α and β, respectively.

The second term of Equation 4.2 is the potential (external) energy functional that is obtained by integrating a potential energy function $P(x,y)$ along the model $\boldsymbol{V}(s)$:

$$\mathcal{P}(\boldsymbol{V}) = \int_0^1 P\big(\boldsymbol{V}(s)\big) \quad \mathbf{4.4}$$

$P(x,y)$ is computed from the image data and has minimum values at object boundaries. A Gaussian potential force is then computed from the potential energy function. In a traditional DM, a potential energy function that drives a deformable model towards an edge in an image $I(x,y)$ is:

$$P(x,y) = -w_e|\nabla[G_\sigma(x,y) * I(x,y)]|^2 \quad \mathbf{4.5}$$

where w_e is a positive weighting parameter, ∇ is the gradient operator, $G_\sigma(x,y)$ is a 2-D Gaussian function with standard deviation σ, * is the 2-D convolution operator.

A deformable model that minimises $\varepsilon(\boldsymbol{V})$ must satisfy the Euler equation given below.

$$\alpha\left|\frac{\partial \boldsymbol{V}}{\partial s}\right|^2 - \beta\left|\frac{\partial^2 \boldsymbol{V}}{\partial s^2}\right|^2 - \nabla P(\boldsymbol{V}) = 0 \quad \mathbf{4.6}$$

Equation 4.6 can be viewed as a force balance equation between the internal forces within the model, F_{int}, as given by Equation 4.7 and the external potential force computed from the image, F_{ext}, as given by Equation 4.8.

$$F_{int}(\boldsymbol{V}) = \alpha\left|\frac{\partial \boldsymbol{V}}{\partial s}\right|^2 - \beta\left|\frac{\partial^2 \boldsymbol{V}}{\partial s^2}\right|^2 \quad \mathbf{4.7}$$

$$F_{ext} = -\nabla P(\boldsymbol{V}) \quad \mathbf{4.8}$$

To solve Equation 4.6, the DM is made dynamic by introducing a time variable into $\boldsymbol{V}$ so that the model becomes a function of time, t, and s. The partial derivative of $\boldsymbol{V}$ with respect to t is computed and then equated to the left hand side of Equation 4.6:

$$\frac{\partial \boldsymbol{V}}{\partial t} = \alpha\left|\frac{\partial \boldsymbol{V}}{\partial s}\right|^2 - \beta\left|\frac{\partial^2 \boldsymbol{V}}{\partial s^2}\right|^2 - \nabla P(\boldsymbol{V}) \quad \mathbf{4.9}$$

When the solution $\boldsymbol{V}(s,t)$ stabilises, the right hand side of Equation 4.9 disappears and a solution of Equation 4.6 is achieved. To find a numerical solution of Equation 4.9, the equation is made discrete and the discrete system is iteratively solved.

Dynamic force formulation

In dynamic force formulation, the DM is directly treated as a function of *s* and *t*, *V(s,t)*. The DM must satisfy:

$$\mu \frac{\partial^2}{\partial t^2} = F_{damp}(\boldsymbol{V}) + F_{int}(\boldsymbol{V}) + F_{ext}(\boldsymbol{V}) \quad \mathbf{4.10}$$

where μ is a coefficient that has a mass unit, F_{int} and F_{ext}, are the internal and external forces respectively, F_{damp} is the damping force defined by Equation 4.11 in which γ is the damping coefficient.

$$F_{damp}(\boldsymbol{V}) = -\gamma \frac{\partial \boldsymbol{V}}{\partial t} \quad \mathbf{4.11}$$

If μ is set to zero, the dynamics of the model become:

$$\gamma \frac{\partial \boldsymbol{V}}{\partial t} = F_{int}(\boldsymbol{V}) + F_{ext}(\boldsymbol{V}) \quad \mathbf{4.12}$$

The internal force is the same as that used in the energy minimisation formulation (Equation 4.7) but the external force does not strictly have to be a potential force. Potential forces used by traditional DMs can be calculated as the negative gradient of a potential energy function while non-potential external forces cannot be expressed as a negative gradient of a potential energy function. The external force can be expressed as a sum of various forces which can be implemented simultaneously to increase the capture range for the model (the maximum distance from an object border at which the force is strong enough to attract an initial model and pull it towards the border).

Numerical methods that can be used to implement parametric deformable models include finite difference methods, dynamic programming and greedy algorithms. The finite difference method is the simplest and has an added advantage of being computationally efficient.

4.5.2 Implementation

The implementation of the DM was adapted from Dendere (2009) and uses a toolbox for deformable models developed by Xu & Prince (1998a).

Formulation

The DM, *v(s,t)*, was formulated as a function of arc length, *s*, and time, *t*. The model was represented by an $n \times 2$ matrix specifying the spatial coordinates of *n* points on the model. The DM was evolved using the following partial differential equation (PDE):

$$\frac{\partial v}{\partial t} = \alpha \frac{\partial^2 v}{\partial s^2} - \left(\beta \frac{\partial^4 v}{\partial s^4} + \kappa f_e + \lambda f_b \right) \quad \mathbf{4.13}$$

where:

s is the arc length from an arbitrary point to the rest of the points on the curve;

α and β are constants that control the elasticity and rigidity of the DM during deformation;

f_e is the image-dependent external force calculated using Equation 4.8 which attracts the DM towards an object border;

f_b is the balloon force that augments the external force in driving the DM towards image borders;

κ and λ are weighting parameters that control the contribution of the external force and the balloon force, respectively.

Values for the regulating parameters of the DM, α and β, were determined empirically. The external force was in the form of two scalar matrices, *fx* and *fy*. The external force was computed from the grey level image data prior to evolution using Equation 4.8. The optimum standard deviation of the Gaussian filter (σ) required for computing the $P(x,y)$ in Equation 4.5 was determined empirically to ensure that the model converges as close to the required border as possible without being attracted to the borders of other bones. A value for κ, which determines the contribution of the potential force, was computed for each image as a fraction of the inverse of the external force. The contribution of the balloon force was weighted by λ which was also experimentally determined. A balloon force is a non-potential external force suggested by Cohen (1991) to increase the capture range for deformable models. The balloon force was included in this project as a constraint on the model to ensure that it expands during deformation. The balloon force was computed as follows:

$$f_b = \mathbf{n}(\mathrm{s}) \quad \mathbf{4.14}$$

where **n**(s) is the normal unit vector to the curve at point ***V***(s) on the model.

Algorithm

The algorithm for the DM can be summarised as follows:

1. Compute the external image force, f_e
2. Compute the external force regularisation constant, κ.
3. Determine the derivatives of Equation 4.13 using discrete convolution.
4. Initialise the deformable model: the model was initialised as a circle centred at the approximated centroid of the bone of interest, with a radius equal to the width of the bone at this image row as shown in Figure 4.6.
5. Evaluate the distance between an arbitrary point and the rest of the points on the model. Compute new model points by interpolating from the old ones if the average distance is not equal to 1.
6. Evaluate the external force at each model point by interpolation.
7. Evaluate the balloon force.
8. Convolve the current model points with the derivatives determined in step 3.
9. Update the model according to Equation 4.13.
10. Compute the area in the region bounded by the curve and save the latest 10 values. If the change in area in the last 10 values is less than 1 pixel, the model is deemed to have converged and deformation is halted. If the change is more than 1 pixel, deformation continues by repeating steps 5 – 10 until convergence is reached.

When convergence was reached, the algorithm returned two vectors, **x** and **y**, whose elements were the x and y coordinates, respectively, of points on the final position of the model. The final position of the model represents the detected border of the bone.

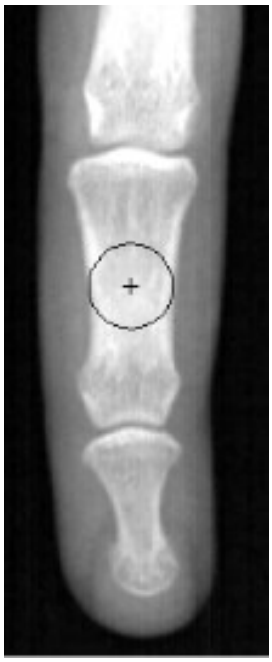

Figure 4.6: Initialisation of a DM: cross represents the bone centroid which is the centre of the initial DM. [Contrast has been enhanced for visualisation].

4.6 Active shape models

4.6.1 Theory

First introduced by Cootes et al. (1993), active shape models (ASMs) have become a popular segmentation technique for medical images and numerous improvements have been suggested by various authors since their introduction. ASMs segment images in an iterative manner that is analogous to DMs but the key difference is that ASMs can only deform to fit a target shape that is consistent with the shapes in the training data (Cootes et al., 1995). The discussion of the theory of ASMs that follows is based on Cootes et al. (1995), Cootes et al. (1994) and Cootes (2000).

The ASM technique builds a point distribution model (PDM) from a set of example shapes in a training set of images. The PDM describes both the average shape and the variability of the shapes. A PDM is built by extracting example shapes of objects in a training set. Each shape is represented by a vector of coordinates for a set of landmark points on the boundary. The landmark points are placed by a user during the training stage. Each labelled point represents a particular part of the object in each of the training shapes and this is critical in ensuring that the method does not fail.

Shape alignment

The coordinates of the labelled points are aligned by geometric transformations (scaling, rotation and translation) of the training shapes so that they correspond as closely as possible. This is achieved by minimising a weighted sum of squares of distances between equivalent points on the example shapes. If $\mathbf{x}_i$ is a vector that describes the i^{th} shape with n points in a training set:

$$\mathbf{x_i} = (x_{i0}, y_{i0}, x_{i1}, y_{i1}, \cdots, x_{ik}, y_{ik}, \cdots, x_{in-1}, y_{in-1})^T \quad \mathbf{4.15}$$

and a geometric transformation consisting of a rotation by θ and a scaling by s is given by:

$$M(s,\theta)\begin{bmatrix} x_{jk} \\ y_{jk} \end{bmatrix} = \begin{bmatrix} (s\cos\theta)x_{jk} - (s\ \sin\theta)y_{jk} \\ (s\ \sin\theta)x_{jk} + (s\ \cos\theta)y_{jk} \end{bmatrix} \quad \mathbf{4.16}$$

then given two similar shapes, $\mathbf{x}_i$ and $\mathbf{x}_j$, values for θ_j, s_j and a translation $\mathbf{t}$ can be chosen for mapping $\mathbf{x}_i$ onto $M(s_j, \theta_j)[\ \mathbf{x}_j] + \mathbf{t}_j$ so as to minimise the weighted sum:

$$E_j = \left(\mathbf{x_i} - M(s_j, \theta_j)[\mathbf{x_j}] - \mathbf{t}_j\right)^T \mathbf{W}\left(\mathbf{x_i} - M(s_j, \theta_j)[\mathbf{x_j}] - \mathbf{t}_j\right) \quad \mathbf{4.17}$$

where $\mathbf{W}$ is a diagonal matrix of weights for each point and $\mathbf{t_j} = (t_{xj}, t_{yj}, \cdots, t_{xj}, t_{yj})^T$. The weights are chosen to give more significance to the points that exhibit the least movement with respect the other points in a shape. A typical weighting matrix that consists of weights for the k^{th} point is defined by:

$$w_k = \left(\sum_{l=0}^{n-1} V_{R_{kl}}\right)^{-1} \quad \mathbf{4.18}$$

where R_{kl} is the distance between points k and l, and $V_{R_{kl}}$ is variance in the distance over the set of shapes. The following algorithm is used to align the shapes in a training set:

1. Align each shape to the first shape in the set through scaling, rotation and translation.
2. Compute the mean shape from the aligned shapes.
3. Normalise the orientation, scale and origin of the current mean shape.
4. Align every shape to the current mean.
5. Repeat steps 2-4 until convergence is reached.

Derivation of the PDM

The aligned shapes are assumed to lie within an ellipsoidal region of a $2n$ dimensional space. The mean shape of the aligned shapes is computed as follows:

$$\bar{\mathbf{x}} = \frac{1}{N}\sum_{i=1}^{N} \mathbf{x_i} \quad \mathbf{4.19}$$

Principal component analysis (PCA) is applied to find the principal axes of a $2n$-dimensional ellipsoid fitted to the shape data. The PCA algorithm is applied in the following steps:

1. Compute the deviation of each shape from the mean:

$$d\mathbf{x_i} = \mathbf{x_i} - \bar{\mathbf{x}} \quad \mathbf{4.20}$$

2. Compute the $2n \times 2n$ covariance matrix:

$$\boldsymbol{S} = \frac{1}{N}\sum_{i=1}^{N} d\mathbf{x_i}\, d\mathbf{x_i}^T \quad \mathbf{4.21}$$

3. Compute the unit eigenvectors, $\mathbf{p}_h$, (h = 1,…, $2n$), and corresponding eigenvalues, λ_h, of the covariance matrix sorted in descending order i.e. $\lambda_h \geq \lambda_{h+1}$.

The principal axes of the ellipsoid are described by the unit eigenvectors of **S**, such that

$$\mathbf{S}\mathbf{p_h} = \lambda_h \mathbf{p_h} \quad \mathbf{4.22}$$

where λ_h is the h^{th} eigenvalue of **S** and

$$\mathbf{p_h}^T \mathbf{p_h} = 1 \; \mathbf{4.23}$$

The eigenvectors of the covariance matrix with the largest eigenvalues describe the most significant modes of variation in the shapes. Most of the variation can usually be explained by a small number of modes, m. The value of m is usually a compromise between accuracy and simplicity. A value for m which retains a proportion, f_v, of the total variation can be determined as follows:

$$\sum_{i=1}^{m} \lambda_i \geq f_v \, \lambda_T \quad \mathbf{4.24}$$

where λ_T is the total variance of the shapes given by:

$$\lambda_T = \sum_{i=1}^{2n} \lambda_i \quad \mathbf{4.25}$$

Any shape, **x**, in the set can be described by adding a linear combination of the eigenvectors to the mean shape, $\bar{\mathbf{x}}$:

$$\mathbf{x} = \bar{\mathbf{x}} + \mathbf{Pb} \quad \mathbf{4.26}$$

where $\mathbf{P} = (\mathbf{p}_1\ \mathbf{p}_2 \ldots \mathbf{p}_m)$ is the matrix of the first m eigenvectors and $\mathbf{b} = (b_1\ b_2 \ldots b_m)^T$ is a vector of weights. This allows new shapes to be generated by varying **b**. The limits for $\mathbf{b}_i$ can be chosen such that the Mahalanobis distance, D_M, from the mean shape is less than a pre-set value D_{max}.

$$D_M^2 = \sum_{i=1}^{m} \left(\frac{b_i^2}{\lambda_i}\right) \leq D_{max}^2 \quad \mathbf{4.27}$$

Image search

To locate the boundary points of an object with a similar shape to the mean shape, the ASM is initialised by a specifying a rough starting position. The ASM then attempts to find the shape and pose parameters that cause the model to coincide with the object of interest in the image. An instance of the model in a test image is defined by the starting position, orientation and scale:

$$\mathbf{X} = M(s,\theta)[\mathbf{x}] + \mathbf{X}_c \quad \mathbf{4.28}$$

where **x** is the shape of the model instance in the model coordinate space, $\mathbf{X}_c = (X_c,Y_c, X_c,Y_c,\ldots, X_c,Y_c)^T$ is the shape of the model instance in the coordinate space of a test image and $M(s,\theta)$ is a rotation by θ and scaling by s, $(X_c,Y_c,)$ is the spatial position of the centroid of the model.

An iterative process is carried out by examining the regions of the image around each landmark and adjusting the pose, scale and shape parameters in order to move the landmarks to locations that better match the object in the image. The goal is to find a translation (dX_c,dY_c), rotation $(d\theta)$ and a scaling factor $(1+ds)$ that best map the current shape (**X**) to a new shape (**X**+d**X**). The initial position is given by Equation 4.28 and a set of residual adjustments d**x** in the model coordinate space such that:

$$M(s(1+ds),(\theta+d\theta)[\mathbf{x}+d\mathbf{x}] + (\mathbf{X}_c + d\mathbf{X}_c) = (\mathbf{X} + d\mathbf{X}) \quad \mathbf{4.29}$$

Thus

$$M(s(1+ds),\theta+d\theta)[\mathbf{x}+d\mathbf{x}] = (M(s,\theta)[\mathbf{x}]+d\mathbf{X}) - (\mathbf{X}_c + d\mathbf{X}_c) \quad \mathbf{4.30}$$

Solving for $d\mathbf{x}$ yields:

$$d\mathbf{x} = M((s(1+ds))^{-1}, -(\theta+d\theta)[\mathbf{y}] - \mathbf{x} \quad \mathbf{4.31}$$

where

$$\mathbf{y} = M(s,\theta)[\mathbf{x}] + d\mathbf{X} - d\mathbf{X}_c \quad \mathbf{4.32}$$

Shape constraints are applied throughout the iteration in order to maintain similarity with the example shapes used during the training of the ASM. In order to apply the shape constraints, $d\mathbf{x}$ is transformed into the model parameter space to yield $d\mathbf{b}$. A least squares approximation is then used to calculate the shape parameter adjustments, $d\mathbf{b}$ using the following equation:

$$d\mathbf{b} = \mathbf{P}^T d\mathbf{x} \quad \mathbf{4.33}$$

Equation 4.33 allows changes to the pose variables and adjustments dX_c, dY_c, $d\theta$ and ds, required to better match the model to the target object to be calculated. The changes are computed in an iterative manner:

$$X_c \rightarrow X_c + w_m dX_c$$

$$Y_c \rightarrow XY_c + w_m dY_c$$

$$\theta \rightarrow \theta + w_\theta d\theta$$

$$s \rightarrow s(1 + w_s ds)$$

$$\mathbf{b} \rightarrow \mathbf{b} + \boldsymbol{W}_b d\boldsymbol{b}$$

where w_m, w_θ and w_s are scalar weights, and $\mathbf{W}_b$ is a diagonal matrix of weights – one for each mode. The process of computing and updating the shape parameters is repeated until no significant changes occur.

Cootes et al. (1994) suggest that the ASM image search be implemented in multi-resolution framework to improve the efficiency and robustness of the algorithm. In this approach, the search for the target object described above is initially conducted in a coarse, low resolution version of the image and subsequently refining the search in a higher resolution, finer version of the image. A Gaussian image pyramid is built for each training and test image with the

base image (level 0) being the original image. Images for the subsequent levels are formed by smoothing and subsampling the original image to yield an image with half the number of pixels of the image in the preceding higher level image. The number of levels, L_{max}, is defined by the user. The algorithm for multi-resolution image search can be summarised in the following steps:

1. Set $L = L_{max}$
2. While $L \geq 0$
   a. Compute model point positions in image at level L.
   b. Search at preset number of sample points on either side of the current point (n_s).
   c. Update pose and shape parameters to fit model to new points.
   d. Return to *a* unless more than the desired proportion of points found within $n_s/2$ of current position (p_{close}) or the maximum allowable number of iterations at each level has been reached.
   e. If $L > 0$ then move search to next level (L-1)
3. Result is given by the parameters after convergence at level 0.

4.6.2 Implementation

The implementation of the ASM was based on the algorithm suggested by Cootes et al. (1995) and Cootes et al. (1994) by modifying a freely available ASM tool (Abu-Gharbieh et al., 1998; Hamarneh et al., 1998) to suit the application required herein.

Training

Excised bones were scanned to provide training shapes for the ASM in order to avoid needless radiation exposure to participants. The museum in the Department of Human Biology at University of Cape Town provided excised middle phalanges of the middle finger. Since the ASM was to be applied for segmentation of the middle phalanx in the left hand, it required training using bones from the left hand. The following classification scheme was used to determine whether a bone is from the left or right hand:

1. In the dorsal view i.e. the bone placed on a flat surface as though the palm is facing down, the projection of the superior margin of the proximal facet is off-centre and located on the opposite side of the hand where the bone is from. This method, illustrated in Figure 4.7, has an accuracy rate of 96% for correct identification of hand side for middle phalanx bones (Case & Heilman, 2006).

2. With the bone on a flat surface on its dorsal aspect i.e. as though the palm is facing upwards, the side of the proximal base that is higher is on the side where the bone is from i.e. if left side is higher the bone is from left hand This method has an accuracy rate of 90% (Case & Heilman, 2006).

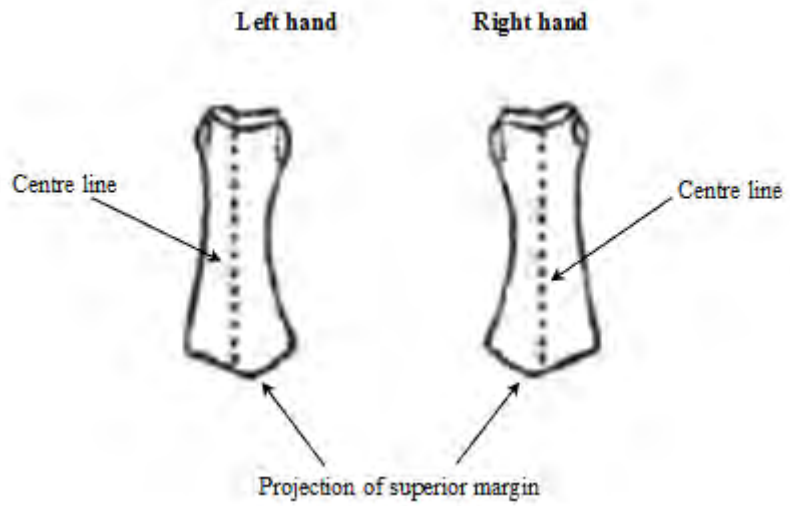

Figure 4.7: Determining the hand side for a middle phalanx.

Using this scheme, 96 bones were identified as being from the left hand. A common practice in pattern recognition for training and testing classifiers or statistical models is to split a given dataset into a small training set and a large test set. Therefore, the bones were divided into a training set of 30 bones for computing the mean ASM shape and a test set of 66 bones. The bones were scanned using tube settings of 140 kVp and 50 mA; the reason for using these values is explained in Chapter 6. The absence of soft tissue was not expected to affect the ASM training as the landmark points were placed manually on the bone edge by a mouse click. In the X-ray images of the bones, landmark points for the ASM were placed at the prominent features of the bone and two additional points were added between each pair of prominent features. For each bone, 46 points were used to fully describe the bone shape as shown in Figure 4.8. The number of landmark points used here is comparable to the 42 points used by Sotoca et al. (2003) and Figure 4.8 shows that 46 points adequately describe the bone shape.

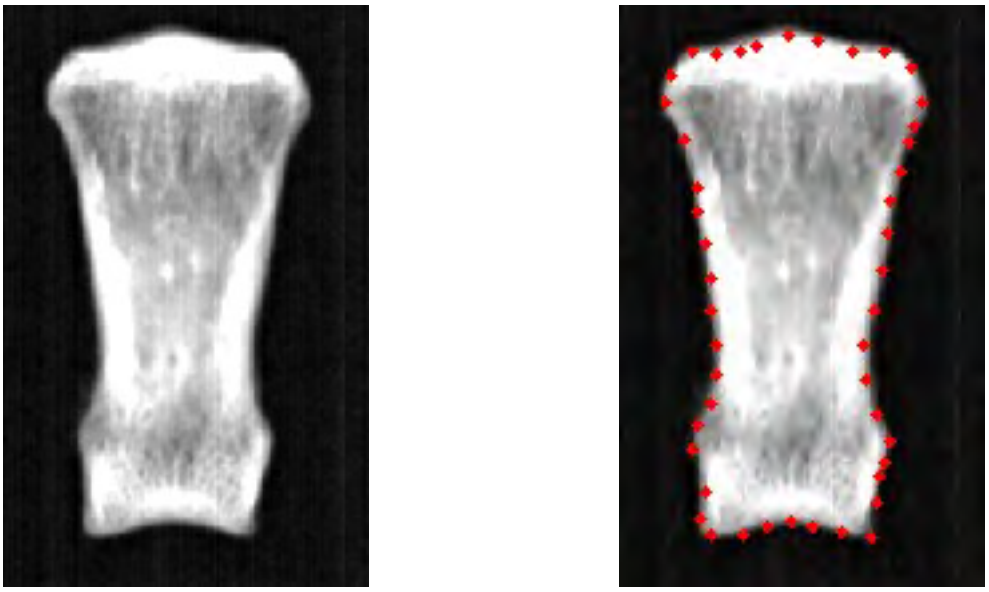

(a) (b)

Figure 4.8: Placement of landmark points in bone images for shape description for ASM training: (a) example bone image; (b) landmark points on bone in image. [Contrast has been enhanced for visualisation].

The shapes derived from the training set were aligned and the PDM was derived using the shape alignment algorithm and PDM derivation algorithms, respectively. These algorithms were described in Section 4.6.1 and illustrated in Figure 4.9.

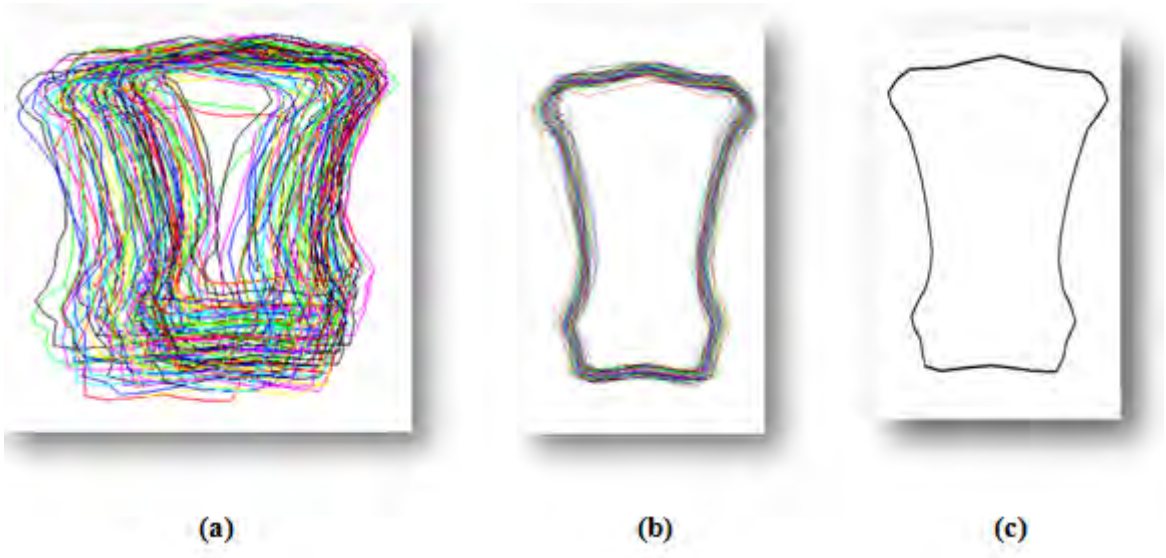

(a) (b) (c)

Figure 4.9: ASM training: (a) extracted shapes from training examples; (b) aligned shapes; (c) mean shape.

Image search

The image search commences by initialising the ASM in the image. Initial experiments showed that the final segmentation is highly dependent on the quality of the initialisation. One way of initialising the ASM is to mark a few landmark positions on the target ROI or marking an approximate position of the centroid of the target ROI. In line with the aim of automation and minimising user input, the centroid option was taken. The ASM was therefore automatically initialised by aligning the centroid of the mean shape in the PDM with the centroid determined by the technique described in Section 4.4. Figure 4.10 shows an example of ASM initialisation.

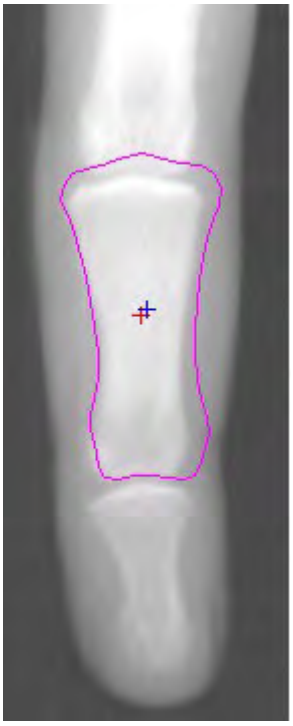

Figure 4.10: ASM initialisation: red cross indicates estimated position of target ROI centroid; blue cross shows position of the ASM centroid. [Contrast has been enhanced for visualisation].

After initialising the ASM, the multi-resolution image search technique described in Section 4.6.1 was carried out using the experimentally determined parameter values. Once the ASM had converged, the user was shown the detected border superimposed on the test image. The user was prompted to indicate if the resulting shape adequately fits the target bone, is too big, or too small. If the resulting shape was too big (or small) the scaling factor applied to the initial mean shape was reduced (or increased) by 0.05 and the search was repeated until a satisfactory result was achieved.

4.7 Evaluation of segmentation

The segmentation accuracy of the two methods was evaluated by computing the difference in the location of the borders detected by the methods and the ground truth using the Hausdorff distance. The purpose of this exercise was to identify the method which provides more accurate detection of the bone borders. Accuracy in this context means closer to the ground truth. 15 volunteers were recruited and their left hands were scanned to provide test images for the segmentation evaluation. Two graduate students were asked to perform manual segmentation of the test images under the guidance of a qualified radiographer by marking positions of the prominent features on the bone edges and two additional points were placed between each pair of prominent features using a mouse click. The average of the borders produced by manual segmentation in each test image was used as the ground truth for comparison.

The Hausdorff distance (HD) can be used to determine the degree of resemblance between two objects superposed on one another (Huttenlocher et al., 1993). The HD can be defined as follows:

Given two finite set points $A = \{a_1, a_2, \dots a_p\}$ and $B = \{b_1, b_2, \dots b_q\}$, the Hausdorff distance between the two sets is:

$$H(A,B) = \max\big(h(A,B), h(B,A)\big) \quad \mathbf{4.34}$$

where $h(A,B)$ is the directed Hausdorff distance from *A* to *B*, $h(B,A)$ is the directed HD from *B* to *A* defined as:

$$h(A,B) = max_{a\in A} min_{b\in B} \|a-b\| \quad \mathbf{4.35}$$

$$h(B,A) = max_{b\in B} min_{a\in A} \|b-a\| \quad \mathbf{4.36}$$

$\|a-b\|$ is a distance metric and the most commonly used metric is the Euclidean distance.

By letting *A* in Equation 4.34 be the spatial coordinates of the points on the border representing the ground truth and *B* the spatial coordinates of the points on the algorithm-determined border, the HD can be used to compare two or more segmentation techniques against a ground truth (Khutlang et al., 2010; Nain et al., 2007). The objective is to rank segmentation techniques to determine the technique that yields borders that are closer to the ground truth. This ranking method can also be useful for fine-tuning variable parameters for

segmentation techniques in order to obtain borders that are as close to ground truth as possible.

In this project, the DM and ASM segmentation algorithms were applied to the test images and the output of each method was an $n \times 2$ matrix describing the spatial coordinates of a series of n pixels on the border of the bone of interest. The HD was used to quantify the deviation of the algorithm-determined borders from the ground truth in order to identify the technique that provides borders that are closer to the ground truth i.e. the technique with the smaller deviation from the ground truth.

4.8 Results of DM and ASM-based segmentation

The results achieved with the proposed segmentation methods are discussed in this section. The method used for evaluating the methods and results of the evaluation are also discussed.

4.8.1 Deformable model segmentation

Optimum values for the DM parameters are given in Table 4.1. These values were determined empirically to yield the best possible segmentation according to the segmentation evaluation method. Higher values for α limit the elasticity of the model, causing the deformation to take longer since the model was initialised as a small circle inside the bone and requires significant stretching in order to get close to the border. Values for β, which controls the rigidity of the model, had little influence on the deformation of the model. Higher values for β allow the model conform to smooth curves while smaller values are essential for ragged borders such as those found in magnetic resonance images of the brain and other organs. The given values for α and β provided good balance between accurate conformation to the bone border and deformation speed. The given values for the weighting parameter for the balloon force in Equation 4.13 (λ), standard deviation for the Gaussian function in Equation 4.5 (σ), and weighting parameter for potential energy function in Equation 4.5 (ω_e), were chosen to ensure that DM conforms to the border of the bone without straying to the other unwanted bones.

Table 4.1: Values for the parameters of the DM.

Parameter	Value
α	0.1
β	0.1
λ	0.05
σ	2
ω_e	0.2

Figure 4.11 shows a typical segmentation result produced by the DM using the parameter values given in Table 4.1.

(a) (b)

Figure 4.11: Typical result of DM segmentation: (a) test image; (b) detected border. [Contrast has been enhanced for visualisation].

4.8.2 Active shape model segmentation

The empirically-determined values used for the various parameters for the ASM are given in Table 4.2.

Table 4.2: Parameter values for ASM training and segmentation.

Parameter	Value
f_v	90%
$D_{\max}$	3 pixels
L_{max}	3
n_s	3
p_{close}	3 pixels

The ASM algorithm was first tested on the test set of excised bones and after yielding satisfactory results, *in-vivo* testing was conducted in images of volunteers. Figure 4.12 shows a typical result of ASM segmentation in images of excised bones and Figure 4.13 shows typical segmentation in *in-vivo* images.

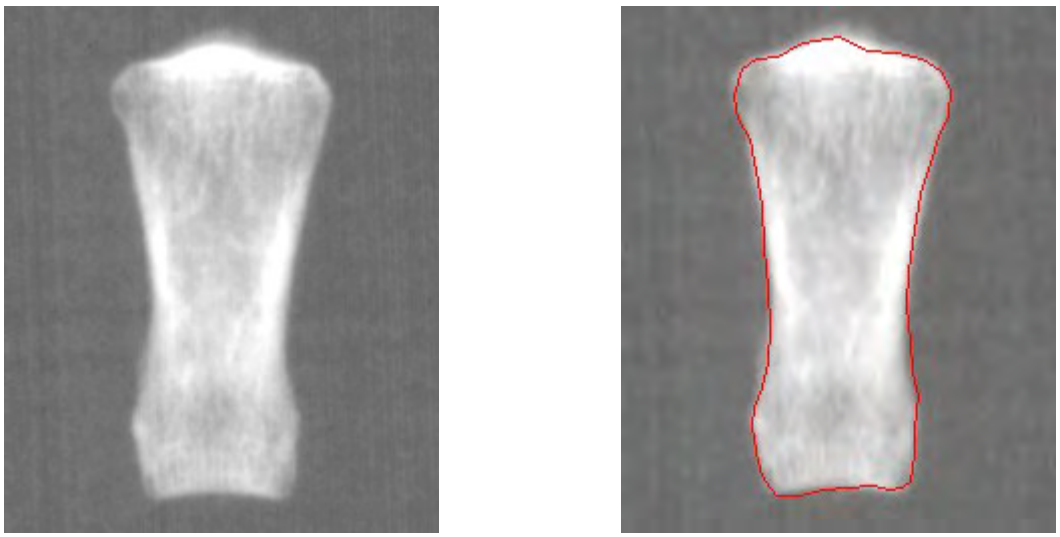

(a) **(b)**

Figure 4.12: Typical ASM-based segmentation in images of excised bones: (a) test image; (b) detected border. [Contrast has been enhanced for visualisation].

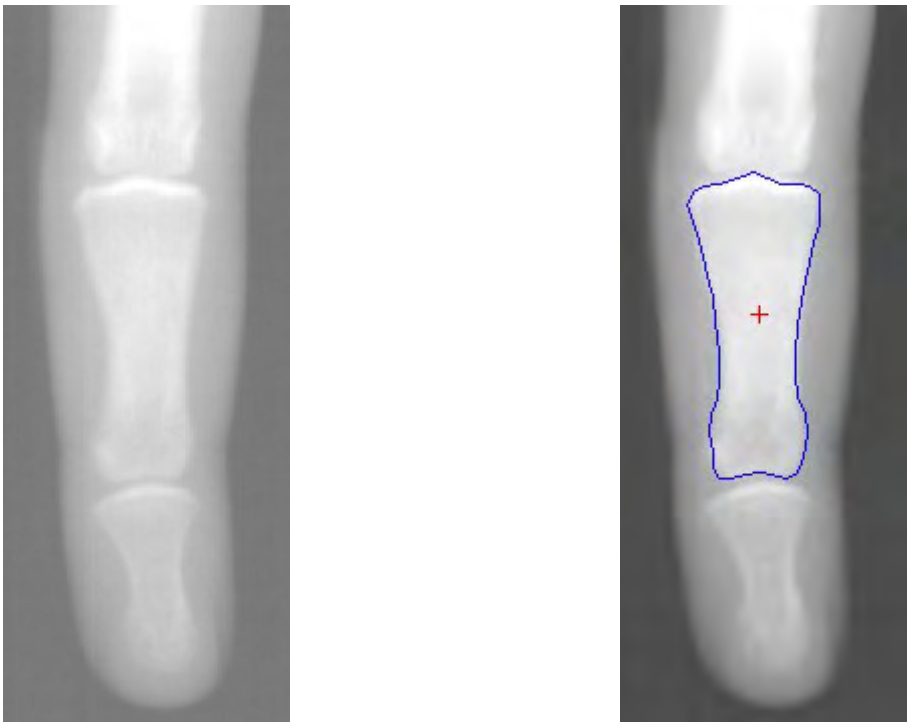

(a) (b)

Figure 4.13: Typical ASM-based segmentation in in-vivo images: (a) test image; (b) detected border; red cross indicates estimated centroid of bone. [Contrast has been enhanced for visualisation].

4.8.3 Evaluation of segmentation

The ASM algorithm was first tested on a dataset similar to that used for training. The test set consisting of 66 images of excised bones. Visual comparison of the ASM-determined borders with the reference borders showed close similarity and hence accurate segmentation, with an average HD of 5.72 pixels, a minimum of 3.74 pixels and a maximum of 8.58 pixels. Table 4.3 summarises the results of the differences between borders detected by the two algorithms and reference borders while Figure 4.14 and Figure 4.15 show examples of the comparison between bone borders produced by the methods and reference borders for *in-vivo* segmentation.

Table 4.3: Hausdorff distances for ASM and DM-determined borders.

Method	Hausdorff distance (pixels)		
	Mean (standard deviation)	***Minimum***	***Maximum***
ASM (excised bones)	5.72 (1.04)	3.74	8.58
ASM (*in-vivo*)	5.58 (0.93)	4.03	7.83
Deformable model	10.3 (2.25)	6.57	14.7

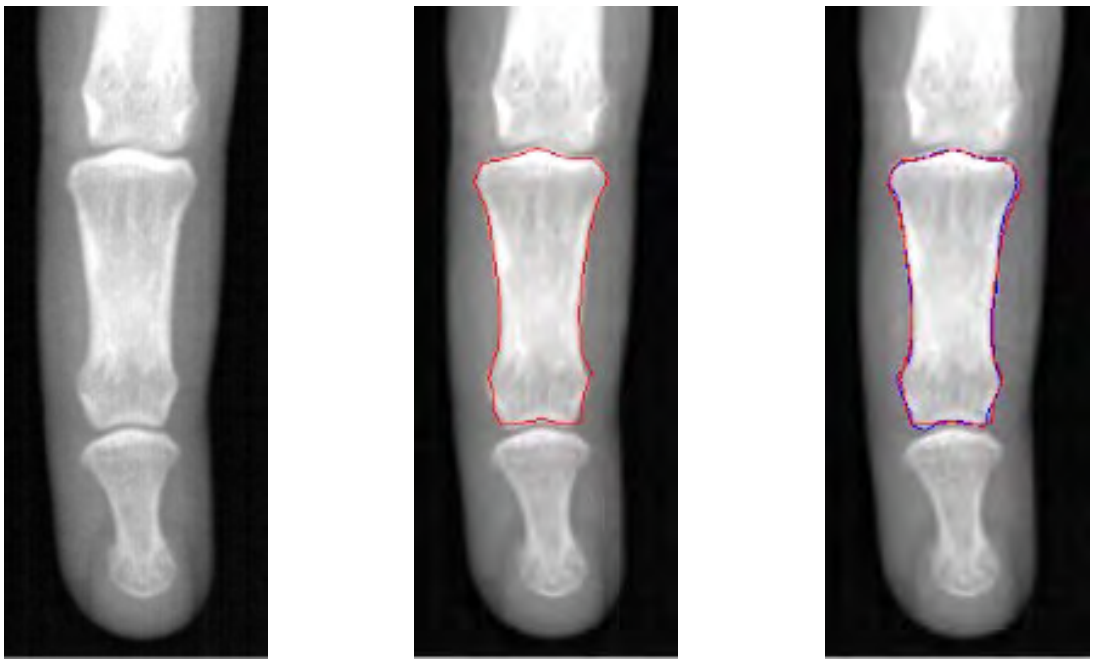

(a) **(b)** **(c)**

Figure 4.14: An example of ASM-determined border and reference border: (a) test image; (b) detected border; (c) detected border (red), reference border (blue) – Hausdorff distance = 4.53pixels. [Contrast has been enhanced for visualisation].

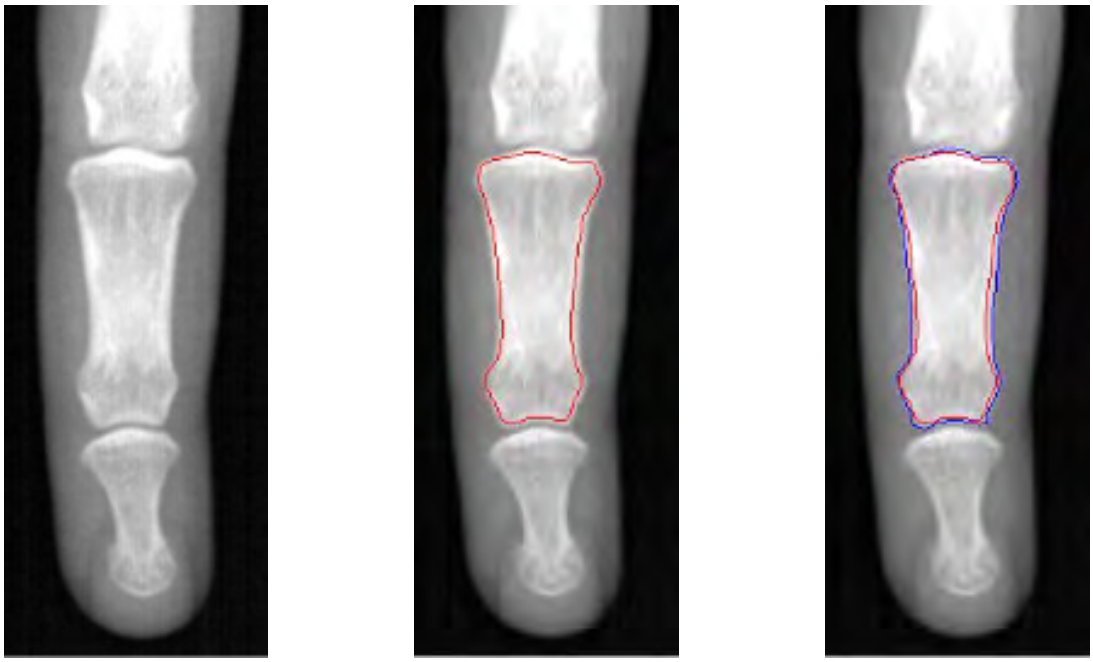

(a) (b) (c)

Figure 4.15: An example of DM-determined border and reference border; (a) test image; (b) detected border; (c) detected border (red), reference border (blue) – Hausdorff distance = 6.57pixels. [Contrast has been enhanced for visualisation].

4.9 Discussion

Results showed that the DM tends to converge farther from the actual bone border compared to the ASM. This could be solved by increasing the width of the Gaussian filter used in the calculation of the external image force or initialising the model outside the ROI. However, the presence of other bones close to the bone of interest renders these possible solutions impractical as they would cause the model to be attracted to the other bones. Even though only a small area of the bone is excluded by the deformable model, this area is a significant portion of the cortical bone and this is expected to distort BMD measurements. In contrast, the ASM tends to detect the border of the bone with higher accuracy although it is also to prone errors due to the presence of other bones. However, the initialisation method used in this study reduces the chances of such errors occurring as it ensures the initial ASM is close to the target ROI and the algorithm also allows for the correction of the segmentation by re-running the algorithm if necessary.

An advantage of the deformable model algorithm is that it is completely automated and requires no user interaction. However, while user interaction is mandatory for the ASM algorithm, only one click of the mouse (indicating that the final result is satisfactory) is necessary in most cases due to the degree of automation for initialisation; out of the 15 test

images, only two images required a re-run of the segmentation algorithm, which resulted in successful segmentation. An example of such a scenario is shown in Figure 4.16. The ASM algorithm only requires confirmation from the user about the acceptability of the result and does not use any user-dependent variable such as manual initialisation to perform the segmentation. The algorithm, therefore, still fulfils the objective of eliminating user-dependency on the segmentation result.

The mean HDs obtained on the excised bones (5.72 pixels) and on human subjects (5.58 pixels) are close and therefore an ASM trained from images of excised bones is suitable for segmenting actual hand images.

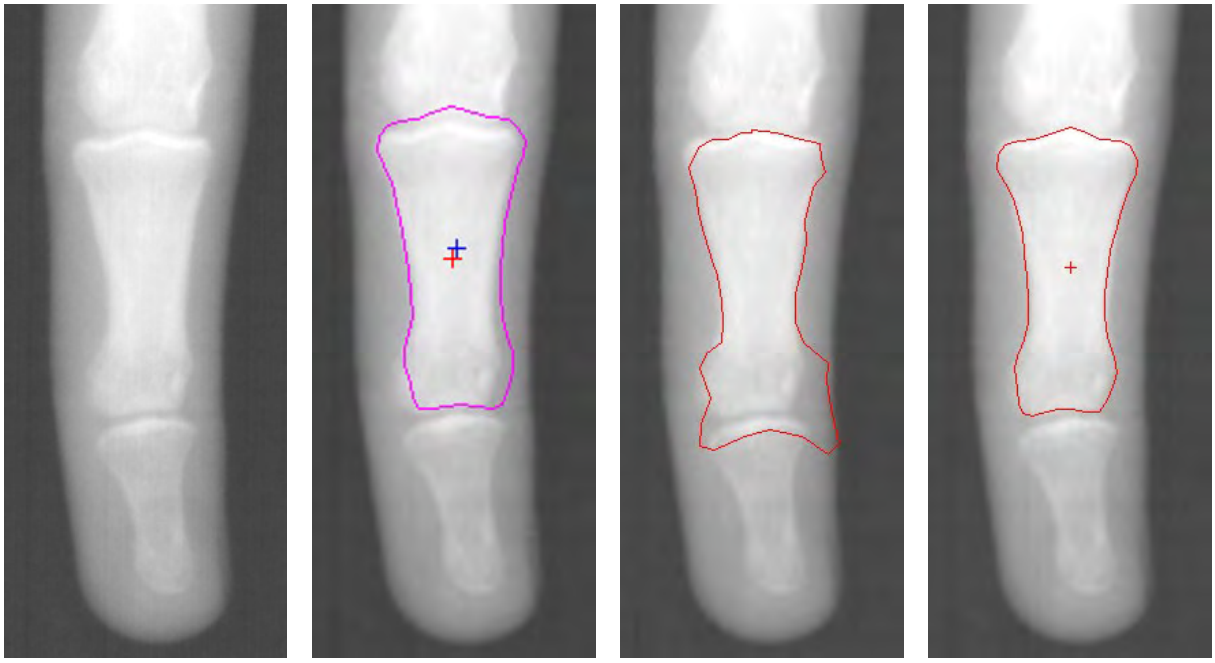

(a) (b) (c) (d)

Figure 4.16: Example of ASM segmentation that requires correction: (a) test image; (b) initialisation - red cross indicates estimate of bone centroid, blue cross indicates centroid of ASM; (c) result of first attempt; (d) result of second attempt. In this case, the user indicates that the detected contour is too big at the prompt that shows the first result. A second segmentation is attempted with the mean shape scaled down. [Contrast has been enhanced for visualisation].

Gulam et al. (2000) employed a DM for segmenting the middle phalanx of the middle finger and while they expressed satisfaction with the results, they did not validate the accuracy of the segmentations. Also, their deformable model was initialised by manually selecting points on the border of the bone. Unlike the automated technique used here, their method of initialisation is time-consuming and would not be suitable for a mass screening application. Sotoca et al. (2003) have used an ASM to segment the middle phalanx from hand

radiographic images. However, they do not validate the accuracy of the segmentation but claim success based on results of BMD measurements that use the ASM segmentation. Their algorithm also relied on user-defined input for initialisation of the ASM. The result of ASM segmentation is highly dependent on initialisation and having a user-defined starting point introduces subjectivity in the results which could impact the precision of BMD measurements. This drawback has been addressed in this project.

In conclusion, the ASM technique is more accurate than a DM for segmenting the middle phalanx of the middle finger in the digital radiographic images used in this project, and will be used in the algorithms for measuring BMD in hand images.

5. COMPUTED DIGITAL ABSORPTIOMETRY - IMPLEMENTATION

5.1 Introduction

Computed digital absorptiometry (CDA) is a technique for assessing bone mass in finger bones using standard radiographic images captured on a digital X-ray machine. An aluminium step wedge is scanned simultaneously with the hand and is used as a calibration device to obtain bone mass in units of equivalent aluminium thickness (mmAl) (Ross, 1997). Assessment of finger bones using an aluminium step wedge as a calibration device has been shown to have high accuracy and repeatability capable of making it a primary method for rapid assessment of patient risk for osteoporotic fractures (Bouxsein et al., 1997; Fiter et al., 2001; Ravn et al., 1996; Ross, 1997; Sotoca et al., 2003; Versluis et al., 1999; Wasnich, 1998). CDA was introduced in Section 3.7 and its implementation on a slot-scanning radiography machine is described in this chapter.

The Lodox Statscan has pre-set values for scan parameters for different regions of the body according to patient size. These values were chosen to optimise image quality and dose (Irving et al., 2008). While values for source voltage and tube current are dependent on patient size, settings for collimator width, focal spot size, pixel size, spatial resolution and scan speed are dependent on body region and the following are the pre-set values for the hand for a medium sized patient:

- Source voltage – 50 kVp.
- Tube current – 160 mA.
- Collimator width – 0.4 mm.
- Focal spot size – Small (0.6×0.6 mm).
- Spatial resolution – 4.16 lp/mm.
- Scan speed – 70 mm/s.
- Pixel size – 120 μm.

These are the values that were used for CDA measurements.

5.2 Step wedge calibration

Several designs for the step wedge, with varying numbers of steps and step sizes, have been used in bone studies of small animals (Haidekker et al., 2004; Fleming et al., 2000), larger

animals (Kolbeck et al., 1999; Symmons, 2004) and human phalanges (Sotoca et al., 2003; Gulam et al., 2000; Sas et al., 2001; Yang et al., 1994). Commercial, film-based equipment (radiographic absorptiometry) also use a wide range of aluminium wedge designs for hand measurements, for example the Bonalyzer (Tokyo, Japan) uses a wedge with step thickness between 1 and 15 mm while the Osteogram (El Segundo, USA) has a wedge with step thickness between 1 and 7 mm (Ross, 1997).

Studies in the literature involving step wedges do not explicitly explain the calibration of the step wedge to establish the relationship between the step thickness and grey levels. The method of Colbert et al. (1967) fits a straight line to the calibration data. The method was adopted by Haidekker et al. (2004), who use an aluminium step wedge for radiographic absorptiometry (RA) bone mass measurements in rats, to fit a straight line to the wedge thickness/film optical density data. The relationship, based on the Beer-Lambert law, used by Haidekker et al. (2004) is:

$$\ln(D - D_0) = \ln(D_m - D_0) - \mu d \quad \mathbf{5.1}$$

where D is the measured local density of the film, D_0 is the lowest film density, D_m is the maximum density (in a region where the film has been exposed to a saturation dose of X-rays) and d is the step thickness. Haidekker et al. (2004) used the Sobel edge detector for segmenting the wedge. They segmented the steps by computing the average pixel value per line parallel to the length of the step and mark the step edge when the difference between lines exceed a pre-defined threshold.

A standard wedge is 40 mm long, has a 10 mm height and a 22.5° slope (Sotoca et al., 2003). The aluminium wedge used in this project, shown in Figure 5.1, is a modified version of a standard wedge. The wedge is 10 mm wide, 45 mm long and has 15 steps at 1 mm increments. The first step is 1 mm thick while the 15th step is 15 mm thick. The step wedge was machined to a tolerance of 0.1 mm. In comparison, Sas et al. (2001) used a 12-step wedge with a maximum step thickness of 12 mm for human phalangeal bone assessment.

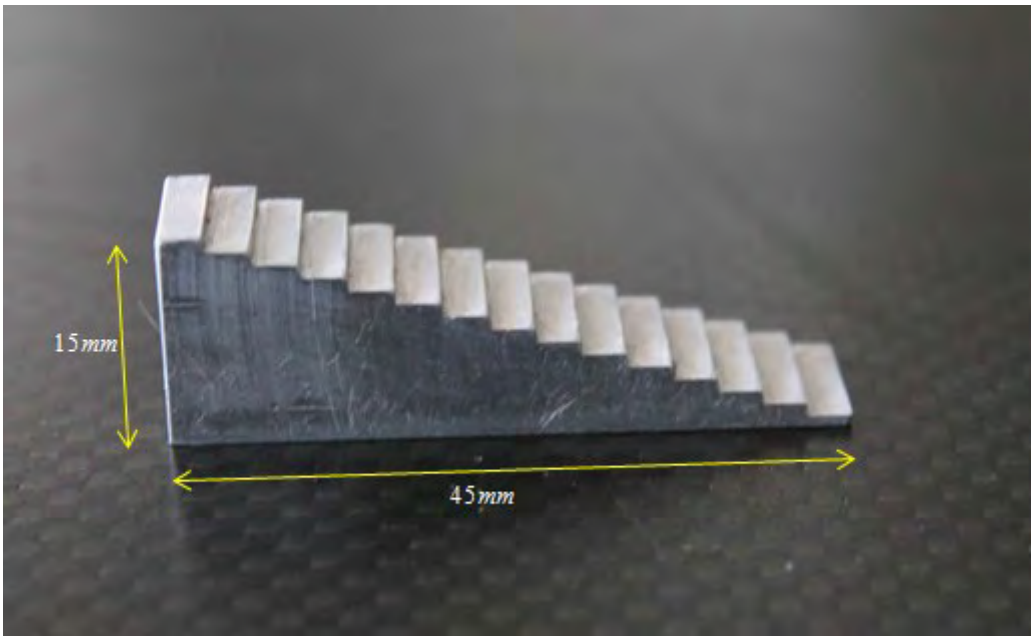

Figure 5.1: Aluminium step wedge.

The first step in the calibration of the wedge was to segment and identify the steps of the wedge in a test image. This was achieved by using the Canny edge detection algorithm (Canny, 1986) using the following steps:

1. The input image was filtered using a Gaussian filter.
2. The intensity gradient was found by convolution with horizontal and vertical Sobel operators.
3. Non-maximum suppression was applied to remove non-edge pixels.
4. Two thresholds were applied to the remaining pixels to identify edge pixels.

The edge detector was able to detect all the steps of the wedge. Morphological opening and closing were applied to eliminate small objects. Edge pixel linking was carried out to ensure that the detected edges were continuous. The wedge was rotated to make its vertical edges parallel to the edge of the image using the method described in Section 4.3. The average step grey level was computed in a ROI that is 7 pixels inside each step. This distance from the step edges was empirically determined in order to exclude pixels at the edges of the steps to avoid potential overlap of steps as well as ensuring that background pixels are excluded when computing the average step grey level while retaining a large region of the step. The algorithm automatically identified each step based on grey level values (i.e. the 15 mm step

has the highest intensity and so on). Figure 5.2 shows an example of the process for identifying step ROIs.

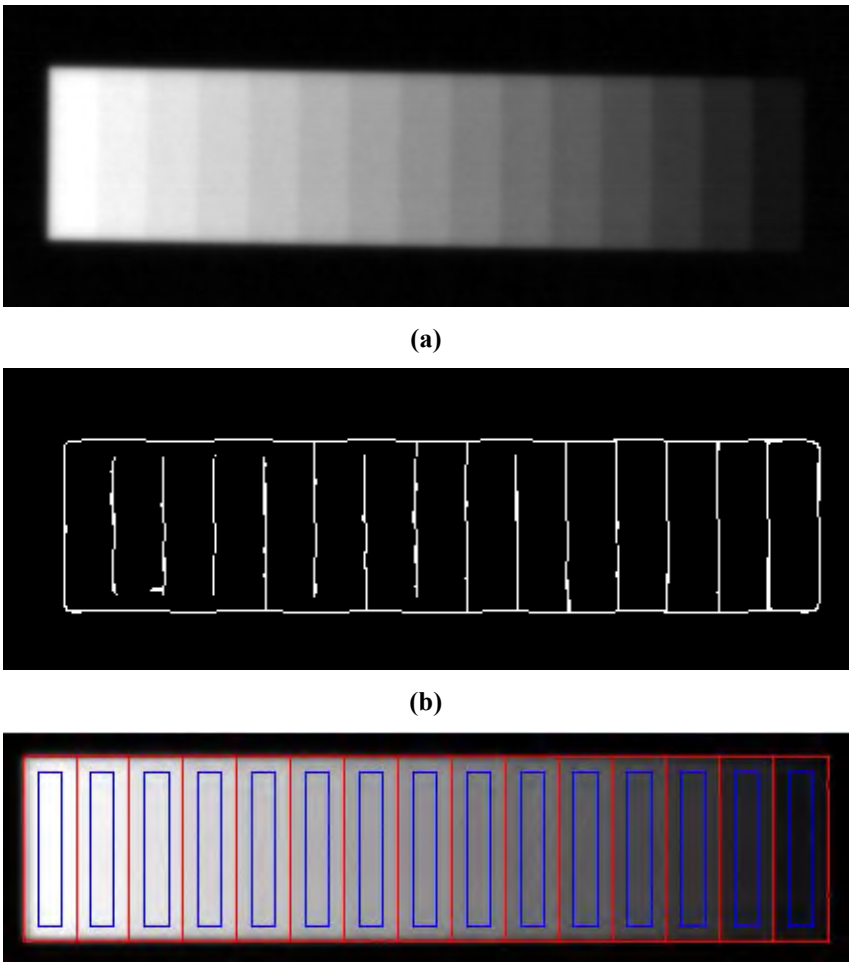

(a)

(b)

(c)

Figure 5.2: Identification of step ROI: (a) Example image; (b) Canny edge detection; (c) Step ROIs: the red pixels represent the edges of each step while blue pixels mark the ROI within each step. [Contrast has been enhanced for visualisation].

According to the Beer-Lambert law, the relationship between the grey level and the step thickness is exponential. Therefore, an exponential function was fit to the wedge data as used by Dawson (2009) as follows:

$$GL = Ae^{-Bt} + C \quad \mathbf{5.2}$$

where *GL* is the average step grey level and *t* is the step thickness. *A*, *B* and *C* are constants that are determined using the average step grey levels and known step thicknesses.

During the analysis of the wedge in each image, a non-linear least squares procedure was carried out using the Levenberg-Marquardt method (Levenberg, 1944; Marquardt, 1963) to

find values for the constants A, B and C in Equation 5.2. The algorithm for the Levenberg-Marquardt method is given in Appendix B.

5.2.1 Evaluation of wedge calibration

The coefficient of determination, R^2, was calculated for the fitted curve to evaluate the goodness-of-fit. The coefficient of determination describes how well the computed curve fits the data points that were used to compute the curve and was calculated as follows:

$$R^2 = 1 - \frac{SSE}{SST} \quad \mathbf{5.3}$$

where SSE is the summed square of residuals:

$$SSE = \sum_{i=1}^{n} (y_i - \hat{y}_i)^2 \quad \mathbf{5.4}$$

where y_i and $\hat{y}_i$ are the known step thickness and the step thickness predicted from the fitted curve, respectively. SST is the sum of squares about the mean:

$$SST = \sum_{i=1}^{n} (y_i - \bar{y})^2 \quad \mathbf{5.5}$$

where

$$\bar{y} = \frac{1}{n} \sum_{i=1}^{n} y_i \quad \mathbf{5.6}$$

A value for R^2 that is close to 1 indicates a good fit and a value of 1 indicates a perfect fit. The root mean square error (RMSE), which estimates the standard deviation of the random component in the data, was also computed:

$$RMSE = \sqrt{MSE} \quad \mathbf{5.7}$$

where MSE is the mean square error found using the residual degrees of freedom (the number of response values minus the number of fitted coefficients estimated from the response values), u, as follows:

$$MSE = \frac{SSE}{u} \quad \mathbf{5.8}$$

A value for RMSE that is close to 0 would indicate a good fit.

To evaluate the accuracy of the step wedge calibration, a 12-step aluminium test wedge was made and imaged together with the 15-step calibration wedge. The thickness of each step of the 12-step test wedge was calculated using Equation 5.2 with values for the constants *A*, *B* and *C* determined using the calibration step wedge. The measurement error was calculated as the percentage error of the known step thickness.

5.3 Bone mass computation

The aluminium wedge was simultaneously scanned with a test subject. However, due to the beam geometry as discussed earlier (see Section 3.3), it was suggested that the wedge be placed in front of the middle finger, as shown in Figure 5.3, instead of beside the finger like in other studies (Gulam et al., 2000; Ravn et al., 1996; Sas et al., 2001; Symmons, 2004). The placement of the wedge as shown ensured that it was exposed to the same X-ray intensity as the middle finger. Alternatively, the wedge could be placed beside the finger and in that case correction of the non-uniform exposure using image processing techniques would become necessary. However, such techniques may require a dark-field (image with no X-ray exposure) and a bright-field (X-ray image with no attenuating object) that are obtained by averaging several acquisitions in order to minimise noise (Moreau et al., 1994).

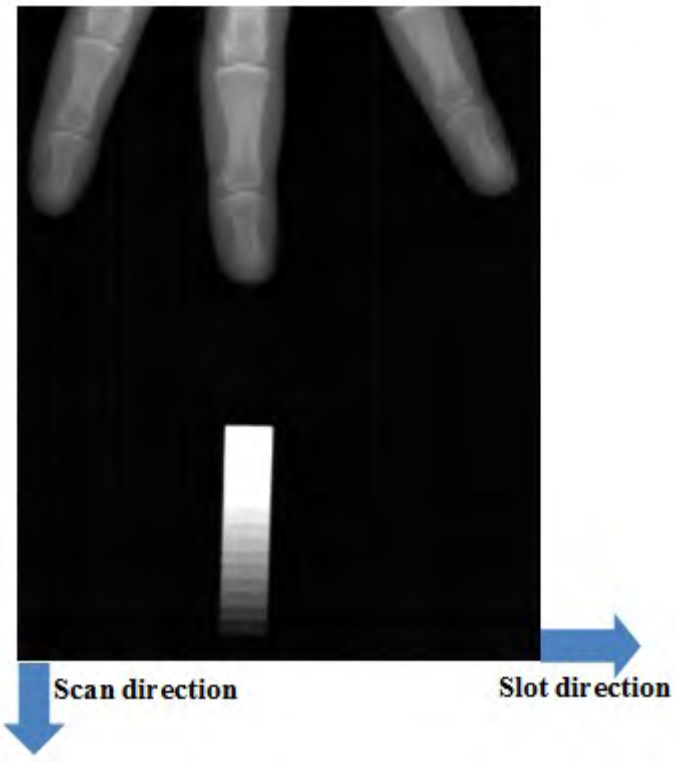

Figure 5.3: Suggested CDA scan set up. [Contrast has been enhanced for visualisation].

The CDA algorithm was designed to be fully automated. During the processing of a test image for *in-vivo* measurement, the hand and the wedge are separated by cropping the image to produce two images, one containing the wedge and another containing the hand. This is achieved, automatically, by applying Otsu's thresholding algorithm (Otsu, 1979) given in Appendix A. In the binary image produced by thresholding, the wedge is the detected object that is most extreme in the scan direction and the image is cropped halfway between the separation of the wedge and the tip of the middle finger. The ASM segmentation scheme described in Chapter 4 is applied to the hand image to detect the border of the middle phalanx of the middle finger and compute the average grey level of the bone. The ASM algorithm worked well on the images used for CDA, despite being trained on images captured with different tube settings (140 kVp and 50 mA). The wedge calibration scheme described earlier in this chapter is then applied to the wedge image to determine the values for the constants in Equation 5.2. Finally, the aluminium thickness corresponding to the average grey level of the bone is calculated using Equation 5.2 to yield the bone mass with units of mmAl.

5.3.1 Evaluation

To evaluate the CDA technique, measurements were taken in 19 excised bones harvested from bodies donated to the department of Human Biology at the University of Cape Town for teaching purposes; cadaver studies for evaluating bone measurements typically use 10 - 20 subjects (Blake & Fogelman, 2010). The ash weight of the bones was determined through incineration to examine the correlation between CDA measurement and ash weight. Approval for the evaluation study was obtained from the university's Human Research Ethics Committee (reference number, 251/2012).

A representative of soft tissue was required for the excised bones. Perspex was a good candidate as it has X-ray attenuation similar to soft tissue (Moreau et al., 1994; Steel et al., 1997) and was readily available. Therefore, during the image acquisition, the bones were placed on a block of Perspex which represented the soft tissue. To determine the thickness of the Perspex block, an image of a Perspex step wedge, shown in Figure 5.4, was acquired and the average grey level of each step was calculated. The Perspex step wedge was scanned using the same tube settings as those for the images of volunteers which provided the test set for evaluation of the segmentation methods. The average grey level of the soft tissue region adjacent to the middle phalanx of the middle finger was calculated in each volunteer's image. The equivalent Perspex thickness for the soft tissue in each volunteer was computed from the average soft tissue grey level in a similar manner to CDA measurements. The thickness of the

Perspex block for representing soft tissue for the excised bones was the average equivalent Perspex thickness of the volunteers' soft tissue.

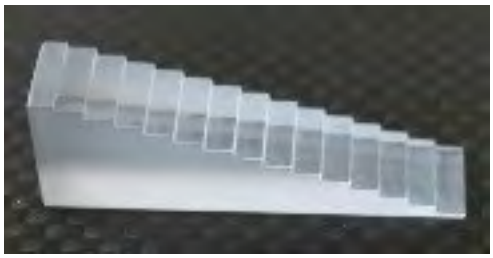

Figure 5.4: Perspex step wedge: height 15 mm, length 45 mm and width 10 mm; each step has a 1 mm increment.

Alternatively, water may be used as a representative of soft tissue by placing the bones in a water bath. In this case the soft tissue would actually surround the bone as opposed to a stacked arrangement if a Perspex block is used. Although in reality (and in the case of a water bath) soft tissue above the bone would cause scattering of X-rays, differences in the sequential placement of the different tissues in the beam path should not make much difference to the transmitted X-ray since fingers have small amounts of soft tissue. Figure 5.5 shows a typical image of the excised bones.

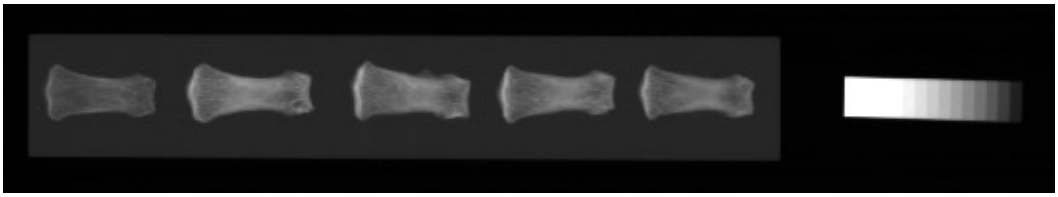

Figure 5.5: Typical image obtained by scanning the aluminium step wedge and excised bones placed on a Perspex block.

After scanning and taking measurements, the bones were placed in a custom-designed stainless steel tray and were subsequently incinerated in a cremating oven at the Maitland Crematorium in Cape Town (the bones were incinerated after dual-energy measurements discussed in Chapter 7 had been taken). The resulting ash (Figure 5.6) for each bone was weighed using a RADWAG PS360/C/1 (RADWAG, Poland) digital electronic scale with an accuracy of 0.001*g*.

Figure 5.6: Incinerated bones in stainless steel tray.

The recommended method for evaluating the short-term precision of a densitometry technique is to take two measurements per individual in a minimum of 30 subjects or three measurements per individual in a minimum of 14 subjects and computing the coefficient of variation of the measurements (El Maghraoui & Roux, 2008; Glüer et al., 1995; ISCD, 2014). Precision refers to the repeatability of a measurement technique. Thirty three volunteers who were available for the precision study were divided into two groups of 16 and 17 for evaluating the precision of CDA and DXA (Section 7.6.2), respectively. To evaluate the precision of the CDA method, 3 repeated measurements were taken in each of the 16 subjects selected for the CDA precision study. The coefficient of variation, CV, was calculated as the root-mean-square (RMS) average of standard deviations of the repeated measurements by entering each subject's values into a spreadsheet precision tool provided by the International Society for Clinical Densitometry (ISCD, 2006).

The coefficient of variation is the most commonly used measure for repeatability in bone measurements (Blake & Fogelman, 2010; El Maghraoui & Roux, 2008). The CV of a measurement technique should be less than 2% for the technique to have medical prognosis value (Sotoca et al., 2003). Precision errors of between 1 – 2% are small compared with the variability between people; therefore such precision errors have little influence on the ability of a technique to predict fracture risk (Ross, 1997).

5.4 Results

5.4.1 Wedge calibration

Figure 5.7 shows a typical plot of the wedge data and the curve fitted to the data (extrapolated to 20 steps) and Figure 5.8 shows a plot of the fit residuals (difference between the known step thickness and the thickness predicted by the curve).

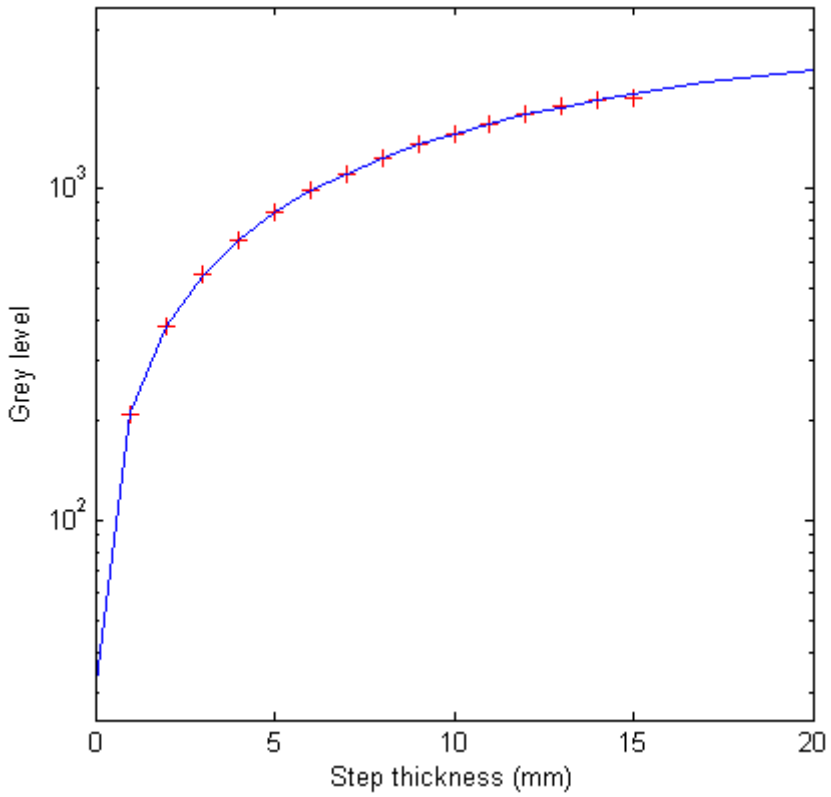

Figure 5.7: Variation of grey level with step thickness for the aluminium step wedge.

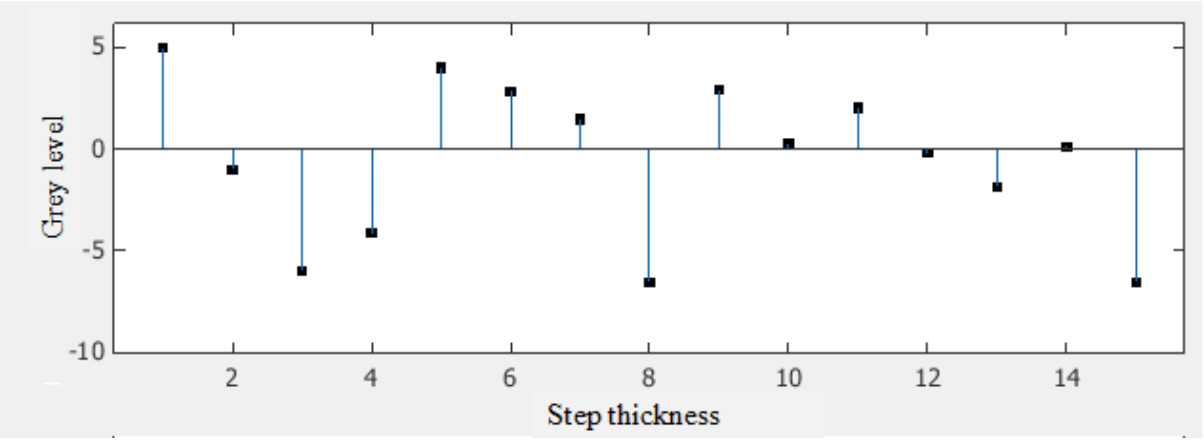

Figure 5.8: Plot of fit residuals for the aluminium step wedge calibration data.

In this example, the values for the coefficient of determination (R^2) and the root mean square error (RMSE) for the fit were 0.9999 and 4.86 respectively. These values together with the relatively small residual values indicate that the fitted curve adequately describes the fitted data. The average percentage error in the prediction of the test wedge thickness using the calibration wedge was 1.14%; indicating that the calibration equation measures the equivalent aluminium thickness for a given grey level with high accuracy.

5.4.2 Evaluation

To evaluate the usefulness of the CDA technique, the correlation between the measured value and the ash weight of each incinerated bone was examined, and precision of the method was assessed by computing the coefficient of variation (CV) of repeated *in-vivo* measurements.

Figure 5.9 shows the plot of ash weight against the computed equivalent aluminium thickness. The Pearson product-moment correlation coefficient, *R*, which is a measure of the strength of the linear relationship between the two entities, was 0.92. The value of the correlation coefficient shows that there is a strong correlation between the equivalent aluminium thickness and ash weight.

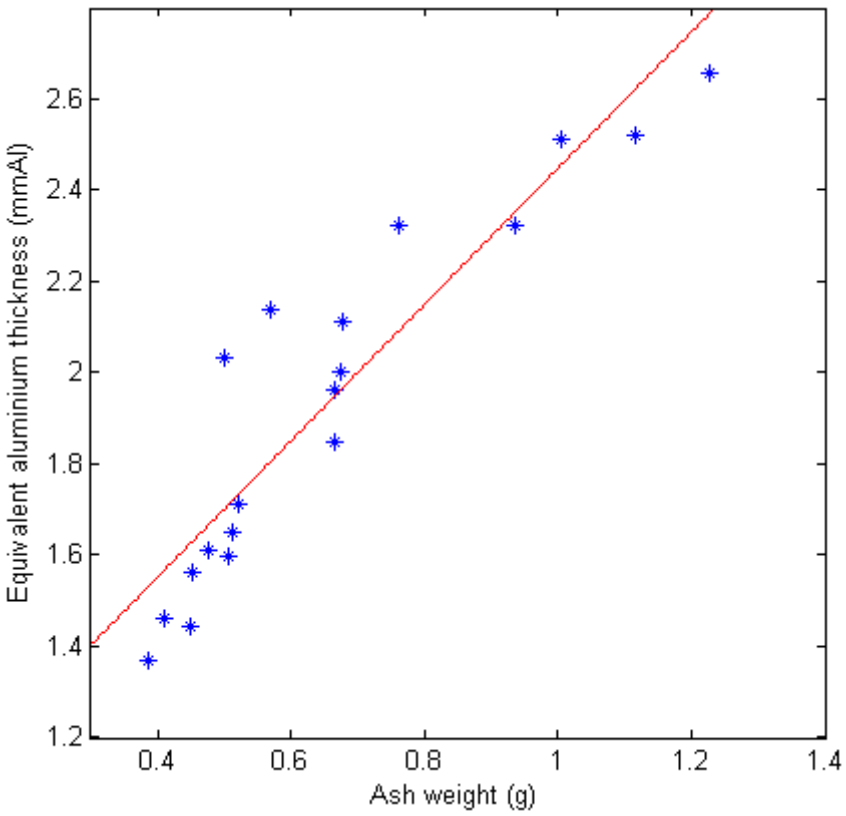

Figure 5.9: Correlation between equivalent aluminium thickness (mmAl) and ash weight: *R* = 0.92.

The range of the bone mass of the excised bones was 1.37 to 2.66 mmAl with an average of 1.94 mmAl while the range for *in-vivo* bone mass was 2.34 – 5.18 mmAl with an average of 3.78 mmAl. The *in-vivo* bone mass precision was 0.49%.

5.5 Discussion

Computed digital absorptiometry (CDA) is a simple method for measuring bone mass in finger bones using an ordinary X-ray image that includes an aluminium wedge for calibration. In this project, a CDA method for bone mass measurement has been implemented on a slot-scanning radiography system and evaluated using excised bones. The default values on the Statscan for source voltage and tube current were used (50 kVp and 160 mA); this source voltage is comparable to the values employed in other studies. Source voltages for CDA and radiographic absorptiometry (film based) in the literature are between 48 kVp and 60 kVp (Bouxsein et al., 1997; Gulam et al., 2000; Ravn et al., 1996; Ross, 1997; Sotoca et al., 2003).

The CDA method developed here is fully automated and requires no user input. In comparison, Haidekker et al. (2004), who report on CDA for small animals, used a semi-automated method. Their method required a user to crop around the wedge, thus locating the wedge in the image, and the segmentation of the wedge and identification of steps was achieved by the algorithm. For wedge calibration, Haidekker et al. (2004) fitted a straight line to the wedge data, despite the relationship between step thickness and bone mass being exponential. The calibration was based on the work of Colbert et al. (1967) who suggested fitting a straight line to wedge data. A possible reason why a straight line was fitted to data that is known to have an exponential (Beer-Lambert law) relationship is the limited computing power that was available at that time. However computing power has advanced significantly since the 1960s and modern computers can easily and quickly compute exponential fits for given data. In this project, an exponential fit was used to establish the relationship between step thickness and step grey level. The exponential relationship adequately described the wedge data as shown by the high coefficient of determination, low RMSE and low residuals. The derived exponential equation for the step thickness/grey level relationship also showed to have good predictive accuracy for equivalent aluminium thickness for a given grey level as evident in the measurements of the test wedge.

Bone mass measurements produced by the CDA method were strongly correlated to ash weight (R = 0.92); suggesting that CDA can be used for accurate prediction of phalangeal

bone mass measurements on a slot-scanning radiography system. This correlation value compares well with other reported results, for example Bouxsein et al. (1997) recorded a correlation of 0.89 for CDA while Yang et al. (1994) had a correlation of 0.93 for radiographic absorptiometric measurements.

The method has high precision as shown by the low CV value of 0.49%. The precision achieved in this project is higher than what other studies that perform wedge-based measurements have achieved as shown in Table 5.1. Differences in the precision values may be attributed to factors such as differences in test samples (Glüer et al., 1995) and measurement techniques, and whether measurements were taken *in-vivo* or in excised bones (Bouxsein et at., 1997).

Table 5.1: Comparison of BMD precision of the method in this project with other studies that have used aluminium wedge-based bone measurements.

Author	Technique	CV (%)
This study	CDA	0.49
Bouxsein et al. (1997)	CDA	0.7
Ravn et al. (1996)	RA	1.5
Yang et al. (1994)	RA	0.60
Sotoca et al. (2003)	RA	0.91

CDA does not account for soft tissue attenuation and dual-energy X-ray absorptiometry has an advantage over CDA in this regard as it accounts for soft tissue attenuation in the bone measurement. Despite this drawback, the CDA method has shown good predictive ability of bone mass and high precision which would make it a suitable method for mass screening for osteoporosis. Mass screening of suspected cases using wedge-calibrated phalangeal measurements may lead to the exclusion of patients with normal bone from having a central DXA scan. For example, a study by Buch et al. (2010) concluded that up to 20% reduction in cases requiring central DXA scans for detecting low BMD can be achieved using RA-based measurements.

6. DUAL-ENERGY IMAGE ACQUISITION

6.1 Introduction

This chapter discusses the generation of the dual-energy spectra used for capturing the low- and high-energy images used for DXA measurements in this project. The factors that were considered in determining the X-ray tube settings are discussed. As stated earlier, the Lodox Statscan has pre-set scan parameters for the imaging of different body regions. This chapter discusses the determination of source voltage and current as well as filtration; default values for collimator width, focal spot size, pixel size, spatial resolution and scan speed were used (see Section 5.1).

As discussed under objectives (Section 1.1), this project explores the feasibility of incorporating an additional detector into a slot-scanning radiography system so that dual-energy images may be acquired in a single scan. Acquiring the dual-energy images in a single scan is desirable because the patient would be irradiated with X-rays only once, leading to reduced radiation dose. To simulate the presence of two detectors on the current system, images were captured in two consecutive scans using the same tube settings (the current system has a single detector). Three factors were taken into consideration for optimisation of the dual-energy image acquisition, namely spectral separation, entrance dose and image quality. The objective was to achieve the highest possible spectral separation between the low- and high-energy spectra at minimal entrance dose and capture the high- and low-energy images with sufficient quality to enable accurate BMD measurements.

Images were captured on the Lodox Statscan workstation, saved in 16-bit DICOM format and transferred to a laptop computer for processing. The laptop computer has an Intel i7 Core processor and 8GB RAM running on Windows 7 (Microsoft, USA). All computations and image processing were carried out using Matlab R2012a (Mathworks, USA).

6.2 Scintillator configuration

The low-energy image was acquired using the normal detector set-up for slot-scanning radiography with an added filter (pre-filter) as shown in Figure 6.1. The purpose of the pre-filter is to reduce patient dose by removing low-energy photons that are unlikely to penetrate the patient.

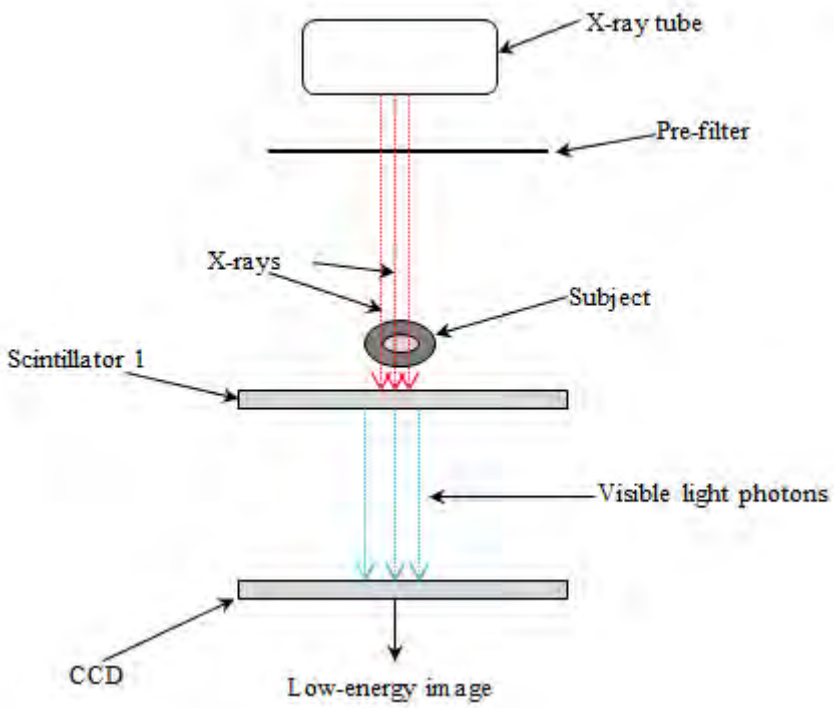

Figure 6.1: Schematic diagram for the low-energy scan.

The detector arrangement for the high-energy scan was adapted from the method of Seely et al. (2001) and is shown in Figure 6.2. For the high-energy scan, the top scintillator (*Scintillator1*) simulates the presence of the first detector which, in a two-detector system, would capture the low-energy image. *Scintillator1* absorbs the low-energy photons, converting them into light photons while allowing high-energy photons to pass through to the second scintillator. The visible light photons may be transferred to a charge coupled device (CCD) using a fibre optic device (represented here by glass). In this project, however, light from *Scintillator1* was not captured in the dual-scintillator set-up; rather, the data was captured from *Scintillator1* in separate scan, as the aim was to explore the dual-scintillator concept and show feasibility without having to construct such a system in its entirety. *Scintillator1* effectively acts as a filter for the high-energy beam by absorbing the low-energy photons. The post-filter removes any residual low-energy photons and also prevents any visible light photons emitted by *Scinitillator1* from reaching *Scintillator2*. The lower scintillator (*Scintillator2*) would absorb the high-energy photons and similarly convert them into light photons, which are transferred to a second CCD that records the high-energy image.

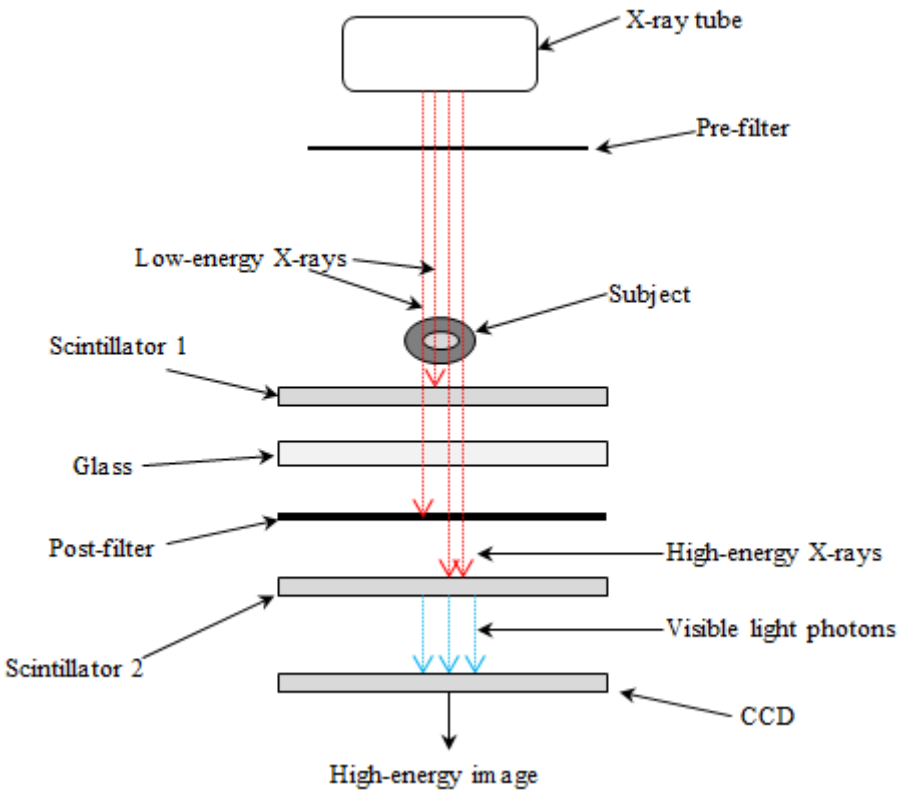

Figure 6.2: Schematic diagram for the high-energy scan.

The scintillator arrangement for the high-energy scan shown in Figure 6.2 is similar to the dual-energy detector of Seely et al. (2001) (see Section 3.6.1). The detector proposed by Seely et al. (2001) is, however, designed for conventional radiography and, also, it detects low- and high-energy beams that have been generated separately in a pulsed fashion. The arrangement of scintillators for this project has been used to generate the low-energy and high-energy spectra instead of just selectively detecting the low- and high-energy photons as in the case of Seely et al. (2001).

6.3 Preliminary cadaver study

A preliminary study was carried out to assess the variation of image quality with source voltage. A cadaver hand was sourced and imaged to assess, by qualitative visual inspection, how the quality of the high-energy image varies with source voltage. The aim was to establish the voltage level at which the image quality becomes unacceptably low. The imaging started at the minimum voltage setting on the Lodox Statscan (50 kVp) and was incremented at 10 kVp intervals to 140 kVp. The maximum tube voltage of the Lodox Statscan is 150 kVp. However, in order to limit the risk of arcing the tube, the maximum tube

voltage was avoided. The scans showed that high-energy images captured with source voltage of 70 kVp or less were visibly grainy with increasing severity as the voltage decreased. Therefore, only source voltages above 70 kVp were considered for the rest of the project.

6.4 Image Quality

A quantitative evaluation of images acquired at source voltages of 80 – 140 kVp with various tube currents was required in order to determine the voltage/current combination that yields images with the highest quality. The quality of the dual-energy images is important in achieving high accuracy in the measurements. Poor spatial resolution and high levels of noise would adversely affect key image processing procedures such as image registration and are likely to distort BMD measurements. It was therefore imperative that the dual-energy images be acquired with sufficiently high quality to ensure high accuracy in the DXA measurements. Detective quantum efficiency (DQE) was chosen as a measure of image quality in this project.

6.4.1 Detective quantum efficiency

DQE requires measurements of the system's modulation transfer function (MTF) and noise power spectrum (NPS). These parameters were measured and calculated according to the IEC 62220-1 standard methodology (International Electrotechnical Commission, 2003) and the DQE was calculated as follows (Garcia-Molla et al., 2010; Neitzel et al., 2004):

$$DQE(f) = \frac{MTF^2(f)}{NNPS(f) \cdot q \cdot X} \quad \mathbf{6.1}$$

where *NNPS* is the normalised NPS, q is the signal-to-noise ratio per exposure and X is the air Kerma at the detector surface. The DQE was calculated as an average of the DQE in the slot and scan directions.

The IEC 62220-1 Protocol for DQE measurement

The IEC62220-1 protocol is a standardised method for measuring the DQE of a digital detector. It can be used for accurate and reliable measurement of DQE (Illers et al., 2005). The protocol specifies standard conditions required for the determination of DQE including the amount of added aluminium filtration and beam geometry. It also specifies methods for measuring NPS, MTF and measurement of air Kerma at the detector. Air Kerma is the sum of kinetic energy of each charged particle liberated per unit mass of air; it is virtually equal to

the absorbed dose in air (Boone, 2000) and the IEC protocol recommends the use of a dosimeter with an ionisation chamber to measure air Kerma. The beam geometry is defined to minimise the effects of image blur, with a source-to-detector distance of at least 150 cm, a 16×16 cm X-ray field at the detector and the required added aluminium filtration placed as close to the source as possible. The source-to-detector distance on the Statscan is fixed at 130 cm and therefore the acquired images would have more blur than recommended, however the difference of 20 cm was not expected to have a significant adverse effect on the use of the protocol.

Air Kerma at detector surface

The air Kerma was measured using a Radcal 9010 (Radcal Corporation, California) dosimeter in conjunction with a 60 cm^3 ionisation chamber. The IEC62220-1 protocol recommends that the air Kerma should be measured at the level of the detector surface with the detector, grids and any covers removed in order to reduce any backscatter. Alternatively, if this is not possible as in the case of the Lodox Statscan where the X-ray source and the detector function as a single unit, the ionisation chamber may be placed between the source and the detector. The air Kerma at the detector surface can then be calculated using the inverse square law (in the case of conventional radiography). In this project, the ionisation chamber was placed 30 cm above the detector as shown in Figure 6.3 to reduce the effect of backscatter. In linear slot-scanning systems, the dose varies with the inverse of the distance from the source (Irving et al., 2008; Potgieter et al., 2005) and therefore the air Kerma at the detector surface was calculated as follows:

$$X_d = \frac{SC}{SD} \cdot X_m \quad \mathbf{6.2}$$

where X_m is the air Kerma measured by the dosimeter, *SC* and *SD* are the source-to-chamber and source-to-detector distances, respectively.

Signal-to-noise ratio per exposure

The IEC protocol specifies four standard beam qualities (RQA3, RQA5, RQA7, and RQA9) and the signal-to-noise ratio per exposure for each beam quality. Alternatively, the conversion factor can be determined using a spectral model. In this project, 10 mm of added aluminium filtration was used for DQE measurements as required for the RQA3 beam. However, the RQA3 standard signal-to-noise ratio per exposure could not be applied here

since the beam quality was not constant (the aim was to evaluate DQE at various tube voltages and currents). Therefore, the spectral model alternative was used and the signal-to-noise ratio per exposure was derived from simulated spectra for each voltage using the spectral model described in the next section (see Section 6.5).

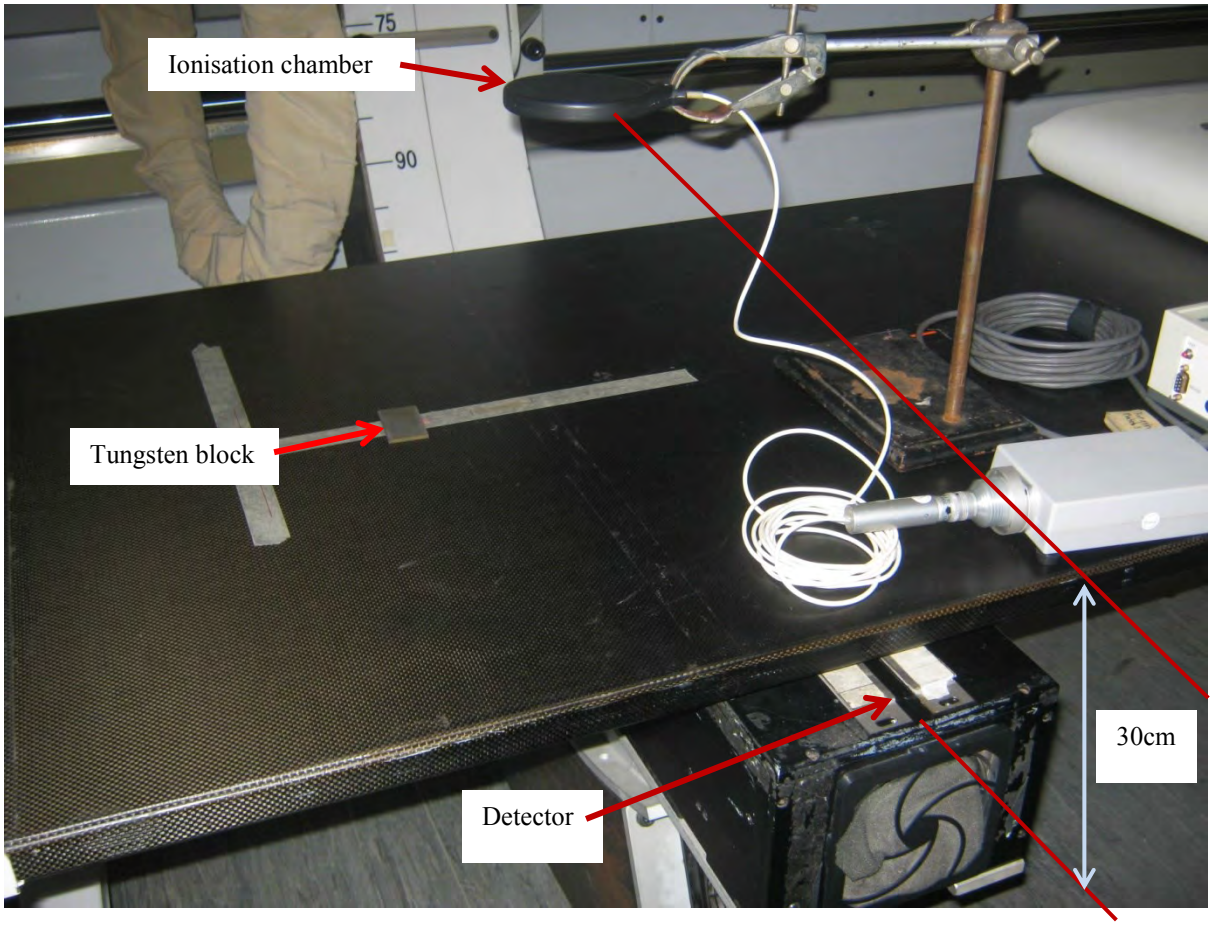

Figure 6.3: Apparatus for imaging tungsten block and measurement of air Kerma for computing the DQE.

Modulation transfer function (MTF)

The system MTF can be measured by imaging a test object containing a narrow slit or a sharp edge (Williams et al., 2007). The IEC protocol recommends the sharp edge method. A 3 mm-thick tungsten edge device (tungsten block in Figure 6.3) was used in this project. The device has previously been used for measuring the MTF of the Lodox Statscan (Scheelke et al., 2005). According to the protocol, the device has to be placed on the detector at an angle of between 1.5-3° to the detector axis to measure MTF perpendicular to that axis. However, this was not possible on the Lodox Statscan due to the fact that the detector unit has to move

across the device during the scan and therefore the device was placed on the scan table at approximately 3° to the slot direction.

Post-processing operations for image enhancement available on the imaging workstation were disabled for all the scans so that raw pixel data was used for the measurements. The method used for computing the MTF was adapted from the method used by Samei et al. (1998) to match the recommendations of the IEC protocol as follows:

1. Regions of interest for computing the MTF in the slot and scan directions were manually selected by cropping the image at the device edges as shown in Figure 6.4.

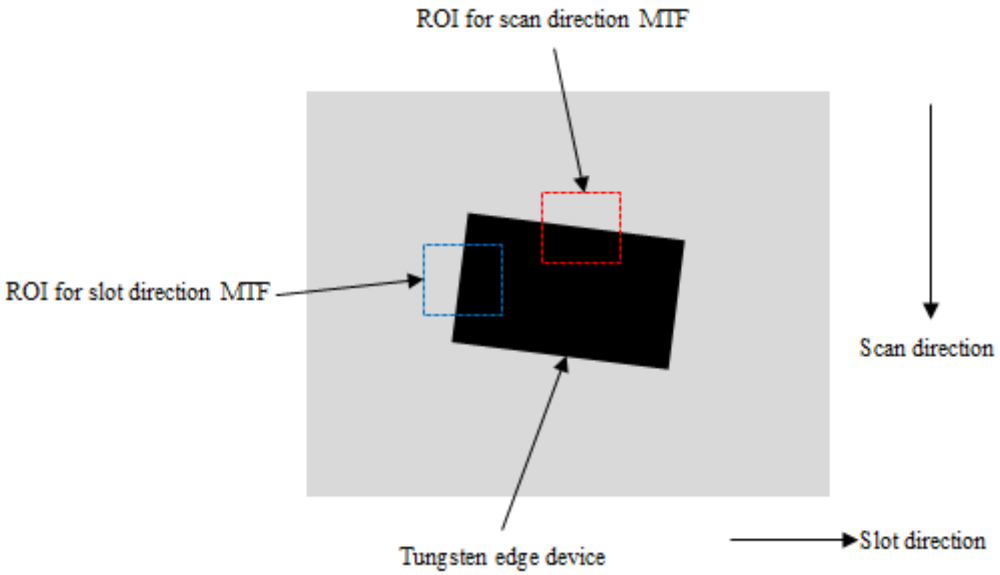

Figure 6.4: Cropped image of the edge device to mark the ROIs used in the calculation of MTF.

2. The angle of the edge was determined. First a thresholding operation in the cropped image was applied (the threshold used was the average grey level of the tungsten and background regions). The location of a line representing the edge was obtained using the image gradient. The Hough transform of the binary image containing the edge line was computed within a ±180° range with an angular sampling of 1°. A second Hough transform was computed within a ±10° sub-region of the previous result to yield the angle of the edge.
3. The edge spread function (ESF) was obtained by re-projecting the pixel grey level data in the original image along the direction of the estimated angle into a 1-D array of sub-pixel elements as illustrated in Figure 6.5.

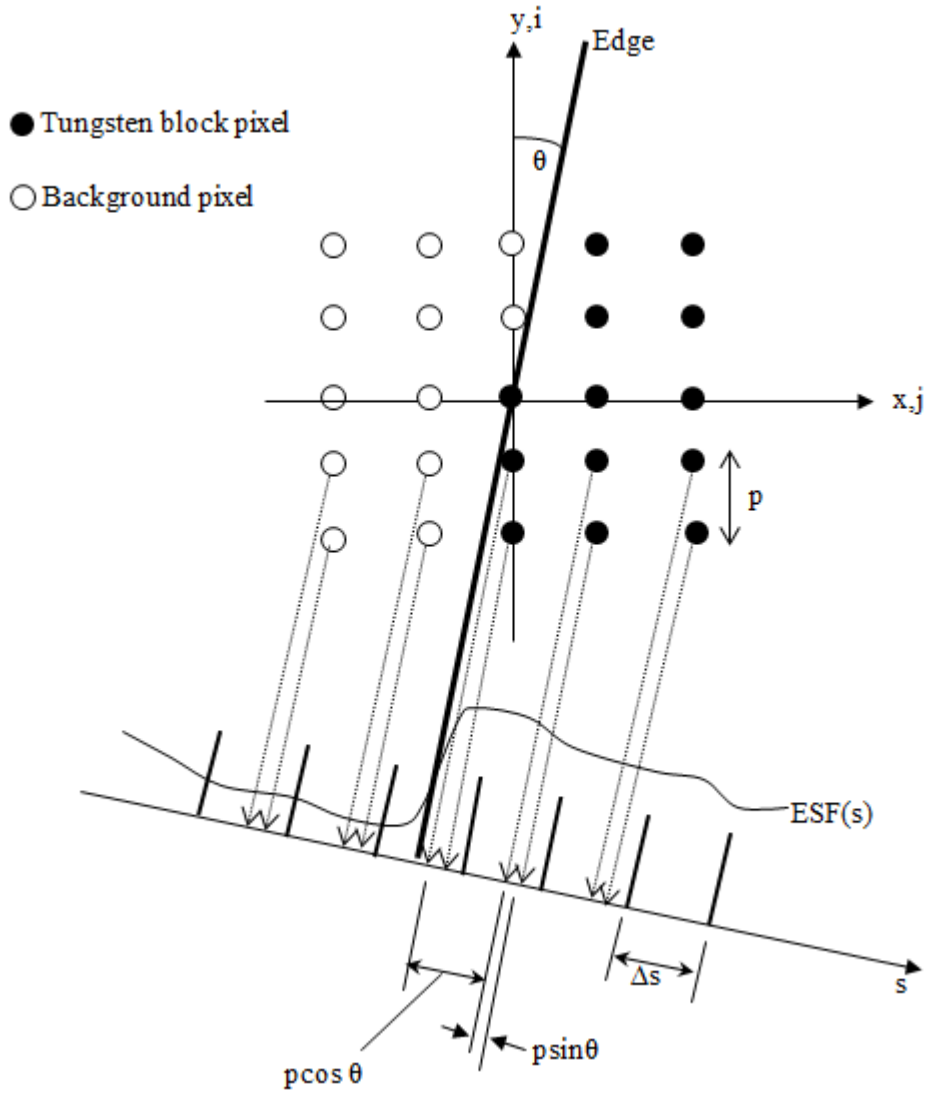

Figure 6.5: Re-projection and binning of the 2-D edge image data onto a 1-D plane perpendicular to the edge.

For each row re-projection, the ESF as a function of the distance, *s*, from the edge was sampled as:

$$E_j^i = \int ESF(s)\delta(s + ip\sin\theta - jp\cos\theta)ds \quad \mathbf{6.3}$$

where E^i_j is a set of samples of the ESF for pixels in row *i* and column *j* at a distance *s(i,j)* given by:

$$s(i,j) = pj \cdot \cos\theta - pi \cdot \sin\theta \quad \mathbf{6.4}$$

and p is the pixel size. The re-projection of row pixels onto the s-axis forms a pattern of finely spaced, discrete samples of the ESF. The ESF was computed by re-ordering the samples into bins with a width of Δs:

$$ESF_k = \frac{1}{n_k}\sum_{ij} E_{ij}\text{bin}(s(i,j) - k\Delta s) \quad \mathbf{6.5}$$

where k is the bin number, n_k is the number of pixels whose distance from the edge is between (k-0.5)Δs and (k+0.5)Δs and

$$\text{bin}(s(i,j) - k\Delta s) = f(x) = \begin{cases} 1, & |s(i,j) - k\Delta s| \leq \frac{\Delta s}{2} \\ 0, & \text{elsewhere} \end{cases} \quad \mathbf{6.6}$$

4. The line spread function (LSF) was calculated by differentiating the ESF.
5. A fast Fourier transform of the LSF was computed to yield the MTF.

Noise power spectrum (NPS) and normalised NPS

The noise power spectrum (NPS) was computed from flat-field images (images acquired with no attenuating devices) using at least 4 million pixels as recommended by the IEC protocol. Although the IEC protocol considers correction for non-uniform background effects as optional, slowly varying spatial background effects were corrected by fitting and subtracting a 2-D second order polynomial in each image. The region of interest (ROI) in which the NPS is evaluated was divided into half-overlapping sub-ROIs of 256×256 pixels as shown in Figure 6.6.

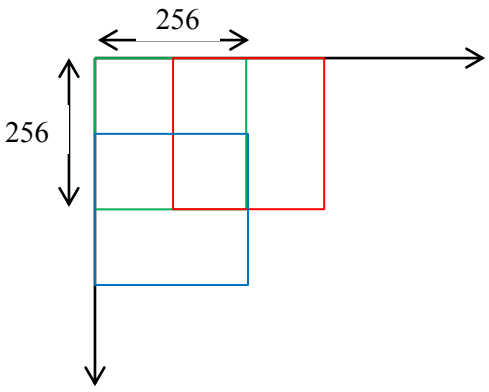

Figure 6.6: Overlapping sub-ROIs for NPS calculation.

The 2-D NPS was calculated according to Equation 6.7 (Garcia-Molla et al., 2010):

$$NPS(u_n, v_k) = \frac{\Delta x \Delta y}{M \times 256 \times 256} \sum_{m=1}^{M} \left| \sum_{i=1}^{256} \sum_{j=1}^{256} \left(I(x_i, y_j) - S(x_i, y_j) \right) \exp\left(-2\pi \cdot i\left(u_n x_i + v_k y_j \right) \right) \right|^2 \quad \mathbf{6.7}$$

where u and v are the spatial frequency variables, Δx and Δy are the pixel spacing in the horizontal and vertical directions respectively, M is the number sub-ROIs, $I(x_i,y_i)$ is the linearised data and $S(x_i,y_i)$ is the fitted 2-D polynomial. The normalised NPS (NNPS) was computed by dividing the NPS by the square of the corresponding air Kerma (Garcia-Molla et al., 2010).

6.5 Spectral separation

The amount of spectral separation between the high- and low-energy spectra was crucial when considering the dual-energy scan settings since, for quantitative dual-energy imaging, a high spectral separation is required in order to minimise the overlap between the spectra (Skipper & Hangartner, 1996). While achieving total separation of the two beams in the diagnostic X-ray range may be difficult, minimal overlap would ensure maximum separation of effective beam energies and therefore a high degree of independence of the dual-energy equations (Skipper & Hangartner, 1996). Numerical simulations were carried out to study the X-ray spectra at different tube voltages and the effect of filtration on the separation of the low- and high-energy spectra.

The X-ray spectra were generated using the Spektr toolbox (Siewerdsen et al., 2004) which is based on the tungsten anode spectral model using interpolating polynomials (TASMIP) algorithm (Boone & Seibert, 1997). The technique computes X-ray spectra at 1 keV energy intervals up to 150 keV for source voltages between 30 and 140 kVp. In each simulation, the generated spectrum was filtered, as required, according to Beer-Lambert law using a database of mass attenuation coefficients for different elements and compounds obtained from the National Institute of Standards and Technology (National Institute of Standards and Technology, 2005). For the simulations, the following conditions were used:

1. Gd_2O_2S:Tb scintillators - only this scintillator type was available during the course of the project.
2. Borosilicate glass (the type of glass for the glass separator in Figure 6.2)
3. 2 mm inherent aluminium filtration – the Lodox Statscan has 2 mm inherent aluminium filtration.

The average energies for the low- and high-energy spectra were computed with and without the attenuating tissue found in the finger, with their difference giving the spectral separation.

The Spektr toolbox allows for the thickness of different biological tissues to be included as attenuating materials in the simulations. The average anterior/posterior thickness of the middle phalanges in South African population ranges between 9.48 mm for black women and 10.54 mm for white men (Navsa, 2010). Therefore for the simulations, 9-11 mm thickness of bone was used together with 20 mm soft tissue. Simulations were carried out in the 80 – 140 kVp range. Aluminium and copper were the only filter materials which had been tested on the Lodox Statscan. An earlier study on the Lodox Statscan concluded that including additional 1.8 mm aluminium filtration at 80 kVp reduces the dose without adversely affecting the image quality (Perks et al., 2013) and therefore 1.8 mm additional aluminium filtration was included for source voltages up to 100 kVp. Another study showed that additional 0.1 mm copper filtration has a similar effect for source voltages of 110 kVp and higher (Trauernicht et al., 2012). In this project, the copper filtration was increased to 0.2 mm for greater dose reduction – the difference in image quality was negligible when compared to 0.1 mm copper. Therefore simulations for source voltages of 110 kVp and above included 0.2 mm copper filtration. The effects of possible alternative filters and scintillators, other than those used in the project, on the spectral separation were explored.

Manufacturers of densitometers quote effective energies for the low- and high-energy spectra of their respective machines. In order to facilitate comparison of the spectra in this project with those of commercial machines, the effective energies of the various spectra were measured. This was achieved by measuring the intensity of an un-attenuated beam and the intensity attenuated by a 0.5 mm thin block of aluminium to yield the attenuation factor (I/I_0) (Boone, 2000). By assuming that the beam is monoenergetic and applying the Beer-Lambert equation, the mass attenuation coefficient was calculated:

$$\frac{\mu}{\rho} = -\left(\frac{\ln\left(\frac{I}{I_0}\right)}{\rho t}\right) \quad \mathbf{6.8}$$

where μ/ρ is the mass attenuation coefficient, ρ is the density, t is the thickness of the aluminium block, I is the intensity of the attenuated beam and I_0 is the intensity of the un-attenuated beam. The computed mass attenuation coefficient was then compared to the table of mass attenuation coefficients for aluminium provided by the National Institute of Standards and Technology (National Institute of Standards and Technology, 2005) to determine the corresponding effective energy for that mass attenuation coefficient value.

6.6 Entrance dose

DXA is an extremely low dose imaging technique in which a typical examination delivers radiation dose that is less than the average daily background radiation or an overseas flight (Genton et al., 2002). The associated radiation dose for a scan depends on machine parameters such as focal spot size, collimation, scan speed, tube current and voltage (Njeh et al., 1999). Despite the low radiation doses associated with DXA scans, keeping the dose to a minimum would be beneficial for patients. This project therefore strived to minimise the dose for the DXA scan.

Entrance surface dose is the measure of radiation exposure at the point where the X-ray beam enters the anatomical site under investigation. Unlike effective dose, entrance dose does not take into account the radiation sensitivity of different organs and tissues, but does, however, account for backscatter (Gogos et al., 2003). Entrance surface dose is used as the standard for setting dose levels for common radiographic examinations (Mooney & Thomas, 1998). The entrance dose was measured using the same dosimeter used for the measurement of air Kerma during DQE measurements. The ionisation chamber was placed on the scan table (approximately the same height as the hand during a scan). Each recorded dose was taken as an average of five measurements to minimise measurement error and each measurement was corrected for temperature and pressure.

6.7 Results

6.7.1 Preliminary cadaver study

In a preliminary study in which a cadaver hand was scanned, source voltages of 70 kVp and below produced high-energy images that were grainy as illustrated in Figure 6.7 while the low-energy images appeared to be unaffected.

80 kVp 70 kVp 50 kVp

Figure 6.7: Reduction in quality of the high-energy image with decreasing source voltage. [Contrast has been enhanced for visualisation].

6.7.2 Image quality

Results showed that for fixed tube current, image quality increases with source voltage and for a fixed source voltage, image quality increases with current. Figure 6.8 illustrates the increase in DQE with voltage at a fixed current of 50 mA while Figure 6.9 shows how the DQE increases with current at a fixed tube voltage of 140 kVp; the DQE plots shown are for the high-energy images (a similar trend was observed in the low-energy images).

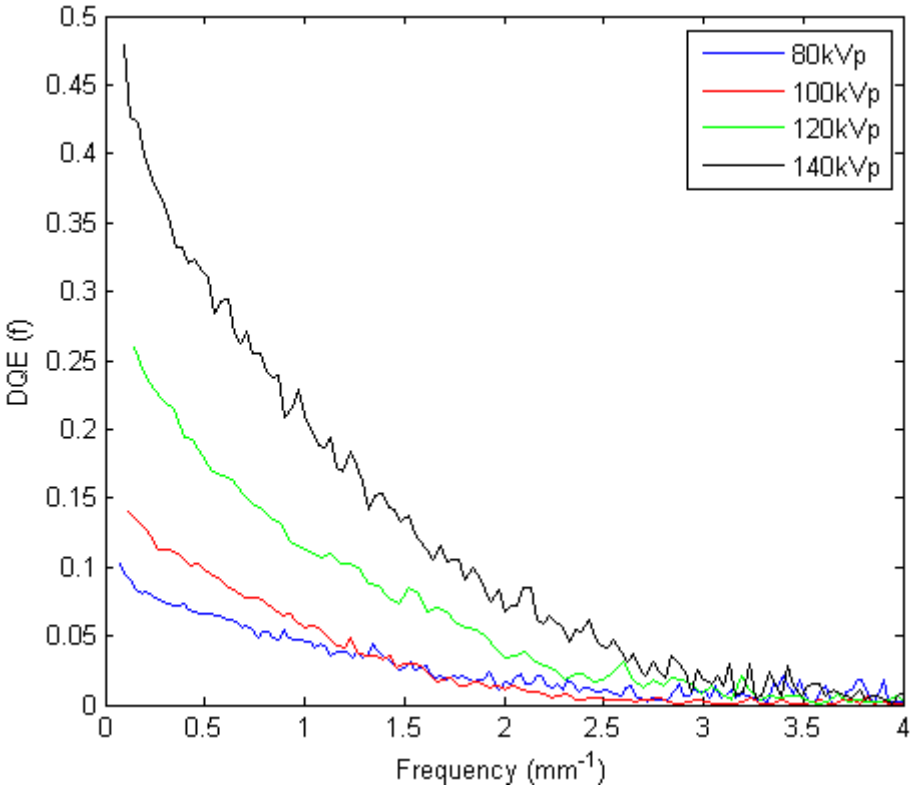

Figure 6.8: Variation of DQE with source voltage.

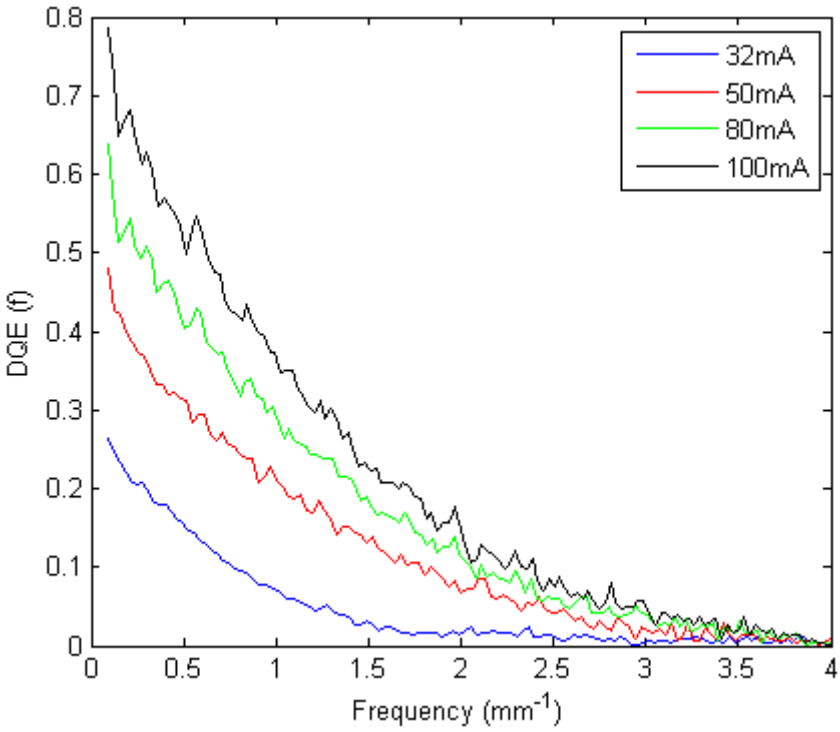

Figure 6.9: DQE for various tube currents at 140 kVp tube voltage.

Given two source voltage levels at the same tube current, the higher voltage yielded a higher DQE. However, the DQE at lower voltage could be raised above that of the higher voltage by

raising the tube current of the lower voltage. For example in Figure 6.10, a higher DQE is achieved at 80 kVp than 140 kVp by using a tube current of 160 mA.

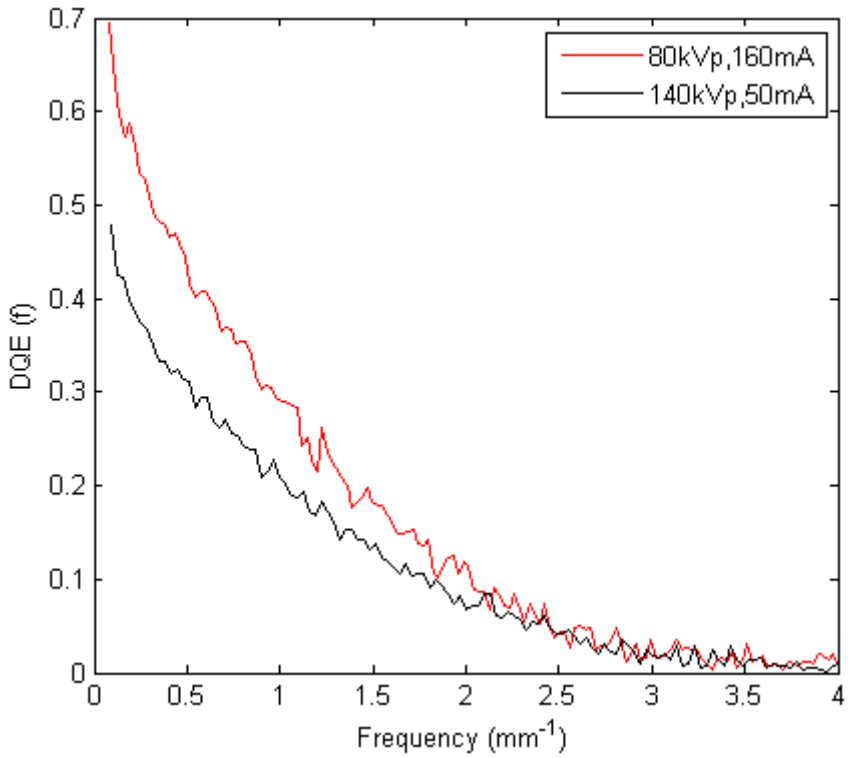

Figure 6.10: Achieving higher DQE at lower voltage by raising tube current.

For source voltages greater than 100 kVp, the presence of a post-filter also increased the DQE as illustrated in Figure 6.11 for 120 kVp.

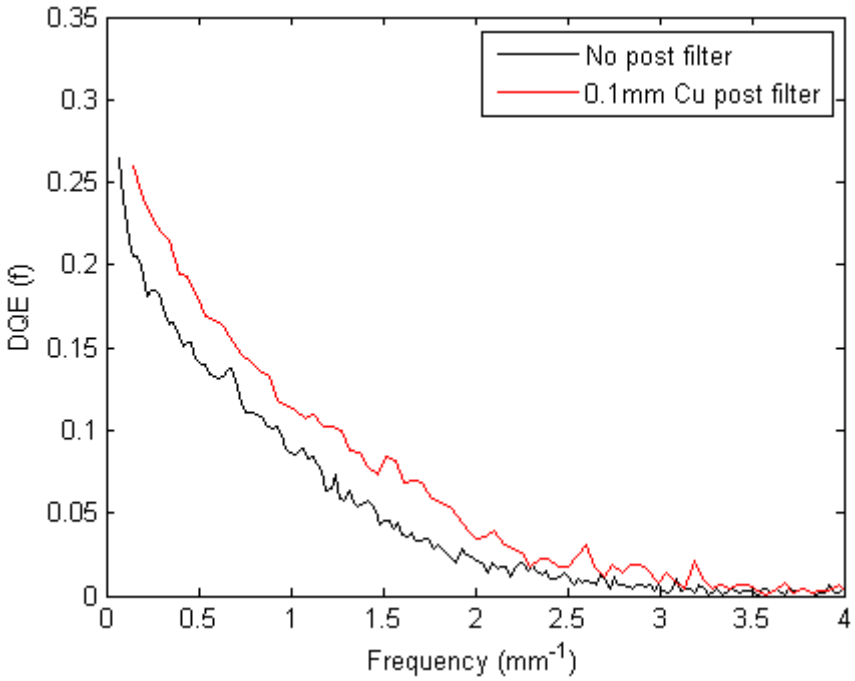

Figure 6.11: Increase in DQE caused by 0.1 mm copper post-filter for 120 kVp.

6.7.3 Spectral separation

Table 6.1 summarises differences in average energies of simulated X-ray spectra for various configurations. In the table, *pre-filter* refers to the filtration between source and patient while *post-filter* refers to filtration applied between the glass and the second scintillator (see Figure 6.2).

Table 6.1: Average energies of various simulated X-ray spectra: HE = high-energy; LE = low-energy; Cu = copper; Al = aluminium.

Voltage (kVp)	**80**		**100**		**120**		**140**	
Pre-filter	1.8 mm Al		1.8 mm Al		0.2 mm Cu		0.2 mm Cu	
Post-filter	None	0.1 mm Cu	None	0.1 mm Cu	None	0.1 mm Cu	None	0.1 mm Cu
HE (keV)	49.49	50.93	59.48	61.86	76.20	78.21	84.99	87.00
LE (keV)	47.58	47.58	53.76	53.76	65.79	65.79	70.19	70.19
HE-LE (keV)	1.91	3.35	5.72	8.10	10.42	12.43	14.79	16.81
HE/LE	1.04	1.07	1.11	1.15	1.16	1.19	1.21	1.24

As expected, the introduction of the patient's hand as part of the attenuating material in the spectral analysis resulted in higher average energies. However, there was no significant change in the trend of the spectral separation i.e. spectral separation increased with increasing

source voltage. Table 6.2 shows the average energies when a patient with 11 mm thick phalanges and 20 mm soft tissue is examined; this would be a patient at the high end of the phalanx size in South Africa - the average thickness of the middle phalanx in an average white South African man is 10.54 mm (Navsa, 2010).

Table 6.2: Average energies of various simulated X-ray spectra with patient tissue (11 mm bone and 20 mm soft tissue) attenuation included: HE = high-energy; LE = low-energy; Cu = copper; Al = aluminium.

Voltage (kVp)	**80**		**100**		**120**		**140**	
Pre-filter	1.8 mm Al		1.8 mm Al		0.2 mm Cu		0.2 mm Cu	
Post-filter	None	0.1 mm Cu	None	0.1 mm Cu	None	0.1 mm Cu	None	0.1 mm Cu
HE (keV)	54.44	54.97	66.23	68.03	80.35	81.87	89.30	90.78
LE (keV)	53.68	54.44	61.30	61.30	69.48	69.48	74.41	74.41
HE-LE (keV)	0.76	0.53	4.93	6.73	10.87	12.39	14.89	16.37
HE/LE	1.01	1.01	1.08	1.11	1.16	1.18	1.20	1.22

Tables 6.1 and 6.2 show that the average beam energy increases with source voltage. Including a post filter also increased the average energy of the high-energy spectrum by filtering out low-energy photons. According to Skipper and Hangartner (1996), the ratio of the average energy of the high-energy beam and that of the low-energy beam should be about 1.5 for useful spectral separation; this effectively ruled out 80 kVp whose ratio is close to 1. As shown in Tables 6.1 and 6.2, the spectral ratio increases with source voltage and the highest values were achieved at 140 kVp although they were still lower than the 1.5 benchmark suggested by Skipper and Hangartner (1996).

Introducing a post filter for the high-energy spectrum raised the average photon energy by removing low-energy photons and consequently increasing the spectral separation between the low- and high-energy spectra. For example, at 100 kVp, including a 0.1 mm copper post-filter raised the average energy of the high-energy spectrum, resulting in an increase in the spectral separation from 5.72 keV to 8.10 keV as shown in Figure 6.12. Using a thicker post-filter raised the spectral separation even further; for instance 0.1 mm copper post-filter yields 16.81 keV spectral separation for 140 kVp and doubling the copper thickness to 0.2 mm results in a spectral separation of 18.54 keV. However, a 0.1 mm copper post-filter was used due to the limited space in the detector unit slot, which in addition to the two scintillators and the glass strip, could not accommodate a thicker post-filter.

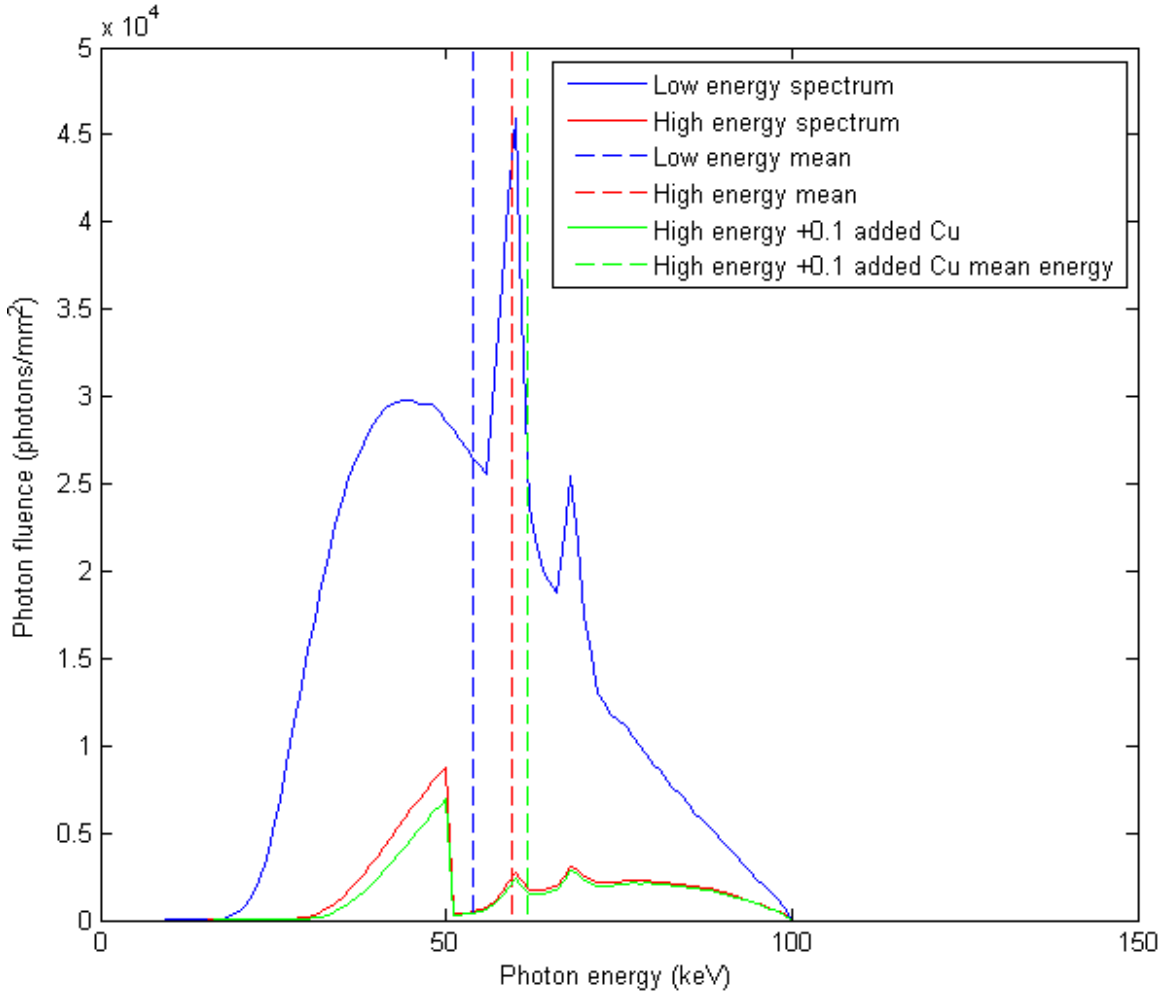

Figure 6.12: The effect of a 0.1 mm copper post-filter on spectral separation for 100 kVp; low-energy mean = 53.76 keV; high-energy mean without post-filter = 59.48 keV; high-energy mean with post-filter = 61.86 keV.

An alternative post filter with a higher atomic number would remove low-energy photons more effectively; an example would be tin, which has an atomic number of 50 compared to 29 for copper. Figure 6.13 shows simulated spectra illustrating the effect of using 0.1 mm tin post-filter instead of copper for a source voltage of 140 kVp; the spectral separation increases from 16.81 to 20.63 keV. However, tin was not available during the course of the project.

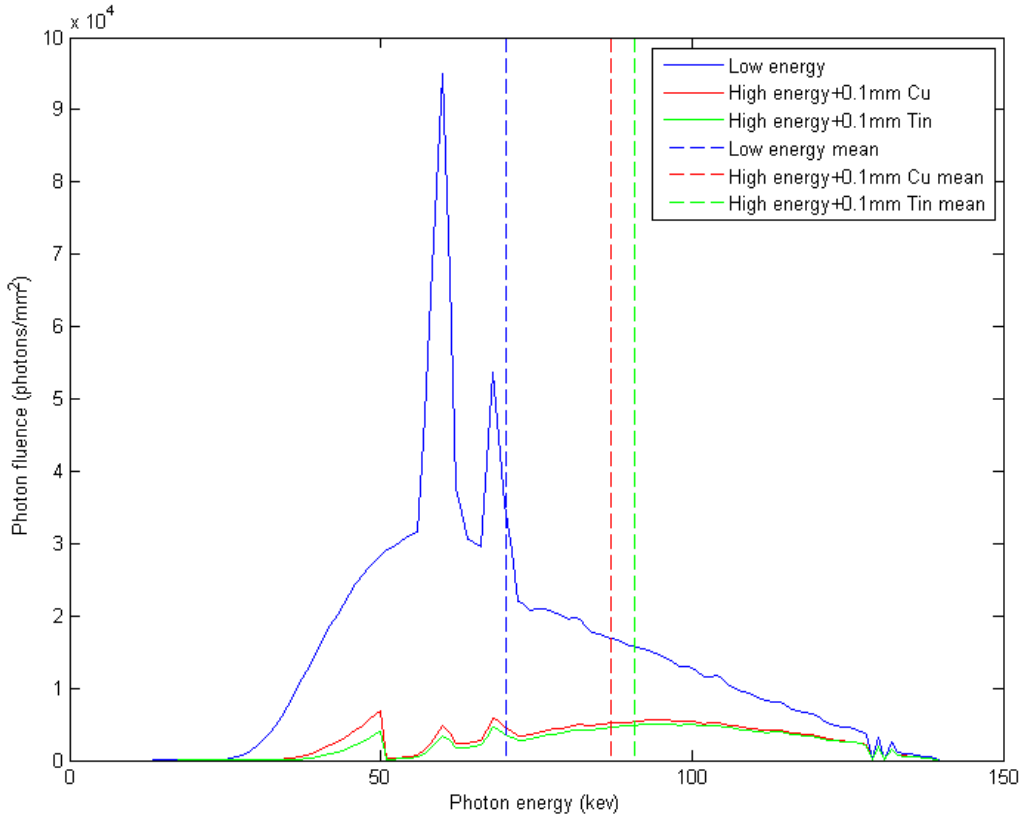

Figure 6.13: The effect of 0.1 mm tin post-filter on the high-energy spectrum compared with 0.1 mm copper post-filter at 140 kVp.

Replacing the gadolinium-based (Gd_2O_2S:Tb) *Scintillator 1* (see Figure 6.2) with a cesium-based scintillator (CsI) could lead to higher spectral separation. The reason for this that while CsI and Gd_2O_2S:Tb are characterised by similar detection efficiency for photon energies lower than about 30 keV, the K-edge of a CsI scintillator occurs at about 33 keV and that of Gd_2O_2S:Tb occurs at about 50 keV; CsI has a much higher detection efficiency between these two energies (Boone, 2000). Therefore, due to the higher detection efficiency of the CsI scintillator in the 33 – 50 keV range, a CsI scintillator would remove low-energy photons more effectively than the Gd_2O_2S:Tb resulting in a higher spectral separation as illustrated by the simulated spectra in Figure 6.14.

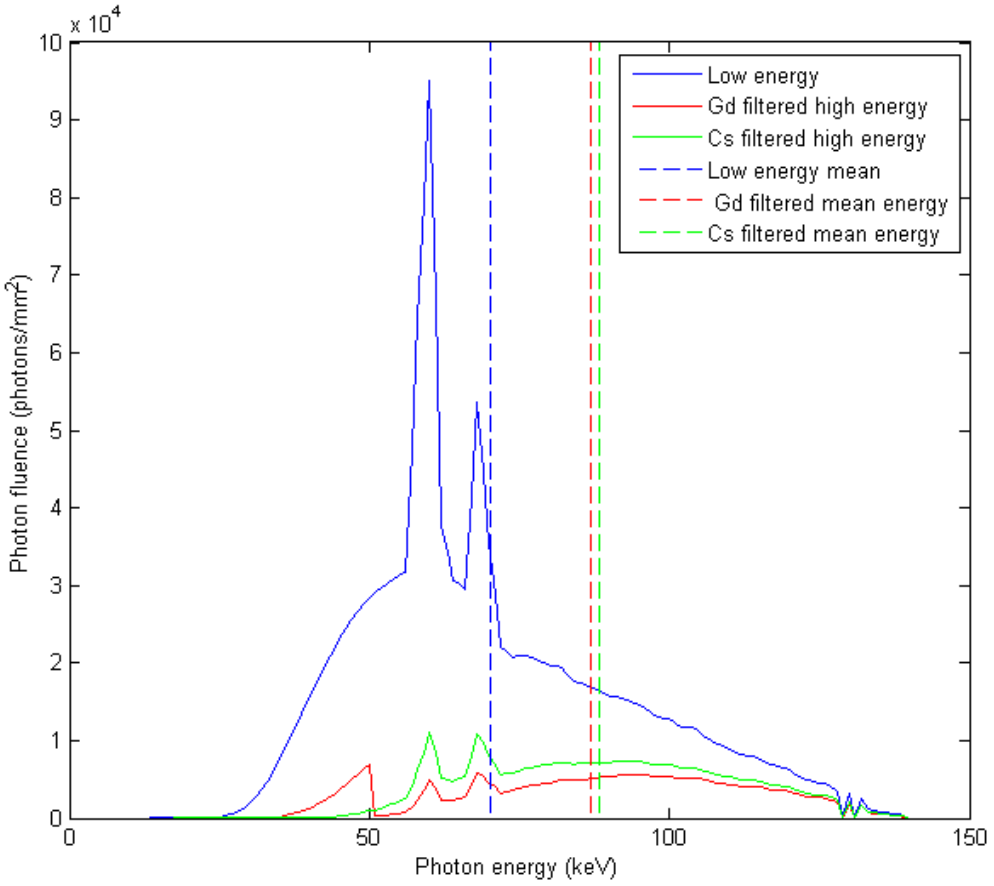

Figure 6.14: Effect of replacing Gd2O2S:Tb Scintillator1 with a CsI scintillator on the spectral separation for 140 kVp.

Table 6.3 shows the effect of the CsI scintillator on the simulated dual-energy spectra. A similar spectral separation achieved at 140 kVp with Gd_2O_2S:Tb scintillator can be achieved at 100 kVp with a CsI scintillator. Also, the ratio of the high-energy average to low-energy average becomes higher at 100 kVp than at 140 kVp.

Table 6.3: Average energies for CsI Scintillator1: Al = aluminium; Cu = copper; Sn = tin.

Voltage (kVp)	**80**	**100**		**120**			**140**		
Pre-filter	1.8 mm Al	None	1.8 mm Al	0.2mm Cu			0.2 mm Cu		
Post-filter	None	None		None	0.1 mm Sn	0.1 mm Cu	None	0.1 mm Sn	0.1 mm Cu
HE (keV)	58.87	68.54	69.13	80.58	83.05	81.36	87.41	90.29	88.30
LE (keV)	46.71	51.49	52.84	65.79	65.79	65.79	70.19	70.19	70.19
HE-LE (keV)	12.16	17.05	16.30	14.80	17.26	15.58	17.22	20.10	18.11
HE/LE	1.26	1.33	1.31	1.22	1.26	1.24	1.25	1.29	1.26

Table 6.4 summarises the measured effective energies for various tube voltages at a fixed current of 50 mA. Simulations (Tables 6.1 and 6.2) and measurements of effective energies (Table 6.4) have shown that the highest difference in the average and effective energies of the low-energy (LE) and high-energy images (HE) are achieved at 140 kVp.

Table 6.4: Measured effective energies for various source voltages: Al = aluminium; Cu = copper; HE = high-energy; LE = low-energy.

Voltage (kVp)	**80**		**100**		**120**		**140**	
Pre-filtration	1.8 mm Al		1.8 mm Al		0.2 mm Cu		0.2 mm Cu	
Post-filter	None	0.1 mm Cu	None	0.1 mm Cu	None	0.1 mm Cu	None	0.1 mm Cu
HE (keV)	47.88	51.19	54.72	58.49	71.46	76.38	76.39	87.29
LE (keV)	41.9	41.9	47.88	47.88	66.84	66.84	71.46	71.46
HE – LE (keV)	5.98	9.29	6.84	10.61	4.62	9.54	4.93	15.83

6.7.4 Entrance dose

Entrance dose increased with increasing source voltage and tube current. Table 6.5 summarises the entrance dose, obtained using the dosimeter and ionisation chamber, for various source voltages at a fixed current of 50 mA while Figure 6.15 shows the variation of dose with tube current at a fixed source voltage of 140 kVp.

Table 6.5: Entrance dose for various source voltages at 50 mA: 1.8 mm aluminium pre-filtration was included for source voltages of 100 kVp and below while source voltages of 120 kVp and above included 0.2 mm copper pre-filtration.

Voltage (kVp)	80	100	120	140
Dose (μGy)	15.39	21.46	27.28	38.10

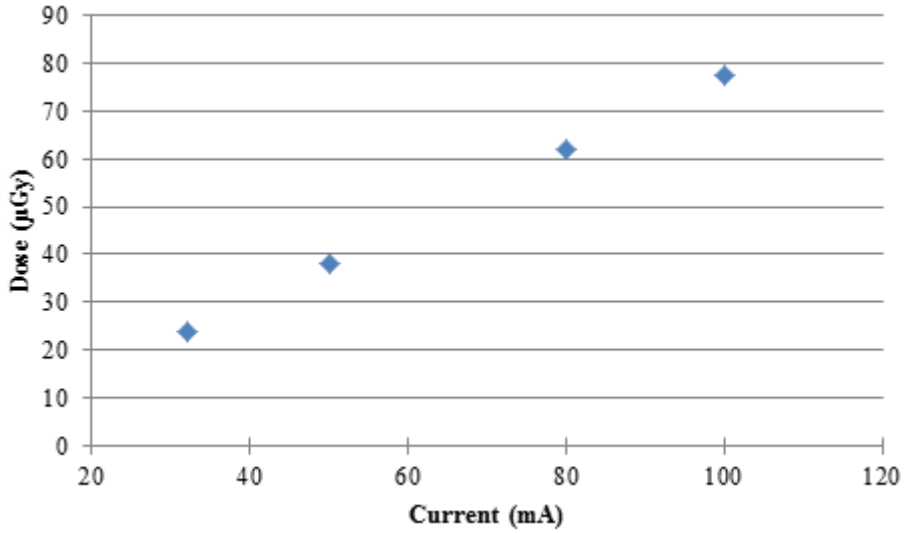

Figure 6.15: Variation of dose with tube current at 140 kVp.

6.7.5 Selection of tube settings

A voltage setting of 140 kVp was chosen for the scans as it yielded the highest DQE and spectral separation. The next task was to select the current setting by balancing image quality and entrance dose. Figure 6.15 shows how the entrance dose varies with current at 140 kVp while Figure 6.9 shows the variation of DQE with tube current at 140 kVp for the high-energy image. Increasing the tube current reduces the NPS and hence DQE increases with increasing tube current, although at the expense of increasing entrance dose as shown in Figure 6.15.

Entrance dose for DXA machines varies from as low as 0.9 µGy to 530 µGy for different body regions (Njeh et al., 1999). A current setting of 50 mA was chosen. The entrance dose at this setting is 38.1 µGy which is comparable to the entrance dose for a spine or femur scan on the Hologic Discovery which is quoted as 40 µGy (Dotmed, 2013). The dose was chosen to match that of the Hologic Discovery DXA machine which uses the same high-energy voltage setting used in this project (140 kVp).

The effective energies of the high-energy and low-energy beams at the chosen settings are 87.29 keV and 71.46 keV respectively. Table 6.6 compares the effective energies used in this project and those used in some of the most common commercial densitometers.

Table 6.6: Comparison of effective energies of the spectra used in this project and those used in commercial devices.

	Dual-energy technique	HE (keV)	LE (keV)	HE-LE (keV)
This project	Dual scintillator	87.29	71.46	15.83
Norland	K-edge	80	45	35
GE Lunar	K-edge	70	38	32
Hologic Discovery	Switching	105	52	53
Osteometer	K-edge	55	28	27

6.8 Discussion

This project has used a dual-scintillator arrangement to explore the possibility of including a second detector on the Lodox Statscan to enable the capturing of dual-energy images of the hand in a single scan. The chosen technique factors for capturing the dual-energy images are 140 kVp, 50 mA, 0.2 mm copper pre-filter and 0.1 mm copper post-filter. The technique factors were chosen to optimise spectral separation between the low- and high-energy images, entrance dose and image quality. While the majority of research work in field of densitometry has paid little attention to image quality, its importance in this project was underlined by the poor-quality of high-energy images obtained at voltages lower than 80 kVp (see Figure 6.7). While segmentation techniques to be employed for identifying the bone of interest may work well in images of reduced quality, the image registration methods for aligning the low- and high-energy images are likely to be less successful. Also, if the image quality becomes too low, the bone density calculation may be adversely affected.

An advantage of the dual-energy generation technique employed in this project is that it does not require pulse counting detectors, which are required by systems that use K-edge filtration for DXA. Comparison with commercial densitometers has shown that the spectral separation achieved here is lower than those found in commercial densitometers (see Table 6.6). Also, the effective energies of the dual-energy spectra used in this project are higher than those used in commercial DXA machines; in particular, the effective energy of the low-energy image is higher than it is in other machines. Conversely, the difference in the effective energies is lower than in commercial DXA machines.

One way of increasing the spectral separation would be to employ a post-filter with a higher atomic number which would remove low-energy photons more effectively thereby raising the average energy of the high-energy image. A good example would be tin. Another option for

raising the average energy of the high-energy spectrum (and hence the spectral separation) would be to replace the Gd_2O_2S:Tb *Scintillator1* (see Figure 6.2) with a CsI scintillator which has a higher detection efficiency between 33 keV and 50 keV. A CsI scintillator would therefore remove low-energy photons more effectively leading to higher average energy for the high-energy spectrum. Also, the CsI scintillator would enable similar spectral separation achieved at 140 kVp with a Gd_2O_2S:Tb scintillator to be achieved at 100 kVp; a lower kVp setting would be preferable as the difference in soft-tissue and bone attenuation is higher at lower beam energies, with an additional advantage of lower dose.

Another possible avenue to explore, should the spectral separation achieved here prove to be insufficient, is to capture the dual-energy images using separately generated beams with added filtration for the high-energy beam. Since the bone measurements are taken in the hand, the scans would be quick and examination time would still be shorter than central DXA. For example, the accuDXA2 (Lone Oak Medical Technologies, USA), a dedicated peripheral DXA device for the middle phalanx of the middle finger, uses source voltages of 50 kVp and 70 kVp for the low-and high-energy spectra respectively; the high-energy spectrum is filtered using zinc (Lone Oak Medical Technologies, 2012).

Gulam et al (2000) implemented phalangeal DXA measurements on a clinical digital radiography machine (Siemens Medical Systems, Erlangen, Germany) using 40 kVp, 318 mA and 125 kVp, 28 mA for the low- and high-energy spectra, respectively. The high-energy spectra had additional 1.7 mm copper filtration. The tube voltages were the lowest and highest available on the machine; the images were acquired in two separate scans. The authors mention that the settings were merely chosen to maximise the differential attenuation of the bone and soft tissue but they do not state the effective energies of the spectra. Although the spectral separation achieved in this project is lower than that used in the commercial machines, Gulam et al. (2000) acknowledge that the DXA technique can work well with low spectral separation.

7. DXA-BASED BONE MEASUREMENTS

7.1 Introduction

This chapter discusses the processes used to compute areal and volumetric BMD of the bone of interest. The first step was to align the dual-energy images using an image registration algorithm followed by bone segmentation. Two methods for computing BMD were explored. The implementation and evaluation of the methods are described and the chapter concludes with a discussion of the findings.

7.2 Image registration

The low- and high-energy images were acquired in two separate scans. The differences in hand placement on the scan table and the spread of fingers between the scans resulted in some misalignment of the images. It was therefore necessary to register the cropped images so that the location of each point on the finger in the two images is at the same spatial coordinate with respect to the origin of each image. Studies on DXA measurements that have been reported do not perform registration of the dual-energy images, possibly due to the fact that the images are captured simultaneously in those studies.

Image registration techniques can be classified as feature-based or intensity-based (Goshtasby, 2005). Intensity-based registration techniques align images by comparing intensity distribution patterns between the target and reference images whereas feature-based techniques attempt to match the locations of landmark points identified in the images. An intensity-based technique was chosen for this project to achieve an automated processing which does not require any user interaction.

7.2.1 Similarity metric

The image registration that was implemented in this project is an iterative technique that optimises a pre-defined similarity metric for the images being registered. A similarity metric provides a quantitative measure of the resemblance between two images. The metric chosen was Mutual Information (MI) which is useful for registering monomodal (captured by the same imaging device or imaging techniques) and multimodal (captured by different imaging devices or techniques) medical images (Cole-Rhodes & Varshney, 2011; El-Baz et al., 2011; Gao et al., 2008; Hajnal et al., 2001). MI is an area-based technique that uses raw pixel intensities without assuming any specific relationship between the test images, making it more robust than most metrics and does not require any pre-processing thus allowing the

registration to be fully automated (Cole-Rhodes & Varshney, 2011). It has been widely applied for registration of medical images (Cole-Rhodes & Varshney, 2011; Maes et al., 2003; Pluim et al., 2003).

The MI metric can be defined using the concept of image entropy. The entropy of an image, *X*, is given by:

$$H(X) = -\sum_{x} p_X(x) \log p_X(x) \quad \mathbf{7.1}$$

where *p(x)* is a probability distribution function (PDF) (Russakoff et al., 2004). Given two images, *A* and *B*, MI is closely related to joint entropy of the images which is calculated as (Russakoff et al., 2004):

$$H(A,B) = -\sum_{a,b} p_{AB}(a,b) \log p_{AB}(a,b) \quad \mathbf{7.2}$$

MI is defined as:

$$MI = H(A) + H(B) - H(A,B) \; \mathbf{7.3}$$

7.2.2 Optimiser

The goal of the image registration technique used here is to optimise the similarity metric. This was achieved using the (1+1)-Evolution Strategy (ES) (Styner et al., 2000). ES belongs to the evolutionary algorithms category of optimisation methods (Bäck, 1996; Styner et al., 2000). Evolutionary algorithms are popular tools in optimisation, machine learning and solution of design problems. These algorithms use simulated Darwinian evolution to search for solutions to complex problems; genetic algorithms and evolution strategies are the basic classes of evolutionary algorithms (Whitely, 2001). Evolution strategies are the preferred approach to optimisation problems due to the self-adaptation of strategy parameters, which results in greater flexibility of the evolution strategy and they are more robust than other optimisation methods (Bäck, 1996; Styner et al., 2000; Whitley, 2001). The basic types of evolution strategies are the (μ,λ)-ES and the (μ + λ)-ES; μ refers to the 'parent' parameter population and λ the population of 'child' parameters (Whitley, 2001). In (μ,λ)-ES, the children replace the current parents as the new parents for the next iteration. In (μ + λ)-ES, new parents are picked from the current parents and children for the next iteration. The (1+1)-ES was chosen as the optimiser for this project as it has a high convergence rate (Styner et al.,

2000). In this particular application, the purpose of the ES was to find a set of parameters that produce the best possible registration result.

The optimiser requires a growth factor (c_{grow}) and shrink factor (c_{shrink}), which determine whether the parent values increase or decrease, respectively, during mutation, and the maximum number of iterations. The role of the optimiser is to establish a transformation for the moving image that maximises the MI metric. The ES iterates by randomly selecting a new position in the parameter space, which is controlled by a probability function centred at the current location. In an ES, a parameter vector, $\underline{p}$, represents an entity to be optimised. The fitness of the vector is determined by its energy value, $e(\underline{p})$, low energy values indicate high fitness and vice versa. For the current application, $\underline{p}$ represents the transformation for the moving image and constitutes the population for each optimisation step. As a result of an optimisation step, a new population (children) is generated by mutation of the current population (parents). The children are added to the current population, which is then reduced back to the former size by retaining only the fittest individuals of the combined population. In the (1+1)-ES, the number of parents and the number of children generated are both equal to 1 i.e. $\mu = 1$ and $\lambda = 1$. A mutation is a random vector of the multi-dimensional normal distribution with mean $\underline{p}_{\text{parent}}$ and covariance matrix $\sum^2$. The covariance matrix is adapted at each optimisation step. It is increased by a factor c_{grow} if the new population consists of fitter individuals, otherwise it is reduced by a factor c_{shrink} (Styner et al., 2000).

7.2.3 Implementation of registration algorithm

The low-energy image was designated the fixed image while the high-energy image was designated the moving image. Figure 7.1 shows a flowchart of how the registration of the moving image was achieved.

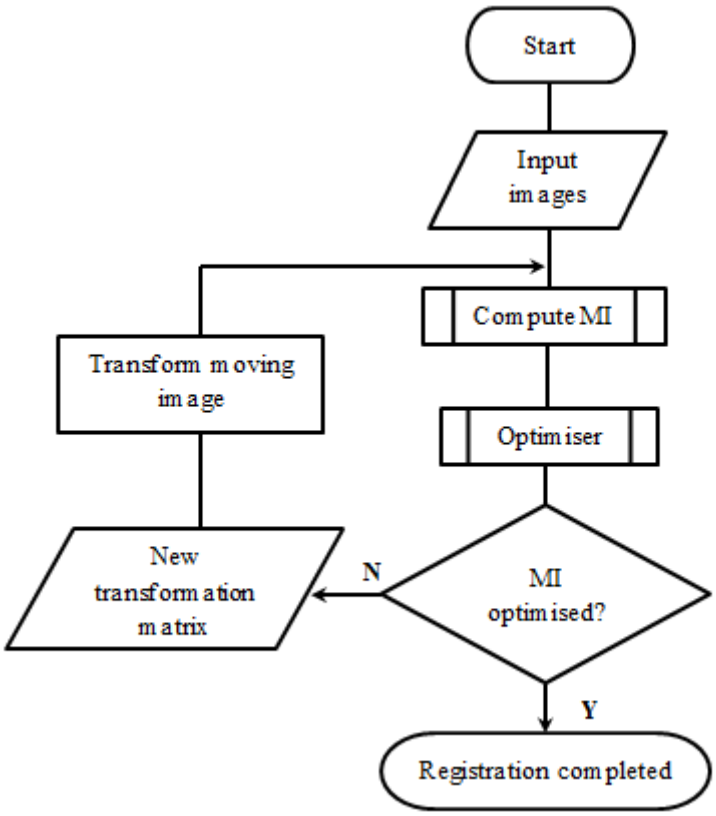

Figure 7.1: Flowchart of image registration process.

The registration algorithm was driven by the optimiser. To compute the MI at each iteration, the probability distribution of each image was made discrete by binning the values into histograms. The Mattes algorithm was employed (Mattes et al., 2001) which draws a single set of pixel locations from each image instead of drawing a different set at each iteration for computation of MI. The marginal and joint PDFs were evaluated at the positions of the uniformly spaced bins using the set of pixels and entropy values were computed by summing over the bins. A zero order B-spline kernel was used to compute the PDF of the fixed image while a third order B-spline kernel was used for the moving image (Raghunathan et al., 2005). The optimiser perturbs the parent parameters to yield a transformation matrix which is then applied to the moving image. The MI is re-calculated and the process repeats until MI is maximised.

7.2.4 Evaluation

Evaluation of the image registration was carried out to ensure that the algorithm does, indeed, align the images as required. This was achieved by selecting a corresponding set of five points on the middle phalanx in the unregistered and registered images. The spatial difference

between the sets of points was quantified by the Hausdorff distance described in Section 4.7. The low-energy image was the fixed image during image registration and therefore points marked in the low-energy image were the reference values in the evaluation.

7.3 Areal BMD – Method 1

The first method used for deriving bone mineral density was based on the technique described in Section 3.5.2. The computation of BMD using this technique is based on ratios of attenuation coefficients of bone and soft tissue using Equations 3.14, 3.15 and 3.16.

This technique requires the values of the mass attenuation coefficient of bone at the two energy levels to be known. The effective energies for the low- and high-energy spectra were determined during the evaluation of spectral separation as described in Section 6.5. The values of the mass attenuation coefficient of bone at the two energies were computed using methods and parameters derived by Okunade (2007). Elemental mass attenuation coefficients of bone constituents were found as follows:

$$\mu/\rho\,(x) = a_1 + a_2 x^{-1.6} + a_3 x^{-2.7} + a_4 x^{-3.5} + a_5 x^{-4.5} \quad \mathbf{7.4}$$

where $x = E/100$ keV, E is the X-ray energy and a_1-a_5 are energy-dependant and element-specific parameters that provide the best fit between known and computed mass attenuation coefficient values.

The mass attenuation coefficient values for the constituent elements of bone (calcium, phosphorous, carbon, oxygen, nitrogen, sodium, magnesium, hydrogen and sulphur) were computed using Equation 7.4. The aggregate value of the mass attenuation coefficient of bone was computed as a weighted sum of the elemental coefficients, leading to the computation of BMD using Equations 3.15 and 3.16. However, as shown in the results, the accuracy of computing BMD using the ratio of attenuation coefficients was not satisfactory and BMD was computed using an alternative method described in the following section.

7.4 Areal BMD – Method 2

To compute the areal BMD (*a*BMD) the soft tissue attenuation was suppressed and *a*BMD was calculated at pixel locations inside the ROI using a calibration function derived using known amounts of a bone-equivalent material.

7.4.1 Bone attenuation

The first step in the estimation of *a*BMD is the suppression of soft tissue attenuation so that only attenuation caused by the bone mineral remains i.e. generation of a bone-mineral image. The localisation of the bone in the finger by the active shape model segmentation algorithm described in Section 4.6.2 allowed the surrounding soft tissue to be identified as the area outside the bone in the finger detected at the thresholding stage as illustrated in Figure 7.2.

Figure 7.2: Identification of soft tissue adjacent to the middle phalanx. [Contrast has been enhanced for visualisation].

An assumption was made that the soft tissue thickness surrounding the bone is uniform, i.e. soft tissue adjacent to the bone is representative of soft tissue around the bone. As discussed in Section 3.5.2, by multiplying the high-energy image with a constant, β, so that the difference between the high- and low-energy images in the soft tissue regions adjacent to the bone becomes zero, the attenuation caused by the soft tissue surrounding the bone can be removed:

$$I_b = I_l - \beta I_h \quad \mathbf{7.5}$$

where I_b is the resulting bone-only image in which soft tissue attenuation has been suppressed, I_l and I_h are the low- and high-energy images respectively. β is computed as a

ratio of the mean grey level of the adjacent soft tissue regions in the low-energy and high-energy images:

$$\beta = {\bar{I}_{l(st)}}\Big/{\bar{I}_{h(st)}} \quad \mathbf{7.6}$$

It was found that the constant, β, requires a small adjustment to ensure that all the surrounding soft tissue is removed. This may be due to the assumption that the soft tissue in the finger is homogeneous. However, the adjustment required was small i.e. an adjustment of 3% of β was empirically determined as sufficient to remove all adjacent soft tissue for the images that were used. This adjustment may also have had the effect of removing the attenuation due to the non-mineral component of bone and the marrow in the marrow compartment (an aspect that is not taken into account in the generation of the bone attenuation by the basic principles of dual-energy absorptiometry - see Section 3.5.2). Therefore, as a result of the adjustment, the image I_b in Equation 7.5 can be considered to represent attenuation caused by the mineral content of bone.

Figure 7.3 shows an example of a bone-only image generated from a pair of dual-energy images. The next step was to calibrate the grey level values of the bone-only image to establish the relationship between pixel intensity and *a*BMD.

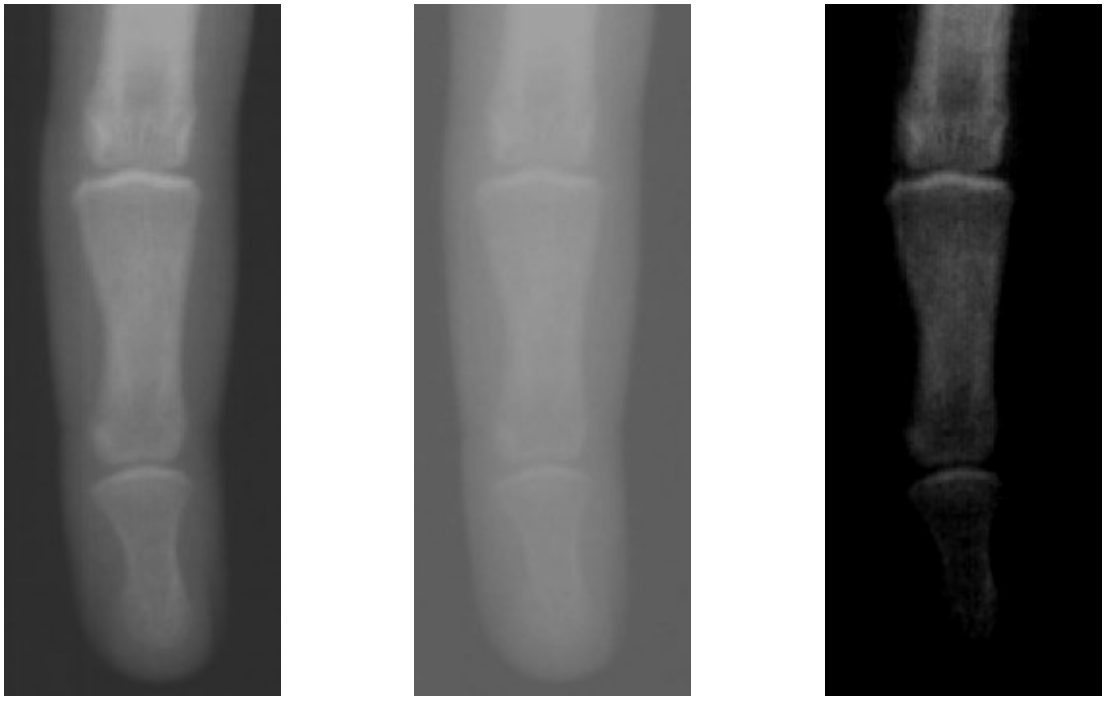

(a) **(b)** **(c)**

Figure 7.3: Generation of bone-only image: (a) low-energy image (b) high-energy image (c) bone-only image. [Contrast has been enhanced for visualisation].

7.4.2 Calibration phantom design

The calibration procedure used in this project involves imaging known amounts of bone-equivalent material contained in a soft tissue-equivalent material and examining the relationship between the mineral density and pixel intensity in the bone-only image in order to establish a mapping function between the two entities. This technique is similar to basis material decomposition calibration method, using image subtraction instead of polynomials to generate the bone-only image.

Phantoms are available for calibration and quality assurance purposes for central DXA systems. An example is the European spine phantom, a semi-anthropomorphic phantom which contains a spine insert consisting of three vertebrae of increasing mineral density (Kalender et al., 1995). The major manufacturers of DXA systems also make phantoms for quality assurance for their products. However, these phantoms are designed for central DXA and have a mineral content range that is higher than that found in hand bones. For example the Bona Fide Phantom (CIRS, Virginia) features a Perspex-embedded calcium hydroxyapatite step-wedge with a mineral density range of 0.7 – 1.5 g/cm^2 (CIRS, 2014) and the range for the European spine phantom is 0.5 – 1.5 g/cm^2. A custom designed phantom with density values in the range found in finger bones was therefore necessary for this project. The range of the mineral densities used in this project was based on the results of Gulam et al. (2000). Using DXA to measure BMD of the middle phalanx, Gulam et al. (2000) obtained an average BMD of 0.289 ± 0.025 g/cm^2 in a group of pre-menopausal women and 0.245 ± 0.032 g/cm^2 in a group of post-menopausal women. In order to cater for the possible demographic differences in BMD values and to accommodate possible extreme cases, the BMD range was stretched. The range used in the phantom, therefore, was 0.18 – 0.48 g/cm^2.

Perspex and CHA were selected for construction of the phantom. Perspex has X-ray attenuation characteristics similar to soft tissue (Moreau et al., 1994; Steel et al., 1997) while CHA is the major mineral component of bone (Lang, 2010) and is the most commonly used material for BMD calibration (Blake & Fogelman, 2010). Perspex also has the added advantages of machinability (i.e. can easily be drilled, cut and shaped as needed), it is affordable and readily available (Gingold & Hasegawa, 1992).

The new calibration phantom consisted of 13 compartments of known surface area in a Perspex block arranged in a single file. The thickness of Perspex in the compartments is the

same as that of the block used as a representative of soft tissue during the evaluation of CDA (see Section 5.3.1).

Two compartments were reserved to provide the baseline 'soft tissue' for computing the constant (β) in Equation 7.5 used for suppression of 'soft tissue' attenuation. The overall value for β was computed as the average of the β values computed in the two baseline compartments. The remaining 11 compartments were filled with different, carefully measured masses of CHA within 0.001g to provide the required mineral density range using the RADWAG digital electronic scale described in Section 5.3.1.

During calibration, the phantom was placed at the centre of the table, aligning the compartments with the central axis of the X-ray beam. This kind of set up would ensure that all the calibration data is exposed to the same X-ray intensity since, due to the fan beam geometry of the slot-scanning system discussed in Section 3.3, areas at the periphery of the phantom would be exposed to X-ray photons of reduced intensity.

Figure 7.4 shows the phantom placed on the scanning table. The phantom shown has some compartments (marked by the red rectangle in Figure 7.4) which had been intended for quality assurance purposes (i.e. evaluating the calibration) but had to be abandoned due to the beam geometry phenomenon stated above.

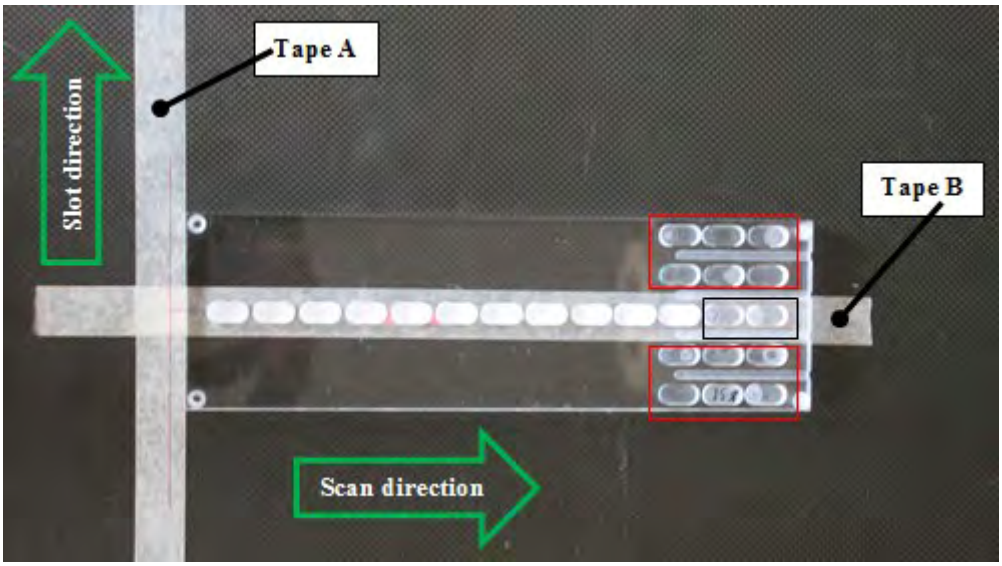

Figure 7.4: Calibration phantom: Black rectangle indicates the baseline compartments; Tape A marks the start point for the scan and Tape B marks the central axis of the slot direction used for placing the CHA compartments at the centre of the X-ray beam. The compartments marked by the red rectangle were not used.

7.4.3 Grey level – mineral density relationship

To derive the relationship between mineral density and image grey level, dual-energy images of the phantom were acquired and registered using the method discussed in Section 7.2.3. The same technique used for suppressing soft tissue attenuation in *in-vivo* images was applied to the aligned images of the phantom to suppress Perspex attenuation in the compartments containing CHA. Figure 7.5 shows typical scans of the phantom and the resulting image with Perspex attenuation suppressed in the CHA compartments.

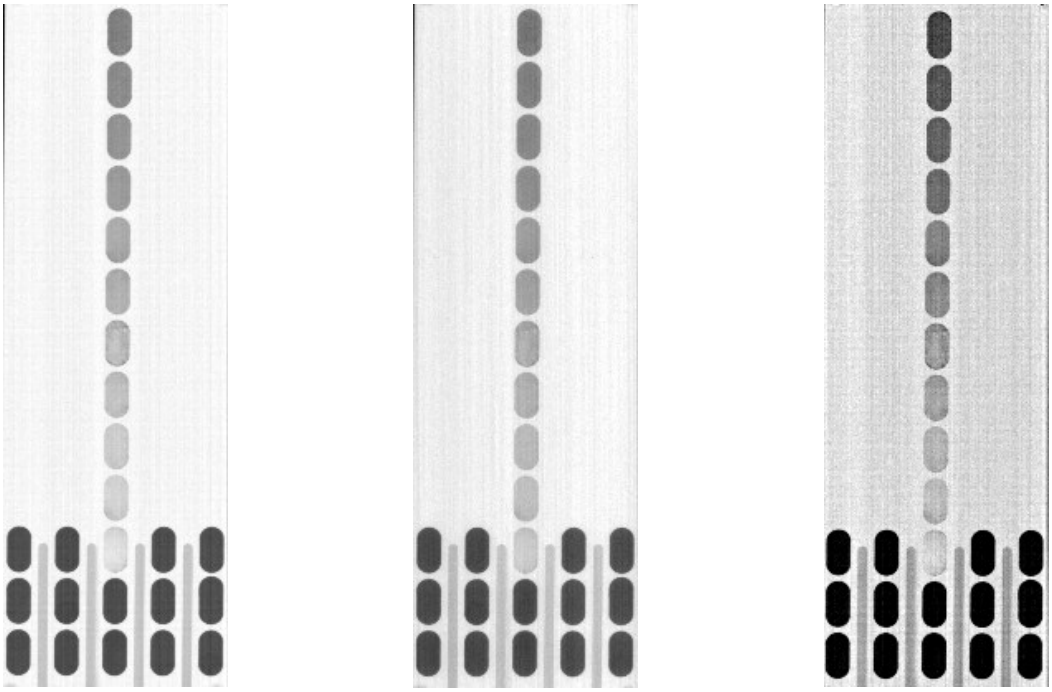

(a) (b) (c)

Figure 7.5: Typical images of the phantom: (a) low-energy image; (b) high-energy image; (c) output image with suppressed "soft tissue" in the baseline compartments. [Contrast has been enhanced for visualisation].

The average grey level of each of the 11 compartments in the output image was calculated. Figure 7.6 shows the variation of average grey level with mineral density. The relationship between mineral density and X-ray attenuation is exponential (Beer-Lambert law):

$$I = I_0 e^{-\left(\frac{\mu}{\rho}\right)\sigma} \quad \mathbf{7.7}$$

where I and I_0 are the attenuated and emitted X-ray intensities respectively, μ/ρ is the mass attenuation coefficient, σ is the area density of the attenuating material. The exponential relationship is also evident in Figure 7.6.

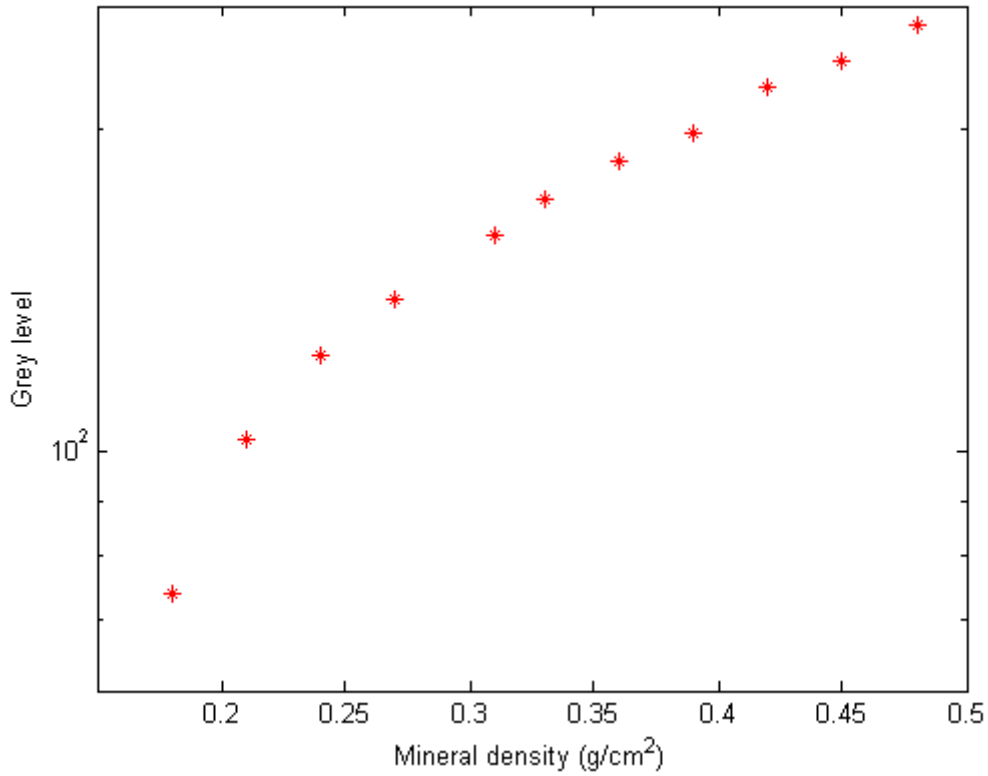

Figure 7.6: Variation of grey level with CHA density – grey level has been plotted on a logarithmic scale to show the exponential relationship.

A non-linear least squares fit operation was carried out to fit an exponential function to the density data in order to establish a mapping function between the CHA density and pixel intensity in a similar form as that used for the aluminium step wedge (see Section 5.2):

$$GL = Ae^{-B\sigma} + C \quad \mathbf{7.8}$$

where GL is the grey-level and σ is the known density of the CHA.

Once values for the constants (A, B and C) have been determined, Equation 7.8 can be used for computing the corresponding mineral density for a given grey level.

To test the accuracy of the calibration, the compartments of the phantom were emptied. Five compartments of the phantom were re-filled with various, known amounts of CHA (measured on the digital scale), different from those used during calibration. The phantom was imaged to provide the test data for evaluating the accuracy of the calibration. The amount of CHA in the test images was calculated using the calibration function as described in next section (see Section 7.4.4). The coefficient of determination, R^2, and the root mean square error that

characterise the goodness-of-fit were also calculated in same way as done for CDA (see Section 5.2.1).

7.4.4 Computation of areal BMD

To compute the areal BMD (*a*BMD) in a set of dual-energy images, the active shape model segmentation scheme described in Chapter 4 was applied to the low-energy image to identify the pixels inside the ROI (middle phalanx) – the choice of applying the segmentation in the low-energy image was arbitrary as the algorithm works equally as well in the high-energy image. The dual-energy images were then aligned using the image registration algorithm described earlier in this chapter. Once the images had been aligned, pixel locations for the finger would correspond in both images. The bone attenuation image was generated and the *a*BMD (σ) at each pixel location (*x*,*y*) within the ROI shown in Figure 7.7 was computed by making density the subject of Equation 7.8:

$$\sigma_{x,y} = \frac{\ln A - \ln\left(GL_{x,y} - C\right)}{B} \quad \mathbf{7.9}$$

where *A*, *B*, and *C* are constants determined during calibration and $GL_{x,y}$ is the grey level at pixel location (*x,y*).

The bone mineral content (BMC) at each pixel location was calculated as a product of the *a*BMD and pixel area; the pixel BMCs were summed to yield the total BMC:

$$BMC = \sum_{i=1}^{N} \sigma_i p^2 \quad \mathbf{7.10}$$

where *N* is number of pixels in the ROI and *p* is the pixel size; the pixel size used in this project is 120 μm. The BMC was divided by the bone area to yield the *a*BMD.

$$aBMD = \frac{BMC}{Np^2} \quad \mathbf{7.11}$$

Figure 7.7: Image ROI used for BMD computation. [Contrast has been enhanced for visualisation].

7.5 Volumetric BMD

The basis material decomposition technique was adopted in the calculation of volumetric BMD (*v*BMD) of a bone. The technique is commonly used for calibrating DXA systems and computation of BMD in patient images as described in Section 3.6.2 (Gulam et al., 2000; Lang, 2010; Mazess et al., 1991). Attempts to measure *v*BMD with arbitrary units in the phalanges have been made previously (Gulam et al., 2000; Kleerekoper et al. 1994; Ross, 1997; Sas et al., 2001). Sas et al. (2001) used a lateral scan in addition to the anterior-posterior radiographic absorptiometry scan to estimate the thickness of the bone which enabled the volume to be calculated. In the other previously attempted method, a circular cross-sectional shape for the bone is assumed and the bone is modelled as a summation of a series of very thin cylinders (Gulam et al., 2000; Kleerekoper et al. 1994; Ross, 1997). The 'circular cross-section' method, which, like the method proposed in this project, uses a single scan, is implemented in this project for the purpose of comparison.

For femoral DXA examination, 3-D reconstruction of bone shape and BMD distribution have been suggested (Kolta et al., 2005; Langton et al., 2009; Whitmarsh et al., 2011). Kolta et al. (2005) proposed the application of a non-stereo corresponding contours algorithm to obtain a 3-D reconstruction of the femur. The contours of the bone were extracted from a pair of

biplanar DXA scans, an anterior-posterior scan and a lateral scan. Hip geometric parameters such as the femoral neck axis length (FNAL) and hip axis length (HAL) could then be computed from the reconstructed shape. Langton et al. (2009) suggested the application of generalised procrustes analysis (GPA) to construct an average 3-D shape of the femur using shape data derived from CT scans of excised human femurs. Generalised procrustes analysis is a statistical analysis method that can be used for comparing shapes and producing a mean shape using geometric transformations. The average 3-D shape was warped onto a regular 2-D radiographic image using thin plate splines (TPS) to provide a patient-specific bone shape. Thin plate splines is a technique that interpolates a surface that passes through a set of control points and can be used for shape matching by minimising an energy function (Chui & Rangarajan, 2003). Whitmarsh et al. (2011) took the work of Kolta et al. (2005) further, proposing a technique that provides 3-D bone shape as well as 3-D BMD distribution. Their technique employs two statistical models, one for bone shape and one for BMD, constructed from CT scans by applying procrustes analysis and thin plate splines. Patient-specific information would then be acquired by warping the statistical models onto a single DXA scan. These techniques, however, only provide information about bone shape and BMD distribution but not a precise value for the BMD. Volumetric BMD measurements of the spine have also been suggested using pairs of biplanar DXA scans by estimating the width of the bone in the lateral scan which would then be used to compute the volume of the bone (Leonard et al., 2006).

Radiographic images provide two-dimensional information that lack depth information, which is needed in the computation of volume. The basis material decomposition technique decomposes a pair of dual energy images into images of equivalent basis material thickness using polynomials determined by a calibration process that uses the known thicknesses of the basis materials. The basis materials have attenuation properties similar to the constituent tissue of the anatomy being examined. For this reason, Perspex and aluminium are commonly used in bone densitometry (Cardinal & Fernster, 1990; Gingold & Hasegawa, 1992; Lehman et al., 1981). A crossed step wedge that has aluminium and Perspex increasing in perpendicular directions is usually imaged during calibration (Cardinal & Fernster, 1990; Gingold & Hasegawa, 1990; Gulam et al., 2000; Holdsworth et al., 2000; Moreau et al., 1994; Moreau et al., 1997a; Moreau et al., 1997b). Figure 7.8 illustrates how a crossed aluminium/Perspex wedge would look in a radiographic image. The assumption is that within the diagnostic X-ray range, the attenuation of any biological tissue can be represented by a linear combination of x thickness of aluminium and y thickness of Perspex. In dual-energy

medical imaging, basis material decomposition performs a pixel-by-pixel analysis of the low- and high-energy images to produce separate images for soft tissue and bone using the polynomials determined during calibration. The value of each pixel in the bone image represents the equivalent aluminium (or any bone equivalent material used during calibration) thickness of the patient at that pixel; this can be considered as the thickness of bone at that pixel location and the same applies for the soft tissue image.

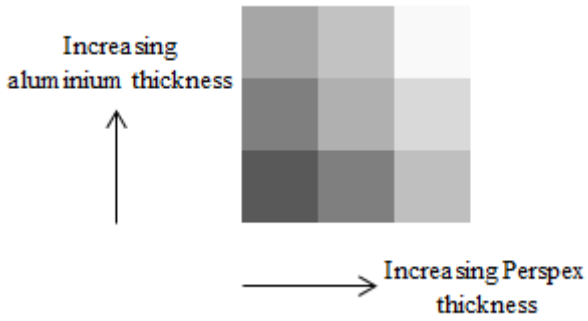

Figure 7.8: Radiograph of a crossed wedge. The crossed wedge is made by combinations of 3 thicknesses of aluminium and 3 thicknesses of Perspex.

In this project, a hypothesis was made that with careful and accurate calibration, the thickness of bone and soft tissue can be estimated from the dual-energy images and used to calculate the bone volume. This would enable the computation of *v*BMD. Basis material decomposition has been used for assessing the thickness of soft tissue and bone-like tissue (calcified atherosclerotic plaques) in arterial specimens (Moreau et al., 1994; Moreau et al., 1997a; Moreau et al., 1997b). Atherosclerosis is a disease that results from the accumulation of plaque in the walls of arteries. The studies of Moreau et al. (1994; 1997a; 1997b) describe the analysis of calcified atherosclerotic plaques in excised arteries that have been cut open longitudinally, using dual-energy X-ray imaging. The studies measure the thickness of the calcified atherosclerotic plaques (which has similar attenuation characteristics to bone) in the arteries (soft tissue) using basis material decomposition with accuracy within 25 µm (Moreau et al., 1994) and 60 µm (Moreau et al., 1997a). The results obtained in these studies indicate that the thickness of bone-like material embedded in soft tissue can be measured with good accuracy using basis material decomposition.

7.5.1 Basis material decomposition – Theory

Basis material decomposition is a technique that breaks down the attenuation coefficient into components resulting from Compton scatter and photoelectric absorption using dual-energy measurements. Lehmann et al. (1981) introduced the application of dual-energy basis material decomposition techniques to single projection radiography, using the technique to visualise lesions and airways behind bone, and removing bowel gas in intravenous pyelography. The theory of basis material decomposition proposed by Lehmann et al. (1981) is discussed here.

In the diagnostic range, the two principal means for X-ray attenuation are photoelectric absorption and Compton scattering. Above the K-edge, the mass attenuation coefficient of a material can be approximated as follows:

$$\frac{\mu(E)}{\rho} \cong a_c f_c(E) + a_p f_p(E) \quad \mathbf{7.12}$$

where

$$a_c = \frac{z}{A} \times Avogadro's\ number \quad \mathbf{7.13}$$

$$a_p f_p(E) \cong a_c C_p \frac{Z^{3.8}}{E^{3.2}} \quad \mathbf{7.14}$$

$$C_p = 9.8 \times 10^{-24}$$

E is the energy, ρ is the density, a_c and a_p are characteristic constants of the material. Z and A are the atomic number and mass number, respectively. f_c and f_p are the energy dependencies of the Compton scattering and photoelectric absorption, respectively. f_c is the Klein-Nishina function given by:

$$f_c(\gamma) = C_0\left(\frac{1+\gamma}{\gamma^2}\left(\frac{2(1+\gamma)}{1+2\gamma} - \frac{1}{\gamma}\ln(1+2\gamma)\right) + \frac{1}{2\gamma}\ln(1+2\gamma) - \frac{1+3\gamma}{(1+2\gamma)^2}\right) \quad \mathbf{7.15}$$

$$\gamma = {}^{E}/_{m_0 c^2} = {}^{E}/_{510.975\,keV}$$

$$C_0 = 2\pi r_0^2$$

where m_0 is the rest mass energy of the electron and r_0 is the electron radius.

If the log attenuation, J, is measured at two energies (h and l), then for thickness L:

$$J_h = \left(\left(a_p f_p \right)_h + (a_c f_c)_h \right) L \quad \mathbf{7.16}$$

$$J_l = \left(\left(a_p f_p \right)_l + (a_c f_c)_l \right) L \quad \mathbf{7.17}$$

When any two known materials are present, a pair of equations can be solved for the thickness, *L*, of each:

$$J_h = L_1\left((a_{p1} f_p)_h + (a_{c1} f_c)_h \right) + L_2\left((a_{p2} f_p)_h + (a_{c2} f_c)_h \right) \quad \mathbf{7.18}$$

$$J_l = L_1\left((a_{p1} f_p)_l + (a_{c1} f_c)_l \right) + L_2\left((a_{p2} f_p)_l + (a_{c2} f_c)_l \right) \quad \mathbf{7.19}$$

Since any two linearly independent sums of two basis functions (the Compton and photoelectric components in Equation 7.12) span the space, they are also adequate basis functions. It follows then that any material ξ can be expressed as a linear combination of any other two materials α and β, the basis set materials:

$$\frac{\mu_\xi(E)}{\rho_\xi} = a_1 \frac{\mu_\alpha(E)}{\rho_\alpha} + a_2 \frac{\mu_\beta(E)}{\rho_\beta} \quad \mathbf{7.20}$$

where

$$a_1 = \frac{a_{c\xi}\left({Z_\xi}^{3.8} - {Z_\beta}^{3.8} \right)}{a_{c\alpha}\left({Z_\alpha}^{3.8} - {Z_\beta}^{3.8} \right)} \quad \mathbf{7.21}$$

and

$$a_2 = \frac{a_{c\xi}\left({Z_\xi}^{3.8} - {Z_\alpha}^{3.8} \right)}{a_{c\beta}\left({Z_\beta}^{3.8} - {Z_\alpha}^{3.8} \right)} \quad \mathbf{7.22}$$

The material ξ can be assigned to a vector in the basis plane; by defining T_1 and T_2 as follows:

$$T_1 = a_1 t_\xi \frac{\rho_\xi}{\rho_\alpha},\ T_2 = a_2 t_\xi \frac{\rho_\xi}{\rho_\beta} \quad \mathbf{7.23}$$

where *t* is the thickness, with T_1 and T_2 both having units of length. The characteristic angle of the material in the basis plane is given by:

$$\theta = \tan^{-1}\left(\frac{T_2}{T_1} \right) \quad \mathbf{7.24}$$

$$\theta = \tan^{-1}\left(\frac{\rho_\alpha a_{c\alpha}\left(Z_\xi{}^{3.8} - Z_\alpha{}^{3.8}\right)}{\rho_\beta a_{c\beta}\left(Z_\xi{}^{3.8} - Z_\beta{}^{3.8}\right)}\right) \quad \mathbf{7.25}$$

The length of the vector directed from the origin is proportional to the thickness of material ξ. The basis images will display T_1 and T_2 at every pixel and contain all the energy information contained in the original measurements.

In a typical X-ray imaging system, the incident spectrum is broadband and the log signal is a non-linear function of material thickness. In order to estimate T_1 and T_2 (the thicknesses of basis materials α and β), algorithms that find a solution to the non-linear integral equation giving detected intensity as a function of material thickness are employed. These algorithms use a Taylor series whose coefficients are determined during calibration.

7.5.2 Basis material decomposition – Implementation

Perspex and calcium hydroxyapatite (CHA) were chosen as basis materials for this project. The square crossed-wedge used in other published studies (Cardinal & Fernster, 1990; Gingold & Hasegawa, 1990; Gulam et al., 2000; Holdsworth et al., 2000; Moreau et al., 1994; Moreau et al., 1997a; Moreau et al., 1997b) was avoided because when placed in a slot-scanning X-ray beam, the calibration data would not be exposed to uniform X-ray intensity due to the beam geometry discussed in Section 3.3. Instead, six Perspex blocks were made, each with seven holes for the CHA thickness. The CHA had a maximum thickness of 12 mm with seven calibration points, while the Perspex had a maximum thickness of 18 mm with seven calibration points (see Table 7.1); similar values were used by Gulam et al (2000) for calibration of hand DXA measurements using basis material decomposition.

Table 7.1: Step thickness (mm) for CHA and Perspex for deriving coefficients of basis material decomposition polynomials.

CHA	0	2	4	6	8	10	12
Perspex	0	3	6	9	12	15	18

The different basis material thicknesses were combined to give a total of 49 combinations. A cross-section of the one of the Perspex blocks is shown in Figure 7.9. For each Perspex block (i), six holes for the CHA had a fixed Perspex thickness, P_i, and the first step provided the stand-alone Perspex thickness (P_i without CHA) and stand-alone CHA thickness, C_{i0} (CHA without Perspex). A region with the un-attenuated X-ray intensity (in a region with no

Perspex block) would be cropped in an image to provide the zero CHA/zero Perspex combination to complete the required 49 combinations.

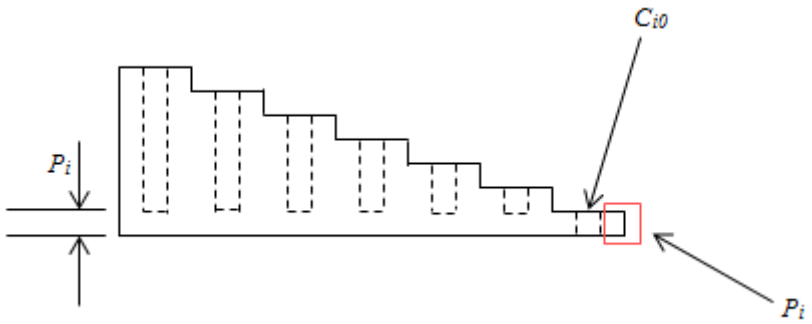

Figure 7.9: Cross section of Perspex blocks used for basis material decomposition calibration. The first step of the block provides the stand-alone Perspex thickness (P_i without CHA – marked with red square) and stand-alone CHA thickness, C_{i0} (CHA without Perspex).

During calibration for basis material decomposition, the Perspex blocks were placed in single file at the centre of the fan beam and scanned to produce dual-energy images. In this arrangement, the calibration material is exposed to the same X-ray intensity at the centre of the beam. Figure 7.10 shows typical dual-energy images of the phantom blocks.

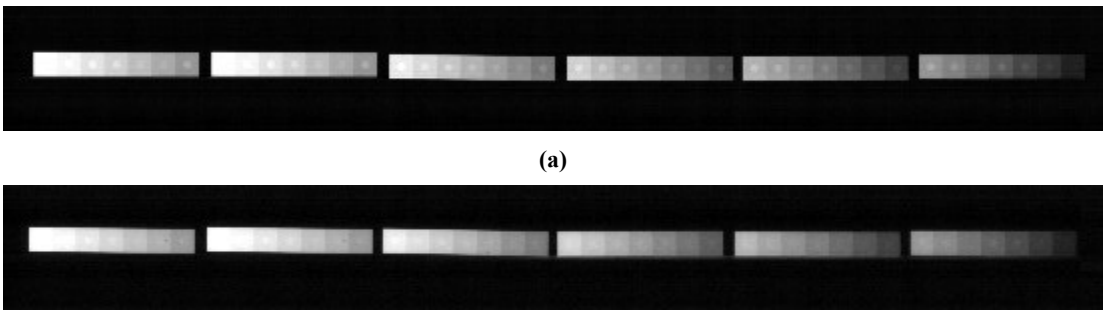

(a)

(b)

Figure 7.10: Typical images of the phantom blocks: (a) low-energy image; (b) high-energy image. [Contrast has been enhanced for visualisation].

The two images were divided into 6 sub-images, one for each Perspex block. The corresponding high- and low-energy sub-images for each block were aligned using the registration algorithm described earlier and the CHA-filled holes were located in the block using the known geometry of the block and the known position of each hole. The average grey level for each hole in both images was calculated. Each Perspex-CHA thickness combination had a pair of associated equations, giving the thicknesses of Perspex and CHA

(Equations 7.26 and 7.27) yielding 49 simultaneous equations for the CHA thicknesses and 49 simultaneous equations for the Perspex thicknesses.

$$T_1 = k_{11} + k_{12}\log I_h + k_{13}\log I_l + k_{14}\log^2 I_h + k_{15}\log^2 I_l + k_{16}\log I_h \log I_l + \ldots \quad \mathbf{7.26}$$

$$T_2 = k_{21} + k_{22}\log I_h + k_{23}\log I_l + k_{24}\log^2 I_h + k_{25}\log^2 I_l + k_{26}\log I_h \log I_l + \ldots \quad \mathbf{7.27}$$

where T_1 and T_2 are the thicknesses of the Perspex and CHA, I_h and I_l are the high- and low-energy grey levels, respectively, and k_{ij} are coefficients determined during calibration. The system of simultaneous linear equations for each basis material can be expressed in matrix form:

$$\mathbf{Ax} = \mathbf{b} \quad \mathbf{7.28}$$

where **A** is an $m \times n$ matrix of log intensity measurements, **x** is an $n \times 1$ vector of coefficients $k_1 - k_n$ and **b** is an $m \times 1$ vector of known material thicknesses. The system of equations is overdetermined since the number of simultaneous equations, m, is greater than the number of coefficients, n, that need to be computed. To solve the system of equations, both sides of Equation 7.28 were multiplied by the transpose of matrix **A**:

$$\mathbf{A}^T\mathbf{Ax} = \mathbf{A}^T\mathbf{b} \quad \mathbf{7.29}$$

This transformed the overdetermined system into a square system of size n i.e. the number of simultaneous equations is now equal to the number of coefficients and Equation 7.29 can be re-written as:

$$\mathbf{Mx} = \mathbf{f} \quad \mathbf{7.30}$$

where $\mathbf{M} = \mathbf{A}^T\mathbf{A}$ and $\mathbf{f} = \mathbf{A}^T\mathbf{b}$.

The resulting system (Equation 7.30) was solved using the least squares with QR factorisation (LSQR) algorithm (Paige & Saunders, 1982). The algorithm for the LSQR method is given in Appendix C.

In order to assess the accuracy of the basis material decomposition in measuring the thickness of different tissues, a test phantom was constructed and imaged. The test phantom was a block of Perspex with six holes of different depths filled with CHA. The thickness of Perspex and CHA in each hole was computed from dual-energy images of the test phantom using the derived coefficients for Equations 7.26 and 7.27. The computed Perspex and CHA thickness values were compared with known values to evaluate the measurement errors.

7.5.3 Computation of *v*BMD

To find the volume of a bone, the bone was divided into a large number of tiny regions of known cross-sectional area (pixels) and the thickness of the bone in each region was found using the basis material decomposition equations.

As discussed in Section 2.1, bone is a composite tissue with mineral as the major component and small amounts of collagen and water. Finger bones also have bone marrow in the marrow compartment. In an X-ray image of a finger, the attenuation measured in the region that contains bone will be an aggregate of attenuation caused by mineral component of bone, non-mineral component of bone (collagen + water + bone marrow in the marrow cavity) and soft tissue surrounding the bone (see Figure 7.11a and Figure 7.12). Applying the basis material decomposition equations to the dual-energy images of the finger will yield the thickness of soft tissue (given by Equation 7.26) and thickness of mineral component of bone (given by Equation 7.27) at every pixel position. In the bone region of the finger, the thickness of soft tissue given by Equation 7.26 is the sum of soft tissue surrounding the bone and non-mineral component of bone whereas in the region adjacent to the bone the equation gives only the thickness of soft tissue adjacent to the bone. Applying the assumption that the soft tissue adjacent to the bone is representative of the soft tissue surrounding the bone and subtracting this soft tissue from the finger, as shown in Figure 7.11b, leaves behind soft tissue that is the non-mineral component of bone. In other words the computed thickness of soft tissue is greater in the bone region of the finger than in the region adjacent to the bone and the difference is caused by the non-mineral component of bone. Therefore subtracting the adjacent soft tissue thickness from the soft tissue computed in the bone region gives the thickness of non-mineral component of bone. The thickness of the soft tissue adjacent to the bone is computed as the average of the pixel-wise thicknesses in the region. The sum of the mineral and non-mineral components of bone gives the total thickness of bone which can then be used to compute the volume of the bone.

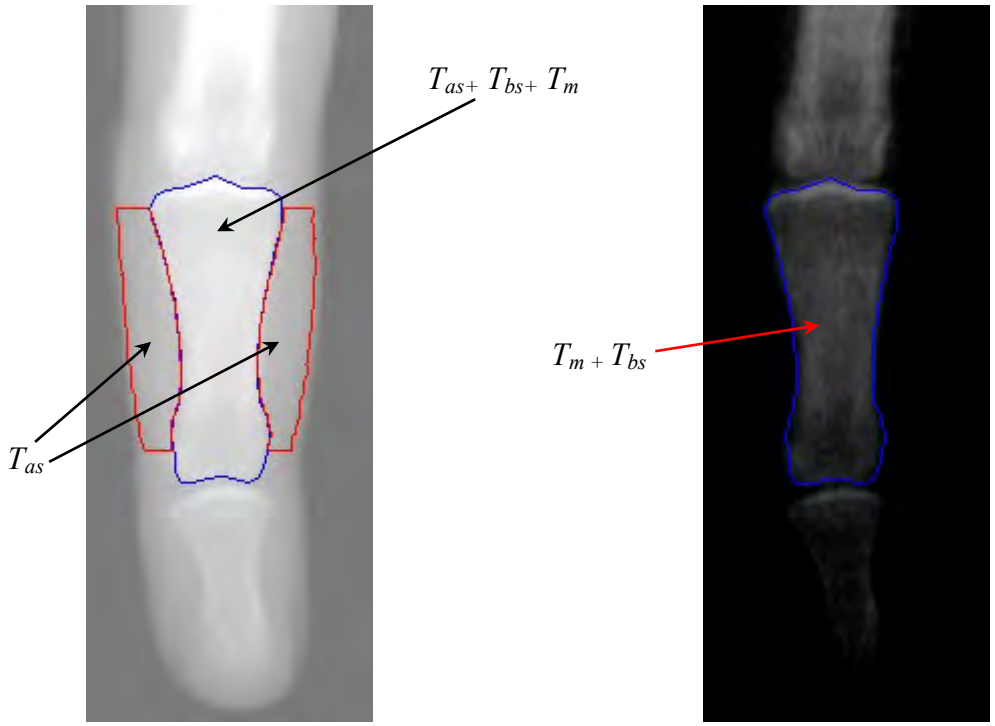

Figure 7.11: Tissues in the finger: (a) a low-energy image showing all tissue in the finger; (b) image of finger after the soft tissue surrounding the bone has been removed. T_{as} is the thickness of soft tissue adjacent to the bone; T_{bs} is the thickness of the non-mineral component of bone; T_m is the thickness of the mineral component of bone [Contrast has been enhanced for visualisation].

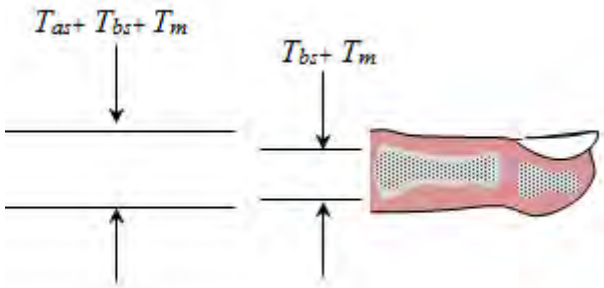

Figure 7.12: Cross-section of finger showing the tissues involved in the computation of bone volume. T_{as} is the thickness of soft tissue adjacent to the bone; T_{bs} is the thickness of the non-mineral component of bone; T_m is the thickness of the mineral component of bone.

The thickness of the bone (mineral component + non-mineral component) at each pixel i, $T_{(x,y)i}$, is therefore given by:

$$T_{(x,y)i} = (T_{(m)i} + T_{(bs)i}) - T_{as} \quad \mathbf{7.31}$$

where $T_{(m)i}$ is the thickness of the mineral component of bone, $T_{(bs)i}$ is the thickness of the non-mineral component of bone and T_{as} is the average of the pixel-wise thickness of the soft tissue adjacent to the bone.

A summation of the product of the pixel area (120 μm × 120 μm) and the bone thickness, $T_{(x,y)i}$, at every pixel position (N pixels) in the ROI yields the total bone volume, V:

$$V = \sum_{i=1}^{N} T_{(x,y)i} p^2 \quad \mathbf{7.32}$$

The *v*BMD can now be computed using the BMC obtained from the computation of *a*BMD as follows:

$$v\text{BMD} = {}^{BMC}/_{V} \quad \mathbf{7.33}$$

7.6 Evaluation

To assess the performance of the bone measurement techniques described thus far, the accuracy and precision of the system were evaluated. The accuracy of the system was evaluated by comparing the BMC of excised bones obtained on the system to the ground truth obtained by incinerating the bones and weighing their ash. The precision of the system was evaluated by taking 3 BMC, *a*BMD and *v*BMD measurements in 17 volunteers and computing the coefficient of variation (CV) of the measurements. Finally, *in-vivo* areal BMD (*a*BMD) measurements taken on the Lodox Statscan in volunteering subjects were compared to those taken on a clinical DXA machine by assessing the agreement of the measurements. Prior approval for the evaluation studies was obtained from the university's Human Research Ethics Committee (reference number, 251/2012).

7.6.1 Accuracy

Accuracy describes how closely a measurement represents the true value of the quantity being measured. To evaluate the accuracy of bone measurements, phantoms of known BMC and BMD (Gulam et al., 2000; Steel et al., 1997) or cadaver specimens (Bouxsein et al., 1997) may be used. Fresh cadavers are normally used for evaluating densitometry techniques. However, for this project, fresh cadavers were not available. It was noted that the soft tissue in cadavers that are not fresh, though preserved, becomes hardened particularly on palmar side. In some cases, the attenuation recorded in the soft tissue regions was almost equal to that recorded in the bone regions and it was suspected that this would distort BMD

measurements. Therefore, excised bones were imaged together with a soft tissue-equivalent material to simulate the presence of surrounding soft tissue. Scanning human bones in the presence of material representing soft-tissue can be used in evaluating BMD measurements (Hagiwara et al., 1994) and phantoms based on this technique are commercially available (Phantom Laboratory, 2014).

The 19 excised bones that were used for evaluation of the CDA were scanned and their BMDs and BMCs measured. The bones were placed on a Perspex block which represented soft tissue attenuation as described for CDA (see Section 5.3.1).

The reference volume for each bone was determined by placing the bone in a measuring cylinder containing a pre-set amount of water and noting volume of water displaced. In this method, the volume of the displaced water is equal to the volume of the bone. It is important to note that this method only provided a rough estimate of the bone volume since the smallest division on the cylinder is 1 ml (cm^3) and therefore the volume could only be estimated to the nearest 0.5 ml. Dual-energy images of the bones were acquired and Figure 7.13 shows an example of the dual-energy images for five bones.

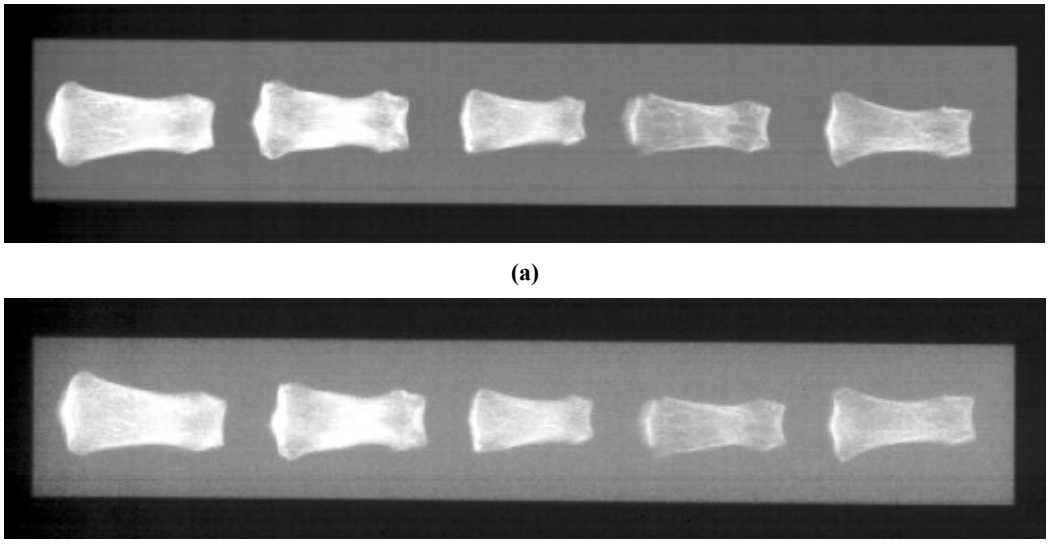

(a)

(b)

Figure 7.13: Typical scans of individual bones on Perspex blocks: (a) low-energy image; (b) high-energy image. [Contrast has been enhanced for visualisation].

The reference *a*BMD and *v*BMD for evaluation were obtained by dividing the ash weight (measured during evaluation of the CDA method) by the reference area and reference volume respectively. The reference area for each bone was generated by manual segmentation in the

acquired images and multiplying the number of pixels inside the bone region by the pixel area. Accuracy error was expressed as the percentage error as follows:

$$Error\ (\%) = \frac{|Measured\ value - reference\ value|}{Reference\ value} \times 100 \quad \mathbf{7.34}$$

7.6.2 *In-vivo* evaluation

The objectives of the *in-vivo* evaluation study were to compare the agreement between the Lodox Statscan measurements and those of an established clinical densitometer as well as to evaluate the system precision.

It has been suggested that studies for *in-vivo* comparison of measurements between densitometers should be conducted using healthy individuals (Gagnon et al., 2010; Gillette-Guyonnet et al., 2003; Hagiwara et al., 1994; Heilmann et al., 1998; Omsland et al., 2008; Rhodes et al. 2013) and individuals who have a history of bone disorders should be excluded (Heilmann et al., 1998; Rhodes et al. 2013). For this project, similar to Heilmann et al. (1998) who used a young population to compare forearm DXA measurements on several densitometers, participants for *in-vivo* evaluation were recruited from university students and members of staff. The volunteers included both men and women with representation of all ethnicities (African, Caucasian, Asian, Indian and Coloured) found in South Africa. The age range was 18 – 62 years and the average age was 25.94 years and the standard deviation 8.17 years. In comparison, the average age for the study of Heilmann et al. (1998) was 24.6 years (standard deviation of 1.5 years) and the average age for the study of Hagiwara et al. (1994) was 31.5 years (standard deviation of 4.5 years). In this project, the participants were divided into a precision and a machine-comparison group. The former was used to evaluate the system precision while the machine-comparison group was used to evaluate the agreement between the Lodox Statscan and an established densitometer.

In the precision group, consisting of 17 participants, 3 repeated measurements of BMC, *a*BMD and *v*BMD of the middle phalanx of the left middle finger were made to evaluate the *in-vivo* precision; each measurement required a pair of low- and high-energy images of the hand. The system precision for each entity (BMC, *a*BMD and *v*BMD) was computed using the spreadsheet precision tool provided by the International Society for Clinical Densitometry (ISCD, 2006) as done for the CDA technique (Section 5.3.1).

For each subject in the machine-comparison group, measurements of BMC and *a*BMD of the bone of interest were made on the Lodox Statscan and on a Hologic Discovery W DXA

machine. The BMCs produced by the two machines for each subject were paired for the purpose of assessing the agreement between the machines when measuring BMC. Similarly, the *a*BMDs were also paired to assess the machines' agreement for *a*BMD measurement. The study was conducted over the course of a few days and the Lodox Statscan DXA system was calibrated using the calibration phantom each day before scanning the subjects. Measurements on the Lodox Statscan required each subject to have two consecutive scans to acquire the low- and high-energy images. Only one scan per subject was required on the Hologic as it acquires the low- and high-energy images simultaneously. The Hologic machine is designed for femoral, spinal and forearm *a*BMD measurements. However, according to technicians at Hologic, either the software used for forearm *a*BMD or that used for rat whole body analysis may be used for measuring *a*BMD of the fingers. The forearm software was used for the phalangeal measurements as it was readily available. The entrance dose was measured for each scan on the two machines using the Radcal dosimeter.

Some studies use the Pearson product-moment correlation coefficient or linear regression analysis when assessing the degree of agreement between machines (Blake et al., 2005b; Hagirawa et al., 1994; Kiel et al., 1995; Lai et al., 1992; Nalda et al., 2011; Rhodes et al., 2013). However the use of the correlation coefficient in such cases is misleading as the correlation coefficient is a measure of the relationship between the two sets of measurements and may mask systematic differences (Bland & Altman, 1986). Other studies have used the Bland-Altman plot as a measure of agreement between two densitometry machines (Blake et al., 2005b; Gillette-Guyonnet et al., 2003; Nalda et al., 2011; Rhodes et al., 2013; Symmons, 2004) although without a precise criterion for good agreement. The Bland-Altman plot is produced by plotting the difference of each measurement pair against their mean (Bland & Altman, 1986). In this project, the Bland-Altman plot was used to determine, visually, if the difference between the two machines was heteroscedastic. The concordance correlation coefficient (Lin, 1989; Lin, 2000) was used as a measure of agreement between the machines. This technique quantifies how far, matched pairs of measurements are from the line of equality (Lin, 1989; Nalda et al., 2011):

$$\rho_c = \frac{2\sigma_{XY}}{\sigma_{XX} + \sigma_{YY} + (\mu_X - \mu_Y)^2} \quad \mathbf{7.35}$$

where X and Y are the paired samples, μ and σ are the mean and standard deviation respectively. The criterion for good agreement using this technique is a concordance correlation coefficient that is greater than 0.9 (Nalda et al., 2011).

It is important to note that, at this point, the purpose of the *in-vivo* study is not to assess the Lodox Statscan's ability to identify patients that have reduced BMD according to the WHO criteria, but to assess system precision and whether it yields measurements that agree with those of a commercial densitometer.

7.7 Results

7.7.1 Image registration

Evaluation of the image registration algorithm was carried out to verify that the algorithm does align the images as required. Figure 7.14 shows the low-energy and high-energy input images before alignment as well as the points from both images superimposed on the low-energy image; the red crosses mark the landmark points in the low-energy image while the blue crosses represent landmarks in the high-energy image; the HD is 11.4 pixels.

(a) (b)

Figure 7.14: Mis-alignment in typical input images for the registration algorithm: (a) input images, rotated to align finger with vertical axis; (b) landmark points used for evaluation superimposed on low-energy image; red crosses mark the landmark points in the low-energy image while the blue mark the landmark points in the high-energy image. [Contrast has been enhanced for visualisation].

The aligned images are shown in Figure 7.15 and the landmarks in both the low-energy image (red crosses) and the high-energy (blue crosses) are shown superimposed on the low-energy image; the HD is 1.4 pixels.

(a) (b)

Figure 7.15: Typical result of image registration algorithm: (a) output images; (b) landmark points used for evaluation superimposed on low-energy image; red crosses mark the landmark points in the low-energy image while the blue crosses represent landmarks in the high-energy image. [Contrast has been enhanced for visualisation].

Errors in the placement of the landmark points used for the evaluation contribute to the difference in their spatial positions in the image spaces. However, the evaluation fulfilled the need to demonstrate that the image registration algorithm does, indeed, align the images as indicated by the reduction in HDs for the landmark points before and after registration (11.4 and 1.4 pixels).

7.7.2 DXA calibration for Method 2

Figure 7.16 shows a typical result of a curve fitted to the calibration data derived from the phantom and Figure 7.17 shows a plot of the residuals (the difference between the known grey levels and the grey levels predicted from the fitted curve).

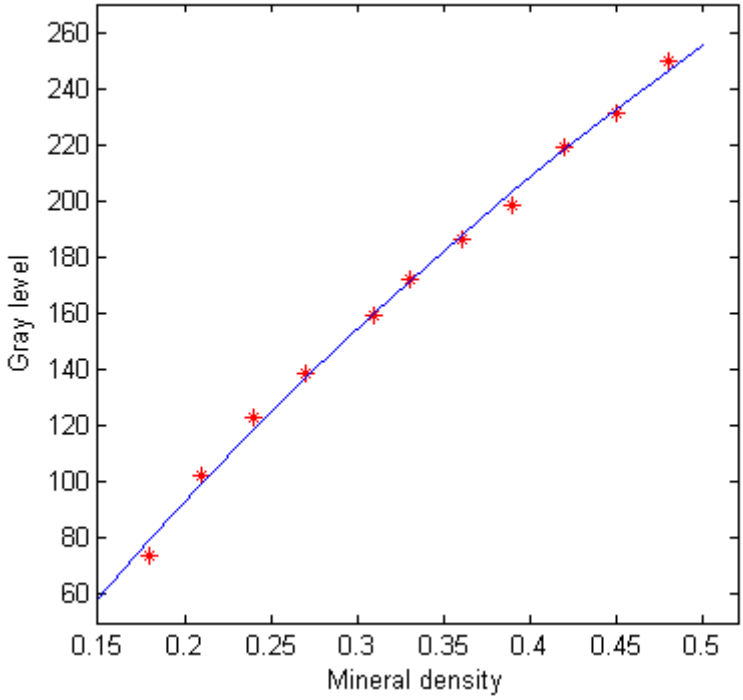

Figure 7.16: An example of a curve fitted to DXA calibration data.

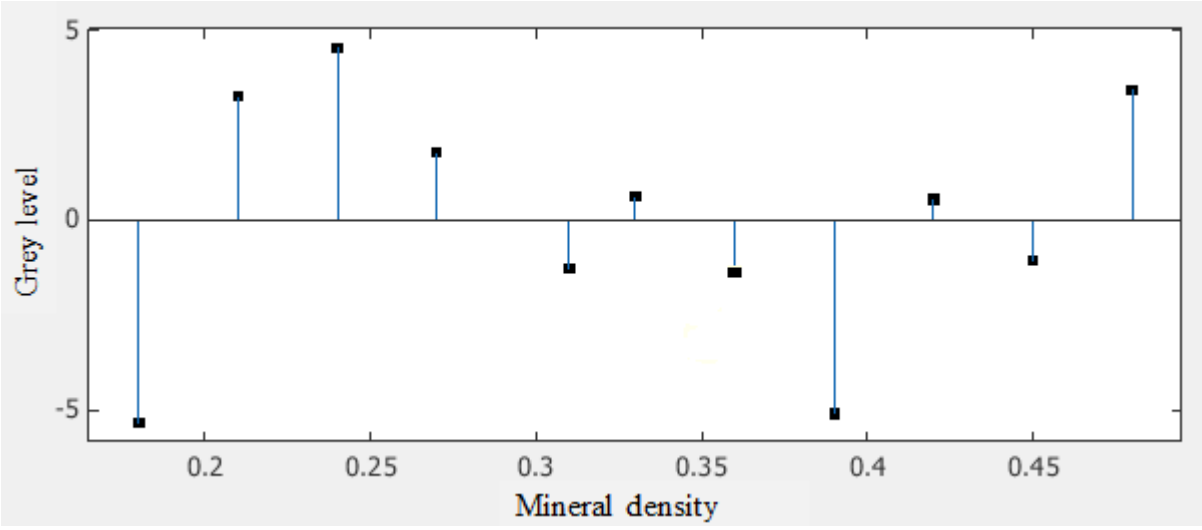

Figure 7.17: Plot of fit residuals for the example DXA calibration data.

The typical values for R^2 and RMSE obtained for the fit were 0.9965 and 3.64 respectively, and these values together with the relatively small residual values indicate that the fitted curve accurately described the fitted data.

Results of the evaluation of the calibration accuracy showed that the calibration function can measure the amount of CHA in the test phantom within 0.03g and a maximum error of 5.3%. These measurement errors were small enough to conclude that the accuracy of the calibration was acceptable.

7.7.3 Accuracy

Initial evaluation of the system performance was made by measuring the bone mineral content (BMC) of 19 excised phalangeal bones using the two DXA methods described earlier (Method 1 and Method 2). Figure 7.18 shows the variation of ash weight and the BMC derived by Methods 1 and 2 while Figure 7.19 represents the comparison of the BMC derived by the two methods and ash weight. Results show that the DXA Method 1, which uses the ratio of attenuation coefficients, consistently over-estimates the BMC while DXA Method 2 generally yields values that are closer to the ash weight despite showing a tendency to under-estimate the BMC for higher values. Furthermore, the BMC error for Method 1 increased with decreasing mineral content. The average error for Method 1 was 26% compared to 4.85% for Method 2. Therefore, Method 1 was discarded and further measurements were made using DXA Method 2.

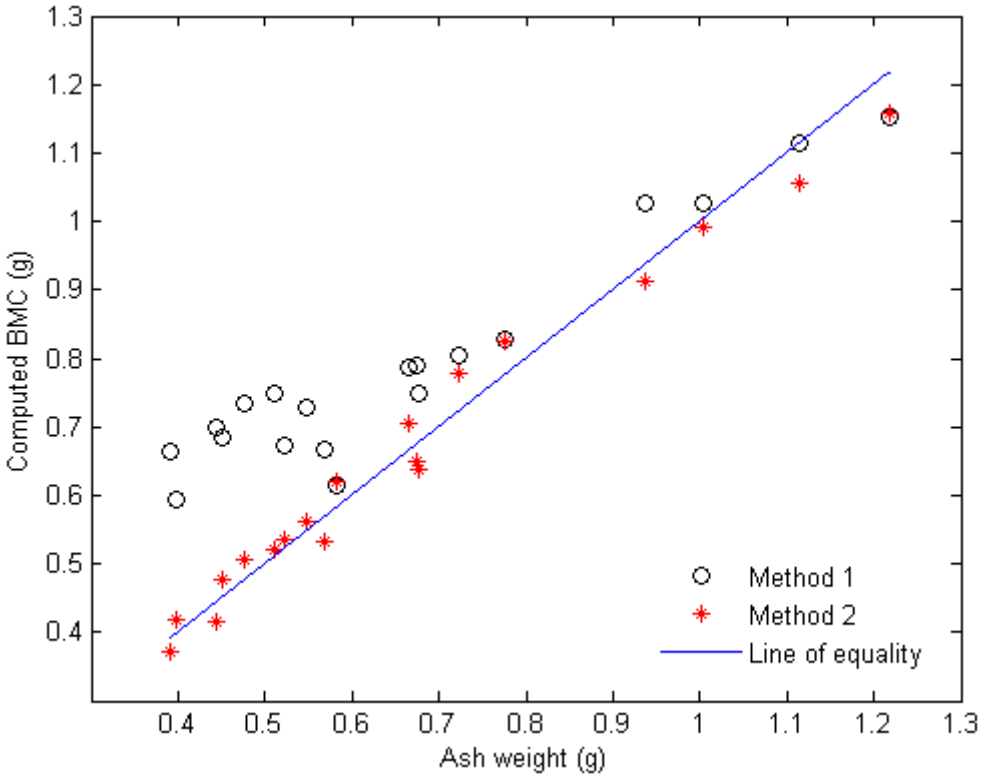

Figure 7.18: Plot of ash weight against BMC derived by the two DXA methods.

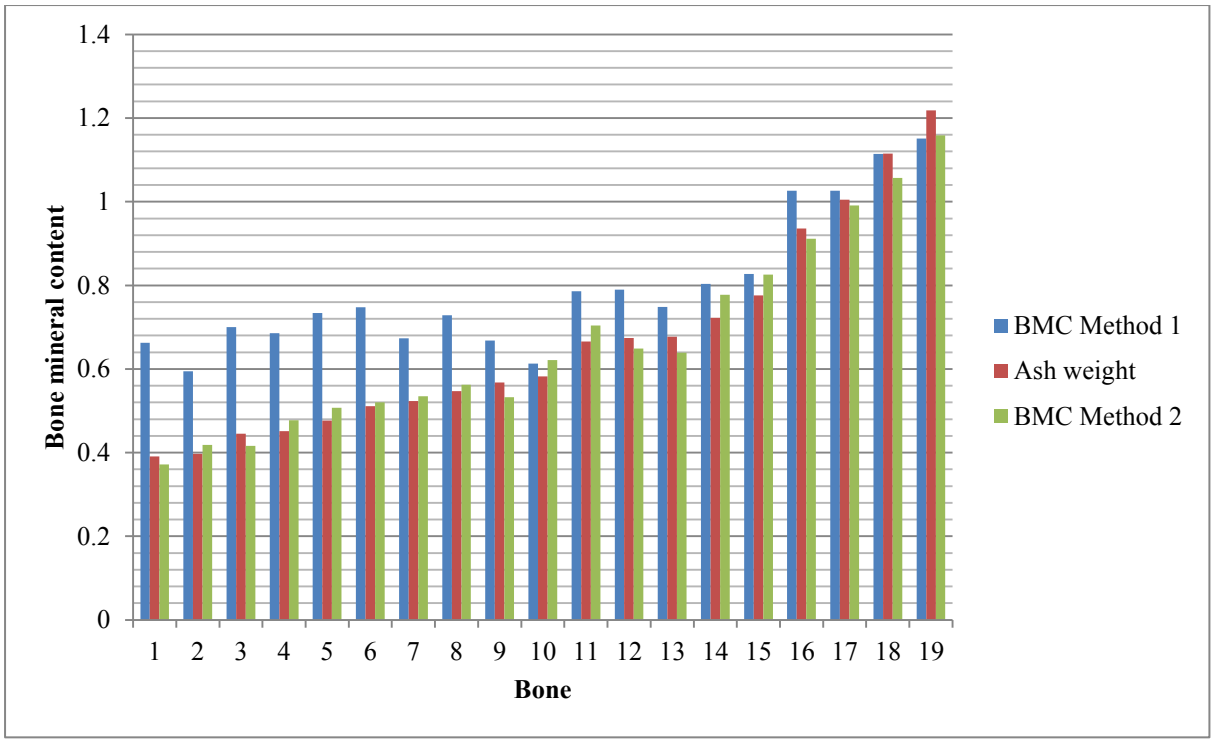

Figure 7.19: Comparison of BMC accuracy error for DXA Methods 1 and 2.

Figure 7.20 shows a plot of the computed *a*BMD (Method 2) against the reference *a*BMD obtained using the ash weight and the reference area; the average *a*BMD error was 5.49%.

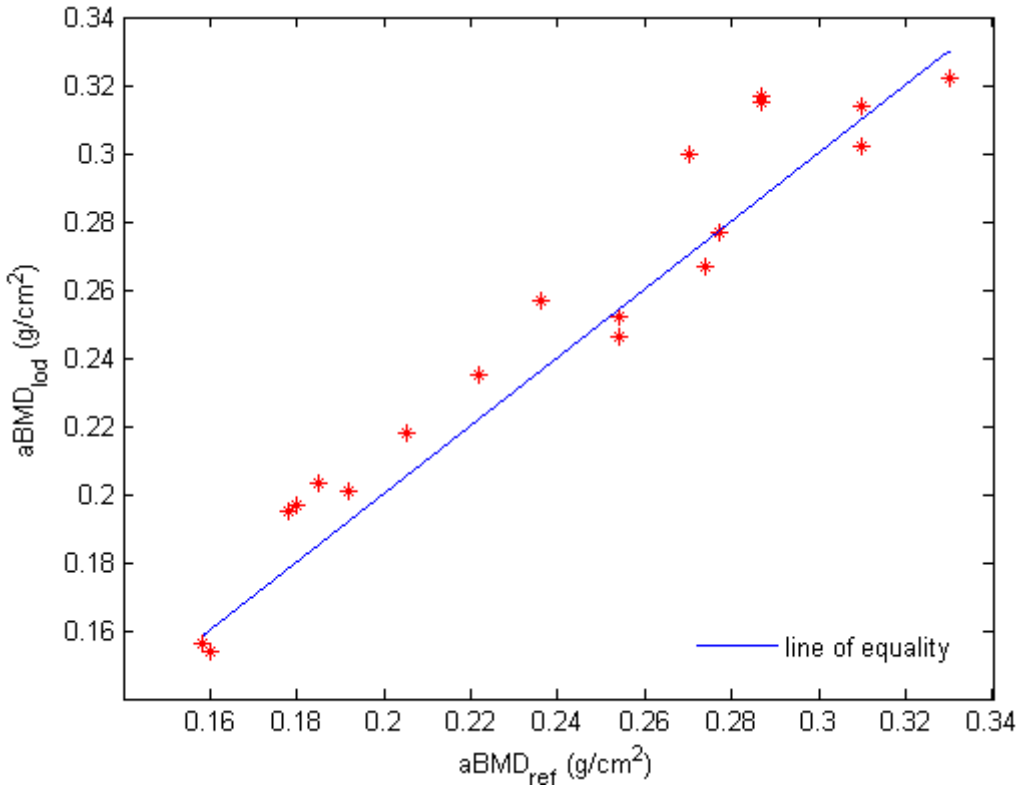

Figure 7.20: Plot of computed *a*BMD (aBMD$_{lod}$) against reference *a*BMD (aBMD$_{ref}$).

Evaluation of the basis material decomposistion showed that both CHA and Perspex thickness can be measured within 0.1 mm. Measurement errors for Perspex and CHA thickness were below 3% indicating that the basis material decomposition polynomials can measure the thicknesses of soft tissue and bone mineral with high accuracy. After achieving this level of accuracy with the computation of tissue thickness, the computation of bone volume was evaluated. Table 7.2 summarises the volume measurements of the test bones.

Table 7.2: Results of volume measurements in the test bones; Std = standard deviation.

	Computed	**Reference**
Volume range (cm^3)	0.96 – 2.72	1.00 – 2.50
Mean volume (cm^3)	1.71	1.61
Mean error (Std) (%)	10.91(6.49)	-

Figure 7.21 compares the computed volumes using the basis material decomposition-based method suggested in this project and the 'circular cross-section' method against the reference volumes. The average error for the basis material decomposition method was 10.91% compared to 24.91% for the 'circular cross-section' method. Thus the basis material decomposition-based method estimates phalangeal bone volume with less error than the 'circular cross-section' method.

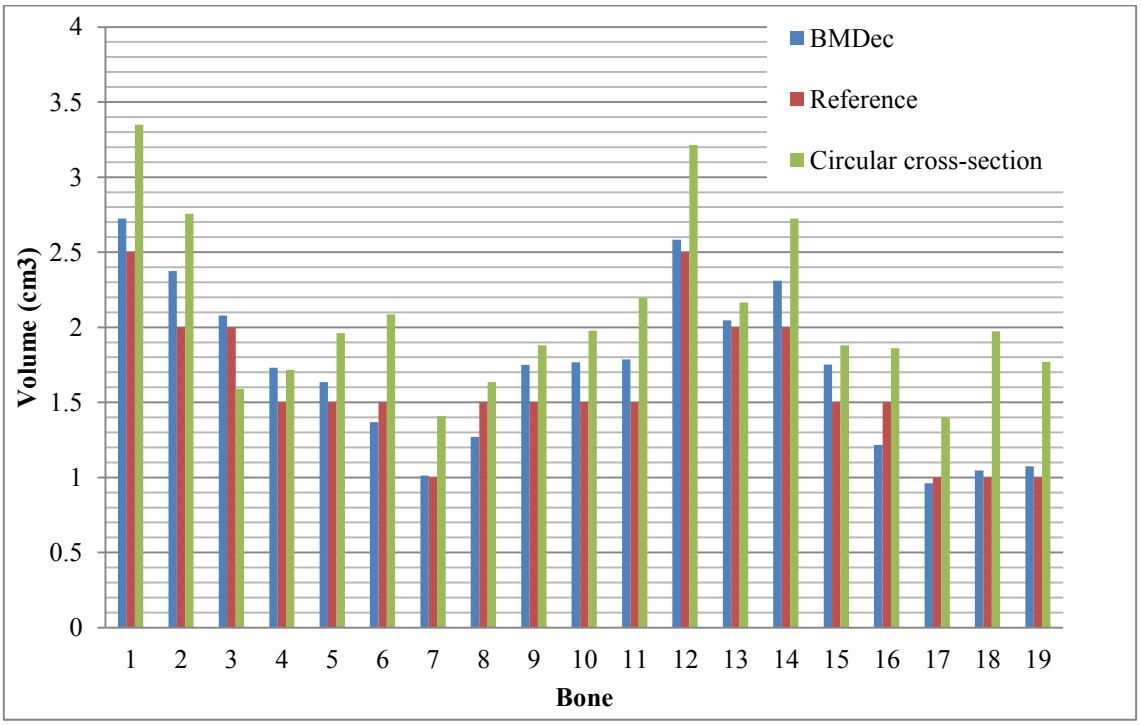

Figure 7.21: Comparison of volume computation using basis material decomposition (BMDec) and 'circular cross-section' method with reference volume for the 19 bones.

Figure 7.22 shows a plot of the computed *v*BMD against the reference *v*BMD, obtained by dividing the ash weight by the reference volume, for the excised bones. The average error of the computed *v*BMD, calculated as the percentage ratio of the absolute difference to the reference value, was 12.77%. This error is higher than that registered for the *a*BMD (5.49%). A possible explanation for this is the large uncertainty in the reference volume estimates i.e. the volume range for the bones was 1-2.5 cm^3 measured to the nearest 0.5 cm^3 which resulted in an average 10.91% error in the bone volume estimate; in comparison, the average error in the determination of bone area was 3%.

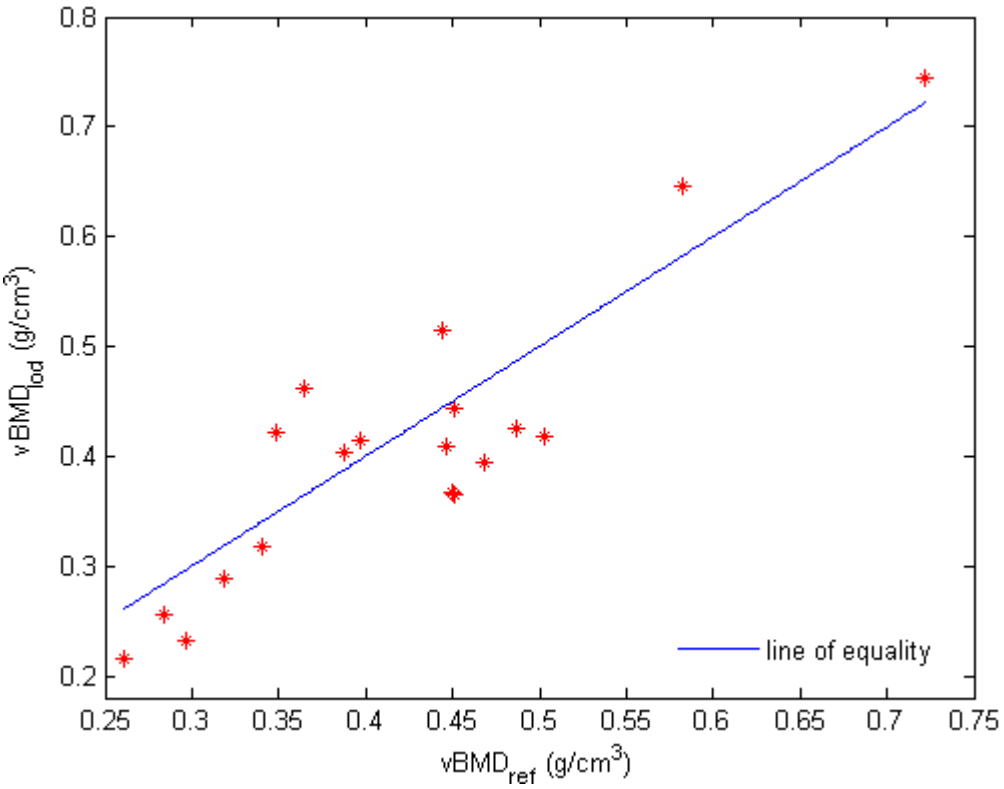

Figure 7.22: Plot of computed *v*BMD ($vBMD_{lod}$) against reference *v*BMD ($vBMD_{ref}$).

Table 7.3 summarises the results of the computed and reference measurements taken in the excised bones.

Table 7.3: Summary of the excised bone measurements; Std = standard deviation.

	Computed (Lodox Statscan)					Reference (Manual measurement)				
	Area (cm^2)	**Volume (cm^3)**	**BMC (g)**	***a*BMD (g/cm^2)**	***v*BMD (g/cm^3)**	**Area (cm^2)**	**Volume (cm^3)**	**BMC (g)**	***a*BMD (g/cm^2)**	***v*BMD (g/cm^3)**
Min	1.96	0.96	0.37	0.15	0.22	2.03	1.00	0.39	0.16	0.26
Max	3.59	2.73	1.16	0.32	0.74	3.69	2.50	1.22	0.33	0.72
Mean (Std)	2.64 (0.45)	1.71 (0.54)	0.67 (0.23)	0.25 (0.05)	0.41 (0.13)	2.72 (0.46)	1.61 (0.46)	0.67 (0.24)	0.24 (0.05)	0.42 (0.11)

7.7.4 *In-vivo* evaluation

After evaluation using excised bones, *in-vivo* evaluation was carried out by taking measurements in human subjects to evaluate system precision and to compare measurements on the system and those taken on a densitometer found in clinical practice. The subjects had their 3rd middle phalanx *a*BMD and BMC measured on the system developed in this project and on a Hologic Discovery DXA machine which provided a reference for comparison. Note that only *a*BMD and BMC were compared since the Hologic system cannot provide *v*BMD values. Due to the machines being in different locations, the machine comparison group consisted of only 44 participants (19 males and 25 females) who were able to have measurements taken on both machines. Table 7.4 summarises the details of the participants in the machine-comparison group and Table 7.5 summarises the results of the measurements taken on the two machines.

Table 7.4: Details of subjects in the machine-comparison group; Std = standard deviation.

Variable	Male	Female
Mean age (Std) (years)	25.4(6.8)	22.6(3.7)
Mean height(Std) (m)	1.71(0.07)	1.60(0.09)
Mean weight (Std) (kg)	72.7(6.91)	61.3(7.99)
Mean BMI (Std)	24.8(0.91)	23.8(1.74)

Table 7.5: Results of *a*BMD and BMC measurements in the machine-comparison group; Std = standard deviation.

Variable	Lodox Statscan		Hologic Discovery	
	Male	**Female**	**Male**	**Female**
Mean *a*BMD (Std) (g/cm^2)	0.346(0.035)	0.317(0.032)	0.339(0.033)	0.313(0.028)
Mean BMC (Std) (g)	1.022(0.188)	0.772(0.156)	1.047(0.200)	0.796(0.159)

The Bland-Altman plot for *a*BMD, shown in Figure 7.23, did not show any evidence of heteroscedasticity i.e. there is no relationship between the differences in measurements of the two machines and their averages. The average difference of the paired *a*BMD measurements was 0.005 g/cm^2 with a standard deviation of 0.013 g/cm^2.

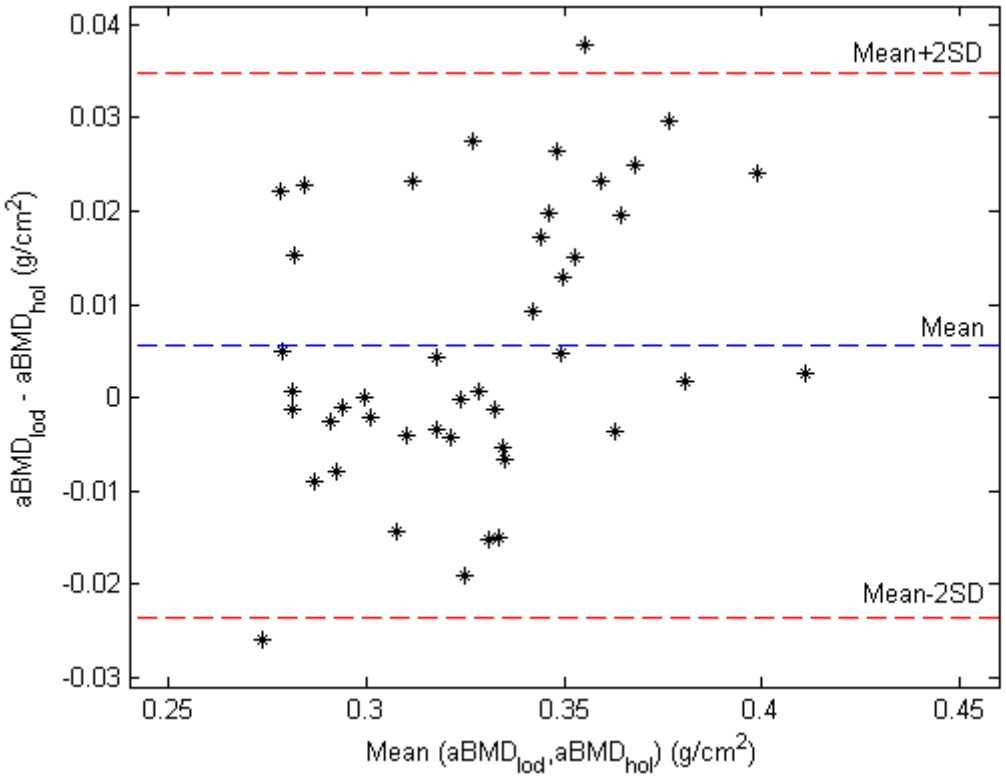

Figure 7.23: Bland-Altman plot for *a*BMD measurements on the Lodox Statscan ($aBMD_{lod}$) and Hologic Discovery ($aBMD_{hol}$); Mean difference = 0.005 g/cm^2.

The Bland-Altman plot for BMC, shown in Figure 7.24, also did not show any evidence of heteroscedasticity. The average difference of the paired BMC measurements was -0.024g with a standard deviation of 0.037g.

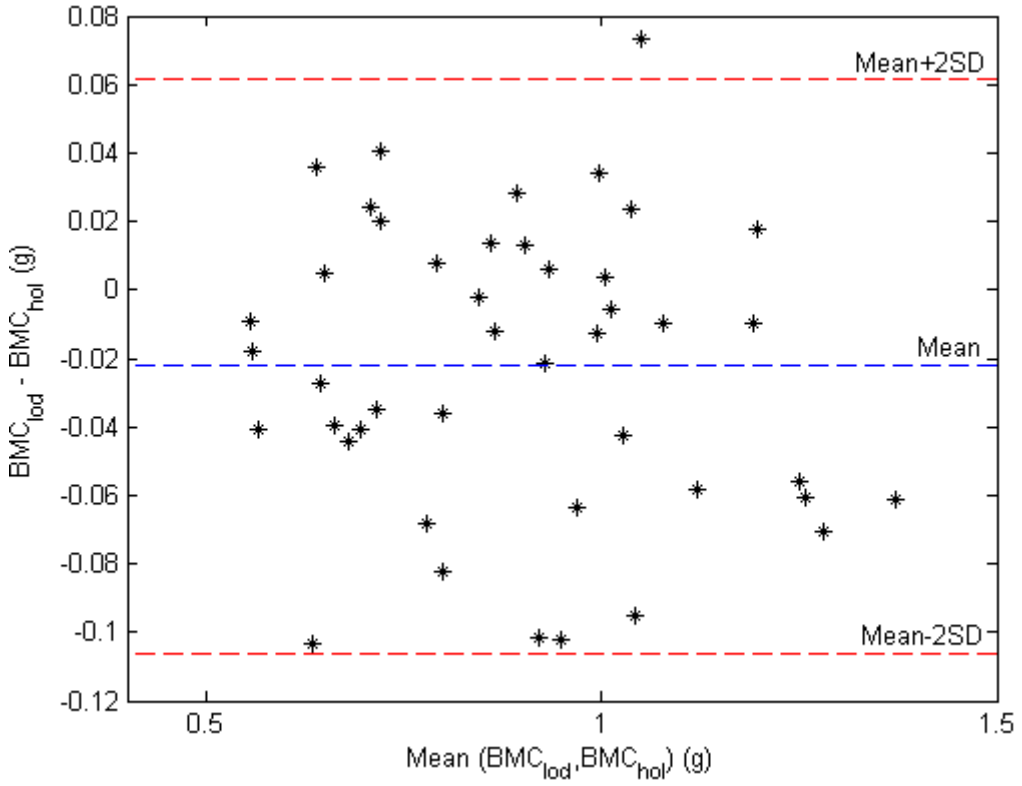

Figure 7.24: Bland-Altman plot for BMC measurements on the Lodox Statscan (BMC_{lod}) and Hologic Discovery (BMC_{hol}); average difference = -0.024g.

Lin's concordance correlation coefficient (Lin, 1989; Lin, 2000) with 95% confidence interval for the *a*BMD pairs was 0.92 (0.85 – 0.95) while that for the BMC pairs was 0.98 (0.93 – 0.99).

The precision of the system was evaluated by performing 3 measurements in 17 subjects (8 males and 9 females) and computing the root-mean-square percentage coefficient of variation (CV) of the measurements. Table 7.6 summarises the results of the precision study. The CV values for BMC, *a*BMD and *v*BMD were 1.48%, 1.35% and 1.80%, respectively.

Table 7.6: Results of *in-vivo* precision measurements taken in the precision group; Std = standard deviation.

Variable	Male	Female
Age range (years)	23 - 57	24 - 62
Mean age (Std) (years)	33.6(11.4)	37.2(12.0)
Mean height (Std) (m)	1.72(0.08)	1.57(0.10)
Mean weight (Std) (kg)	73.3(8.22)	59.0(8.86)
Mean BMI (Std)	24.7(1.18)	23.7(1.98)
Mean *a*BMD (Std) (g/cm^2)	0.35(0.04)	0.31 (0.04)
Mean BMC (Std) (g)	1.05(0.23)	0.83(0.25)
Mean *v*BMD (Std) (g/cm^3)	0.57(0.1)	0.45(0.09)

The average entrance dose for the scans was 38.1 μGy on the Statscan while the average dose for the Hologic was 45.81 μGy.

7.8 Discussion

This chapter has described the application of two DXA methods for measuring BMD. The chosen method, which had better accuracy, involves deriving the attenuation caused by the bone by suppressing the soft tissue attenuation in the finger. The suppression of soft tissue was achieved by multiplying the high-energy image with a constant found as a ratio of the attenuation of the soft tissue region adjacent to the middle phalanx in the low- and high-energy images. A small adjustment to the constant, β, used for the suppression of soft tissue was necessary to ensure that all the surrounding soft tissue is removed during the computation of *a*BMD. This could be a consequence of the assumption that the soft tissue in the fingers is homogeneous since other regions of the soft tissue cause higher X-ray attenuation than the average. However, an adjustment of 3% is still small enough to conclude that the variation in tissue composition is low. The adjustment may have had an added effect of reducing the attenuation caused by the non-mineral component of bone; which is not accounted for in the physical principles of dual-energy absorptiometry. The technique worked well for the fingers but is not expected to replicate the same performance at axial sites where the variation in soft tissue composition is much higher. This may be the reason why it is not commonly used in DXA machines designed for spine and hip BMD measurement.

The approach to the task of DXA calibration taken in this project is simpler and cheaper than the rotating disc technique employed by Hologic machine. The approach used here does not

require additional hardware to incorporate a rotating disc into the machine. The calibration technique used in this project is analogous to the basis material decomposition technique; the techniques differ only in the way the bone images are generated (i.e. image subtraction versus basis decomposition) but similarly calibrate the bone image using a mineral reference of known amount. The technique employed here is, however, simpler than basis material decomposition as it requires only one phantom, whereas basis material decomposition requires a crossed wedge for deriving the calibration polynomials that are used to produce the bone image and another one for calibrating the bone image.

Beam hardening has been cited as one of the sources of error in DXA (Blake et al., 1992; Gingold & Hasegawa, 1992; Wahner & Fogelman, 1994). The errors depend on the composition as well as thickness of the anatomical site under examination and the beam energy (Gingold & Hasegawa, 1992). In the beam hardening effect, photons with lower energy are preferentially absorbed from the incident beam compared to the photons with higher energy. This leads to progressive shift in spectral distribution towards higher energies with increasing body thickness (Blake et al., 1992). A major advantage of measuring finger BMD is the significant reduction of the effects of beam hardening and scatter (Yang et al., 1994). Also, in this project, relatively high photon energies have been used for assessing fingers, which have smaller amounts of overlying soft tissue compared to the femur or lumbar spine. The small amounts of soft tissue around the finger bones are not expected to absorb a significant proportion of the high-energy photons used for X-ray imaging and therefore the dual-energy method inherently minimises the effects of beam hardening. Another possible source of error is the anode heel effect (discussed in Section 3.3). However, the anode heel effect, and potential associated errors, is negligible on the Lodox Statscan due to the anode arrangement and collimation in the scan direction (see Section 3.3).

An important contribution made in this chapter is the computation of *v*BMD. Unlike *a*BMD, *v*BMD is not dependent on bone size and is not affected by differences in placement of the anatomical site on the scan table and may be a more suitable parameter for bone status in the management of osteoporosis. The method for *v*BMD measurement proposed in this project is advantageous over the methods that have been applied before (Gulam et al., 2000; Kleerekoper et al., 1994; Sas et al., 2001). First, the use of two scans (anterior-posterior and lateral) as proposed by Sas et al. (2001) would make the examination time longer as it would require that either the hand or the C-arm is rotated and would expose the patient to more radiation. It is also difficult to differentiate the finger bones in a lateral scan. Second, the

method of assuming fingers can be modelled with circular cross-sections, as done in other publications (Gulam et al., 2000; Kleerekoper et al. 1994; Ross, 1997), is an oversimplification which would limit the accuracy of measurements, since the phalanges have highly irregular shapes. The accuracy error in computing bone volume using the basis material decomposition method was much lower than that achieved using the 'circular cross-section' method (10.91% compared to 24.91%). However, the error in the computation of *v*BMD (12.77 %) was much higher compared to that for computing *a*BMD (5.49%). This larger error may have resulted from the uncertainty (0.5 cm^3) in the method used for deriving the reference volume for each bone which was then used for computing the reference *v*BMD. To overcome this drawback, the reference *v*BMD could be determined through peripheral quantitative CT (pQCT) or to measure the volume of the bone using a bone histomorphometry technique and then deriving the *v*BMD through dividing the ash weight by that volume. In a developing country like South Africa, such advanced techniques are scarce and very expensive. The unavailability of such techniques for validation was one of the limitations faced in this project and hence the 'displaced water' was used as an alternative for deriving the reference volume.

The method suggested in this project also provides a value for *v*BMD instead of 3-D shape or 3-D BMD distribution as proposed by Kolta et al. (2005), Langton et al. (2009) and Whitmarsh et al. (2011) for the femur. Langton et al. (2009) suggest that *v*BMD may be derived from the bone shape resulting from application of their technique; however, they do not explain how this could be achieved. A precise value for *v*BMD may be useful for a diagnosis or screening of osteoporosis using the T-score method (T-scores for *v*BMD would have to be derived). Also, information about bone shape and BMD distribution may not be as useful for hand bones as it is for the femur where the information is used to compute strength-related parameters such as hip axis length and femora neck axis length.

The errors between measured bone data and reference measurements indicate that the DXA technique as implemented here can accurately measure the mineral content, areal and volumetric BMD of the middle phalanx. Most published studies that address dual-energy imaging emphasise the need for high spectral separation between the dual-energy spectra. However, Gulam et al. (2000) point out that the DXA technique works equally well with low spectral separation. The method employed here had a source voltage of 140 kVp which satisfied the need for sufficient spectral separation while achieving both acceptable image quality and acceptable DXA measurements.

The measurements for *a*BMD and BMC obtained on the Statscan were compared to those obtained on a Hologic DXA machine. DXA machines from different manufacturers are known to give different measurements for the same subject (Blake et al., 2005b; Mazess et al., 1991). The differences between measurements on machines from different manufacturers may be explained by the differences in scanning techniques (tube voltage, filtration etc.), image resolution, calibration and segmentation of the bone of interest (Blake et al., 2005b). The machines in this study have shown good agreement for *a*BMD measurements. The entrance dose on both machines was very low, and the dose on the Statscan was lower than that recorded on the Hologic.

Although the use of the left hand has been suggested in this project, if for any reason this is not possible, the right hand can be used; Dhainaut et al. (2011) and Friis-Holmberg et al. (2012) used a similar approach in their studies where measurements were taken in the dominant hand if it was not possible to take the measurement in the non-dominant hand. The algorithm should work just as well for the right hand, despite the ASM segmentation scheme being trained using bones from the left hand, as the differences between the right and left middle phalanx of the middle finger are subtle. However, it would be possible to train the ASM using bones from both hands.

The CV values of 1.48% and 1.35% for BMC and *a*BMD respectively that have been achieved in this project are higher than those that have been reported for similar phalangeal measurements. Gulam et al., (2000) reported CV values of 0.75% and 0.67% for BMC and *a*BMD respectively while the precision of the accuDXA2 is quoted at less than 1% (Lone Oak Medical Technologies, 2012). A CV value of 1.80% for *v*BMD was achieved in this project. Sas et al. (2001) state that their method of using two perpendicular RA scans for *v*BMD has a CV that is less than 1%, they do not report the exact value. Gulam et al. (2000) also do not report on the precision of their *v*BMD technique.

The higher CV values may be attributed to the fact that, in this project, calibration was carried out prior to scanning the test subjects whereas calibration data in the other studies was simultaneously acquired during the scanning of the test subjects. The dose levels may differ across scans and may be different from the levels to which the calibration device was exposed during calibration resulting in variation of the constants A, B and C in Equation 7.8. The effect of variation of the constants is minimised by scanning the calibration phantoms in order to calibrate the system on each day that examinations are conducted. Daily phantom calibration is a common quality assurance practice in densitometry to ensure stable

calibration and allows for correction of minor changes (Blake 1996; Gillette-Guyonnet et al. 2003). A possible explanation for the precision of *v*BMD being much higher than that of the *a*BMD is that the former is computed using more parameters which has an effect of increasing uncertainty. The precision for DXA could improve if the calibration devices are scanned simultaneously with a test subject; this would, however, increase the scan duration since the calibration devices are in the form of blocks arranged in single file which, in a slot-scanning system, would require a longer scan time due to the larger region of interest. However, the CV values achieved here are less than the 2% threshold required for a method to be clinically useful. This means that phalangeal BMD measurements on the Lodox Statscan have potential for clinical use in the management of osteoporosis, particularly for screening suspected cases which may lead to the exclusion of patients with normal bone from having a central DXA scan.

8. CONCLUSION AND RECOMMENDATIONS

8.1 Conclusion

This project has shown that computed digital absorptiometry (CDA) can be used to measure bone mass in hand bones on a slot-scanning radiography (Lodox Statscan) system with high precision. The project has also shown that dual-energy images can be acquired on a slot-scanning radiography system by using two detectors and that the images may be used for computation of phalangeal bone mineral density (BMD). Automated methods that require minimum user interaction for measurement of areal and volumetric phalangeal BMD using dual-energy X-ray absorptiometry (DXA) and bone mass using CDA have been developed and tested. These were the objectives of the project and they have been achieved.

Dual-energy images for DXA were acquired by conducting two separate scans to simulate the acquisition of the dual-energy images using two detectors (i.e. scan 1 = detector 1; scan 2 = detector 2); the objective was to assess the feasibility of including a second detector in the current system without having to construct the two-detector system in its entirety. The low-energy image was captured using the current system with added copper filtration during the first scan. The high-energy image was captured during the second scan, by placing a second scintillator on top of the scintillator in the current system with a glass strip and a 0.1 mm copper filter between the scintillators. A study was carried out to assess the quality of the images and spectral separation achieved with different tube settings with this technique. An advantage of this technique is that it does not require pulse counting detectors, which are required by systems that use K-edge filtration. The exclusion of pulse counting hardware in the detector would make the detector less expensive. BMD computations in images acquired using this dual-scintillator technique yielded acceptable results despite the technique having lower spectral separation than the switching and the K-edge filtration techniques.

Automated methods for identifying the middle finger, segmentation of the region of interest and registration of the dual-energy images have been presented. A calibration phantom for hand DXA was designed. Methods for calibration of the DXA system and measurement of areal bone mineral density were developed and evaluated. A method has also been suggested for measuring volumetric BMD. A calibration step wedge for CDA was also designed and a method for measurement of bone mass in equivalent aluminium thickness units has been presented. The DXA and CDA measurement methods were evaluated by assessing their *in-vivo* precision and accuracy in excised bones, using their ash weight as reference data. The

CDA method produced measurements that had high correlation with ash weight; the Pearson product-moment correlation coefficient was 0.92. The CDA had an *in-vivo* coefficient of variation value of 0.49% indicating that the method has higher precision than that achieved in other published studies. The DXA method proved to be accurate as shown by the small average error in computed bone mineral content (BMC). The system also had clinically acceptable precision despite being lower than what other studies have achieved. The DXA method on the Lodox Statscan was also compared to a clinical DXA machine by assessing the agreement between the two machines for *in-vivo* areal bone mineral density and bone mineral content measurements; the machines had acceptable agreement.

8.2 Original contribution of the project

The main contribution of the project to the field of bone densitometry is a method for measurement of volumetric BMD (*v*BMD) in hand bones in order to address the shortcomings of the areal BMD provided by current DXA methods. This was achieved by applying the basis material decomposition technique to measure the thickness of the bone at each pixel location in the bone region which was then used to calculate the volume of the bone. Unlike other studies that have attempted to measure *v*BMD in hand bones, the method suggested here uses only a single pair of dual-energy images instead two pairs acquired in perpendicular directions and the method does not assume the bone to have an ideal shape. The method also provides a *v*BMD in 'real' units of g/cm^3 instead of *v*BMD in arbitrary units like other studies.

A method has been suggested for automatic location of the middle finger in hand images and estimation of the centroid of the middle phalanx of the middle finger to enable un-assisted segmentation of that bone. The measurement method is therefore not user-dependent; an attribute which would lead to improved precision.

The project has also carried out a comprehensive study to show that a slot-scanning radiography system can be modified to include a second detector so that dual-energy images may be acquired and processed for DXA-based measurement of phalangeal BMD. The system showed that it has high accuracy and clinically acceptable precision. It also showed good agreement with a clinical densitometer at lower entrance dose and can therefore be useful for clinical BMD measurements for screening of osteoporosis.

8.3 Recommendations

While the DXA system has yielded accurate measurements, it has used a high source voltage. The use of CsI scintillators should be explored since simulations showed that the spectral separation achieved in this project at 140 kVp can be achieved at 100 kVp if CsI scintillators are used. A lower source voltage would be more suitable since there is greater tissue contrast at lower energies and this may lead to improved accuracy.

Simulations also showed that a higher spectral separation for DXA scans could be achieved by increasing the thickness of the copper post-filter. Therefore provisions should be made to accommodate a thicker post-filter when the detector unit is modified for dual-energy imaging. An alternative post-filter with a higher atomic number would remove low-energy photons more effectively and consequently increase the spectral separation; an example is tin and should be considered in future studies.

The precision of the DXA system may be improved by acquiring the calibration data simultaneously when a patient is scanned although this would result in longer examination times. However, if the hand is placed before the phantoms in the scan direction so that it would be scanned first as the C-arm sweeps the scan field, a mechanism could be incorporated into the machine to indicate when the hand has been scanned. The patient may then leave as the machine completes the scanning of the calibration phantoms.

A possible line for future development would be to assess if results can be improved by using the average of measurements in all or more bones in the hand. The segmentation scheme described in this project can easily be extended to cater for other bones although the proximity of bones in the carpal region may pose challenges for the ASM as experienced in the study of Sotoca et al. (2003). For example, the average of the middle phalanges of the second, third and fourth fingers may be used as is done in some radiographic absorptiometry machines. A comparison study for CDA, similar to the DXA comparison conducted here, should be conducted at a facility that offers clinical CDA examinations. Also, the effect of non-mineral component of bone and marrow on bone mass measurement using CDA should also be investigated.

This project has shown that phalangeal DXA and CDA measurements on a slot-scanning radiography system (Lodox Statscan) have the accuracy and precision required in a densitometry machine. Further studies need to be carried out to determine if such measurements are able to discriminate patients with reduced axial BMD from those with

normal (or above normal) BMD as defined by the T-score system of the WHO. Such studies would also help to establish whether the volumetric BMD measured by the method described in this thesis offers improved discrimination between the two groups of patients (those with reduced axial BMD and those with normal BMD) compared to the areal BMD. Once this has been achieved, a triage statistical approach recommended by the United Kingdom National Osteoporosis Society, as discussed in Section 2.4, should then be conducted to determine the upper and lower thresholds at which the peripheral measurements on the Lodox Statscan have 90% sensitivity and 90% specificity in identifying patients with osteoporosis as defined by the WHO. Ideally these studies would involve large numbers of participants with and without osteoporotic fractures, including pre- and postmenopausal women as has been done before to determine thresholds in peripheral densitometry devices such as the Metriscan (Alara Inc, USA) and AccuDEXA (Schick Technologies Inc, USA) (Blake et al., 2005a; Clowes et al., 2006). The precision may also be re-evaluated using such populations since the precision was currently evaluated using a limited age range; it has been suggested that subjects that are representative of the target population for a device/technique (Glüer et al., 1995) should also be used in the evaluation of precision. The results of those studies would determine whether hand densitometry could be added as a tool to the Lodox Statscan for clinical assessment of osteoporosis. Since femoral BMD assessment can be conducted on the Lodox Statscan (Flash, 2002), addition of axial and peripheral densitometry would result in a multi-purpose digital X-ray machine that is able to screen (using hand measurements) and diagnose (using axial measurements) osteoporosis in addition to regular radiography. Such a multi-purpose machine could benefit health centres by reducing costs as they would require only one radiography machine rather than separate machines for each application.

Depending on the success of the studies described above, the Lodox technology may also be adapted to produce a smaller, desktop peripheral BMD machine, such as those offered by Alara (Alara Inc., USA) and Schick (Schick Technologies Inc, USA), that can be installed in the offices of general practitioners to increase widespread use of the technology in order to facilitate wider screening of the target population.

APPENDIX A

Otsu's thresholding algorithm

First, the probability distribution of grey levels was computed and the probabilities of class occurrence (ω_0 and ω_1) and class means (μ_0 and μ_1) were computed using a threshold (k):

$$\omega_0 = \sum_{i=1}^{k} p_i = \omega(k)$$

$$\omega_0 = \sum_{i=k+1}^{L} p_i = 1 - \omega(k)$$

$$\mu_0 = \sum_{i=1}^{k} \frac{ip_i}{\omega_0} = \frac{\mu(k)}{\omega(k)}$$

$$\mu_1 = \sum_{i=k+1}^{L} {ip_i}/{\omega_1} = \frac{\mu_T - \mu(k)}{1 - \omega(k)}$$

$$\mu_T = \sum_{i=1}^{L} ip_i$$

where L is the number of grey levels in the image, p_i is the probability distribution of the grey levels. The class variances are given by:

$$\sigma_0^2 = \sum_{i=1}^{k} \frac{p_i}{\omega_0} (i - \mu_0)^2$$

$$\sigma_1^2 = \sum_{i=k+1}^{L} \frac{p_i}{\omega_1} (i - \mu_1)^2$$

A measure of class separation at level k is defined as follows:

$$\eta = \frac{\sigma_B^2(k)}{\sigma_T^2}$$

where

$$\sigma_B^2(k) = \frac{(\mu_T \omega(k) - \mu(k))^2}{\omega(k)(1 - \omega(k))}$$

and

$$\sigma_T^2 = \sum_{i=1}^{L} (i - \mu_T)^2 p_i$$

The optimal threshold, k^*, was chosen as the value that maximises η i.e.:

$$\sigma_B^2(k^*) = \max_{1 \le k < L} \sigma_B^2(k)$$

APPENDIX B

The Levenberg-Marquardt Method

The goal was to fit a function, $\hat{y}(d;\mathbf{p})$ of the independent variable d and a vector of n parameters, $\mathbf{p}$, to a set of m data points (d_i,y_i) by minimising the weighted square errors between $y(d_i)$, the known grey levels, and grey levels derived by the fitted function. In this project, the fitting was achieved by iteratively minimising the chi-squared error given by (Gavin, 2013):

$$\chi^2(\mathbf{p}) = \sum_{i=1}^{m}\left(\frac{y(d_i)-\hat{y}(d_i;\mathbf{p})}{w_i}\right)^2 = \mathbf{y^T W y} - \mathbf{2y^T W\hat{y}} + \mathbf{\hat{y}^T W\hat{y}}$$

where w_i is the error in $y(d_i)$ and $\mathbf{W}$ is a weighting matrix with $W_{ii} = 1/w_i^2$. The goal of each iteration is to find a perturbation $\mathbf{h}$ to the vector $\mathbf{p}$ that reduces χ^2.

The minimisation of the chi-squared error can be achieved by the gradient descent method (Snyman, 2005). In this method, the gradient of the chi-squared objective function with respect to $\mathbf{p}$ is:

$$\frac{\partial\chi^2}{\partial\mathbf{p}} = -(\mathbf{y}-\hat{\mathbf{y}})^{\mathrm{T}}\mathbf{WJ}$$

where $\mathbf{J}$ is an $m\times n$ Jacobian matrix, $\partial\hat{\mathbf{y}}/\partial\mathbf{p}$. The perturbation that moves $\mathbf{p}$ in the direction of the steepest descent is given by:

$$\mathbf{h}_{\mathrm{GD}} = \alpha\mathbf{J}^{\mathrm{T}}\mathbf{W}(\mathbf{y}-\hat{\mathbf{y}})$$

where α is a positive scalar that determines the length of the step in the steepest-descent direction.

Another method that can be used to minimise the chi-squared error is the Gauss-Newton method (Björck, 1996). In this method, the perturbation, $\mathbf{h_{GN}}$ that minimises the chi-squared error is computed as follows:

$$(\mathbf{J}^{\mathrm{T}}\mathbf{WJ})\mathbf{h_{GN}} = \mathbf{J}^{\mathrm{T}}\mathbf{W}(\mathbf{y}-\hat{\mathbf{y}})$$

The Levenberg-Marquardt method adaptively varies the updating of $\mathbf{p}$ between the gradient descent update and the Gauss-Newton update as follows:

$$(\mathbf{J}^{\mathrm{T}}\mathbf{WJ}+\lambda\mathbf{J})\mathbf{h_{LM}} = \mathbf{J}^{\mathrm{T}}\mathbf{W}(\mathbf{y}-\hat{\mathbf{y}})$$

where large values of λ result in a gradient descent update while small values result in a Gauss-Newton update. At large distances from the function minimum, large values for λ are used and smaller values are used as the minimum is approached (Gavin, 2013) and the following update relationship was used (Marquardt, 1963):

$$\left(\mathbf{J}^{\mathrm{T}}\mathbf{W}\mathbf{J} + \lambda \cdot \mathrm{diag}(\mathbf{J}^{\mathrm{T}}\mathbf{W}\mathbf{J})\right)\mathbf{h_{LM}} = \mathbf{J}^{\mathrm{T}}\mathbf{W}(\mathbf{y} - \hat{\mathbf{y}})$$

For the numerical implementation of the Levenberg-Marquardt method, the following metric was defined (Nielsen, 1999):

$$\rho_i(\mathbf{h}) = \frac{\left(\chi^2(\mathbf{p}) - \chi^2(\mathbf{p}+\mathbf{h})\right)}{\left(2\mathbf{h}^{\mathrm{T}}\left(\lambda_i\mathbf{h} + \mathbf{J}^{\mathrm{T}}\mathbf{W}(\mathbf{y} - \hat{\mathbf{y}}(\mathbf{p}))\right)\right)}$$

At iteration i, the step $\mathbf{h}$ was evaluated by comparing $\chi^2(\mathbf{p})$ to $\chi^2(\mathbf{p}+\mathbf{h})$. If ρ_i is greater than a threshold, ε, (a value of 0.1 was used in this project), then $\mathbf{p}+\mathbf{h}$ is better than $\mathbf{p}$ and therefore $\mathbf{p}$ is replaced by $\mathbf{p}+\mathbf{h}$. λ is then reduced by a factor of 0.1 otherwise λ is increased by the same factor if $\mathbf{p}+\mathbf{h}$ is not better than $\mathbf{p}$ and the algorithm proceeds to the next iteration until the chi-squared error is minimised.

APPENDIX C

The LSQR Algorithm

The LSQR method uses the Golub and Kahan algorithm (Golub & Kahan, 1965) to reduce **M** to lower bidiagonal form as follows:

$$\beta_1 u_1 = \mathbf{f}$$

$$\alpha_1 v_1 = \mathbf{M}^T u_1$$

$$i = 1, 2, \ldots \begin{cases} \beta_{i+1} u_{i+1} = \mathbf{M} v_i - \alpha_i u_i \\ \alpha_{i+1} v_{i+1} = \mathbf{M}^T u_{i+1} - \beta_{i+1} v_i \end{cases}$$

where u and v are elements of vectors $u_1, u_2, \ldots, u_k$ and $v_1, v_2, \ldots, v_k$ that are orthonormal basis of the Kyrolov subspaces where k is the number of steps in the bidiagonalisation process. The scalars α_i and β_i are chosen so that vector norms $\|u_i\|_2$ and $\|v_i\|_2$ are equal to 1. Bidiagonalisation is carried out in each iteration. The LSQR algorithm can be summarised as follows (Peng, 2010):

1. Initialisation: $\mathbf{x}_0 = 0$; $\beta_1 u_1 = \mathbf{f}$; $\alpha_1 v_1 = \mathbf{M}^T u_1$; $w_1 = v_1$; $\overline{\phi_1} = \beta_1$; $\overline{\rho_1} = \alpha_1$;
2. For i = 1, 2, …, repeat the following steps until convergence is reached:
   a. $\beta_{i+1} u_{i+1} = \mathbf{M} v_i - \alpha_i u_i$
   b. $\alpha_{i+1} v_{i+1} = \mathbf{M}^T u_{i+1} - \beta_{i+1} v_i$
   c. $\rho_i = \sqrt{\overline{\rho_i}^2 + \beta_{i+1}^2}$
   d. $c_i = \overline{\rho_i}/\rho_i$
   e. $s_i = \beta_{i+1}/\rho_i$
   f. $\theta_{i+1} = s_i \alpha_{i+1}$
   g. $\overline{\rho_{i+1}} = -c_i \alpha_{i+1}$
   h. $\phi_i = c_i \overline{\phi_i}$
   i. $\phi_{i+1} = s_i \overline{\phi_i}$
   j. $\mathbf{x}_i = \mathbf{x}_{i-1} + (\phi_i/\rho_i) w_i$
   k. $w_{i+1} = v_{i+1} - (\phi_{i+1}/\rho_i) w_i$
   l. Check for stopping criteria and repeat steps *a* – *k* if criteria has not been met.

The stopping criteria employed in this project was (Peng, 2010):

$$\|\mathbf{f} - \mathbf{M}\mathbf{x}_i\| = \phi_{i+1} \quad \mathbf{7.36}$$

REFERENCES

Abu-Gharbieh, R., Hamarneh, G., Gustavsson, T., Hamarneh, G. & Gustavsson, T. 1998, "Review - Active Shape Models - Part II: Image Search and Classification", *Proceedings of Swedish Symposium on Image Analysis*, pp. 129.

Adams, J.E. 1997, "Single and dual energy X-ray absorptiometry", *European radiology,* vol. 7 Suppl 2, pp. S20-31.

Adams, J.E. 2013, "Dual-Energy X-Ray Absorptiometry" in *Osteoporosis and Bone Densitometry Measurements*, ed. G. Guglielmi, Springer Berlin Heidelberg, pp. 101-122.

Alioglu, K., Dogu, B., Sirzai, H., Yilmaz, F. & Kuran, B. 2013, "Hand bone mineral density reference values in a Turkish healthy female population", *International journal of rheumatic diseases*.

Alsleem, H. & Davidson, R. 2012, "Quality parameters and assessment methods of digital radiography images", *Radiographer,* vol. 59, no. 2, pp. 46.

Augat, P. & Schorlemmer, S. 2006, "The role of cortical bone and its microstructure in bone strength", *Age and Ageing,* vol. 35, no. suppl 2, pp. ii27-ii31.

Bach-Mortensen, P., Hyldstrup, L., Appleyard, M., Hindso, K., Gebuhr, P. & Sonne-Holm, S. 2006, "Digital x-ray radiogrammetry identifies women at risk of osteoporotic fracture: results from a prospective study", *Calcified tissue international,* vol. 79, no. 1, pp. 1-6.

Bäck, T. 1996, "Evolution strategies: An alternative evolutionary algorithm", *Artificial Evolution: Lecture Notes in Computer Science,* vol. 1063, pp. 1-20.

Barnett, E. & Nordin, B.E. 1960, "The radiological diagnosis of osteoporosis: a new approach", *Clinical radiology,* vol. 11, pp. 166-174.

Bi, X., Berman, M., Al-Dayeh, L. & McLaughlin, J. 2006, *Methods and systems for analyzing bone conditions using mammography device*, 382/128 edn, G06K 9/00, CA, USA.

Björck, A. 1996, *Numerical methods for least squares problems,* Society for industrial and applied mathematics., Philadelphia, USA.

Black, D.M., Thompson, D.E., Bauer, D.C., Ensrud, K., Musliner, T., Hochberg, M.C., Nevitt, M.C., Suryawanshi, S., Cummings, S.R. & for the FIT research group 2000, "Fracture Risk Reduction with Alendronate in Women with Osteoporosis: The Fracture Intervention Trial", *Journal of Clinical Endocrinology & Metabolism,* vol. 85, no. 11, pp. 4118-4124.

Blake, G.M. 1996, "Replacing DXA scanners: cross-calibration with phantoms may be misleading", *Calcified tissue international,* vol. 59, no. 1, pp. 1-5.

Blake, G.M., McKeeney, D.B., Chhaya, S.C., Ryan, P.J. & Fogelman, I. 1992, "Dual energy x-ray absorptiometry: the effects of beam hardening on bone density measurements", *Medical physics,* vol. 19, no. 2, pp. 459-465.

Blake, G.M., Chinn, D.J., Steel, S.A., Patel, R., Panayiotou, E., Thorpe, J., Fordham, J.N. & National Osteoporosis Society Bone Densitometry Forum 2005a, "A list of device-specific thresholds for the clinical interpretation of peripheral x-ray absorptiometry examinations", *Osteoporosis International,* vol. 16, no. 12, pp. 2149-2156.

Blake, G.M., Knapp, K.M. & Fogelman, I. 2005b, "Dual X-ray Absorptiometry: Clinical evaluation of a new cone-beam system", *Calcified tissue international,* vol. 76, no. 2, pp. 113-120.

Blake, G.M. & Fogelman, I. 2010, "An Update on Dual-Energy X-Ray Absorptiometry", *Seminars in nuclear medicine,* vol. 40, no. 1, pp. 62-73.

Blake, G.M. & Fogelman, I. 1997, "Technical principles of dual energy X-ray absorptiometry", *Seminars in nuclear medicine,* vol. 27, no. 3, pp. 210-228.

Bland, J.M. & Altman, D.G. 1986, "Statistical methods for assessing agreement between two methods of clinical measurement", *Lancet,* vol. 1, no. 8476, pp. 307-310.

Boehm, H.F. & Link, T.M. 2004, "Bone imaging: traditional techniques and their interpretation", *Current osteoporosis reports,* vol. 2, no. 2, pp. 41-46.

Bolotin, H.H., Sievanen, H., Grashuis, J.L., Kuiper, J.W. & Jarvinen, T.L. 2001, "Inaccuracies inherent in patient-specific dual-energy X-ray absorptiometry bone mineral density measurements: comprehensive phantom-based evaluation", *Journal of bone and mineral research,* vol. 16, no. 2, pp. 417-426.

Boone, J.M. 2000, "X-ray production, interaction and detection in diagnostic imaging" in *Handbook of medical imaging Volume 1. Physics and Psychophysics*, ed. Beutel J., Kundel H.L., Van Metter R.L., 1st edn, SPIE, Washington, USA, pp. 3-81.

Boone, J.M. & Seibert, J.A. 1997, "An accurate method for computer-generating tungsten anode x-ray spectra from 30 to 140 kV", *Medical physics,* vol. 24, no. 11, pp. 1661-1670.

Bouxsein, M.L., Michaeli, D.A., Plass, D.B., Schick, D.A. & Melton, M.E. 1997, "Precision and Accuracy of Computed Digital Absorptiometry for Assessment of Bone Density of the Hand", *Osteoporosis International,* vol. 7, no. 5, pp. 444-449.

Bouxsein, M.L., Palermo, L., Yeung, C. & Black, D.M. 2002, "Digital X-ray radiogrammetry predicts hip, wrist and vertebral fracture risk in elderly women: a prospective analysis from the study of osteoporotic fractures", *Osteoporosis International,* vol. 13, no. 5, pp. 358-365.

Brigger, P., Hoeg, J. & Unser, M. 2000, "B-spline snakes: a flexible tool for parametric contour detection", *Image Processing, IEEE Transactions on,* vol. 9, no. 9, pp. 1484-1496.

Brismar, T.B., Hindmarsh, T. & Ringertz, H. 1997, "Experimental correlation between T2* and ultimate compressive strength in lumbar porcine vertebrae", *Academic Radiology,* vol. 4, no. 6, pp. 426-430.

Buch, I., Oturai, P.S. & Jensen, L.T. 2010, "Radiographic absorptiometry for pre-screening of osteoporosis in patients with low energy fractures", *Scandinavian Journal of Clinical and Laboratory Investigation,* vol. 70, no. 4, pp. 269-274.

Cameron, J.R., Mazess, R.B. & Sorenson, J.A. 1968, "Precision and accuracy of bone mineral determination by direct photon absorptiometry", *Investigative radiology,* vol. 3, no. 3, pp. 141-150.

Cameron, J.R. & Sorenson, J. 1963, "Measurement of Bone Mineral in vivo: An Improved Method", *Science,* vol. 142, no. 3589, pp. 230-232.

Canny, J. 1986, "A Computational Approach to Edge Detection", *Pattern Analysis and Machine Intelligence, IEEE Transactions on,* vol. PAMI-8, no. 6, pp. 679-698.

Cardinal, H.N. & Fenster, A. 1990, "An accurate method for direct dual-energy calibration and decomposition", *Medical physics,* vol. 17, no. 3, pp. 327-341.

Carter, D.R. & Spengler, D.M. 1978, "Mechanical properties and composition of cortical bone", *Clinical orthopaedics and related research,* vol. (135), no. 135, pp. 192-217.

Case, D.T. & Heilman, J. 2006, "New siding techniques for the manual phalanges: a blind test", *International Journal of Osteoarchaeology,* vol. 16, no. 4, pp. 338-346.

Chalker, B., Barnes, D. & Isdale, P. 1985, "Calibration of x-ray densitometry for the measurement of coral skeletal density", *Coral Reefs,* no. 2, pp. 95-100.

Chang, C.H., Hsieh, C.W., Jong, T.L. & Tiu, C.M. 2003, "A Fully Automatic Computerized Bone Age Assessment Procedure Based On Phalange Ossification Analysis", *16th IPPR Conference on Computer Vision, Graphics and Image Processing*, pp. 463.

Cheng, S.N., Chan, H.P., Niklason, L.T. & Adler, R.S. 1994, "Automated segmentation of regions of interest on hand radiographs", *Medical physics,* vol. 21, no. 8, pp. 1293-1300.

Chuaychunu, N., Pititheerapab, Y., Chanwimalueang, T., Lertprasert, P. & Pintavirooj, C. 2007, "Bone mineral density and bone mineral content estimation using low-cost x-ray detector", *Information, Communications & Signal Processing, 2007 6th International Conference on*, pp. 1-4.

Chui, H. & Rangarajan, A. 2003, "A New Point Matching Algorithm for Non-rigid Registration", *Comput.Vis.Image Underst.,* vol. 89, no. 2-3, pp. 114-141.

Chun, K.J. 2011, "Bone Densitometry", *Seminars in nuclear medicine,* vol. 41, no. 3, pp. 220-228.

CIRS 2014, Available: http://www.cirsinc.com/ [2014, 01/29].

Clarke, B. 2008, "Normal bone anatomy and physiology", *Clinical journal of the American Society of Nephrology : CJASN,* vol. 3 Suppl 3, pp. S131-9.

Clowes, J.A., Peel, N.F. & Eastell, R. 2006, "Device-specific thresholds to diagnose osteoporosis at the proximal femur: an approach to interpreting peripheral bone measurements in clinical practice", *Osteoporosis International,* vol. 17, no. 9, pp. 1293-1302.

Cohen, L.D. 1991, "On active contour models and balloons", *CVGIP: Image Understanding,* vol. 53, no. 2, pp. 211-218.

Colbert, C., Spruit, J.J. & Davila, L.R. 1967, "Biophysical properties of bone: determining mineral concentration from the x-ray image", *Transactions of the New York Academy of Sciences,* vol. 30, no. 2, pp. 271-290.

Cole-Rhodes, A.A. & Varshney, P.K. 2011, "Image registration using mutual information." in *Image registration for remote sensing*, eds. J. Le Moigne, N.S. Netanyahu & R.D. Eastman, Cambridge University Press, Cambridge, UK, pp. 131-149.

CompuMed Inc.USA 2004, *Osteoporosis Diagnostics*. Available: http://compumedinc.com/solutions/osteoporosis-diagnostics/ [2014, July 8].

Cootes, T.F. 2000, "Model-Based Methods in Analysis of Biomedical Images" in *Image Processing and Analysis*, eds. R. Baldock & J. Graham, Oxford University Press, pp. 223-248.

Cootes, T.F., Hill, A., Taylor, C.J. & Haslam, J. 1993, "The use of active shape models for locating structures in medical images", vol. 687, pp. 33-47.

Cootes, T.F., Taylor, C.J., Cooper, D.H. & Graham, J. 1995, "Active Shape Models-Their Training and Application", *Computer Vision and Image Understanding,* vol. 61, no. 1, pp. 38-59.

Cootes, T.F., Taylor, C.J. & Lanitis, A. 1994, "Active Shape Models: Evaluation of a Multi-Resolution Method for Improving Image Search", *British Machine Vision Conference*, pp. 327.

Cosman, F., Herrington, B., Himmelstein, S. & Lindsay, R. 1991, "Radiographic absorptiometry: A simple method for determination of bone mass", *Osteoporosis International,* vol. 2, no. 1, pp. 34-38.

Crabtree, N.J., Kroger, H., Martin, A., Pols, H.A., Lorenc, R., Nijs, J., Stepan, J.J., Falch, J.A., Miazgowski, T., Grazio, S., Raptou, P., Adams, J., Collings, A., Khaw, K.T., Rushton, N., Lunt, M., Dixon, A.K. & Reeve, J. 2002, "Improving risk assessment: hip geometry, bone mineral distribution and bone strength in hip fracture cases and controls. The EPOS study. European Prospective Osteoporosis Study", *Osteoporosis international,* vol. 13, no. 1, pp. 48-54.

D'Elia, G., Caracchini, G., Cavalli, L. & Innocentia, P. 2009, "Bone fragility and imaging techniques.", *Clinical Cases in Mineral and Bone Metabolism,* vol. 6, no. 3, pp. 234-246.

Damilakis, J., Maris, T.G. & Karantanas, A.H. 2007, "An update on the assessment of osteoporosis using radiologic techniques", *European radiology,* vol. 17, no. 6, pp. 1591-1602.

Dawson, S.P. 2009, *Digital X-ray analysis for monitoring fracture healing*, Doctoral thesis, University of Edinburgh, Scotland.

Dendere R. 2009, *Segmentation of candidate bacillus objects in images of ziehl-neelsen-stained sputum smears using deformable models*, MSc thesis, University of Cape Town.

Deych, R. 2007, *Dual energy X-ray detector*, 250/370.11 edn, G01T 1/20, United States.

Dhainaut, A., Rohde, G., Hoff, M., Syversen, U. & Haugeberg, G. 2011, "Phalangeal densitometry compared with dual energy X-ray absorptiometry for assessment of bone mineral density in elderly women",*Journal of women's health,* vol. 20, no. 12, pp. 1789-1795.

Dhainaut, A., Rohde, G.E., Syversen, U., Johnsen, V. & Haugeberg, G. 2010, "The ability of hand digital X-ray radiogrammetry to identify middle-aged and elderly women with reduced bone density, as assessed by femoral neck dual-energy X-ray absorptiometry", *Journal of clinical densitometry,* vol. 13, no. 4, pp. 418-425.

Dotmed 2014, *Hologic Discovery Bone Densitometer.* Available: http://www.dotmed.com/virtual-trade-show/category/Bone-Densitometer/Bone-Densitometer/Models/Hologic/Discovery/15693 [2014, 02/06].

Drinka, P.J., DeSmet, A.A., Bauwens, S.F. & Rogot, A. 1992, "The effect of overlying calcification on lumbar bone densitometry", *Calcified tissue international,* vol. 50, no. 6, pp. 507-510.

Duboeuf, F., Hans, D., Schott, A.M., Kotzki, P.O., Favier, F., Marcelli, C., Meunier, P.J. & Delmas, P.D. 1997, "Different morphometric and densitometric parameters predict cervical and

trochanteric hip fracture: the EPIDOS Study", *Journal of bone and mineral research,* vol. 12, no. 11, pp. 1895-1902.

El Maghraoui, A. & Roux, C. 2008, "DXA scanning in clinical practice", *QJM,* vol. 101, no. 8, pp. 605-617.

El-Baz, A., Acharya, R., Laine, A. & Suri, J. (eds) 2011, *Medical Image Registration*, 2nd edn, Springer Science+Business Media, LLC, New York.

Fink, H.A., Ewing, S.K., Ensrud, K.E., Barrett-Connor, E., Taylor, B.C., Cauley, J.A. & Orwoll, E.S. 2006, "Association of testosterone and estradiol deficiency with osteoporosis and rapid bone loss in older men", *The Journal of clinical endocrinology and metabolism,* vol. 91, no. 10, pp. 3908-3915.

Fiter, J., Nolla, J.M., Gómez-Vaquero, C., Martínez-Aguilá, D., Valverde, J. & Roig-Escofet, D. 2001, "A Comparative Study of Computed Digital Absorptiometry and Conventional Dual-Energy X-ray Absorptiometry in Postmenopausal Women", *Osteoporosis International,* vol. 12, no. 7, pp. 565-569.

Flash, G. 2002, *Lodox DEXA - Feasibility Report*, Lodox Systems, Cape Town, South Africa.

Fleming, R.H., McCormack, H.A. & Whitehead, C.C. 2000, "Prediction of Breaking Strength in Osteoporotic Avian Bone Using Digitized Fluoroscopy, a Low Cost Radiographic Technique", *Calcified tissue international,* vol. 67, no. 4, pp. 309-313.

FRAX-WHO 2009, *FRAX WHO Fracture Risk Assessment Tool*. Available: http://www.who-frax.org/ [2013, 12/07].

Friis-Holmberg, T., Brixen, K., Rubin, K.H., Gronbaek, M. & Bech, M. 2012, "Phalangeal bone mineral density predicts incident fractures: a prospective cohort study on men and women--results from the Danish Health Examination Survey 2007-2008 (DANHES 2007-2008)", *Archives of osteoporosis,* vol. 7, no. 1-2, pp. 291-299.

Friis-Holmberg, T., Rubin, K.H., Brixen, K., Tolstrup, J.S. & Bech, M. 2014, "Fracture risk prediction using phalangeal bone mineral density or FRAX?-A Danish cohort study on men and women", *Journal of clinical densitometry,* vol. 17, no. 1, pp. 7-15.

Gagnon, D.R., McLean, R.R., Hannan, M.T., Cupples, L.A., Hogan, M. & Kiel, D.P. 2010, "Cross-calibration and comparison of variability in 2 bone densitometers in a research setting: the framingham experience",*Journal of clinical densitometry,* vol. 13, no. 2, pp. 210-218.

Gao, Z., Gu, B. & Lin, J. 2008, "Monomodal image registration using mutual information based methods", *Image and Vision Computing,* vol. 26, no. 2, pp. 164-173.

Garcia-Molla, R., Linares, R. & Ayala, R. 2010, "Study of DQE dependence with beam quality on GE essential mammography flat panel", *Journal of applied clinical medical physics / American College of Medical Physics,* vol. 12, no. 1, pp. 3176.

Garn, S.M. 1962, "An annotated bibliography on bone densitometry", *The American Journal of Clinical Nutrition,* vol. 10, pp. 59-67.

Gavin, H.P. 2013, "The Levenberg-Marquardt method for nonlinear least squares curve-fitting problems"

Genant, H.K., Engelke, K., Fuerst, T., Glüer, C.C., Grampp, S., Harris, S.T., Jergas, M., Lang, T., Lu, Y., Majumdar, S., Mathur, A. & Takada, M. 1996, "Noninvasive assessment of bone mineral and structure: state of the art", *Journal of bone and mineral research,* vol. 11, no. 6, pp. 707-730.

Genton, L., Hans, D., Kyle, U.G. & Pichard, C. 2002, "Dual-energy X-ray absorptiometry and body composition: differences between devices and comparison with reference methods", *Nutrition (Burbank, Los Angeles County, Calif.),* vol. 18, no. 1, pp. 66-70.

Gillette-Guyonnet, S., Andrieu, S., Nourhashemi, F., Cantet, C., Grandjean, H. & Vellas, B. 2003, "Comparison of bone mineral density and body composition measurements in women obtained from two DXA instruments", *Mechanisms of ageing and development,* vol. 124, no. 3, pp. 317-321.

Gingold, E.L. & Hasegawa, B.H. 1992, "Systematic bias in basis material decomposition applied to quantitative dual-energy x-ray imaging", *Medical physics,* vol. 19, no. 1, pp. 25-33.

Gingold, E.L. & Hasegawa, B.H. 1990, "Dual-energy X-ray Processing for Quantitative Projection Imaging", *Nuclear Science Symposium, 1990. Conference record: Including Sessions on Nuclear Power Systems and Medical Imaging Conference, 1990 IEEE*, pp. 1147.

Glüer, C.C., Faulkner, K.G., Estilo, M.J., Engelke, K., Rosin, J. & Genant, H.K. 1993, "Quality assurance for bone densitometry research studies: concept and impact", *Osteoporosis international,* vol. 3, no. 5, pp. 227-235.

Gluer, C.C., Blake, G., Lu, Y., Blunt, B.A., Jergas, M. & Genant, H.K. 1995, "Accurate assessment of precision errors: how to measure the reproducibility of bone densitometry techniques", *Osteoporosis international,* vol. 5, no. 4, pp. 262-270.

Glüer, C.C., Jergas, M. & Hans, D. 1997, "Peripheral measurement techniques for the assessment of osteoporosis", *Seminars in nuclear medicine,* vol. 27, no. 3, pp. 229-247.

Gogos, K.A., Yakoumakis, E.N., Tsalafoutas, I.A. & Makri, T.K. 2003, "Radiation dose considerations in common paediatric X-ray examinations", *Pediatric radiology,* vol. 33, no. 4, pp. 236-240.

Goldman, L.W. 2007, "Principles of CT: radiation dose and image quality", *Journal of nuclear medicine technology,* vol. 35, no. 4, pp. 213-25; quiz 226-8.

Golub, G. & Kahan, W. 1965, "Calculating the Singular Values and Pseudo-Inverse of a Matrix", *Journal of the Society for Industrial and Applied Mathematics: Series B, Numerical Analysis,* vol. 2, no. 2, pp. 205-224.

Gonzalez, R.C. & Woods, R.E. 2002, *Digital Image Processing.* Prentice-Hall, New Jersey, USA.

Goshtasby, A.A. 2005, *2-D and 3-D Image Registration: for Medical, Remote Sensing, and Industrial Applications,* Wiley-Interscience.

Griffiths, M.R., Noakes, K.A. & Pocock, N.A. 1997, "Correcting the Magnification Error of Fan Beam Densitometers", *Journal of Bone and Mineral Research,* vol. 12, no. 1, pp. 119-123.

Gulam, M., Thornton, M.M., Hodsman, A.B. & Holdsworth, D.W. 2000, "Bone mineral measurement of phalanges: comparison of radiographic absorptiometry and area dual X-ray absorptiometry", *Radiology,* vol. 216, no. 2, pp. 586-591.

Hagiwara, S., Engelke, K., Yang, S.O., Dhillon, M.S., Guglielmi, G., Nelson, D.L. & Genant, H.K. 1994, "Dual x-ray absorptiometry forearm software: accuracy and intermachine relationship", *Journal of bone and mineral research,* vol. 9, no. 9, pp. 1425-1427.

Haidekker, M.A., Stevens, H.Y. & Frangos, J.A. 2004, "Computerized methods for X-ray-based small bone densitometry", *Computer methods and programs in biomedicine,* vol. 73, no. 1, pp. 35-42.

Hajnal, J.V., Hawkes, D. & Hill, D. (eds) 2001, *Medical Image Registration, Biomedical engineering series*, CRC Press LLC, New York.

Hakulinen, M.A., Saarakkala, S., Toyras, J., Kroger, H. & Jurvelin, J.S. 2003, "Dual energy x-ray laser measurement of calcaneal bone mineral density", *Physics in Medicine and Biology,* vol. 48, no. 12, pp. 1741-1752.

Hamarneh, G., Abu-Gharbieh, R., Gustavsson, T., Abu-gharbieh, R. & Gustavsson, T. 1998, "Review - Active Shape Models - Part I: Modeling Shape and Gray Level Variations. ", *Proceedings of Swedish Symposium on Image Analysis*, pp. 125.

Han, C., Lee, C. & Peng, W. 2007, "Hand radiograph image segmentation using a coarse-to-fine strategy", *Pattern Recognition,* vol. 40, no. 11, pp. 2994-3004.

Han, X., Xu, C. & Prince, J.L. 2003, "A topology preserving level set method for geometric deformable models", *Pattern Analysis and Machine Intelligence, IEEE Transactions on,* vol. 25, no. 6, pp. 755-768.

Hans, D.B., Shepherd, J.A., Schwartz, E.N., Reid, D.M., Blake, G.M., Fordham, J.N., Fuerst, T., Hadji, P., Itabashi, A., Krieg, M.A. & Lewiecki, E.M. 2008, "Peripheral dual-energy X-ray absorptiometry in the management of osteoporosis: the 2007 ISCD Official Positions", *Journal of clinical densitometry,* vol. 11, no. 1, pp. 188-206.

Hans, D. & Krieg, M.A. 2009, "Quantitative ultrasound for the detection and management of osteoporosis", *Salud publica de Mexico,* vol. 51 Suppl 1, pp. S25-37.

Hansen, S.J., Nielsen, M.M., Ryg, J., Wraae, K., Andersen, M. & Brixen, K. 2009, "Radiographic absorptiometry as a screening tool in male osteoporosis: results from the Odense Androgen Study", *Acta Radiologica (Stockholm, Sweden : 1987),* vol. 50, no. 6, pp. 658-663.

Heilmann, P., Wuster, C., Prolingheuer, C., Gotz, M. & Ziegler, R. 1998, "Measurement of forearm bone mineral density: comparison of precision of five different instruments", *Calcified tissue international,* vol. 62, no. 5, pp. 383-387.

Hobert, K.J., Bogucki, T.M. & Menhardt, W. 2006, *Bone density screening and mammography CAD system*, 382/132 edn, G06K 9/00, NY, USA.

Holdsworth, D.W., Thornton, M.M., Drost, D., Watson, P.H., Fraher, L.J. & Hodsman, A.B. 2000, "Rapid small-animal dual-energy X-ray absorptiometry using digital radiography", *Journal of bone and mineral research : the official journal of the American Society for Bone and Mineral Research,* vol. 15, no. 12, pp. 2451-2457.

Huda, W. 2010, *Review of radiologic physics,* Third Editon edn, Lippincott Williams & Wilkins, Philadelphia.

Huo, Z., Yang, C.Y. & Purdum, M.S. 2010, *Bone mineral density assessment using mammography system*, G01N 23/087 edn, 378/54, NY, USA.

Huttenlocher, D.P., Klanderman, G.A. & Rucklidge, W.J. 1993, "Comparing images using the Hausdorff distance", *Pattern Analysis and Machine Intelligence, IEEE Transactions on,* vol. 15, no. 9, pp. 850-863.

Illers, H., Buhr, E. & Hoeschen, C. 2005, "Measurement of the detective quantum efficiency (DQE) of digital X-ray detectors according to the novel standard IEC 62220-1", *Radiation Protection Dosimetry,* vol. 114, no. 1-3, pp. 39-44.

International Electrotechnical Commission 2003, "Medical electrical equipment - characteristics of digital x-ray imaging devices: Part 1. Determination of the detective quantum efficiency. IEC 62220-1."

International Society for Clinical Densitometry (ISCD) 2013, *2013 ISCD Official Positions – Adult*. Available: http://www.iscd.org/official-positions/2013-iscd-official-positions-adult/ [2014, 01/26].

International Society for Clinical Densitometry (ISCD) 2006. Available: http://www.iscd.org/resources/calculators/ [2014, 07/19].

Irving, B.J., Maree, G.J., Hering, E.R. & Douglas, T.S. 2008, "Radiation dose from a linear slit scanning X-ray machine with full-body imaging capabilities", *Radiation Protection Dosimetry,* vol. 130, no. 4, pp. 482-489.

Ito, M., Hayashi, K., Yamada, M., Uetani, M. & Nakamura, T. 1993, "Relationship of osteophytes to bone mineral density and spinal fracture in men", *Radiology,* vol. 189, no. 2, pp. 497-502.

Jacob, M., Blu, T. & Unser, M. 2004, "Efficient energies and algorithms for parametric snakes", *Image Processing, IEEE Transactions on,* vol. 13, no. 9, pp. 1231-1244.

Jones, C.D., Laval-Jeantet, A.M., Laval-Jeantet, M.H. & Genant, H.K. 1987, "Importance of measurement of spongious vertebral bone mineral density in the assessment of osteoporosis", *Bone,* vol. 8, no. 4, pp. 201-206.

Kalender, W.A., Felsenberg, D., Genant, H.K., Fischer, M., Dequeker, J. & Reeve, J. 1995, "The European Spine Phantom--a tool for standardization and quality control in spinal bone mineral measurements by DXA and QCT", *European Journal of Radiology,* vol. 20, no. 2, pp. 83-92.

Kanis, J.A. 1994, "Assessment of fracture risk and its application to screening for postmenopausal osteoporosis: synopsis of a WHO report. WHO Study Group", *Osteoporosis international,* vol. 4, no. 6, pp. 368-381.

Kanis, J.A. & Glüer, C.C. 2000, "An update on the diagnosis and assessment of osteoporosis with densitometry. Committee of Scientific Advisors, International Osteoporosis Foundation", *Osteoporosis international,* vol. 11, no. 3, pp. 192-202.

Kanis, J.A., McCloskey, E.V., Johansson, H., Cooper, C., Rizzoli, R. & Reginster, J.Y. 2013, "European guidance for the diagnosis and management of osteoporosis in postmenopausal women", *Osteoporosis international,* vol. 24, no. 1, pp. 23-57.

Kass, M., Witkin, A. & Terzopoulos, D. 1988, "Snakes: Active contour models", *International Journal of Computer Vision*, no. 4, pp. 321-331.

Kauffman, J.A., Slump, C.H. & Moens, H.J.B. 2004, "Segmentation of Radiographs of Hands with Joint Damage Using Customized Active Appearance Models", *15th Annual Workshop on Circuits, Systems and Signal Processing*, pp. 261.

Keim, A.R., Comley, D. & Singer, J. 2014, *Bone mineral density measurement apparatus and method*, Google Patents.

Kelly, T.L., Crane, G. & Baran, D.T. 1994, "Single X-ray absorptiometry of the forearm: precision, correlation, and reference data", *Calcified tissue international,* vol. 54, no. 3, pp. 212-218.

Khutlang, R., Krishnan, S., Dendere, R., Whitelaw, A., Veropoulos, K., Learmonth, G. & Douglas, T.S. 2010, "Classification of *Mycobacterium tuberculosis* in Images of ZN-Stained Sputum Smears", *Information Technology in Biomedicine, IEEE Transactions on,* vol. 14, no. 4, pp. 949-957.

Kiel, D.P., Mercier, C.A., Dawson-Hughes, B., Cali, C., Hannan, M.T. & Anderson, J.J. 1995, "The effects of analytic software and scan analysis technique on the comparison of dual X-ray absorptiometry with dual photon absorptiometry of the hip in the elderly", *Journal of bone and mineral research,* vol. 10, no. 7, pp. 1130-1136.

Kim, S.K., Yoo, T.K., Oh, E. & Kim, D.W. 2013, "Osteoporosis risk prediction using machine learning and conventional methods", *Annual International Conference of the IEEE Engineering in Medicine and Biology Society.IEEE Engineering in Medicine and Biology Society.Conference,* vol. 2013, pp. 188-191.

Kleerekoper, M., Nelson, D.A., Flynn, M.J., Pawluszka, A.S., Jacobsen, G. & Peterson, E.L. 1994, "Comparison of radiographic absorptiometry with dual-energy x-ray absorptiometry and quantitative computed tomography in normal older white and black women", *Journal of bone and mineral research : the official journal of the American Society for Bone and Mineral Research,* vol. 9, no. 11, pp. 1745-1749.

Kolbeck, S., Bail, H., Weiler, A., Windhagen, H., Haas, N. & Raschke, M. 1999, "Digital radiography. A predictor of regenerate bone stiffness in distraction osteogenesis", *Clinical orthopaedics and related research,* vol. (366), no. 366, pp. 221-228.

Kolta, S., Le Bras, A., Mitton, D., Bousson, V., de Guise, J.A., Fechtenbaum, J., Laredo, J.D., Roux, C. & Skalli, W. 2005, "Three-dimensional X-ray absorptiometry (3D-XA): a method for reconstruction of human bones using a dual X-ray absorptiometry device", *Osteoporosis international,* vol. 16, no. 8, pp. 969-976.

Kose, K., Matsuda, Y., Kurimoto, T., Hashimoto, S., Yamazaki, Y., Haishi, T., Utsuzawa, S., Yoshioka, H., Okada, S., Aoki, M. & Tsuzaki, T. 2004, "Development of a compact MRI system for trabecular bone volume fraction measurements", *Magnetic Resonance in Medicine,* vol. 52, no. 2, pp. 440-444.

Kotzki, P.O., Mariano-Goulart, D. & Rossi, M. 1991, "Theoretical and experimental limits of triple photon energy absorptiometry in the measurement of bone mineral", *Physics in Medicine and Biology,* vol. 36, no. 4, pp. 429-437.

Krassas, G.E. & Papadopoulou, P. 2001, "Oestrogen action on bone cells", *Journal of Musculoskeletal & Neuronal Interactions,* vol. 2, no. 2, pp. 143-151.

Krupinski, E.A., Williams, M.B., Andriole, K., Strauss, K.J., Applegate, K., Wyatt, M., Bjork, S., Seibert, J.A., ACR, AAPM & Society for Imaging Informatics in Medicine 2007, "Digital

radiography image quality: image processing and display", *Journal of the American College of Radiology : JACR,* vol. 4, no. 6, pp. 389-400.

Kwon, J.W., Cho, S.I., Ahn, Y.B. & Ro, Y.M. 2009, "Noise reduction in DEXA image based on system noise modeling", *Biomedical and Pharmaceutical Engineering, 2009. ICBPE '09. International Conference on*, pp. 1-6.

Lai, K.C., Goodsitt, M.M., Murano, R. & Chesnut, C.H.,3rd 1992, "A comparison of two dual-energy X-ray absorptiometry systems for spinal bone mineral measurement", *Calcified tissue international,* vol. 50, no. 3, pp. 203-208.

Lang, S.B. 1969, "Elastic Coefficients of Animal Bone", *Science,* vol. 165, no. 3890, pp. 287-288.

Lang, T. 2004, "Quantitative Computed Tomography" in *The Physical Measurement of Bone*, eds. C.M. Langton & C.F. Njeh, Institute of Physics Publishing, Bristol, UK, pp. 308-318.

Lang, T.F. 2010, "Bone Mineral Assessment of the Axial Skeleton: Technical Aspects" in *Contemporary Endocrinology: Osteoporosis: pathophysiology and clinical management*, ed. R.A. Adler, 2nd edn, Springer, pp. 23-50.

Lang, T.F., Keyak, J.H., Heitz, M.W., Augat, P., Lu, Y., Mathur, A. & Genant, H.K. 1997, "Volumetric quantitative computed tomography of the proximal femur: precision and relation to bone strength", *Bone,* vol. 21, no. 1, pp. 101-108.

Lang, T.F., Li, J., Harris, S.T. & Genant, H.K. 1999, "Assessment of vertebral bone mineral density using volumetric quantitative CT", *Journal of computer assisted tomography,* vol. 23, no. 1, pp. 130-137.

Langton, C.M., Pisharody, S. & Keyak, J.H. 2009, "Generation of a 3D proximal femur shape from a single projection 2D radiographic image", *Osteoporosis international,* vol. 20, no. 3, pp. 455-461.

Lehmann, L., Alvarez, R., Macovski, A., Brody, W., Pelc, N., Riederer, S. & Hall, A. 1981, "Generalized image combinations in dual kVp digital radiography", *Medical physics,* vol. 8, no. 5, pp. 659-667.

Lekamwasam, S., Rodrigo, M., de Silva, K.I. & Munidasa, D. 2005, "Comparison of phalangeal bone mineral content and density between the dominant and non-dominant sides", *The Ceylon medical journal,* vol. 50, no. 4, pp. 149-151.

Leonard, M.B., Shults, J. & Zemel, B.S. 2006, "DXA estimates of vertebral volumetric bone mineral density in children: potential advantages of paired posteroanterior and lateral scans", *Journal of clinical densitometry : the official journal of the International Society for Clinical Densitometry,* vol. 9, no. 3, pp. 265-273.

Levenberg, K. 1944, "A method for the solution of certain non-linear problems in least squares", *Quarterly Journal of Applied Mathematics,* vol. 2, no. 2, pp. 164-168.

Levitt, T.S., Hedgcock, M.W.,Jr, Dye, J.W., Johnston, S.E., Shadle, V.M. & Vosky, D. 1993, "Bayesian inference for model-based segmentation of computed radiographs of the hand", *Artificial Intelligence in Medicine,* vol. 5, no. 4, pp. 365-387.

Li, C., Liu, J. & Fox, M.D. 2005, "Segmentation of edge preserving gradient vector flow: an approach toward automatically initializing and splitting of snakes", *Computer Vision and Pattern Recognition, 2005. CVPR 2005. IEEE Computer Society Conference on*, pp. 162.

Liberman, U.A., Weiss, S.R., Broll, J., Minne, H.W., Quan, H., Bell, N.H., Rodriguez-Portales, J., Downs, R.W.,Jr, Dequeker, J. & Favus, M. 1995, "Effect of oral alendronate on bone mineral density and the incidence of fractures in postmenopausal osteoporosis. The Alendronate Phase III Osteoporosis Treatment Study Group", *The New England journal of medicine,* vol. 333, no. 22, pp. 1437-1443.

Lin, L.I. 2000, "A Note on the Concordance Correlation Coefficient ", *Biometrics,* vol. 56, pp. 324-325.

Lin, L.I. 1989, "A concordance correlation coefficient to evaluate reproducibility", *Biometrics,* vol. 45, no. 1, pp. 255-268.

Link, T.M., Majumdar, S., Augat, P., Lin, J.C., Newitt, D., Lane, N.E. & Genant, H.K. 1998, "Proximal femur: assessment for osteoporosis with T2* decay characteristics at MR imaging", *Radiology,* vol. 209, no. 2, pp. 531-536.

Lone Oak Medical Technologies 2012, *accuDXA2 Model 7200 User Guide*, Lone Oak Medical Technologies, LLC., USA.

Looker, A.C., Wahner, H.W., Dunn, W.L., Calvo, M.S., Harris, T.B., Heyse, S.P., Johnston, C.C.,Jr & Lindsay, R. 1998, "Updated data on proximal femur bone mineral levels of US adults", *Osteoporosis international,* vol. 8, no. 5, pp. 468-489.

Lotz, J.C., Cheal, E.J. & Hayes, W.C. 1991, "Fracture prediction for the proximal femur using finite element models: Part I--Linear analysis", *Journal of Biomechanical Engineering,* vol. 113, no. 4, pp. 353-360.

Mack, P.B., O'brien, A.T., Smith, J.M. & Bauman, A.W. 1939, "A Method for Estimating the Degree of Mineralization of Bones from Tracings of Roentgenograms", *Science (New York, N.Y.),* vol. 89, no. 2316, pp. 467.

Maes, F., Vandermeulen, D. & Suetens, P. 2003, "Medical image registration using mutual information", *Proceedings of the IEEE,* vol. 91, no. 10, pp. 1699-1722.

Mahmoodi, S., Sharif, B.S., Chester, E.G., Owen, J.P. & Lee, R. 2000, "Skeletal growth estimation using radiographic image processing and analysis", *Information Technology in Biomedicine, IEEE Transactions on,* vol. 4, no. 4, pp. 292-297.

Manos, G.K., Cairns, A.Y., Rickets, I.W. & Sinclair, D. 1994, "Segmenting radiographs of the hand and wrist", *Computer methods and programs in biomedicine,* vol. 43, no. 3-4, pp. 227-237.

Maree, G.J., Irving, B.J. & Hering, E.R. 2007, "Paediatric dose measurement in a full-body digital radiography unit", *Pediatric radiology,* vol. 37, no. 10, pp. 990-997.

Marquardt, D. 1963, "An Algorithm for Least-Squares Estimation of Nonlinear Parameters", *Journal of the Society for Industrial and Applied Mathematics,* vol. 11, no. 2, pp. 431-441.

Mattes, D., Haynor, D.R., Vesselle, H., Lewellyn, T.K. & Eubank, W. 2001, "Nonrigid multimodality image registration", *Proc.SPIE,* vol. 4322, pp. 1609-1620.

Mazess, R., Collick, B., Trempe, J., Barden, H. & Hanson, J. 1989, "Performance evaluation of a dual-energy x-ray bone densitometer", *Calcified tissue international,* vol. 44, no. 3, pp. 228-232.

Mazess, R.B., Trempe, J.A., Bisek, J.P., Hanson, J.A. & Hans, D. 1991, "Calibration of dual-energy x-ray absorptiometry for bone density", *Journal of bone and mineral research,* vol. 6, no. 8, pp. 799-806.

McCalden, R.W., McGeough, J.A., Barker, M.B. & Court-Brown, C.M. 1993, "Age-related changes in the tensile properties of cortical bone. The relative importance of changes in porosity, mineralization, and microstructure", *The Journal of bone and joint surgery.American volume,* vol. 75, no. 8, pp. 1193-1205.

Michaeli, D. 1999, "A New X-Ray Based Osteoporosis Screening Tool Provides Accurate and Precise Assessment of Phalanx Bone Mineral Content", *Journal of clinical densitometry,* vol. 2, no. 1, pp. 23-30.

Miller, P.D., Bonnick, S.L., Rosen, C.J., Altman, R.D., Avioli, L.V., Dequeker, J., Felsenberg, D., Genant, H.K., Gennari, C., Harper, K.D., Hodsman, A.B., Kleerekoper, M., Mautalen, C.A., McClung, M.R., Meunier, P.J., Nelson, D.A., Peel, N.F., Raisz, L.G., Recker, R.R., Utian, W.H., Wasnich, R.D. & Watts, N.B. 1996, "Clinical utility of bone mass measurements in adults: consensus of an international panel. The Society for Clinical Densitometry", *Seminars in arthritis and rheumatism,* vol. 25, no. 6, pp. 361-372.

Miller, P.D., Njeh, C.F., Jankowski, L.G., Lenchik, L. & International Society for Clinical Densitometry Position Development Panel and Scientific Advisory Committee 2002, "What are the standards by which bone mass measurement at peripheral skeletal sites should be used in the diagnosis of osteoporosis?", *Journal of clinical densitometry,* vol. 5 Suppl, pp. S39-45.

Mooney, R. & Thomas, P.S. 1998, "Dose reduction in a paediatric X-ray department following optimization of radiographic technique", *The British journal of radiology,* vol. 71, no. 848, pp. 852-860.

Moreau, M., Dunmore-Buyze, P.J., Holdsworth, D.W. & Fenster, A. 1997a, "X-ray imaging technique for in vitro tissue composition measurements using saline/iodine displacement: Experimental verification", *Medical physics,* vol. 24, no. 3, pp. 351-360.

Moreau, M., Holdsworth, D.W. & Fenster, A. 1997b, "X-ray imaging technique for in vitro tissue composition measurements using saline/iodine displacement: Technique optimization", *Medical physics,* vol. 24, no. 1, pp. 37-49.

Moreau, M., Holdsworth, D.W. & Fenster, A. 1994, "Dual-energy x-ray imaging technique for in vitro tissue composition measurement", *Medical physics,* vol. 21, no. 11, pp. 1807-1815.

Mulder, J.E., Michaeli, D., Flaster, E.R. & Siris, E. 2000, "Comparison of bone mineral density of the phalanges, lumbar spine, hip, and forearm for the assessment of osteoporosis in postmenopausal women",*Journal of clinical densitometry,* vol. 3, no. 4, pp. 373-381.

Nain, D., Haker, S., Bobick, A. & Tannenbaum, A. 2007, "Multiscale 3-D shape representation and segmentation using spherical wavelets", *IEEE Transactions on Medical Imaging,* vol. 26, no. 4, pp. 598-618.

Nalda, E., Mahadea, K.K., Demattei, C., Kotzki, P.O., Pouget, J.P. & Boudousq, V. 2011, "Assessment of the Stratos, a new pencil-beam bone densitometer: dosimetry, precision, and cross calibration", *Journal of clinical densitometry,* vol. 14, no. 4, pp. 395-406.

National Institute of Standards and Technology 2005, *X-ray Form Factor, Attenuation and Scattering Tables*. Available: http://www.nist.gov/pml/data/ffast/ [2013, 09/14].

Navsa, N. 2010, *Skeletal morphology of the human hand as applied in forensic anthropology*, Doctoral thesis, University of Pretoria, South Africa.

Nayak, S., Roberts, M.S. & Greenspan, S.L. 2011, "Cost-effectiveness of different screening strategies for osteoporosis in postmenopausal women", *Annals of Internal Medicine,* vol. 155, no. 11, pp. 751-761.

Neitzel, U., Gunther-Kohfahl, S., Borasi, G. & Samei, E. 2004, "Determination of the detective quantum efficiency of a digital x-ray detector: comparison of three evaluations using a common image data set", *Medical physics,* vol. 31, no. 8, pp. 2205-2211.

Nielsen, H.B. 1999, *Damping parameter in Marquardt's method.*, Department of Mathematical Modelling, Denmark Tehnical University, Denmark.

Niemeijer, M., van Ginneken, B., Maas, C.A., Beek, F.J.A. & Viergever, M.A. 2003, "Assessing the skeletal age from a hand radiograph: automating the Tanner-Whitehouse method ", *PROCEEDINGS- SPIE THE INTERNATIONAL SOCIETY FOR OPTICAL ENGINEERING Image processing; medical imaging,* vol. 5032, pp. 1197-1205.

Njeh, C.F., Fuerst, T., Hans, D., Blake, G.M. & Genant, H.K. 1999, "Radiation exposure in bone mineral density assessment", *Applied Radiation and Isotopes : Including Data, Instrumentation and Methods for use in Agriculture, Industry and Medicine,* vol. 50, no. 1, pp. 215-236.

Njeh, C.F. & Shepherd, J.A. 2004, "Absorptiometric measurement" in *The Physical Measurement of Bone*, eds. C.M. Langton & C.F. Njeh, Institute of Physics Publishing, Bristol, UK, pp. 267-307.

NOFSA 2013, *Making a noise about the silent disease*. Available: http://www.osteoporosis.org.za [2013, November 29].

Ohtsuka, M., Michaeli, D. & Wasnich, R.D. 2002, "Relationship between phalangeal bone density and risk of vertebral fracture", *Journal of clinical densitometry : the official journal of the International Society for Clinical Densitometry,* vol. 5, no. 1, pp. 11-15.

Okunade, A.A. 2007, "Parameters and computer software for the evaluation of mass attenuation and mass energy-absorption coefficients for body tissues and substitutes", *Journal of medical physics,* vol. 32, no. 3, pp. 124-132.

Omsland, T.K., Emaus, N., Gjesdal, C.G., Falch, J.A., Tell, G.S., Forsen, L., Berntsen, G.K. & Meyer, H.E. 2008, "In vivo and in vitro comparison of densitometers in the NOREPOS study", *Journal of clinical densitometry,*vol. 11, no. 2, pp. 276-282.

Orwoll, E.S. & Oviatt, S.K. 1991, "Longitudinal precision of dual-energy X-ray absorptiometry in a multicenter study", *Journal of Bone and Mineral Research,* vol. 6, no. 2, pp. 191-197.

Otsu, N. 1979, "A threshold selection method from gray-level histograms", *IEEE Transactions on Systems, Man and Cybernetics,* vol. 9, no. 1, pp. 62-66.

Paige, C.C. & Saunders, M.A. 1982, "LSQR: An Algorithm for Sparse Linear Equations And Sparse Least Squares", *ACM Trans. Math. Soft.,* vol. 8, pp. 43-71.

Patel, R., Blake, G.M., Fordham, J.N., McCrea, J.D. & Ryan, P.J. 2011, *Peripheral X-ray absorptiometry in the management of osteoporosis*, National Osteoporosis Society.

Patel, R., Blake, G.M., Panayiotou, E. & Fogelman, I. 2010, "Clinical Evaluation of a Phalangeal Bone Mineral Density Assessment System", *Journal of Clinical Densitometry,* vol. 13, no. 3, pp. 292-300.

Peng, Z.Y. 2010, "A matrix LSQR iterative method to solve matrix equation AXB=C", *International Journal of Computer Mathematics,* vol. 87, no. 8, pp. 1820-1830.

Perks, T., Trauernicht, C., Hartley, T., Hobson, C., Lawson, A., Scholtz, P., Dendere, R., Steiner, S. & Douglas, T. 2013, "Effect of aluminium filtration on dose and image quality in paediatric slot-scanning radiography", *Engineering in Medicine and Biology Society (EMBC), 2013 35th Annual International Conference of the IEEE*, pp. 2332-2335.

Phantom Laboratory 2014, *Sectional phantoms*. Available: http://www.phantomlab.com/products/sectional.php [2014, 09/2014].

Picard, D., Brown, J.P., Rosenthall, L., Couturier, M., Lévesque, J., Dumont, M., Ste-Marie, L.-., Tenenhouse, A. & Dodin, S. 2004, "Ability of Peripheral DXA Measurement to Diagnose Osteoporosis As Assessed By Central DXA Measurement", *Journal of Clinical Densitometry,* vol. 7, no. 1, pp. 111-118.

Pietka, E. 1995, "Computer-assisted bone age assessment based on features automatically extracted from a hand radiograph", *Computerized Medical Imaging and Graphics,* vol. 19, no. 3, pp. 251-259.

Pisani, P., Renna, M.D., Conversano, F., Casciaro, E., Muratore, M., Quarta, E., Paola, M.D. & Casciaro, S. 2013, "Screening and early diagnosis of osteoporosis through X-ray and ultrasound based techniques",*World journal of radiology,* vol. 5, no. 11, pp. 398-410.

Pluim, J.P.W., Maintz, J.B.A. & Viergever, M.A. 2003, "Mutual-information-based registration of medical images: a survey", *Medical Imaging, IEEE Transactions on,* vol. 22, no. 8, pp. 986-1004.

Potgieter, J.H., de Villiers, M., Scheelke, M. & de Jager, G. 2005, "An explanation for the extremely low, but variable, radiation dosages measured in a linear slit scanning radiography system", pp. 1138-1145.

Pothuaud, L. & Majumdar, S. 2004, "Magnetic Resonance Imaging" in *The Physical Measurement of Bone*, eds. C.M. Langton & C.F. Njeh, Institute of Physics Publishing, Bristol, UK, pp. 379-411.

Raghunathan, S., Stredney, D., Schmalbrock, P. & Clymer, B.D. 2005, "Image Registration Using Rigid Registration and Maximization of Mutual Information.", *MMVR13. The 13th Annual Medicine Meets Virtual Reality Conference*.

Ralston, S.H. 2005, "Bone densitometry and bone biopsy", *Best practice & research.Clinical rheumatology,* vol. 19, no. 3, pp. 487-501.

Ravn, P., Overgaard, K., Huang, C., Ross, P.D., Green, D. & Mcclung, M. 1996, "Comparison of bone densitometry of the phalanges, distal forearm and axial skeleton in early postmenopausal women participating in the EPIC study", *Osteoporosis International,* vol. 6, no. 4, pp. 308-313.

Reed, M.R., Murray, J.R., Abdy, S.E., Francis, R.M. & McCaskie, A.W. 2004, "The use of digital X-ray radiogrammetry and peripheral dual energy X-ray absorptiometry in patients attending fracture clinic after distal forearm fracture", *Bone,* vol. 34, no. 4, pp. 716-719.

Reid, I.R., Evans, M.C., Ames, R. & Wattie, D.J. 1991, "The influence of osteophytes and aortic calcification on spinal mineral density in postmenopausal women", *The Journal of clinical endocrinology and metabolism,* vol. 72, no. 6, pp. 1372-1374.

Reilly, D.T. & Burstein, A.H. 1974, "The Mechanical Properties of Cortical Bone", *The Journal of Bone & Joint Surgery,* vol. 56, no. 5, pp. 1001-1022.

Remy, F. & Guillot, G. 1998, "Trabecular bone characterization with low-field MRI", *Magnetic resonance imaging,* vol. 16, no. 5-6, pp. 639-642.

Rhodes, L.A., Cooper, W., Oldroyd, B. & Hind, K. 2013, "Cross-calibration of a GE iDXA and Prodigy for Total and Regional Body Bone Parameters: The Importance of Using Cross-calibration Equations for Longitudinal Monitoring After a System Upgrade", *Journal of clinical densitometry*.

Röntgen, W.C. 1896, "On a new kind of ray", *Nature,* vol. 53, pp. 274-276.

Rosen, C.J. 2004, "Anatomy, Physiology and Disease" in *The Physical Measurement of Bone*, eds. C.M. Langton & C.F. Njeh, Institute of Physics Publishing, Bristol, UK, pp. 3-34.

Rosholm, A., Hyldstrup, L., Backsgaard, L., Grunkin, M. & Thodberg, H.H. 2001, "Estimation of bone mineral density by digital X-ray radiogrammetry: theoretical background and clinical testing", *Osteoporosis International,* vol. 12, no. 11, pp. 961-969.

Ross, P. 1997, "Radiographic absorptiometry for measuring bone mass", *Osteoporosis International,* vol. 7, no. 3, pp. 103-107.

Rucci, M., Coppini, G., Nicoletti, I., Cheli, D. & Valli, G. 1995, "Automatic analysis of hand radiographs for the assessment of skeletal age: a subsymbolic approach", *Computers and biomedical research, an international journal,* vol. 28, no. 3, pp. 239-256.

Russakoff, D.B., Tomasi, C., Rohlfing, T. & Maurer, C.R., Jr. 2004, "Image Similarity Using Mutual Information of Regions" in *Computer Vision - ECCV 2004*, eds. T. Pajdla & J. Matas, Springer Berlin Heidelberg, , pp. 596-607.

Ruth, C., Weiss, H.P., Wilson, K.E., Stetten, E.V. & Richardson, T. 2005, *Automatic region of interest locator for AP spinal images and for hip images in bone densitometry.*, 382/132 edn, G06K9/00, United States.

Samei, E., Flynn, M.J. & Reimann, D.A. 1998, "A method for measuring the presampled MTF of digital radiographic systems using an edge test device", *Medical physics,* vol. 25, no. 1, pp. 102-113.

Sectra 2014, *Early prognosis for osteoporosis*. Available: https://www.sectra.com/medical/osteoporosis/ [2014, July 9].

Sas, T.C., de Muinck Keizer-Schrama, S.M., Stijnen, T., van Teunenbroek, A., van Leeuwen, W.J., Asarfi, A., van Rijn, R.R., Drop, S.L. & Dutch Advisory Group on Growth Hormone 2001, "Bone mineral density assessed by phalangeal radiographic absorptiometry before and during

long-term growth hormone treatment in girls with Turner's syndrome participating in a randomized dose-response study", *Pediatric research,* vol. 50, no. 3, pp. 417-422.

Scheelke, M., Potgieter, J.H. & de Villiers, M. 2005, "System characterization of the STATSCAN full body slit scanning radiography machine: theory and experiment", *SPIE Proceedings Vol. 5745 Medical Imaging 2005: Physics of Medical Imaging*, pp. 1179.

Schuit, S.C., van der Klift, M., Weel, A.E., de Laet, C.E., Burger, H., Seeman, E., Hofman, A., Uitterlinden, A.G., van Leeuwen, J.P. & Pols, H.A. 2004, "Fracture incidence and association with bone mineral density in elderly men and women: the Rotterdam Study", *Bone,* vol. 34, no. 1, pp. 195-202.

Seely, J.F., Boyer, C.N. & Holland, G.E. 2001, *Dual energy X-ray densitometry apparatus and method using single X-ray pulse.*, 378/98.9 edn, H05G 1/64, United States.

Seibert, J.A. 2004, "X-ray imaging physics for nuclear medicine technologists. Part 1: Basic principles of x-ray production", *Journal of nuclear medicine technology,* vol. 32, no. 3, pp. 139-147.

Sharif, B.S., Zaroug, S.A., Chester, E.G., Owen, J.P. & Lee, E.J. 1994, "Bone edge detection in hand radiographic images", *Engineering in Medicine and Biology Society, 1994. Engineering Advances: New Opportunities for Biomedical Engineers. Proceedings of the 16th Annual International Conference of the IEEE*, pp. 514.

Siewerdsen, J.H., Waese, A.M., Moseley, D.J., Richard, S. & Jaffray, D.A. 2004, "Spektr: a computational tool for x-ray spectral analysis and imaging system optimization", *Medical physics,* vol. 31, no. 11, pp. 3057-3067.

Siris, E.S., Brenneman, S.K., Miller, P.D., Barrett-Connor, E., Chen, Y.T., Sherwood, L.M. & Abbott, T.A. 2004, "Predictive value of low BMD for 1-year fracture outcomes is similar for postmenopausal women ages 50-64 and 65 and Older: results from the National Osteoporosis Risk Assessment (NORA)", *Journal of bone and mineral research,* vol. 19, no. 8, pp. 1215-1220.

Skipper, J.A. & Hangartner, T.N. 1996, "Optimizing X-ray spectra for dual-energy radiographic bone densitometry", *Biomedical Engineering Conference, 1996., Proceedings of the 1996 Fifteenth Southern*, pp. 297.

Snyman, J.A. 2005, *Practical Mathematical Optimization: An Introduction to Basic Optimization Theory and Classical and New Gradient-Based Algorithms,* Springer Science+Business Media, Inc., New York, USA.

Sornay-Rendu, E., Munoz, F., Garnero, P., Duboeuf, F. & Delmas, P.D. 2005, "Identification of osteopenic women at high risk of fracture: the OFELY study", *Journal of bone and mineral research,* vol. 20, no. 10, pp. 1813-1819.

Sotoca, J.M., Iñesta, J.M. & Belmonte, M.A. 2003, "Hand bone segmentation in radioabsorptiometry images for computerised bone mass assessment", *Computerized Medical Imaging and Graphics,* vol. 27, no. 6, pp. 459-467.

Srinivasan, B., Kopperdahl, D.L., Amin, S., Atkinson, E.J., Camp, J., Robb, R.A., Riggs, B.L., Orwoll, E.S., Melton, L.J.,3rd, Keaveny, T.M. & Khosla, S. 2012, "Relationship of femoral neck areal bone mineral density to volumetric bone mineral density, bone size, and femoral strength in men and women", *Osteoporosis international,* vol. 23, no. 1, pp. 155-162.

Steel, S.A., Swann, P., Langley, G. & Langton, C.M. 1997, "A phantom for evaluating bone mineral density of the hand by dual-energy x-ray absorptiometry", *Physiological Measurement,* vol. 18, no. 3, pp. 233-240.

Steiger, P., Block, J.E., Steiger, S., Heuck, A.F., Friedlander, A., Ettinger, B., Harris, S.T., Glüer, C.C. & Genant, H.K. 1990, "Spinal bone mineral density measured with quantitative CT: effect of region of interest, vertebral level, and technique.", *Radiology,* vol. 175, no. 2, pp. 537-543.

Stein, J.A. 1989, *Bone densitometer*, 378/54 edn, G01B 15/02, United States.

Stierstorfer, K. & Spahn, M. 1999, "Self-normalizing method to measure the detective quantum efficiency of a wide range of x-ray detectors", *Medical physics,* vol. 26, no. 7, pp. 1312-1319.

Styner, M., Brechbuhler, C., Szckely, G. & Gerig, G. 2000, "Parametric estimate of intensity inhomogeneities applied to MRI", *Medical Imaging, IEEE Transactions on,* vol. 19, no. 3, pp. 153-165.

Swanpalmer, J., Kullenberg, R. & Hansson, T. 1998, "Measurement of bone mineral using multiple-energy x-ray absorptiometry", *Physics in Medicine and Biology,* vol. 43, no. 2, pp. 379-387.

Symmons, R. 2004, "Digital photodensitometry: a reliable and accessible method for measuring bone density", *Journal of Archaeological Science,* vol. 31, no. 6, pp. 711-719.

Tapiovaara, M. 2005, "Image quality measurements in radiology", *Radiation Protection Dosimetry,* vol. 117, no. 1-3, pp. 116-119.

Thodberg, H.H. & Rosholm, A. 2003, "Application of the active shape model in a commercial medical device for bone densitometry", *Image and Vision Computing,* vol. 21, no. 13–14, pp. 1155-1161.

Thorpe, J.A. & Steel, S.A. 2008, "The Alara Metriscan phalangeal densitometer: evaluation and triage thresholds", *The British journal of radiology,* vol. 81, no. 970, pp. 778-783.

Thorpe, J.A. & Steel, S.A. 2006, "The DXL Calscan heel densitometer: evaluation and diagnostic thresholds", *The British journal of radiology,* vol. 79, no. 940, pp. 336-341.

Trauernicht, C., Rall, C., Perks, T., Maree, G., Hering, E. & Steiner, S. 2012, "Dose Reduction and Image Preservation After the Introduction of a 0.1 mm Cu Filter into the LODOX Statscan Unit above 110 kVp", *13th International Congress of the International Radiation Protection Association*.

UNFPA 2012, *Ageing in the 21st Century: A Celebration and a Challenge.* Available: http://unfpa.org/ageingreport/ [20113, December/5].

Vaananen, S.P., Isaksson, H., Julkunen, P., Sirola, J., Kroger, H. & Jurvelin, J.S. 2011, "Assessment of the 3-D shape and mechanics of the proximal femur using a shape template and a bone mineral density image", *Biomechanics and modeling in mechanobiology,* vol. 10, no. 4, pp. 529-538.

van Kuijk, C. 2010, "Pediatric bone densitometry", *Radiologic clinics of North America,* vol. 48, no. 3, pp. 623-627.

Versluis, R.G.J.A., Vismans, F.J.F.E., van de Ven, C.M., Springer, M.P. & Petri, H. 1999, "Radiographic Absorptiometry of the Phalanges as a Screening Instrument to Detect Osteoporosis of the Hip", *Acta radiologica,* vol. 40, no. 4, pp. 418-421.

Wahner, H.W. & Fogelman, I. 1994, *The evaluation of osteoporosis: Dual energy X-ray absorptiometry in clinical practice,* 1st edn, Martin Dunitz Ltd, London, UK.

Wasnich, R.D. 1998, "Perspective on fracture risk and phalangeal bone mineral density", *Journal of clinical densitometry,* vol. 1, no. 3, pp. 259-268.

Wehrli, F.W., Ford, J.C., Attie, M., Kressel, H.Y. & Kaplan, F.S. 1991, "Trabecular structure: preliminary application of MR interferometry", *Radiology,* vol. 179, no. 3, pp. 615-621.

Wehrli, F.W., Hilaire, L., Fernandez-Seara, M., Gomberg, B.R., Song, H.K., Zemel, B., Loh, L. & Snyder, P.J. 2002, "Quantitative magnetic resonance imaging in the calcaneus and femur of women with varying degrees of osteopenia and vertebral deformity status", *Journal of bone and mineral research,* vol. 17, no. 12, pp. 2265-2273.

Wehrli, F.W., Song, H.K., Saha, P.K. & Wright, A.C. 2006, "Quantitative MRI for the assessment of bone structure and function", *NMR in biomedicine,* vol. 19, no. 7, pp. 731-764.

Whitley, D. 2001, "An overview of evolutionary algorithms: practical issues and common pitfalls", *Information and Software Technology,* vol. 43, no. 14, pp. 817-831.

Whitmarsh, T., Humbert, L., De Craene, M., Del Rio Barquero, L.M. & Frangi, A.F. 2011, "Reconstructing the 3D shape and bone mineral density distribution of the proximal femur from dual-energy X-ray absorptiometry", *IEEE Transactions on Medical Imaging,* vol. 30, no. 12, pp. 2101-2114.

WHO 2003, "Prevention and management of osteoporosis", *World Health Organization technical report series,* vol. 921, pp. 1-164, back cover.

Wilczek, M.L., Kalvesten, J., Algulin, J., Beiki, O. & Brismar, T.B. 2013, "Digital X-ray radiogrammetry of hand or wrist radiographs can predict hip fracture risk--a study in 5,420 women and 2,837 men", *European radiology,* vol. 23, no. 5, pp. 1383-1391.

Williams, M.B., Krupinski, E.A., Strauss, K.J., Breeden, W.K.,3rd, Rzeszotarski, M.S., Applegate, K., Wyatt, M., Bjork, S. & Seibert, J.A. 2007, "Digital radiography image quality: image acquisition", *Journal of the American College of Radiology : JACR,* vol. 4, no. 6, pp. 371-388.

Williams, M.B., Mangiafico, P.A. & Simoni, P.U. 1999, "Noise power spectra of images from digital mammography detectors", *Medical physics,* vol. 26, no. 7, pp. 1279-1293.

Willis, C.E., Thompson, S.K. & Shepard, J.S. 2004, "Artifacts and misadventures in digital radiography", *Applied Radiology,* vol. 32, no. 1, pp. 11-21.

Xu, C. & Prince, J.L. 2000, " Gradient Vector Flow Deformable Models. " in *Handbook of Medical Imaging: Processing and Analysis.* , ed. I. Bankman, Academic Press, Baltimore, US, pp. 159-170.

Xu, C., Yezzi, A. & Prince, J.L. 2000a, "On the Relationship between Parametric and Geometric Active Contours", *34th Asilomar Conference on Signals, Systems, and Computers*, pp. 483.

Xu, C., Pham, D.L. & Prince, J.L. 2000b, "Image segmentation using deformable models" in *Handbook of Medical Imaging. Volume 2: Medical Image Processing and Analysis*, eds. J.M. Fitzpatrick & M. Sonka, Kluwer Academic/Plenum Publishers, New York, pp. 129-174.

Xu, C. & Prince, J.L. 1998b, "Generalized gradient vector flow external forces for active contours", *Signal Processing,* vol. 71, no. 2, pp. 131-139.

Xu, C. & Prince, J.L. 1998a, "Snakes, shapes, and gradient vector flow", *Image Processing, IEEE Transactions on,* vol. 7, no. 3, pp. 359-369.

Yang, S.O., Hagiwara, S., Engelke, K., Dhillon, M.S., Guglielmi, G., Bendavid, E.J., Soejima, O., Nelson, D.L. & Genant, H.K. 1994, "Radiographic absorptiometry for bone mineral measurement of the phalanges: precision and accuracy study", *Radiology,* vol. 192, no. 3, pp. 857-859.

Yoshioka, H., Ito, S., Handa, S., Tomiha, S., Kose, K., Haishi, T., Tsutsumi, A. & Sumida, T. 2006, "Low-field compact magnetic resonance imaging system for the hand and wrist in rheumatoid arthritis", *Journal of Magnetic Resonance Imaging,* vol. 23, no. 3, pp. 370-376.

Yumru, A.E., Bozkurt, M., Aksoy, H.E., Inci Coskun, E. & Ayanoglu, Y.T. March 2009, "Comparison of Dual X-ray Laser and Dual Energy X-ray Absorptiometry Techniques of Osteodensitometry", *The Journal of international medical research,* vol. 37, pp. 541-546(6)

Yun, W., Wang, Y. & Scott, D.D. 2005, *Dual-band detetctor system for X-ray imaging of biological samples.*, 378/62 edn, G01N 23/04.

Zhang, J., Yan, C.H., Chui, C.K. & Ong, S.H. 2010, "Accurate Measurement of Bone Mineral Density Using Clinical CT Imaging With Single Energy Beam Spectral Intensity Correction", *Medical Imaging, IEEE Transactions on,* vol. 29, no. 7, pp. 1382-1389.